Final Scientific/Technical Report

Federal Agency and Organization Element

U.S. Department of Energy
National Energy Technology Laboratory [DOE-NETL]

Funding Opportunity Number

DE-FOA-0001826: "Developing Technologies to Advance the Understanding of State of Stress and Geomechanical Impacts within the Subsurface"
Area of Interest 2

Agreement Number

DE-FE0031684

Project Title

Improving Subsurface Stress Characterization for Carbon Dioxide Storage Projects by Incorporating Machine Learning Techniques

Principal investigator

William Ampomah
Email: William.Ampomah@nmt.edu Telephone: 575-835-5018

Submitting Institution

New Mexico Institute of Mining and Technology 801 Leroy Place
Socorro, NM 87801
DUNS # 041358904

Teaming Members

NMT: William Ampomah; Robert Balch; George El-kaseeh; Robert Will; Martha Cather; Samuel A. Acheampong; Marcia McMillan; Noah Hobbs
LANL: Lianjie Huang (Co-PI); Xuejian Liu; Yan Qin; Jiaxuan Li; Kai Gao; David Li
CONSULTANTS: Tom Bratton; Donald Lee

Submission Date

March 30, 2023

Project Period

10/1/2018 – 9/30/2022

Limitations On Public Release

None

Signature of Submitting Official

William Ampomah
Email: William.Ampomah@nmt.edu

ACKNOWLEDGEMENT OF FEDERAL FUNDING

This material is based upon work supported by the U.S. Department of Energy, National Energy Technology Laboratory [DOE-NETL], under Award Number DE-FE0031684.

DISCLAIMER

Executive Summary

The overall objective of this project is to develop a framework for reliable characterization and prediction of the state of stress in the overburden and underburden (including the basement) in CO_2 storage reservoirs using machine learning and integrated geomechanics and geophysical methods. Specifically, we developed a workflow encompassing the technologies and/or methods for predicting stress and pressure changes due to CO_2 injection in an active tertiary recovery site and their impacts on subtle fault activation, fractures and occurrence of microseismic events and compare responses to field observations.

In this project, we utilized dataset from the Farnsworth field Unit (FWU) which is operated by Purdure Petroleum. A novel elastic-waveform VSP inversion technique was used to estimate high- resolution spatial and temporal changes of elastic moduli in CO_2 storage reservoirs, which was combined with velocity-stress relationship derived from laboratory tests to obtain subsurface pressure and stress. Clustered microseismic data was jointly inverted for improved focal mechanisms. Least- squares reverse-time migration of microseismic waveform data was performed to directly image fracture/fault zones. Additionally, a deep neural network machine learning technique with convolutional and recurrent layers was used for learning the spectro-temporal structures in microseismic waveforms. The results of this geotechnical data analysis was integrated to develop a high-resolution 3D mechanical earth model extending from the overburden sealing formations to the underburden including the basement. Mechanical properties were derived through integration of mechanical logs, tests, available results from chemo-mechanical laboratory tests, and elastic inversion of seismic data using a combination of Bayesian and stochastic methods as well as machine learning technique. Failure features (faults/fractures) were represented and/or modeled based on seismic and core data analysis. A transient hydrodynamic-geomechanical model was developed through coupling with the calibrated FWU reservoir simulation model. The full physics coupled model was used to train a reduced order proxy model using machine learning algorithm for estimating stress which was then used with appropriate constitutive relationships and forward seismological models to simulate pressure changes and induced microseismicity. An advanced optimization framework was developed to perform a history match to minimize error between field observations and simulated. The history matched proxy model was verified against the full-physics equivalent. The field observations that will be used in the coupled model calibration process include pressure/stress inverted from VSP, moment magnitude from microseismic analysis, real time downhole pressure measurements, production and injection data. Parameter sensitivity and uncertainty analysis was performed to characterize the impact of model parameter uncertainty on stress estimates.

The project will have significant impact on future field implementation of the technology. Because the project field site is an ongoing CO_2 EOR development, the value of the new technology will be demonstrated in an operational context and evaluated as a viable risk mitigation strategy. Cost/benefit will be evaluated together with the various commercial incentives for CO_2 sequestration available to oil and gas operators. The extensive available dataset and ongoing data acquisition under the Southwest Regional Partnership (SWP) Phase III work plan provides flexibility for investigation of multiple approaches and reduces technical risk.

Table of Contents

LIST OF TABLES

Table **Page**

LIST OF FIGURES

Figure **Page**

Chapter 1
Introduction

1.1 Project Overview

In this project, we develop a framework to boost the reliability of characterization and prediction of the state of stress in the overburden and underburden (including the basement) in CO_2 storage reservoirs using novel machine learning and integrated geomechanics and geophysical methods. Specifically, we propose to develop a comprehensive workflow encompassing technologies and/or methods to predict stress and pressure changes caused by CO_2 injection in an active tertiary recovery site and their impacts on subtle fault activation, fractures and occurrence of microseismic events and compare responses to field observations. We are using datasets from the Farnsworth field Unit (FWU) operated by Purdure Petroleum for the research. In particular we will (1) conduct elastic-waveform inversion of 3D surface seismic data and time-lapse 3D VSP data to estimate high-resolution spatial and temporal changes of elastic moduli in CO_2 storage reservoirs, and then use the velocity-stress relationship derived from laboratory tests to obtain subsurface pressure and stress changes; (2) jointly invert microseismic data for improved focal mechanisms; (3) perform least-squares reverse-time migration of microseismic waveform data to directly image fracture/fault zones; (4) use a deep neural network machine learning technique with convolutional and recurrent layers for learning the spectro-temporal structures in microseismic waveforms; (5) integrate the results of our geotechnical data analyses to develop a high-resolution 3D mechanical Earth model extending from the overburden sealing formations to the underburden including the basement; (6) develop a transient hydrodynamic-geomechanical model through coupling with the calibrated FWU reservoir simulation model; (7) develop an advanced optimization framework to perform a history match to minimize error between field observations and simulated results; and (8) verify the history matched proxy model against the full-physics equivalent and forecast future performance and its stress evolution.

1.2 Problem statement

While general mechanisms for induced seismicity are well understood (NAS 2013), current models are not adequately representative of the in-situ properties and conditions dictating the accumulation stress and its release as seismic energy. The ability to predict microseismicity will rely on both theoretical models and statistical methods. Earthquakes and microseismicity result when stored strain energy is released from rock deformation during failure. Such failure can occur in intact rock when stresses exceed the rock strength, or upon re-activation of pre-existing failure planes when shear stresses overcome frictional forces (Zoback, 2007). Forces in the subsurface can be categorized generally by scale. Forces resulting from pressure diffusion and poro-elastic stress transfer act at local and intermediate scale while isostatic forces dominate at regional scale (Grasso, 1992). “Anthropogenic” or “induced” seismicity generally results when pore-pressure changes from fluid injection and production activity modifies the effective stress regime. Fluid injection can reduce the effective frictional forces on pre-existing failure planes (faults and fractures) or generally reduce effective normal stresses in a porous rock volume. Both fluid injection and extraction activity can change state of stress due to rock volumetric changes induced through poroelastic effects. For any fluid injection or production scenario the timing and extent of stress release is a function of in-situ stress orientation, the rock volume affected by pore-pressure diffusion, the rock mechanical and petrophysical (slow slip) properties, and the orientation, size and the strength and permeability characteristics of pre-existing failure planes.

Our existing studies at the FWU confirm the need for comprehensive geomechanical study. Although the Enhanced oil recovery (EOR) field development strategy currently implemented at FWU is, in the short term, volumetrically neutral suggesting minimal anthropogenic stress variations and induced activity, the history of field pressure at FWU since 1955 includes 2000 psia drawdown from initial during depletion, increase to the range of 4700 psia compared to initial pressure during waterflood. The reservoir pressures are measured in pounds per square inch absolute (psia). The aforementioned pressure history is certain to have significant aerially extensive and persistent effects on the state of stress in the subsurface and is typical for similar mature fields under EOR development. Kumar et al. (2017) and SWP have observed evidence of seismic and aseismic activity at FWU. Any incentives (financial or otherwise) for increased CO_2 storage in using EOR (CCUS) will motivate field operational schemes resulting in increased reservoir pressure and the potential for induced microseismicity.

1.3 Project Objectives

The primary objective of this project is to develop a framework to boost the reliability of characterization and prediction of the state of stress in the overburden and underburden (including the basement) in CO_2 storage reservoirs using novel machine learning and integrated geomechanics and geophysical methods. We will use field data and models developed by the Southwest Regional Partnership on Carbon Sequestration (SWP) for the Farnsworth Unit (FWU), a CO2 enhanced oil recovery (EOR) project in Ochiltree County, Texas, to verify the improved capabilities of our proposed methods. Specific objectives for the project include:

1. Employing a novel elastic-waveform inversion technique on time-lapse Velocity Seismic Profile (VSP) data to estimate high-resolution spatial and temporal changes in stress/pressure at the different time-steps for calibration of a 4D mechanical Earth coupled model (MEM).
2. Jointly inverting clustered microseismic data for focal mechanisms of microseismic events to reduce the inversion uncertainty, and directly imaging fracture/fault zones using least-squares reverse-time migration of microseismic data. A moment magnitude computed from microseismic inversion will be used to calibrate the 4D MEM coupled model.
3. Using deep neural network machine learning with convolutional and recurrent layers to improve clustering of microseismic events using their spectro-temporal patterns.
4. Developing a new structural and stratigraphic framework model that is consistent with basin history and fault kinematic principles.
5. Developing a high-resolution stress prediction MEM extending from the overburden sealing formations to the underburden, including the basement, through tight integration of available petrophysical and geophysical data.
6. Developing innovative machine learning assisted process for calibrating a coupled stress prediction model through “history matching” with observations of stress dependent behavior derived from geophysical analyses including and especially those developed in this project.

1.4 Project Approach

To address the research gaps, we proposed to develop a set of analytical tools and advanced integration methodology to vastly improve the reliability of prediction of temporal and spatial stress changes in the subsurface, including the underburden, using a combination of theoretical and statistical methods. We will develop novel analytical tools, including machine learning assisted analyses of active and passive

seismic data, which will yield direct and indirect observations of pressure and stress effects in the subsurface. The integration methodology (Fig. 1.1) is an adaptation of industry accepted practices for calibration of flow simulation models to calibration of a coupled geomechanical model for stress prediction with machine learning to overcome computational challenges. The proposed integration method is unique because we will overcome the inherent limitations posed by non-uniqueness and spatial temporal sampling incompleteness of independent geotechnical data sets for predicting stress in 3D space. The integration workflow will rely on extensive integration of petrophysical, mechanical, and seismological data. We will create high-quality, high-resolution physics-based hydrodynamic and coupled geomechanical forward models for training the stress prediction model through machine learning assisted optimization of comparison with direct and indirect observations of stress from microseismic ($Mo_{(obs)}$) and time-lapse VSP data ($\sigma_{VSP\ (obs)}$). The result of the integration process will be a calibrated physics-based coupled model for predicting stress and failure in the subsurface. We will demonstrate the practical application of the model using prediction of stress and seismicity for a set of simulations representing realistic field operational scenarios and subsurface structural uncertainty.

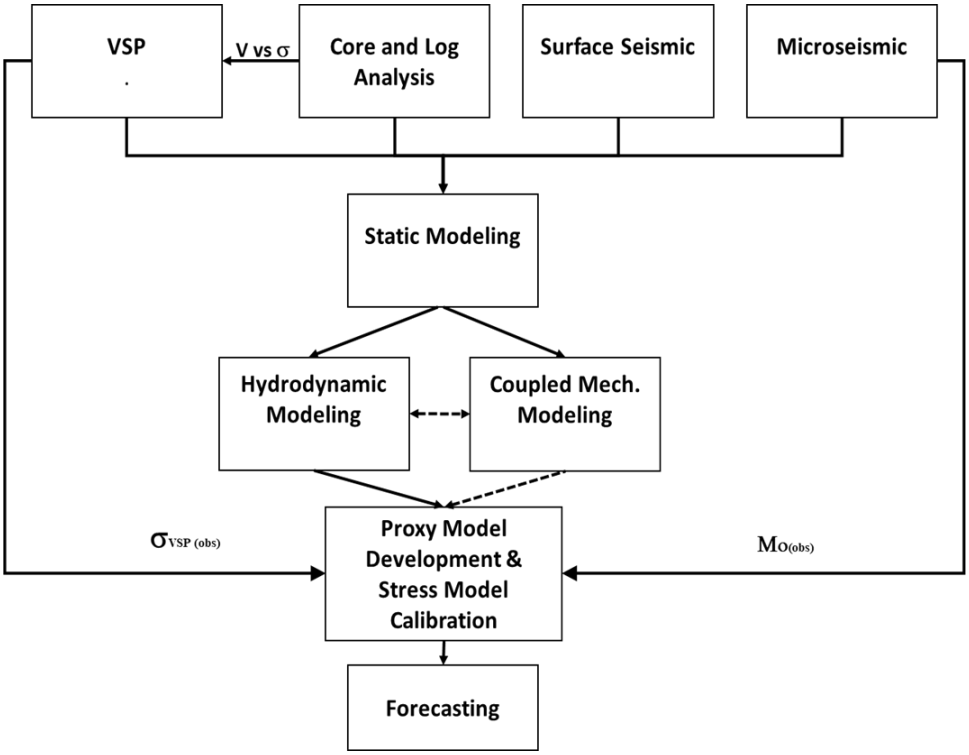

Figure 1.1: The Integration Framework

1.5 Project Approach

The report is divided into various chapters to address the key tasks and deliverables as proposed in the project scope of work. Each chapter is formatted to address specific aspects of the project objectives.

Chapter 1 – Introduction

Chapter 2 – Farnsworth field background, data acquisition and Description Chapter 3 – Wellbore Geomechanics

Chapter 4 – Seismic monitoring at the FWU CO2-EOR field using time-lapse waveform inversion of 3D- 3C VSP data

Chapter 5 – Microseismic Analysis

Chapter 6 – Coupled Geomechanics Models: Construction, initialization and Dynamic testing.

Chapter 7 – Vertical Seismic Profile Stress calibration

Chapter 8 – Coupled Hydromechanical modeling and assessment of induced seismicity at FWU: Utilizing time-lapse VSP and Microseismic data.

Chapter 2
Farnsworth Field Background, Data Acquisition and Description

2.1 Morrow B Background

The Farnsworth field unit (FWU), located in Ochiltree County, northern Texas (Figure 2.1), was discovered by Union Oil of California in 1955. The discovery wells were the No. 1 Russell well and No. 1 -32 Buckhaults well (Parker, 1956). The FWU is located in the western Anadarko Basin, and the depositional environment is an incised valley (Sorenson, 2005). FWU Original Oil in Place (OOIP) is 120 million barrels of oil (MMSTB), and the producing interval is a collection of Pennsylvanian age sands within Upper Morrow B. The Morrow B sands lie between 7550 -7950 ft., have an average thickness of 29 ft. and range in thickness from 0 ft. to 54 ft. (Munson, 1988). The Morrow B reservoir was under pressure at discovery (Ampomah, Balch, Cather, et al., 2016). Table 2.1 summarizes some basic Morrow B reservoir properties. The Morrow B sands, the overlying Morrow Shale and Underlying Morrow Shales are all Morrowan in age. The Atokan Thirteen finger overlies the Morrow Shale, and together they form the caprock intervals for the Morrow B storage compartments. Figure 2.2 shows a vertical cross-section through FWU formations along with a more detailed stratigraphic section of the Atokan and Morrowan formations. The expanded stratigraphic column shows the gamma-ray, resistivity and porosity logs. FWU is located in the Anadarko Basin. The Anadarko basin formed through the collision of the North American and South American plates during the late Morrowan into early Desmoinesan time, resulting in the formation of the Wichita orogeny (among other structural features) (Rascoe & Adler, 1983). Major structural modifications of the Anadarko basin ceased at the end of the Permian age. Subnormal Morrow B pressure is attributed to the erosion of the Permian sandstones and the release of water from the basin. The subsequent deposition of a 1000 ft. thick overlaying caprock caused the hydraulic separation from the rest of the column (Sorenson, 2005).

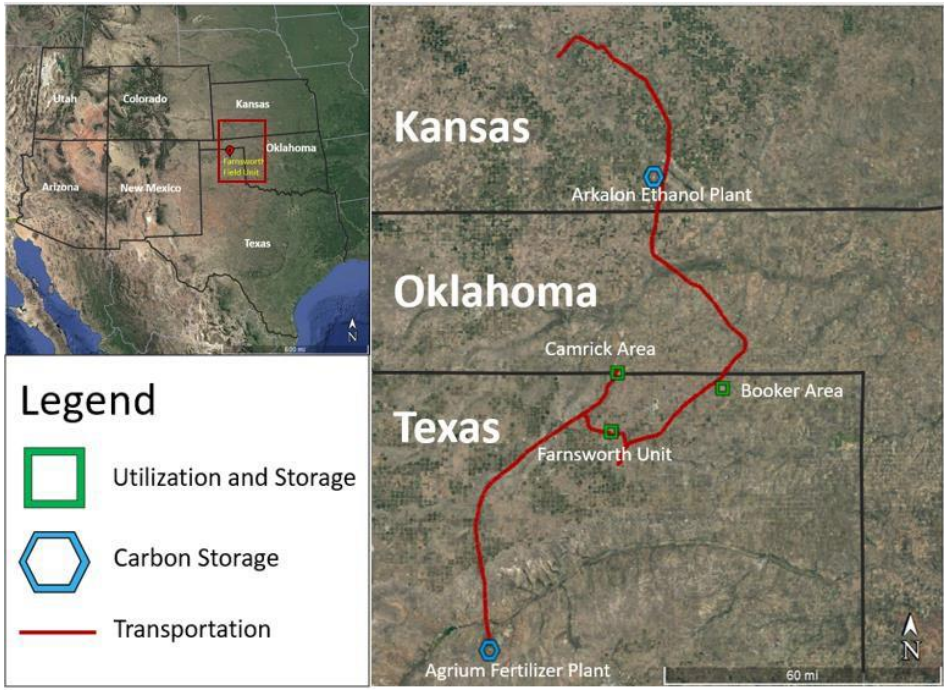

Figure 2.1: A Geographical Reference for the Southwest Regional Partnership on CO_2 Sequestration, The Anadarko Basin and Farnsworth Field Unit (FWU). The highlighted region is magnified to illustrate the sources of CO_2 and the connecting pipeline infrastructure (FWU).

Table 2.1: Basic Morrow B Reservoir Properties.

Reservoir Property	Value	Source
Initial Reservoir Pressure, psi	2217.7	(Gunda et al., 2015)
Initial Reservoir Temperature, ^{o}F	168	(Gunda et al., 2015)
Bubble Point Pressure, psi	2073.7	(Gunda et al., 2015)
Average Porosity, %	14	Ampomah, (2015)
Average Permeability, md	48.2	Ampomah, (2015)
Oil Formation Volume Factor, (rbbl/STB)	1.192	Ampomah, (2015)

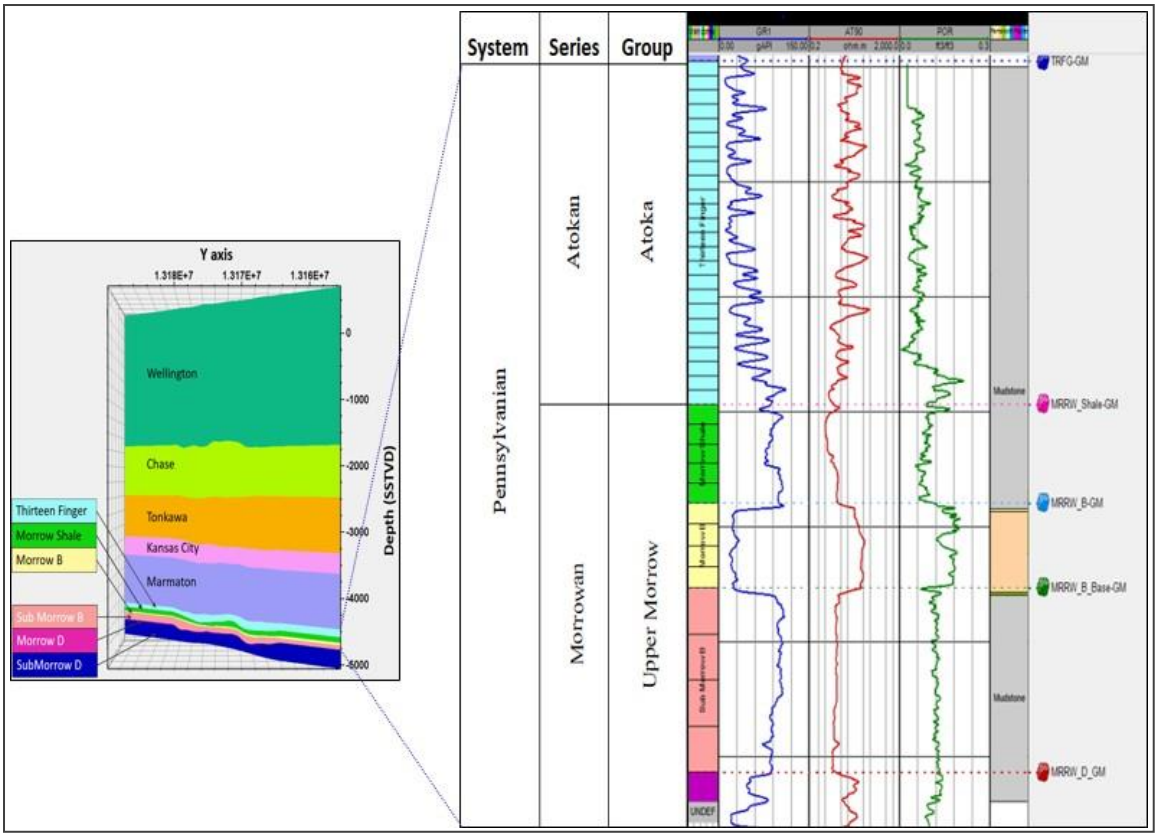

: Figure 2.2: Stratigraphic Column for Farnsworth Field Unit

2.2 Field Operational History and Production

Three different production methodologies have been applied to the Morrow B: primary depletion, water flooding, followed by CO_2-EOR. (Figure 2.3). Morrow B was discovered Union Oil of California in 1955 and was initially produced by depletion. By 1964, Morrow B made 9.8 MMSTB and witnessed declining pressures and production rates. As a result, Union Oil Company of California (UNOCAL) changed the production methodology to water-flooding. The water flooding was progressively implemented from west to east across the Morrow B in a 5-spot pattern. The water flood extended from 1964 to December 2010, a period of 46 years. Initially, waterflooding led to increased production rates at approximately 6000 stock tank barrels per day (STB/D). By 1986, Morrow B had produced 36.3 MMSTB and 28.8 billion cubic feet (BCF) but was once again experiencing declining oil production rates. Considerations for tertiary oil production methodologies were then underway. In 2009, Chaparral Energy acquired FWU and began a CO_2-EOR in December 2010 (Ampomah, Balch, Grigg, et al., 2016; M. D. White et al., 2014). CO_2 was obtained from Arkalon Ethanol Plant in Kansas and an Agrium Fertilizer Plant in Texas (Figure 2.1). The performance on the western Morrow B far superseded that of the eastern side. As such, the CO_2-EOR was implemented only on the west. The OOIP was computed from the simulation model as 68 MMSTB. During the CO_2-EOR operation, FWU has been studied by the Southwest Regional Partnership on Carbon Sequestration (SWP). SWP is one of seven partnerships that form a nationwide network that explores the capture and permanent storage of CO_2 to mitigate against global temperature rise. SWP studies are geared towards assuring CO_2 containment within the FWU storage compartment. Studies also focused on accounting for CO_2 volumes injected and CO_2 volumes permanently stored and understanding the optimum operational considerations for CO_2 storage (Balch et al., 2018).

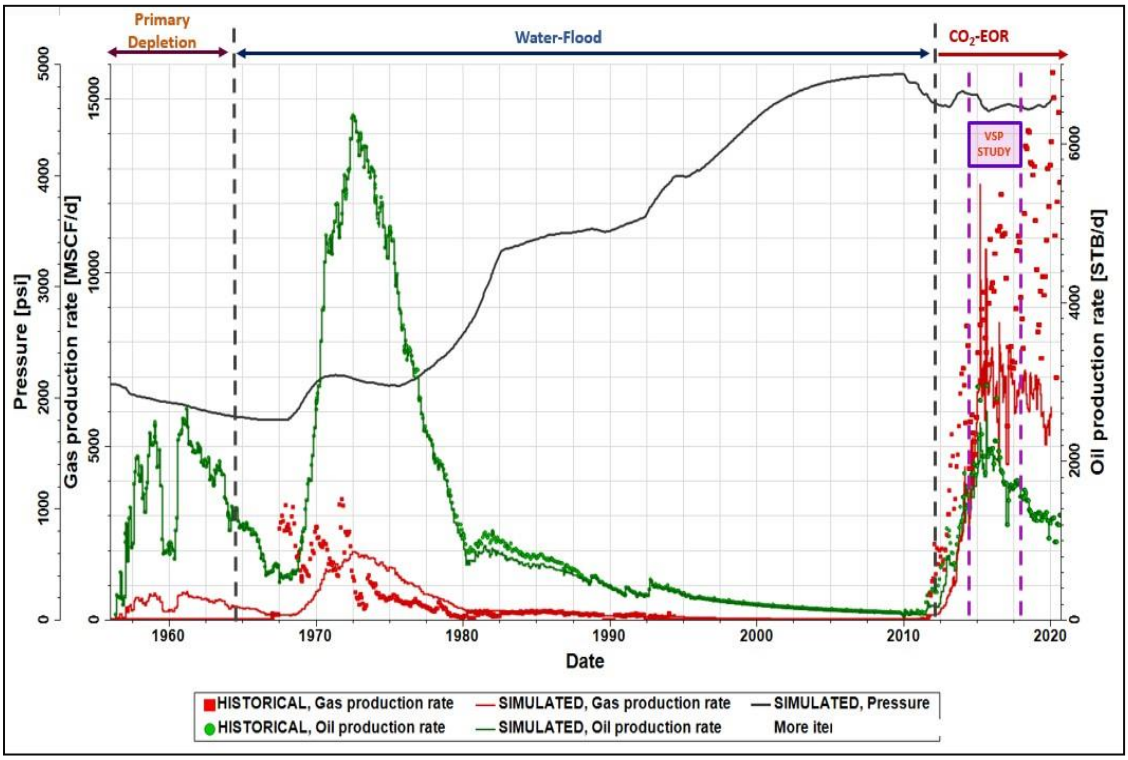

Figure 2.3: Morrow B pressure and production history with the production methodologies are highlighted

2.3 Vertical Seismic Profile Acquisition and Processing

2.3.1 Data Acquisition:

Two baseline 3D vertical seismic profile (VSP) surveys for two wells were acquired simultaneously in 2014 (wells 13-10A and 14-01), and a third one in 2015 (well 32-08). Two monitor (time-lapse) surveys for well 13-10A were acquired, one in January 2015 (~30,000 tons of CO_2 injected) and one in November 2016 (~80,000 tons CO_2 injected). The proximity of wells 13-10A and 14-01 presented the opportunity for simultaneous data acquisition. Ray tracing-based survey evaluation and design (SED) was conducted for the baseline surveys of the two wells to optimize acquisition parameters as well as to reduce data acquisition, processing time, and cost. The SED produced a geometry file with source locations that reflected the maximum usable offset distance. The simultaneous data acquisition reduced number of source points acquired by 2100 points (42%). Illumination maps (hit maps) were generated and analyzed to verify that target horizon (Morrow B) was adequately illuminated, Figure 2.4.

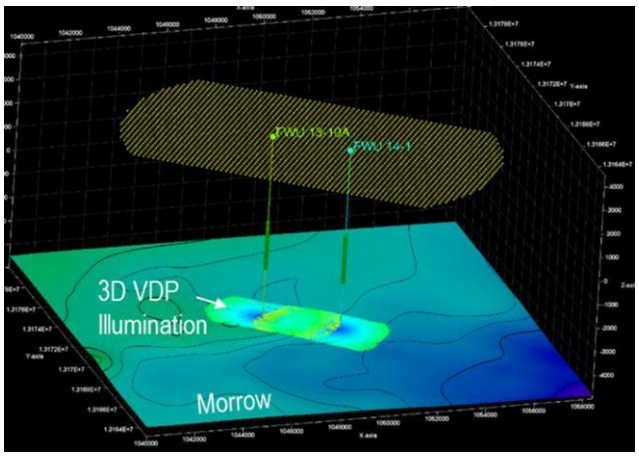

Figure 2.4: Illumination map (hit count at target horizon (Morrow B).

Acquisition parameters were determined based on analyses of the results from the SED study. Optimal survey planning was determined based on existing infrastructure and accessibility within the survey area. For operational reasons and to minimize negative impact on oil production, data acquisition of the three surveys were coordinated with the field operator to coincide with water injection period of water alternating gas (WAG) cycle, Figure 2.5.

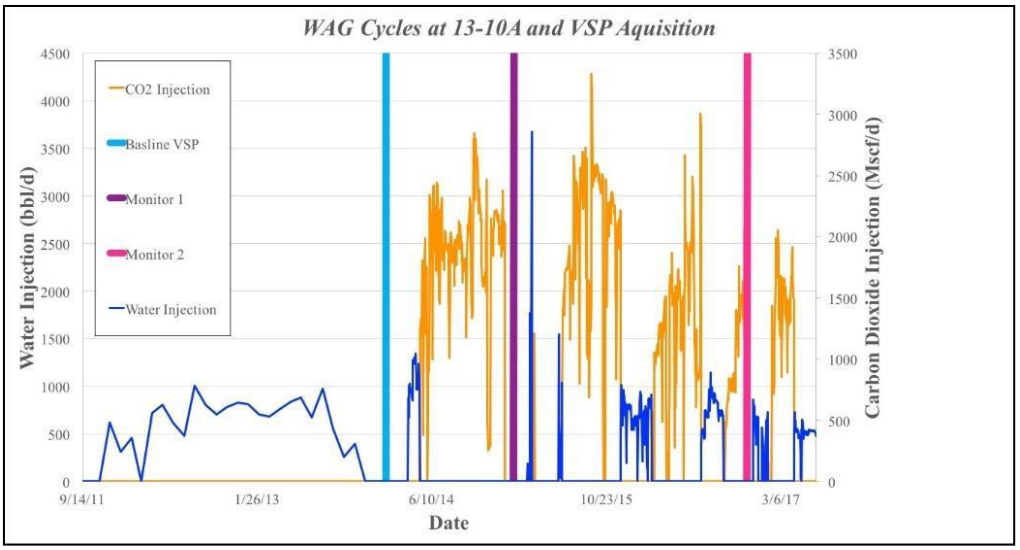

Figure 2.5: Water alternating gas (WAG) cycles is shown in conjunction with baseline, monitor 1 and monitor 2 VSP surveys.

To ensure repeatability and reduce uncertainty in time lapse analysis, source locations from baseline survey for well 13-10A were repeated for the two monitor surveys, same downhole tool and source parameters. In the early stages of processing, co-located sources from the three surveys were selected for subsequent processing. Tables 2.2 lists source parameters for all surveys. Tables 2.3-2.5 list elevations and receiver's parameters for wells 13-10A, 14-01 and 32-08, respectively.

Table 2.2: 3D VSP Source Parameters.

Type	Vibroseis
Source Point Interval	200 feet (60.1 meters)
Source Line Interval	200 feet (60.1 meters)
Sweep	3 sweeps. 2 Hz – 100 Hz (nonlinear)

Table 2.3: 3D VSP Receivers Parameters, Well 13-10A

Permanent Datum	MSL
Ground Level	3014 feet (918.7 meters)
Kelly Bushing	3031 feet (923.8 meters)
Type	40 level three components geophones
Receiver Depth Interval (MD)	3626 to 5576 feet (1105.2 to 1699.6 meters)
Receiver Interval	50 feet (15 meters)

Table 2.4: 3D VSP Receivers Parameters, well 14-01

Permanent Datum	MSL
Ground Level	3022 feet (921.1 meters)
Kelly Bushing	3037 feet (925.7 meters)
Type	40 level three components geophones
Receiver Depth Interval (MD)	3626 to 5576 feet (1105.2 to 1699.6 meters)
Receiver Interval	50 feet (15 meters)

Table 2.5: 3D VSP Receivers Parameters, well 32-08.

Permanent Datum	MSL
Ground Level	2993 feet (912.3 meters)
Kelly Bushing	3009 feet (917.1 meters)
Type	40 level three components geophones
Receiver Depth Interval (MD)	3593 to 5543 feet (1095.1 to 1689.5)
Receiver Interval	50 feet (15 meters)

2.3.2 Data Processing

3D VSP baseline data for each of the three wells was independently processed. For well 13-10A, data from Baseline and Monitor surveys were processed through an identical three-component (3C) processing workflow. Pre-processing included filling source/receiver geometry using information from field report, receiver selection, 3C orientation, noise attenuation, Surface Consistent Amplitude Compensation (SCAC), 3C wavefield separation, deterministic trace-by-trace wave-shaping deconvolution, and static correction. Figures 2.6 and 2.7 show the pre-processing and waveform processing workflows, respectively. This section focuses on processing of baseline and time-lapse surveys for well 13-10A. Time lapse (4D) analyses will be discussed in a separate section.

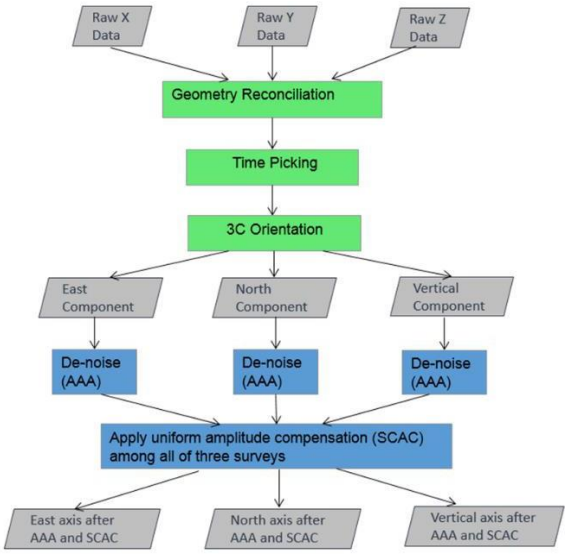

Figure 2.6: Pre-processing workflow for 3C data

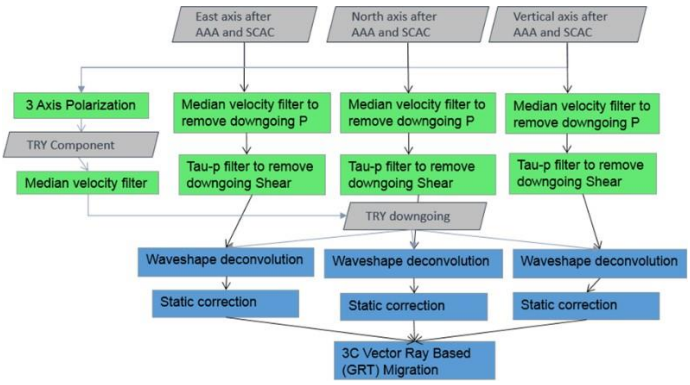

Figure 2.7: 3C waveform processing

2.3.3 Source co-location:

In order to minimize differences due to variation in acquisition geometries of the surveys, only the co-located shot points with receivers in good quality for the three surveys were used in the time-lapse processing. Source points locations within a 10 feet of spatial tolerance from source points of baseline survey were extracted for monitor 1 and monitor 2 surveys, Figure 2.8.

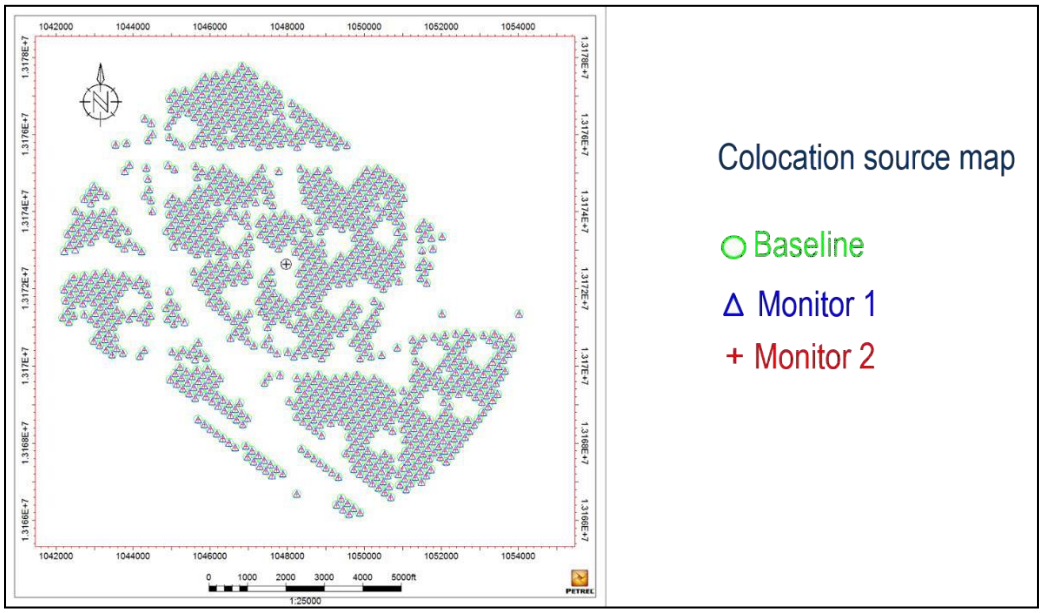

Figure 2.8: Co-located sources: Baseline, Monitor 1 and Monitor 2

2.3.4 Pre-processing and Data Preparation:

Raw data was loaded into processing system and True Vertical Depth (TVD) was applied. Source coordinates and elevation were updated in the seismic headers of each shot gather with values extracted from field report using GPS times as a reference, Figure 2.9.

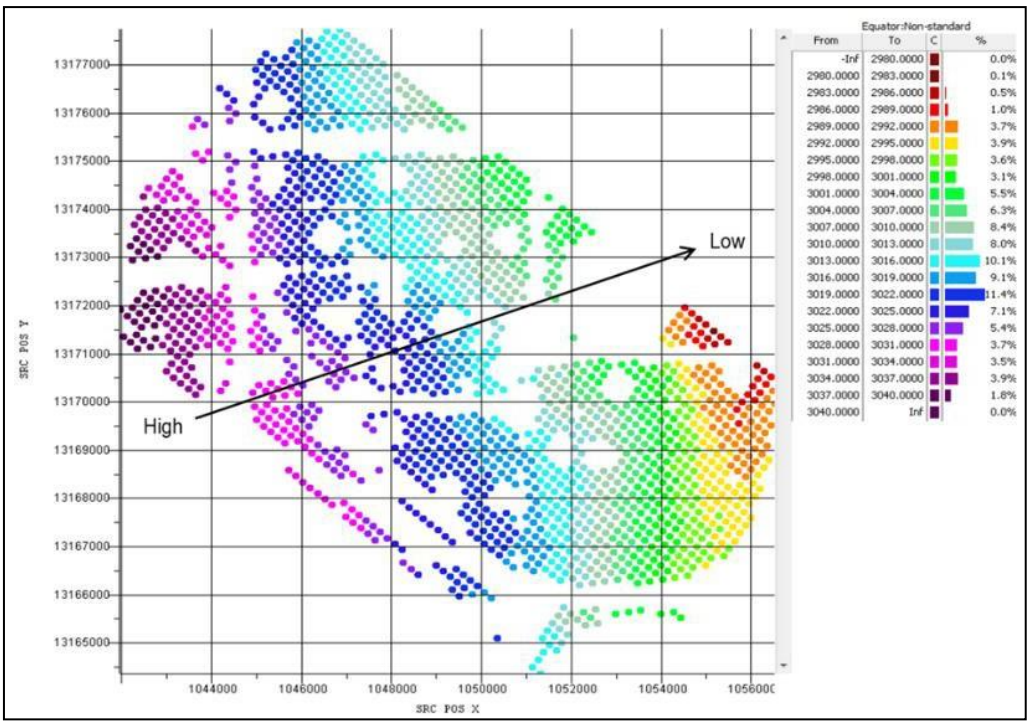

Figure 2.9: Baseline survey source elevation map

Travel-times of downhole geophones were picked on the first peak. For short-offset source locations, the down-going energy is propagating near-vertical, and the first arrivals are very coherent on the vertical (Z) component. As the source moves further away, the first arrivals on Z component become less coherent and horizontal components (X and Y) have to be used for determination of the first breaks. Extensive quality control of the first beak picking was done in the common source and common receiver gather domains. Manual picking was necessary for shot gathers with large source offsets. In general, it was possible to produce reliable transit times for all the source positions. Three different time-picking QC plots were generated and displayed. Figures 2.10 - 2.12 are QC plots for baseline survey. They illustrate consistent time-picking result. No outliers are observed in Figures 2.11 and 2.12, indicating time picks are consistent from receiver to receiver and shot gather to shot gather.

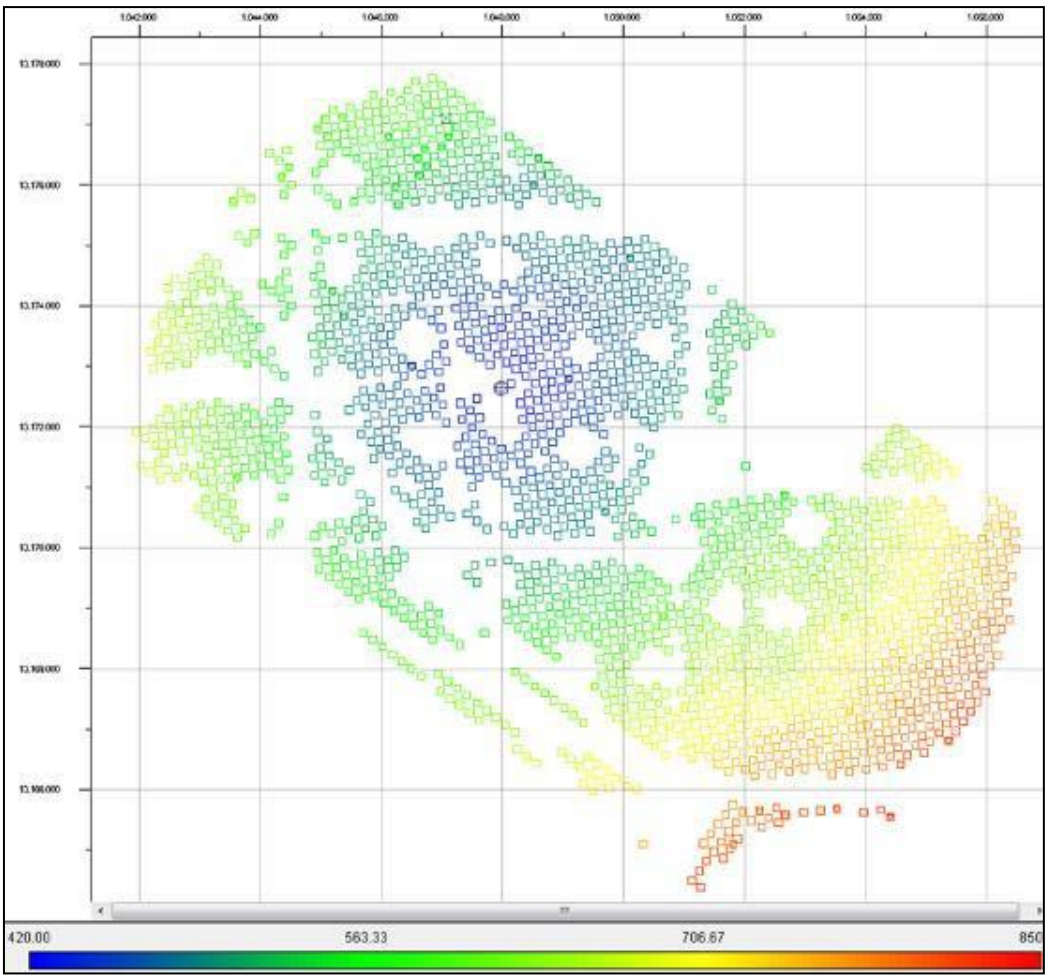

Figure 2.10: Picked first arrival of baseline survey at top receiver

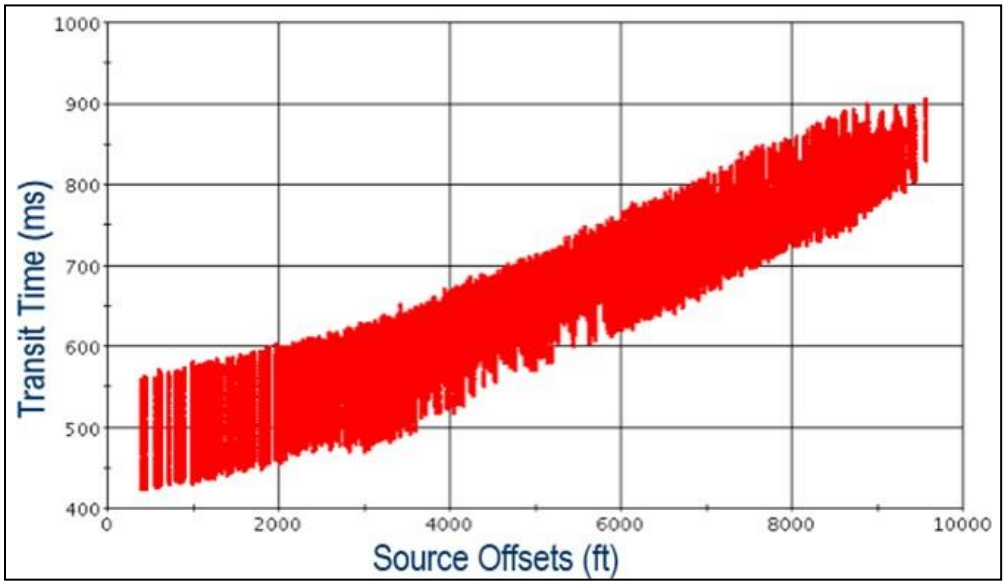

Figure 2.11: Baseline transit time vs. source offsets

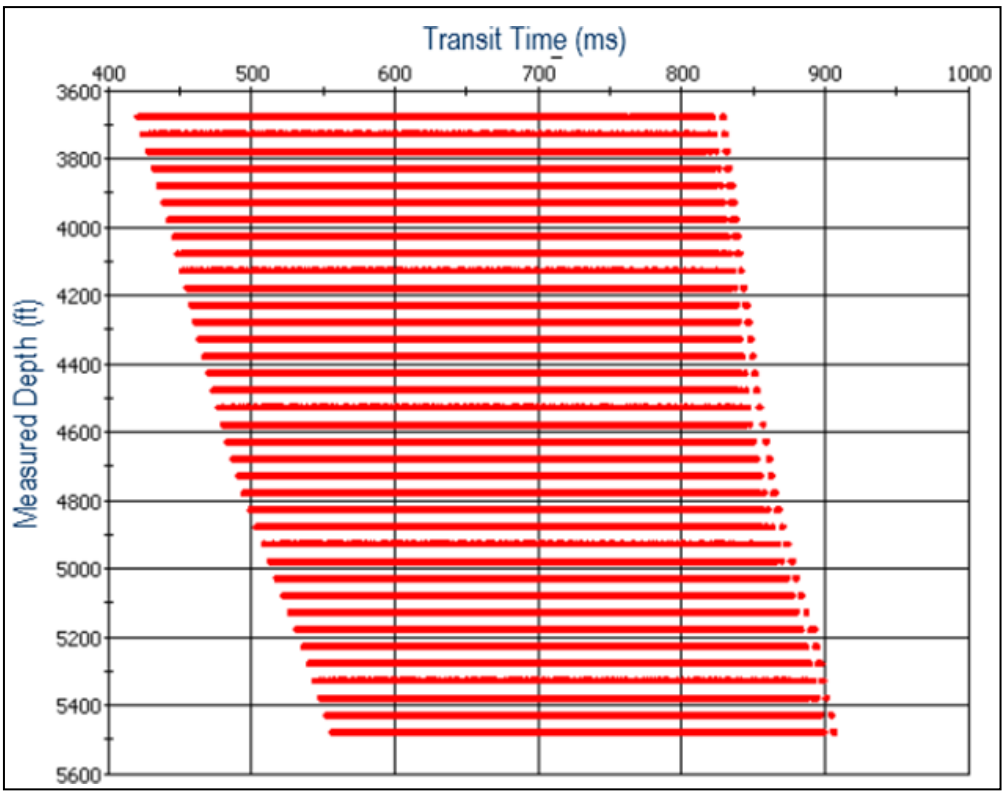

Figure 2.12: Baseline transit time vs. receiver depth

2.3.5 Survey Repeatability Quality Control:

Good repeatability among baseline survey and time-lapse surveys aids in reducing uncertainty in time-lapse analyses. Quality control to verify repeatability is performed at the early stages of processing and any necessary correction is applied. Quality control includes inspecting transit time difference between two surveys, waveform comparison for selected shots and Normalized Root Mean Square (NRMS) and repeatability of raw data. Transit times were compared between baseline and monitor 1 surveys. Figure 2.13 and 2.14 illustrate transit time difference versus receiver depth and time difference histogram. Both plots indicate good repeatability, as time difference is centered around +/- 1ms.

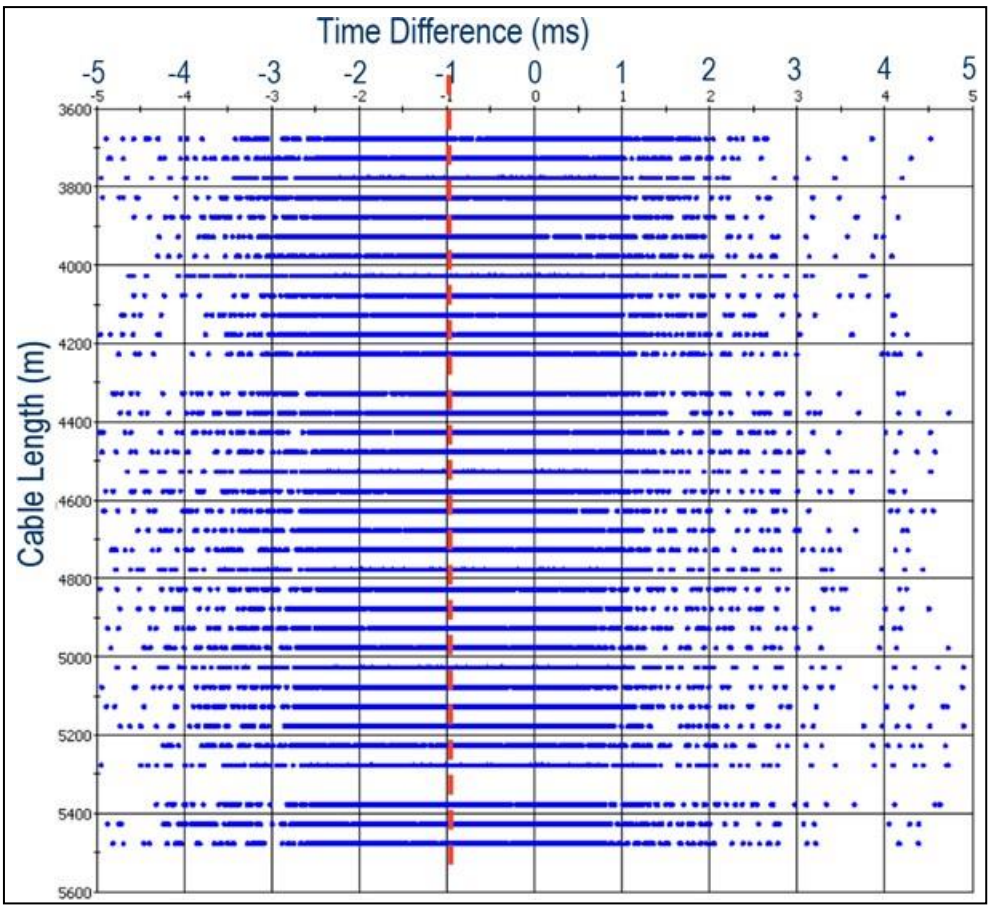

Figure 2.13: Time difference vs. receiver measurement depth between baseline and monitor 1 surveys

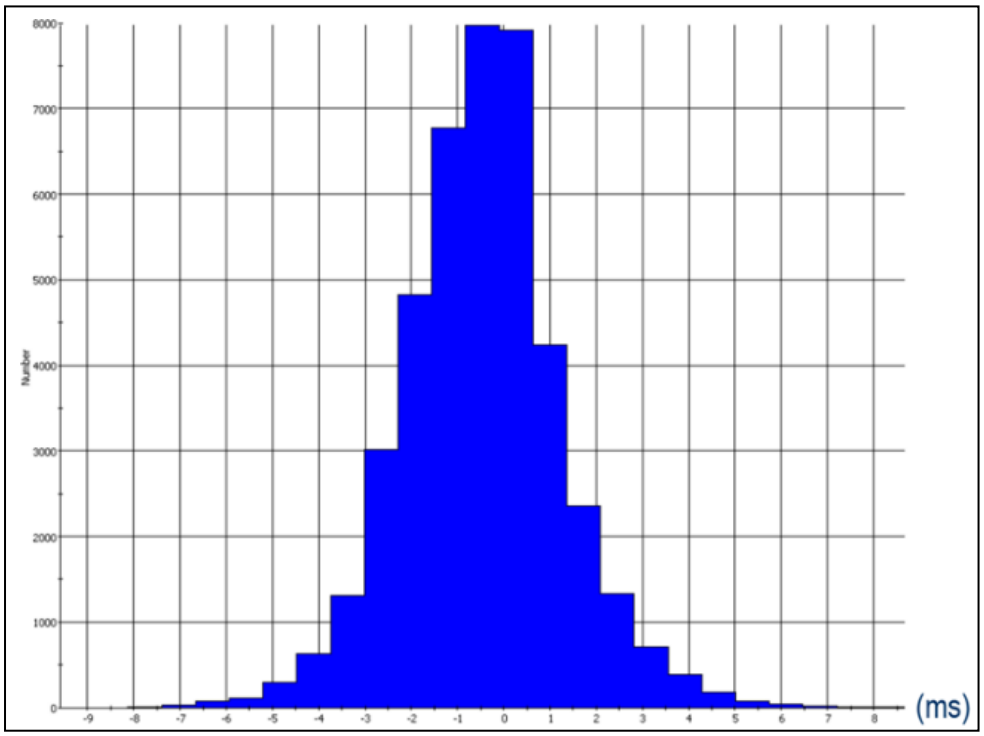

Figure 2.14: Time difference histogram, baseline and monitor 1 surveys

To verify that frequency contents are consistent between the two surveys, amplitude spectrum plots for near, middle and far offsets were generated and compared at a selected source location, Figure 39.

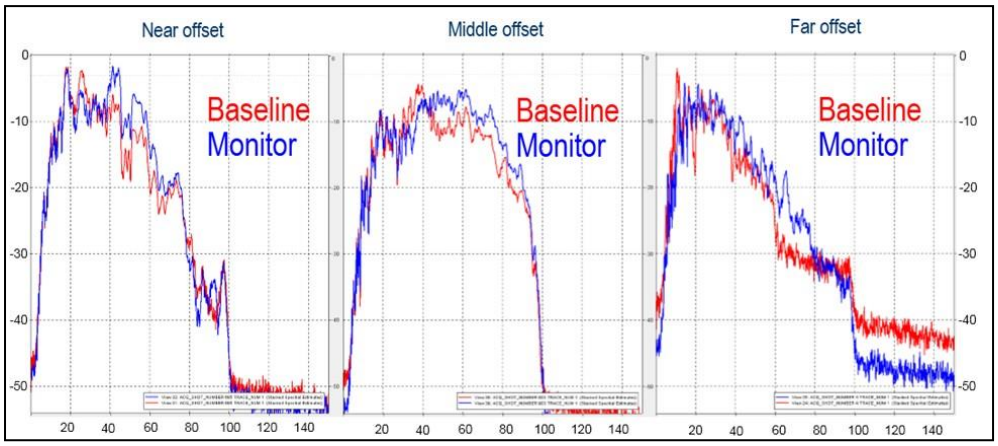

Figure 2.15: Amplitude spectrum comparison between baseline and monitor 1 surveys, near, middle and far offsets

2.3.6 Three-Components Orientation:

As shuttles (geophones) are connected to each other by flexible bridles, each shuttle is oriented arbitrarily during the acquisition from one tool position to another. To orient the recorded wavefield to the earth frame, the optimal relative bearing algorithm is used. This algorithm estimates receiver orientation by incorporating polarization angles and source-receiver geometry. Relative bearing values thus estimated are then used to orient raw dataset to true earth frame (East, North and Vertical). Several plots are generated from relative bearing estimation for QC purpose. One of the QC plots is the total error in bearing at each receiver. If the curve at each receiver reaches a minimum and has a relative low value, the estimated bearing angles are relatively reliable, Figures 2.16 – 2.18.

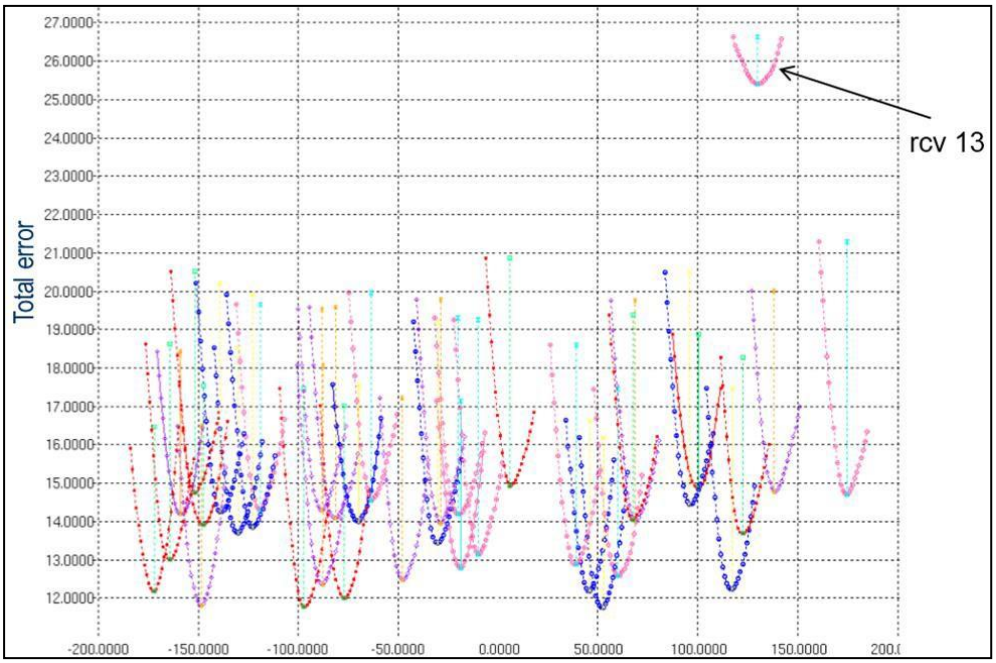

Figure 2.16: Orientation QC for baseline survey. Each curve represents one receiver and minimum of each curve is the optimal relative bearing angle at the receiver. Most of receivers are in good quality except for receiver 13, which has big error compared to other receivers.

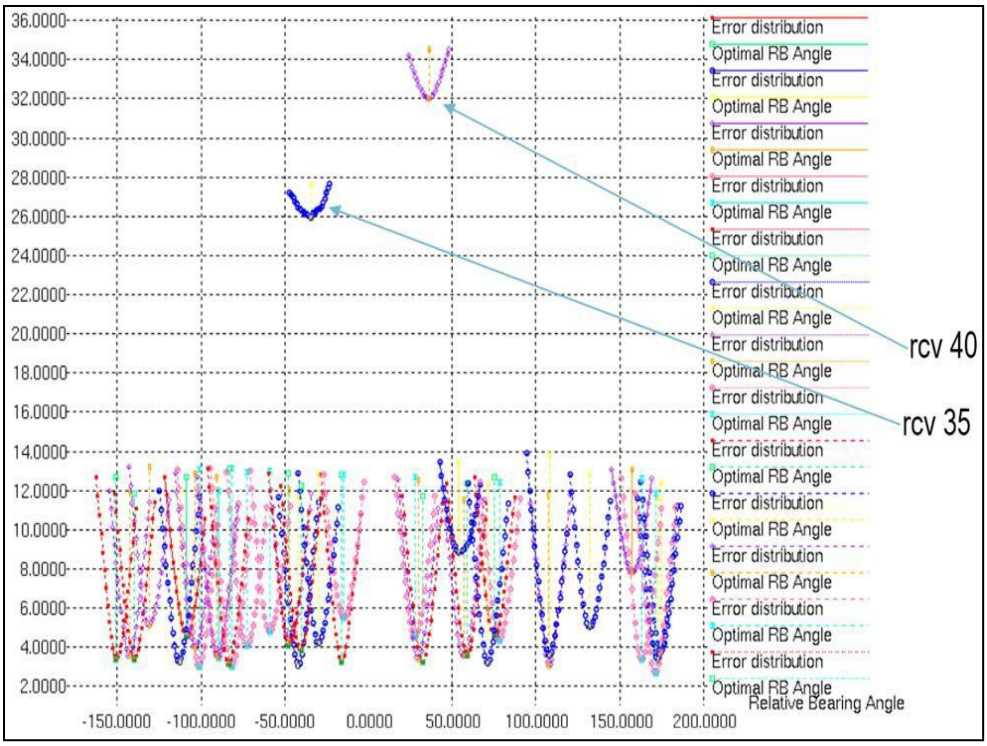

Figure 2.17: QC for monitor 1 survey. Each curve represents one receiver and minimum of each curve is the optimal relative bearing angle at the receiver. Most of receivers are in good quality except for receiver 35 and 40, which has big error compared to other receivers.

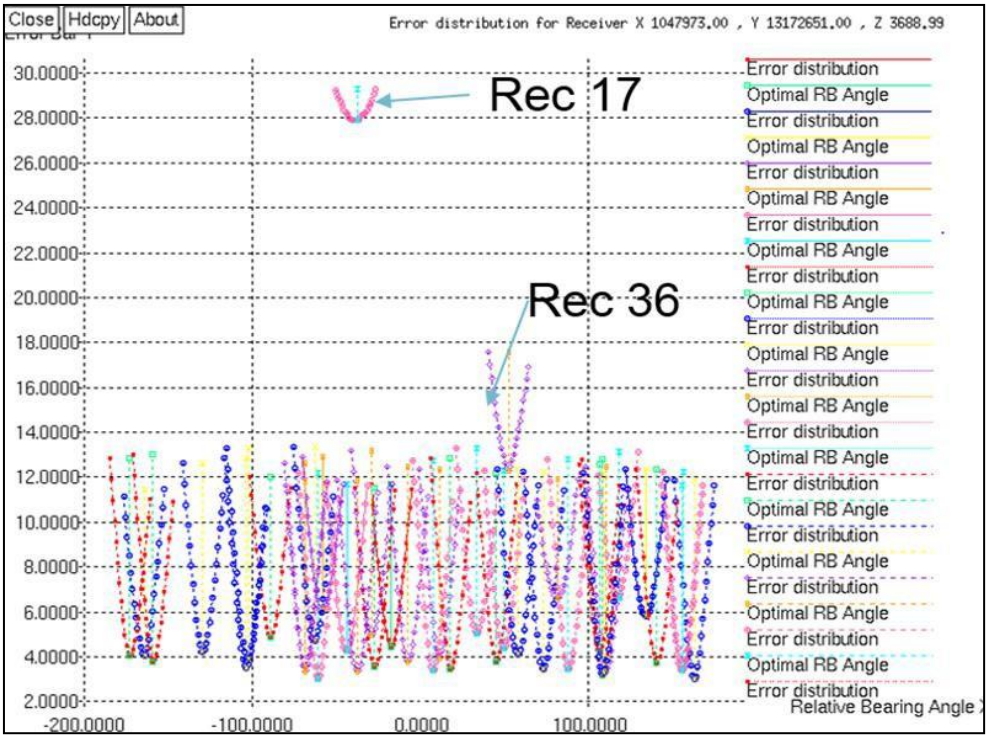

Figure 2.18: Orientation QC for monitor 2 survey. Each curve represents one receiver and minimum of each curve is the optimal relative bearing angle at the receiver. Most of receivers are in good quality except for receiver 17, which has big error compared to other receivers.

.

After the relative bearing is estimated for each receiver, the data are rotated to any reference frame for QC or true earth frame for 3C waveform separation. Figure 2.19 is raw X, Y and Z components from left to right. The X/Y component polarity in shot domain is not consistent with raw data. After the data are oriented to the Earth frame, the polarity of X/Y components in shot domain becomes consistent, Figure 2.20.

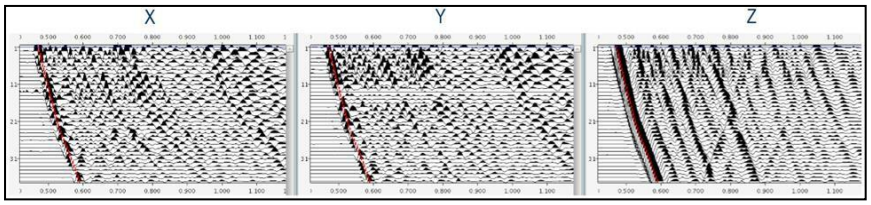

Figure 2.19: 3C waveform before orientation in shot domain

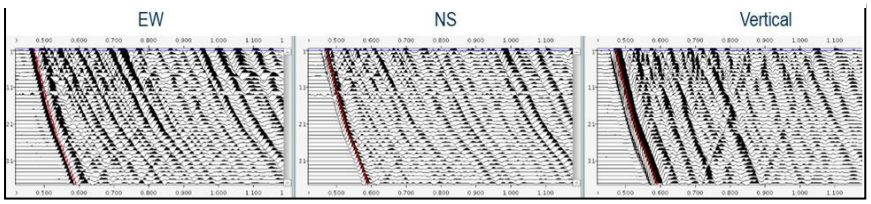

Figure 2.20: 3C waveform after orientation in shot domain

2.3.7 Noise attenuation:

Anomalous Amplitude Attenuation (AAA), a frequency domain spatial median filtering scheme, was employed for noise attenuation. In this scheme, the frequency bands with amplitudes that deviate from the median amplitude by a specified threshold are either scaled (multiplied by a specified scale factor) or replaced with an interpolated band using neighboring traces. For the Farnsworth 3D VSP dataset, the frequency bands with anomalously high amplitudes were scaled down by this process. A comparison of the oriented 3-components from baseline selected shot records before and after AAA is shown in Figures 2.21 and 2.22, respectively.

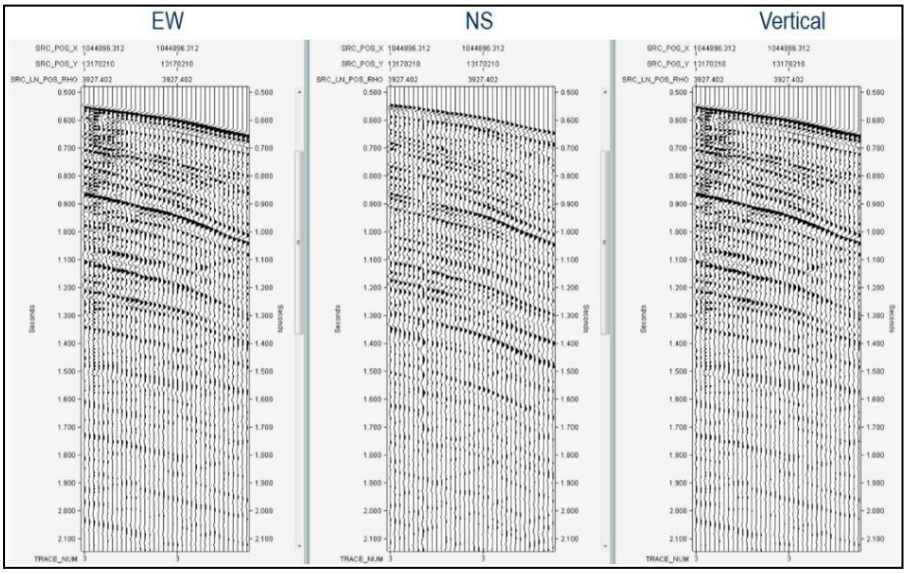

Figure 2.21: Oriented 3 components at middle offset before noise attenuation. Noise can be seen at shallow receivers.

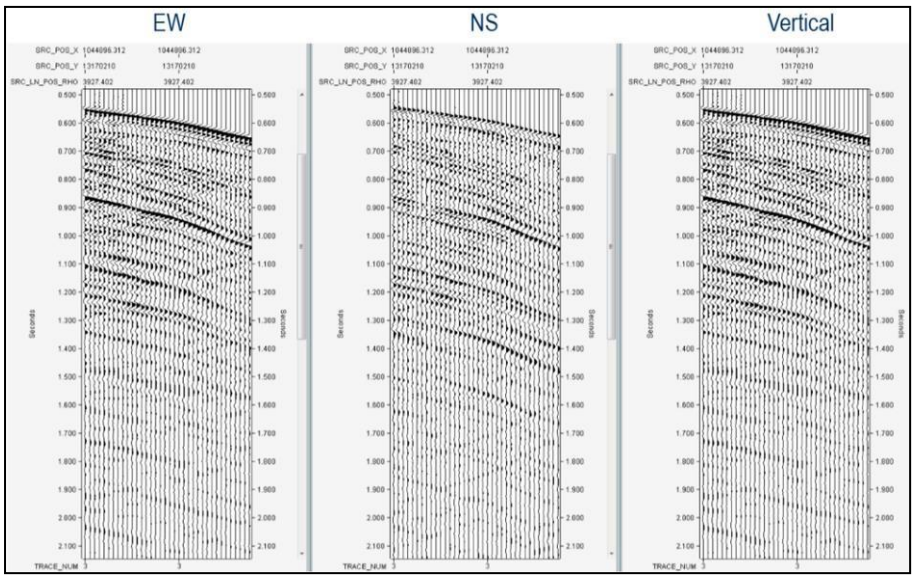

Figure 2.22: Oriented 3 components at middle offset after noise attenuation. Noise is attenuated at shallow receivers.

2.3.8 Surface Consistent Amplitude Compensation:

Lateral variations in surface and near surface conditions result in variable source to ground coupling causing differences in shot amplitudes as recorded by downhole receivers. To correct for amplitude variation in the data caused by above mentioned factors, Surface Consistent Amplitude Compensation (SCAC) algorithm was applied to the Farnsworth 3D VSP dataset. SCAC attempts to balance source, detector and offset amplitudes in a surface consistent manner. After SCAC application, the amplitudes for a given shot, detector, or offset should be the same as for any other shot, detector, or offset, respectively. SCAC does not alter traces signal-to-noise ratio. The process was applied in three steps:

1. Compute RMS amplitudes for a given time window
2. Decompose the amplitudes computed in step 1 into surface-consistent source, detector and offset terms
3. Compute and apply scaling factors to each trace in the previously specified time window. The scaling factor is the ratio of the geometric mean of all the source, detector, and offset terms to the individual trace's source, detector, and offset term. Since SCAC process was being applied to remove the source amplitude variations, only the source term was applied to the data

To match achieve proper amplitude matching among the three surveys, decomposition of terms was simultaneously executed for baseline and the two monitor surveys, figures 2.23 – 2.30.

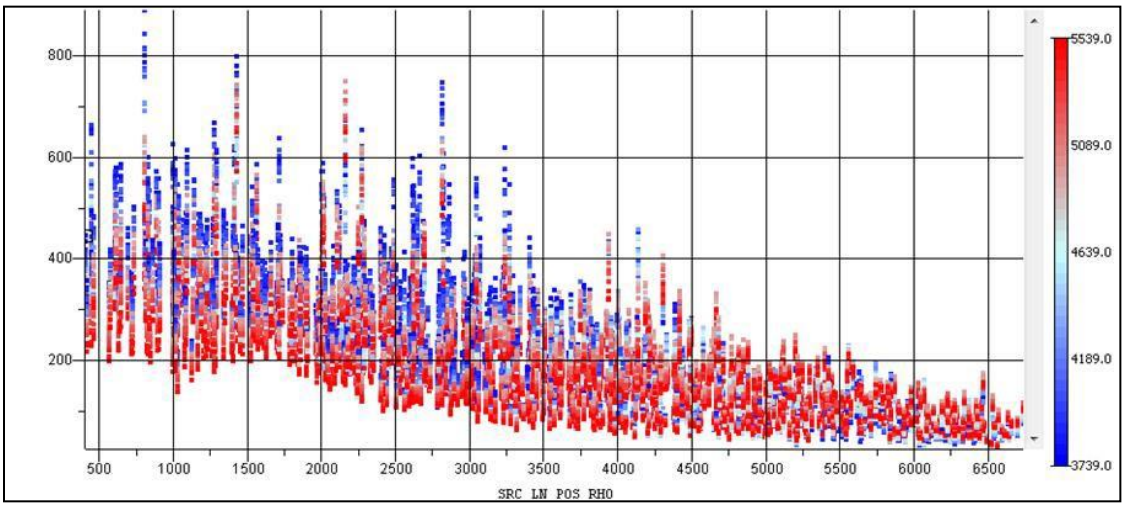

Figure 2.23: Baseline RMS amplitude before SCAC vs source offsets colored by receiver depths, in feet.

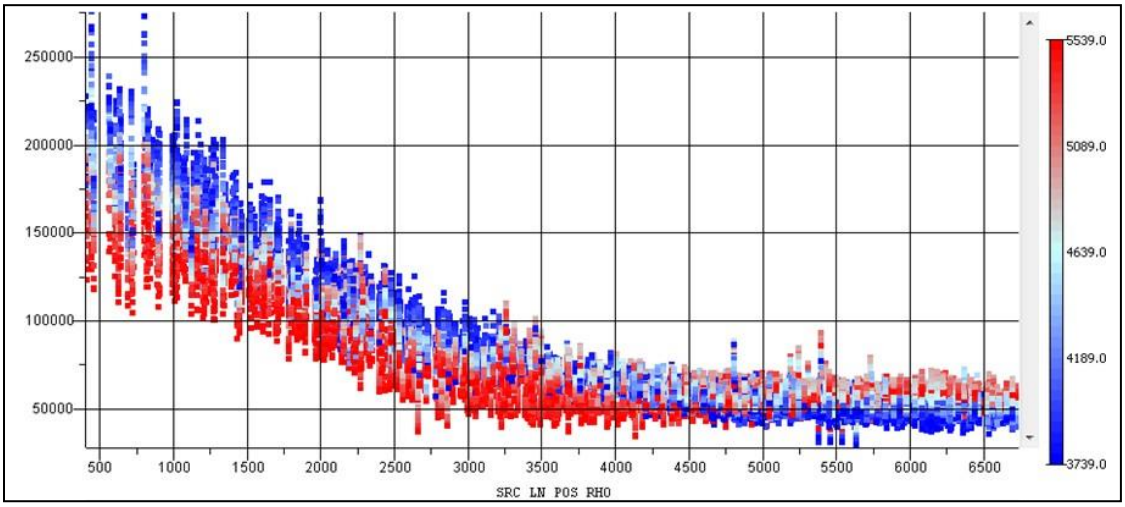

Figure 2.24: Baseline RMS amplitude after SCAC vs source offsets colored by receiver depths, in feet

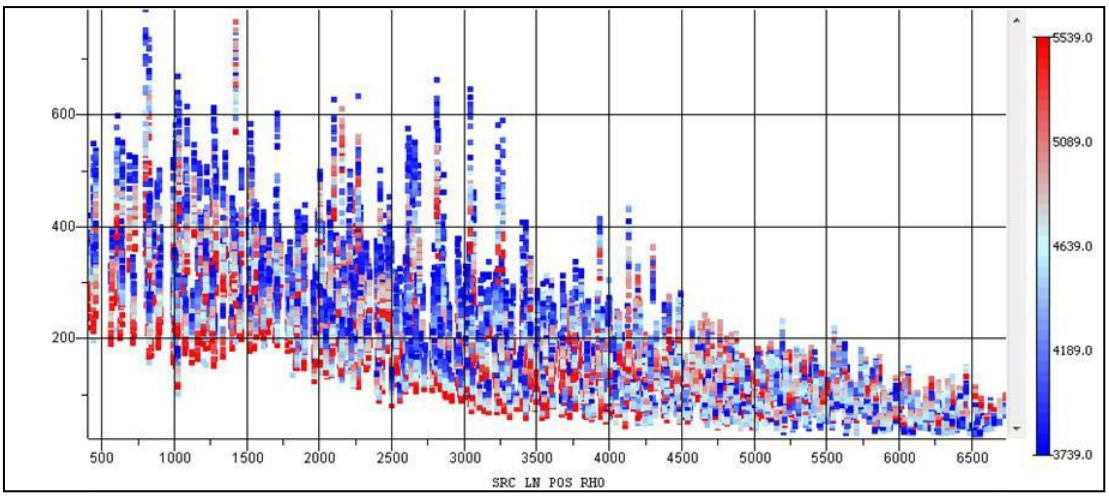

Figure 2.25: Monitor 1 RMS amplitude before SCAC vs source offsets colored by receiver depths in feet.

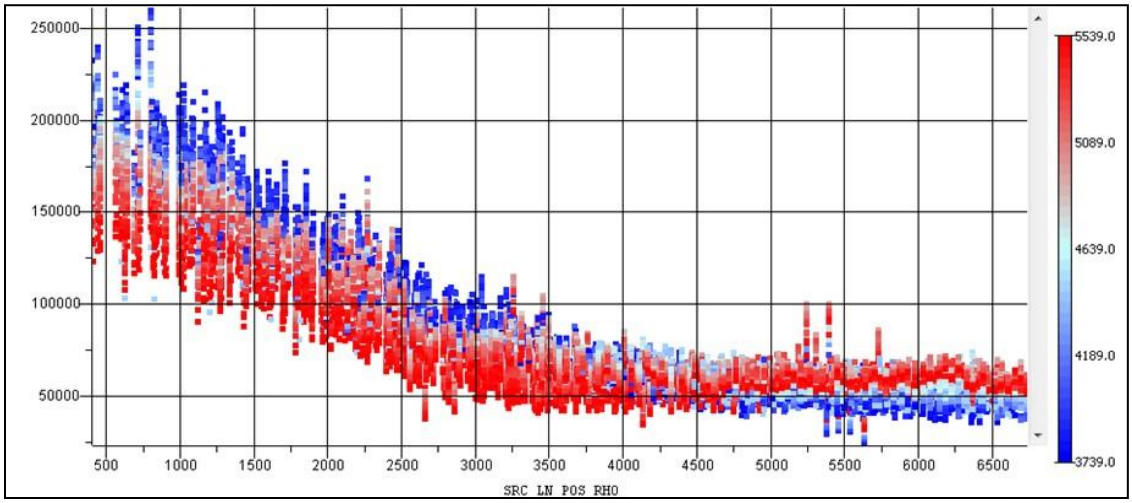

Figure 2.26: Monitor 1 RMS amplitude after SCAC vs source offsets colored by receiver depths, in feet.

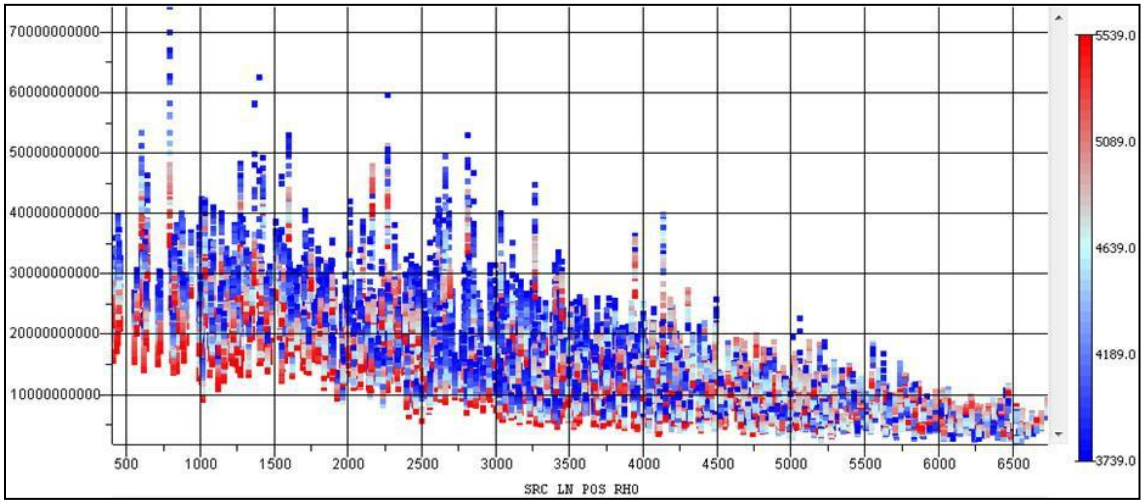

Figure 2.27: Figure 2.27: Monitor 2 RMS amplitude before SCAC vs source offsets colored by receiver depths, in feet

.

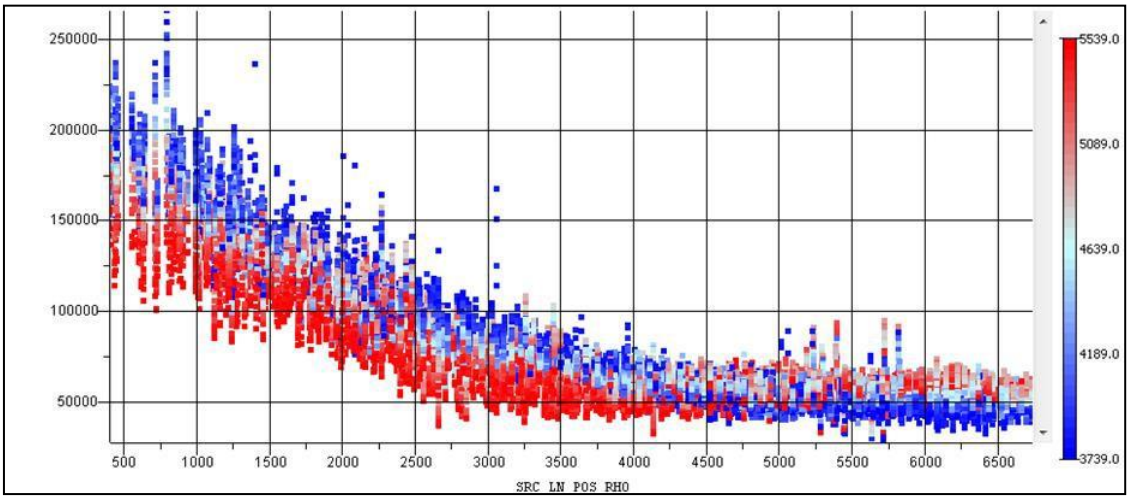

Figure 2.28: Monitor 2 RMS amplitude after SCAC vs source offsets colored by receiver depths, in feet.

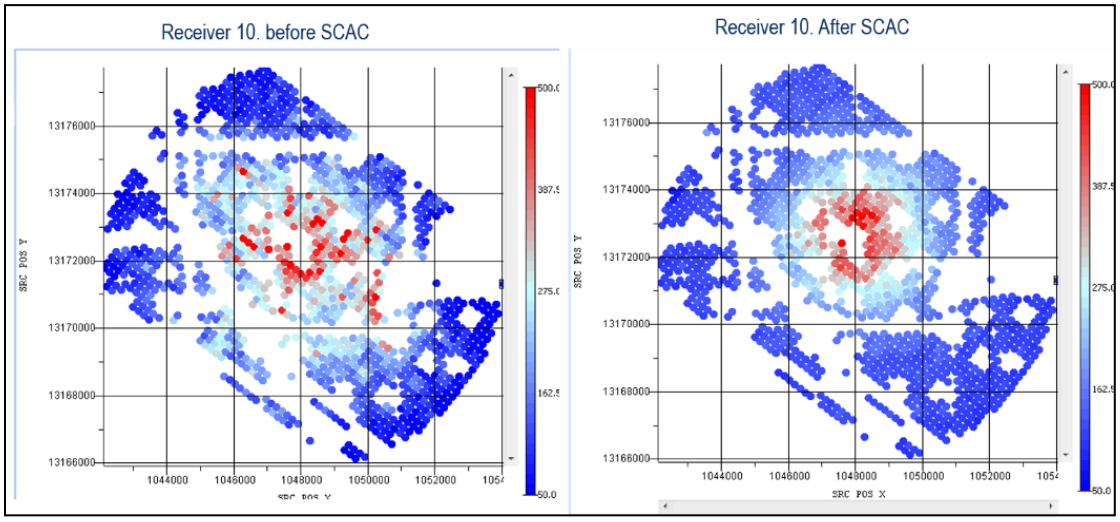

Figure 2.29: Monitor 2 RMS amplitude, before and after SCAC application.

.

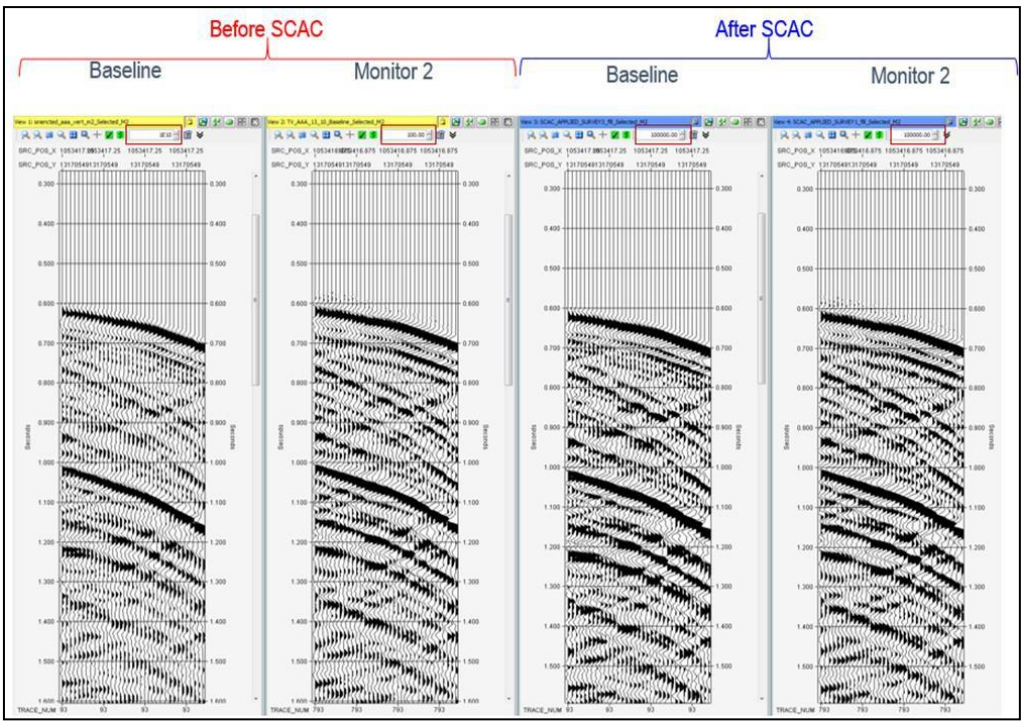

Figure 2.30: Shot gather before and after simultaneous SCAC application for amplitude matching

2.3.9 Three Components Wavefield Separation:

Waveform separation is a two-step process, median filter and tau-P. Waveform separation was applied on each component independently.

2.3.9.1 Median Filter:

A median filter was used to separate up-going from down-going energy in the 3-component data. The median filter is designed on the moveout of the down-going in the vertical component (P-wave) first arrival and is used to enhance the down-going wavefield. The enhanced down-going wavefield is then subtracted from the 3C data, leaving the residual wavefield that contains both the up-going P-wave and some shear wave energy. In this case, a 9-level median filter was applied to the data to enhance the down-going wavefield and the residual was obtained by subtracting the enhanced wavefield. After down-going P-wave was subtracted, some residual down-going shear wave arrivals remained in the total residual wavefield, figure 2.31. Tau-p filtering was used to attenuate the down-going Shear wave data.

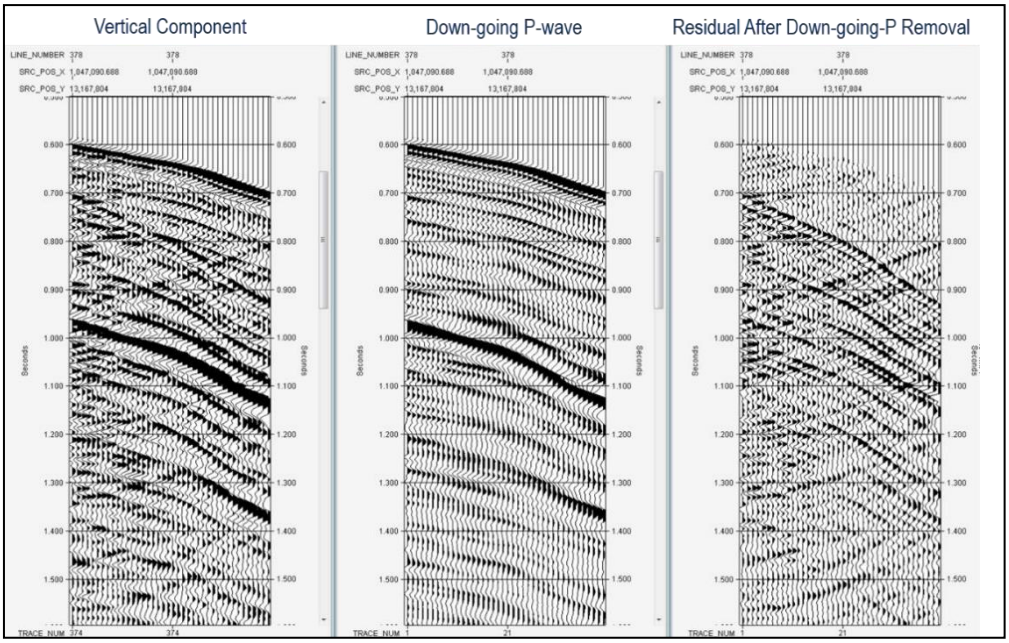

Figure 2.31: Median filter waveform separation of vertical component.

2.3.9.2 Tau-p Filter:

To eliminate down-going sheer-wave, the median filtered source gathers were transformed into the Tau-p domain. Mute was applied to remove down-going sheer-wave from the Tau-p converted gathers. Gathers with up-going P-wave only were subtracted from the original Tau-p gathers to produce down-going sheer-wave only gathers in Tau-p domain. Sheer-wave only gathers were then transformed back to T-X domain, and subtracted from the original T-X gather to produce up-going P-wave only gathers, figure 2.32.

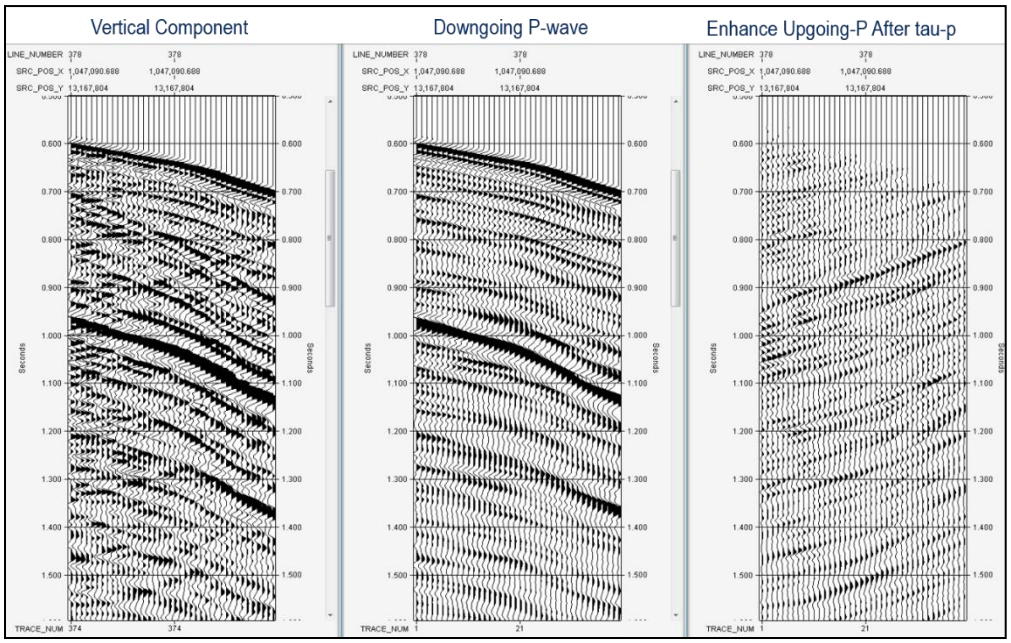

Figure 2.32: Waveform separation of vertical component using median filter and tau-p workflow

2.3.10 Deconvolution:

Deterministic VSP deconvolution is performed to zero-phase the wavelet and to remove reverberations associated with layers above the recording receiver depth. Deconvolution is designed on the down-going wavefield where the down-going wave-train is shaped to the desired wavelet. The estimated operator from the down-going wavefield is then applied to the up-going wavefield to obtain deconvolved up-going reflection data. Deconvolution operator was designed on a 500 ms window of the down-going wavefield at the first break. Based on the spectral analysis of the data, the down-going wavefield was shaped to a zero-phase wavelet representing the impulse response of a Butterworth filter within the frequency band from 3 to 100 Hz. White noise of 1% was added to stabilize the deconvolution operator especially for the far offsets, where higher frequencies are significantly attenuated.

For quality control of the convolution process, plots were generated for the bottom receiver for baseline and monitor 2 surveys, Figures 2.33 and 2.34. Frequency spectra for the same bottom receiver from baseline and monitor surveys were also generated, figures 2.35 and 2.36. Frequency spectra appears to be consistent from near to far offset after deconvolution. Both waveform and spectra between baseline and monitor surveys are very similar, an indication of good repeatability and consistent processing.

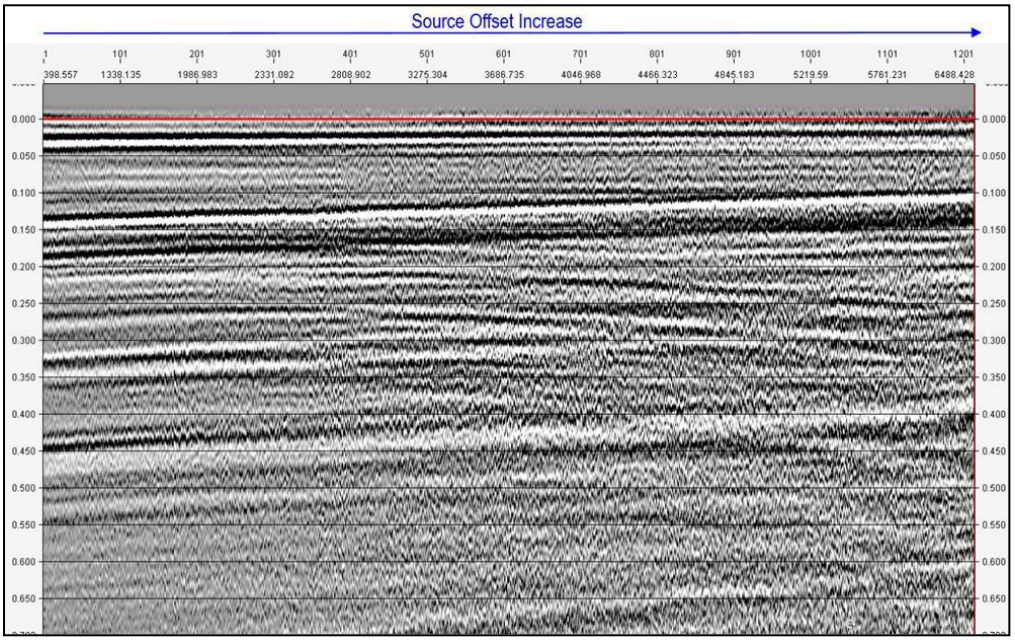

Figure 2.33: Upgoing wavefield of baseline survey at bottom receiver after waveshaping deconvolution

.

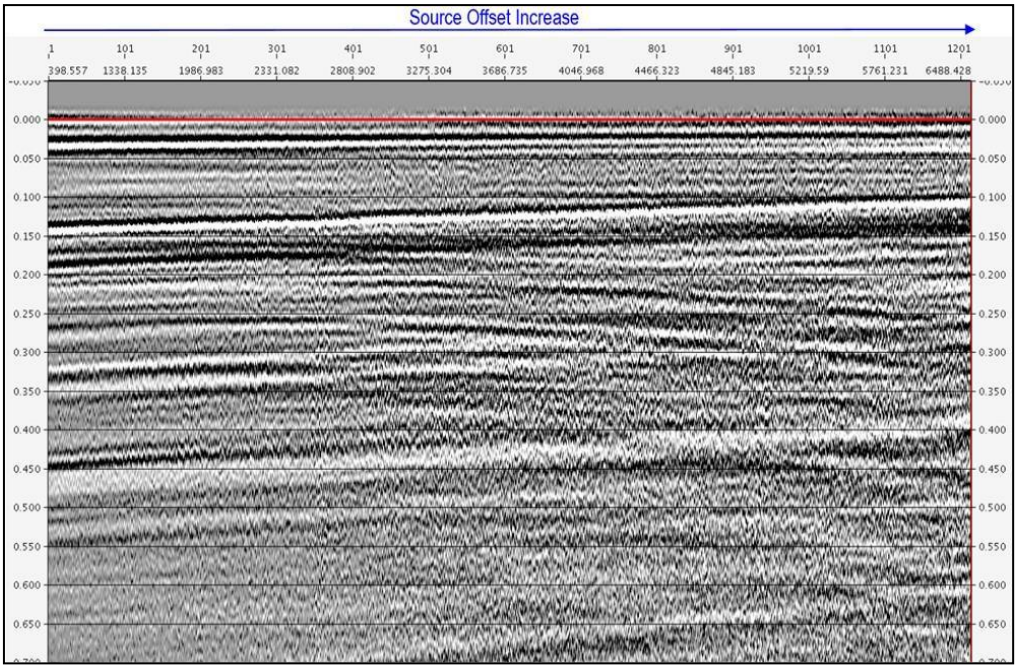

Figure 2.34: Upgoing wavefield of monitor 2 survey at bottom receiver after waveshaping deconvolution.

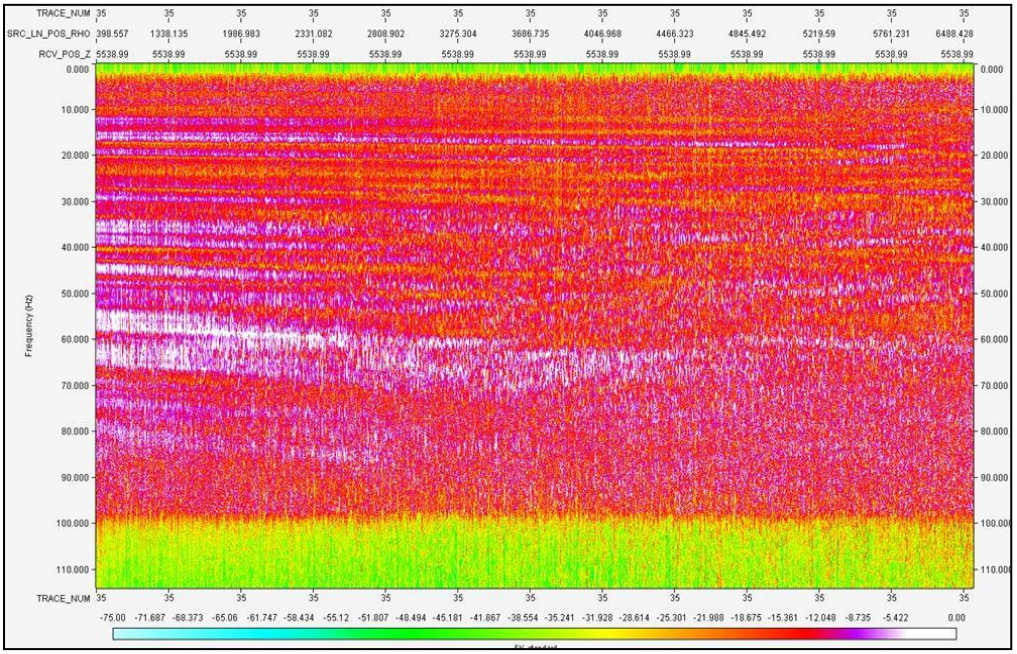

Figure 2.35: Upgoing wavefield spectra of baseline survey at bottom receiver after waveshaping deconvolution.

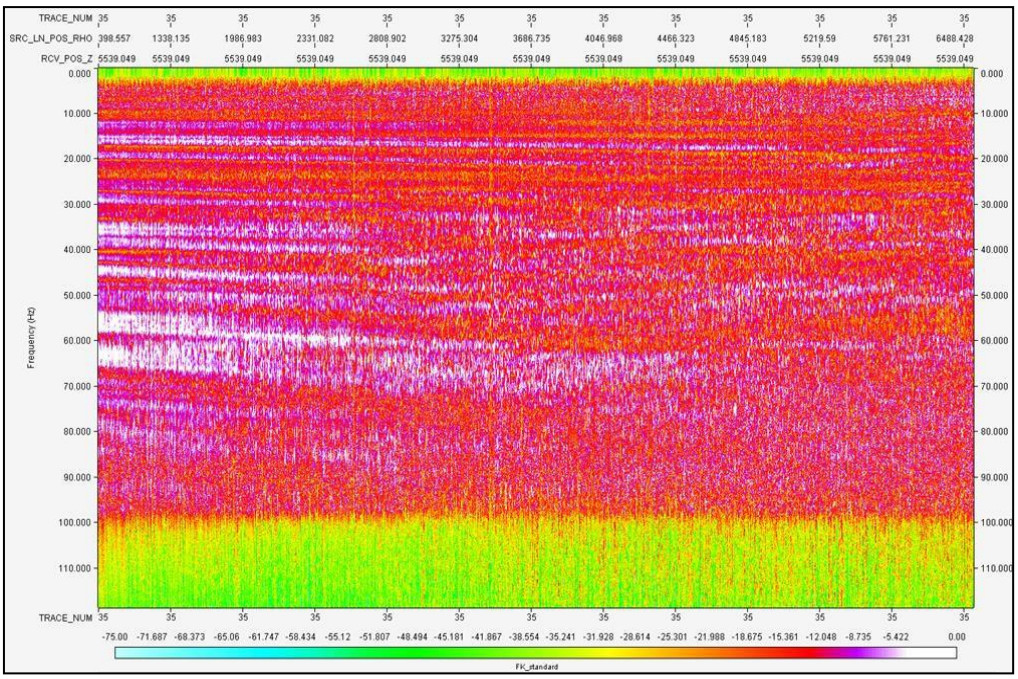

Figure 2.36: Upgoing wavefield spectra of monitor 2 survey at bottom receiver after waveshaping deconvolution.

2.3.11 Velocity Model Building and Depth Imaging:

The signal processed 3D VSP data was imaged using Generalized Radon Transform (GRT) migration, a depth imaging algorithm. 3D depth images of subsurface were generated. Good quality 3D velocity model is an essential pre-requisite to obtain high resolution 3D VSP stack volumes. Checkshot velocities and 3D VSP travel times were integrated to construct a vertically transverse isotropic (VTI) anisotropic depth velocity model.

2.3.12 Velocity Model Building and Calibration:

An initial 3D velocity model for depth imaging was constructed by horizontally extrapolating checkshot velocities away from the two well locations (13 - 10A and 14 - 01). Horizons interpreted on the surface seismic data were incorporated in the initial model building. Travel time tomography using checkshot and 3D VSP direct arrival times were utilized to compute 1D VTI anisotropic parameters. Second iteration of travel time tomography was executed to update P-wave velocities in 3D. The resulting model satisfied both the checkshot and 3D VSP travel times. The average travel time residuals (difference between model time and observed time), for each source location, were computed and applied to the data before imaging to correct for any residual statics.

Common Image Point (CIP) gathers were generated to validate accuracy of the calibrated model in image domain,. CIP gathers are multiple images at a single location created by migrating each receiver separately, then sorting them by receiver depth at a specific image location. Events in CIP gathers should be flat if Images from each receiver at a specific location are similar. In the Farnsworth 3D VSP dataset, CIP tomography (direct travel time tomography) was applied to flatten events in CIP gathers after model calibration.

.

Model building and calibration was accomplished by executing a designed workflow for this dataset, figure 2.37:

1. Build 3D model using two well (13 – 10A and 14 – 01) checkshot times, figure 2.38
2. 1D inversion using near offset travel times from both wells
3. Estimate 1D VTI parameters using 3D VSP travel times
4. 3D tomographic inversion to update Vp
5. CIP Tomography to update Vp below receivers

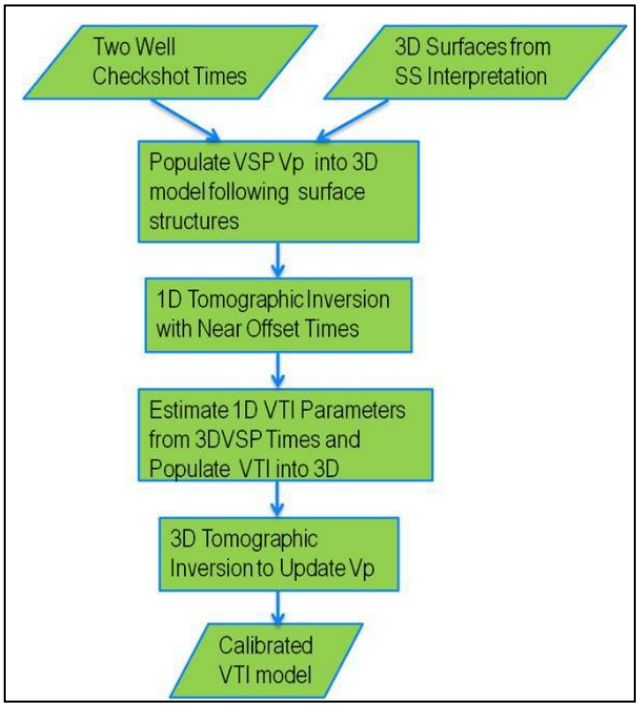

Figure 2.37: Model building and calibration workflow

.

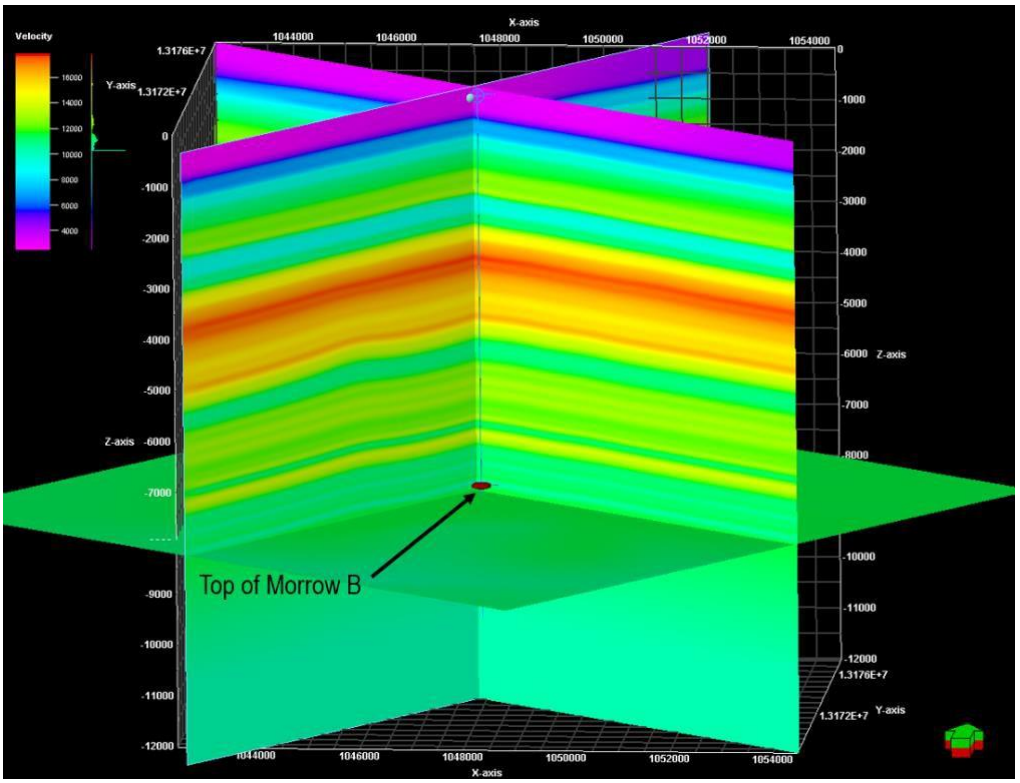

Figure 2.38: Profiles of Vp, Thomsen Epsilon and Thomsen Delta parameters (Thomsen 1986) from calibrated 3D model, with well trajectory and 3D VSP receivers.

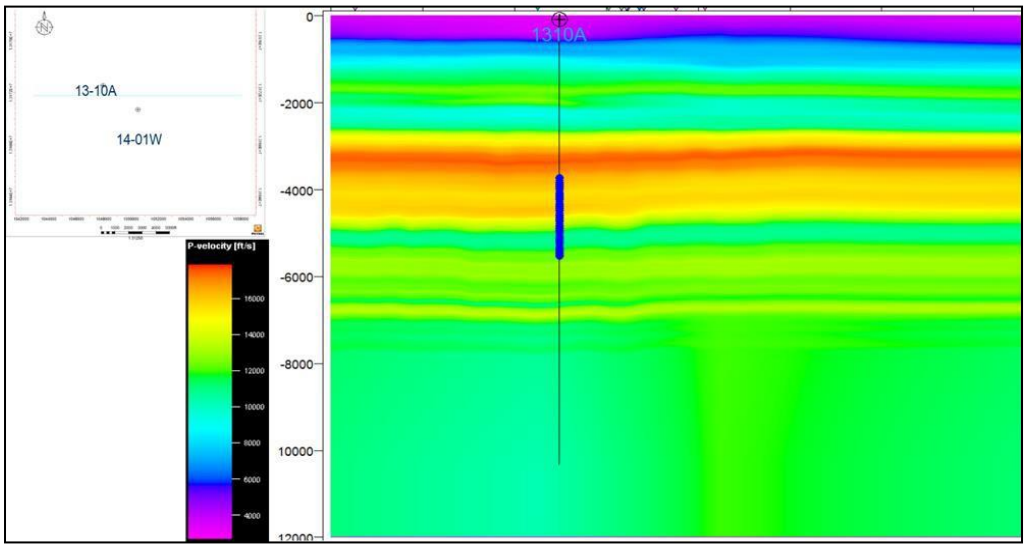

Figure 2.39: wave velocity from calibrated VTI model used in 3D VSP imaging. 3D VSP receiver locations overlain well trajectory

.

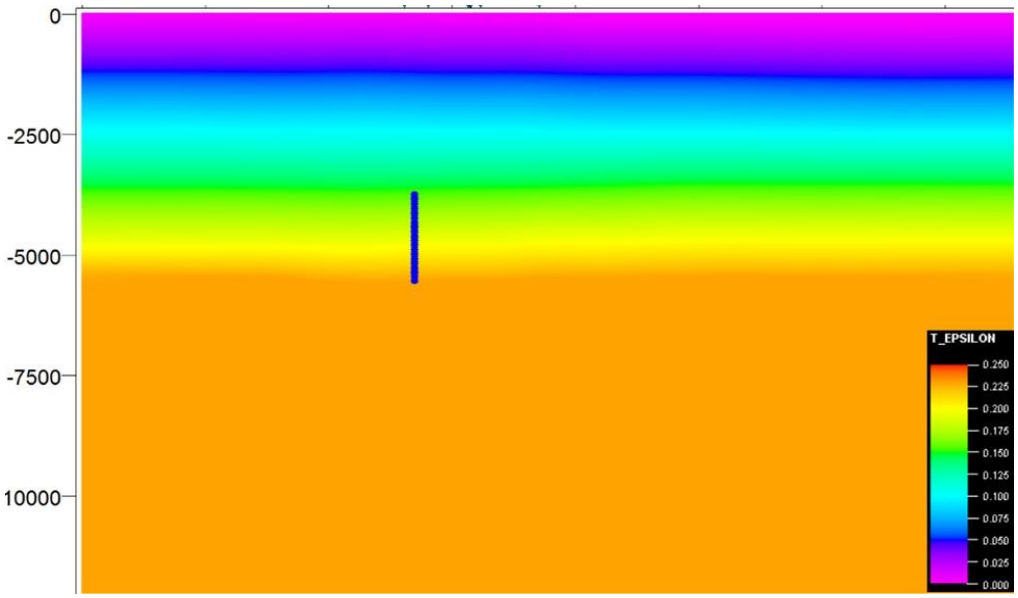

Figure 2.40: Thomsen epsilon from calibrated VTI model used in 3D VSP imaging.

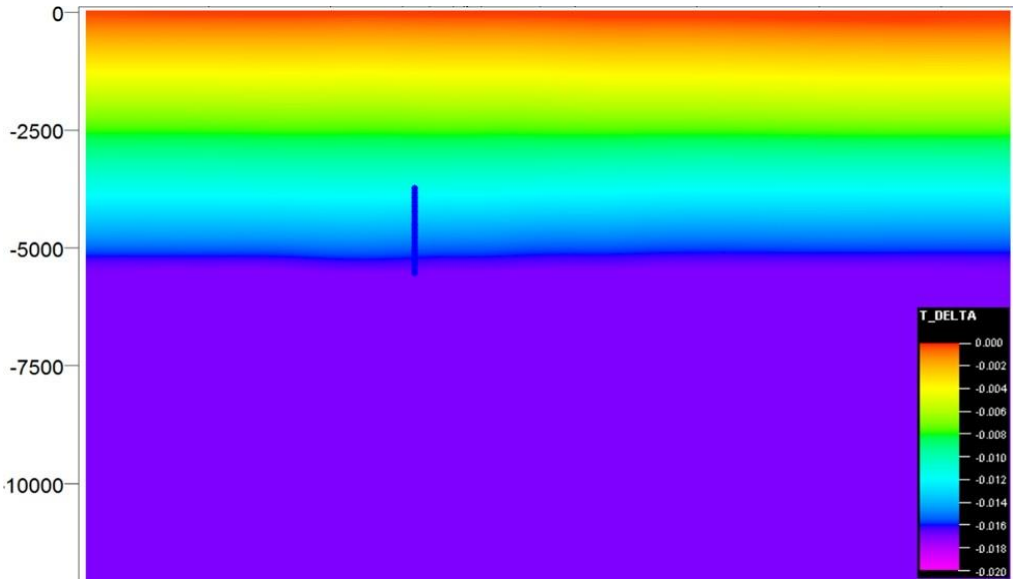

Figure 2.41: Thomsen delta from calibrated VTI model used in 3D VSP imaging.

2.3.13 Depth Imaging:

In Generalized Radon Transform (GRT) imaging algorithm, each point of the subsurface is constructed by diffraction stacks representing contributions from different sources and receivers. These diffraction stack curves are computed using a two-point raytracing inside a 3-D background. Different weightings are accounted for at the summation step along the diffraction stack curve. Dips can be preferentially weighted in the migration using dip and dip aperture, figure 2.42.

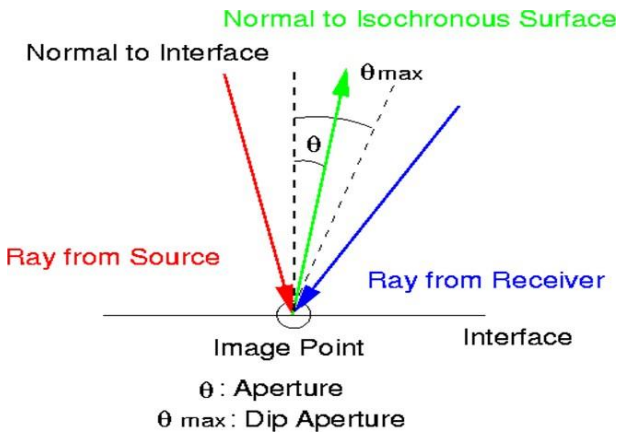

Figure 2.42: Migration aperture definition.Suite of tests were conducted to determine the optimal dip and aperture. Detailed analyses of tests results concluded to limit aperture to +/- 7 degrees, table 2.6:

Table 2.6: Depth imaging ley parameters.

Depth imaging key parameters	
Cross-line Spacing	50 feet (15 meters)
Inline Spacing	50 feet (15 meters)
Depth step (DZ)	10 feet (3 meters)
Dip Aperture	0 +/- 7 degrees

The calibrated model and static corrected deconvolved up-going P-waveforms were the inputs to depth imaging workflow, figure 2.43. Stack volumes and cross sections were generated for baseline, monitor 1 and monitor 2, figures 2.44 - 2.47. Baseline and monitor 2 images were visually compared to verify amplitude consistency and events alignment, no visible differences were observed between the two images, figure 2.48. Selected CIP gathers were displayed for quality control along Inlines for baseline monitor 1, and monitor 2 surveys, figures 2.49 – 2.51. Observed flatness of events within CIP gathers is an indication of a well-calibrated velocity model.

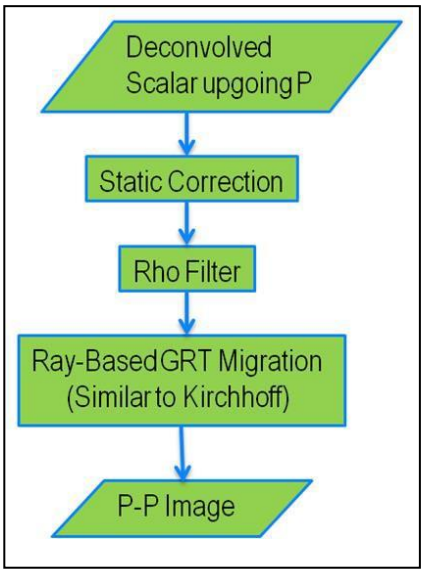

Figure 2.43: Depth imaging workflow for 3D VSP.

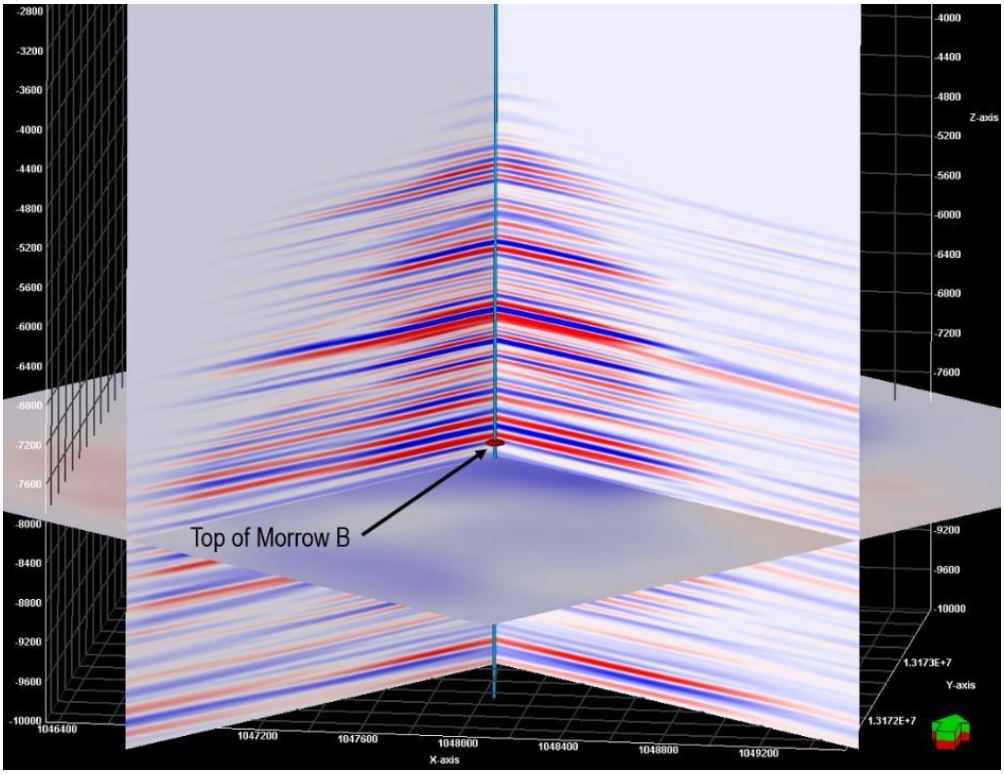

Figure 2.44: Baseline 3D VSP stack volume

.

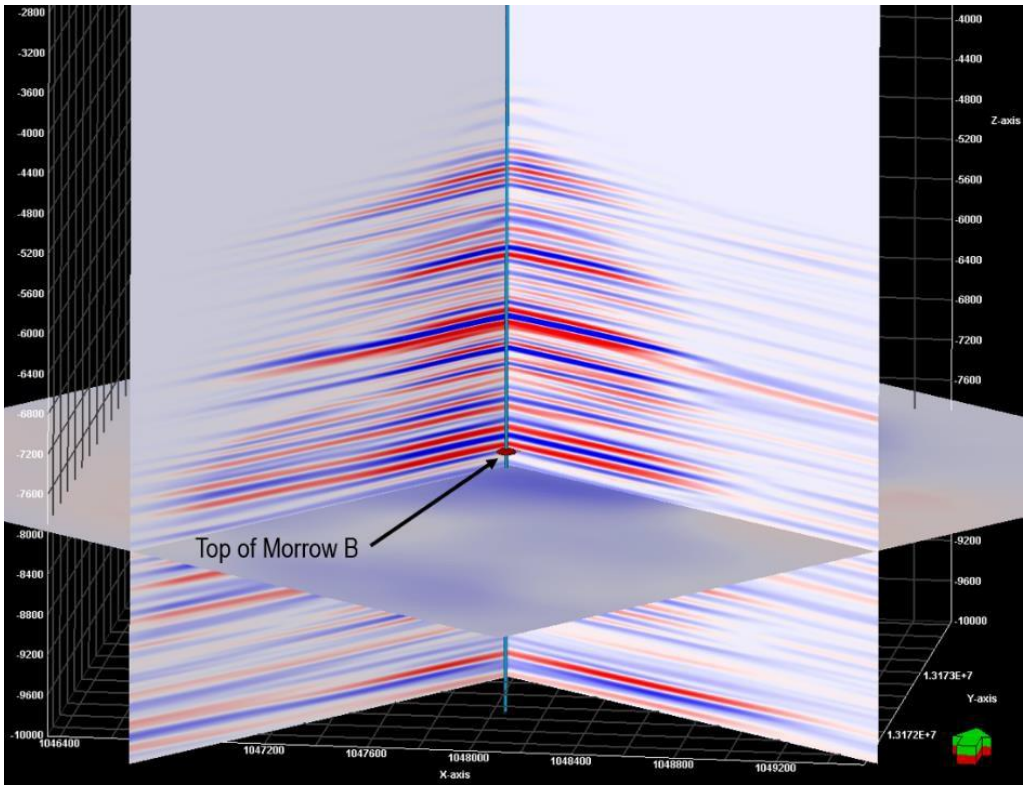

Figure 2.45: Monitor 1 3D VSP stack volume.

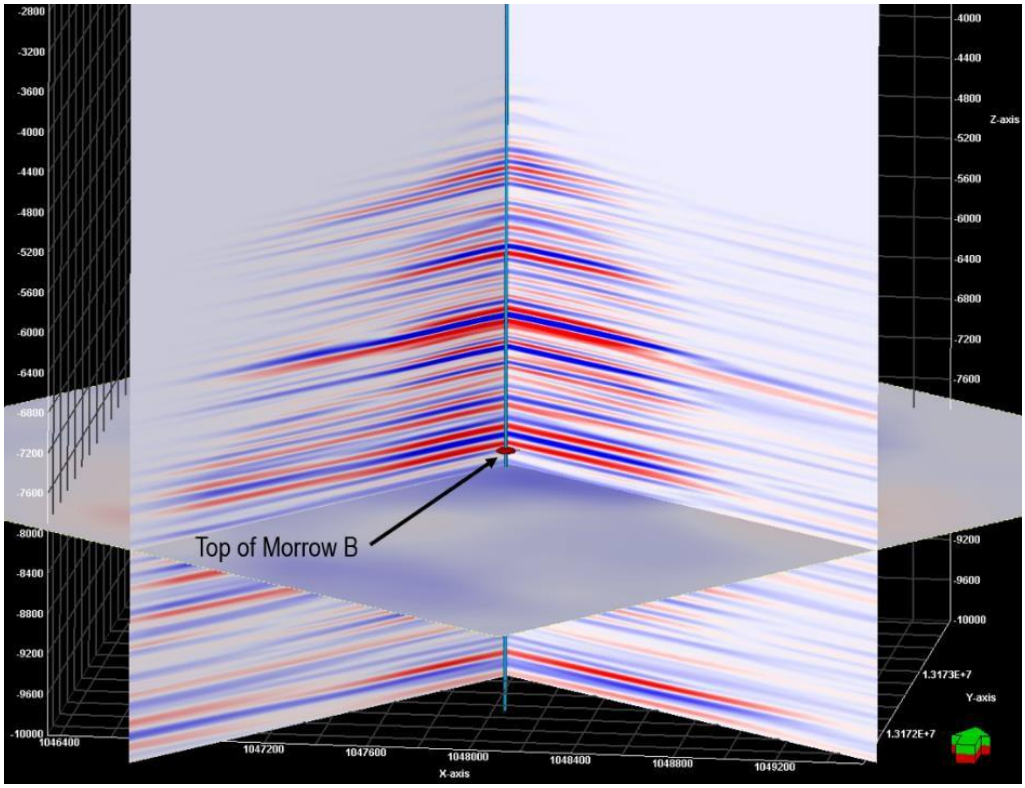

Figure 2.46: Monitor 2 3D VSP stack volume.

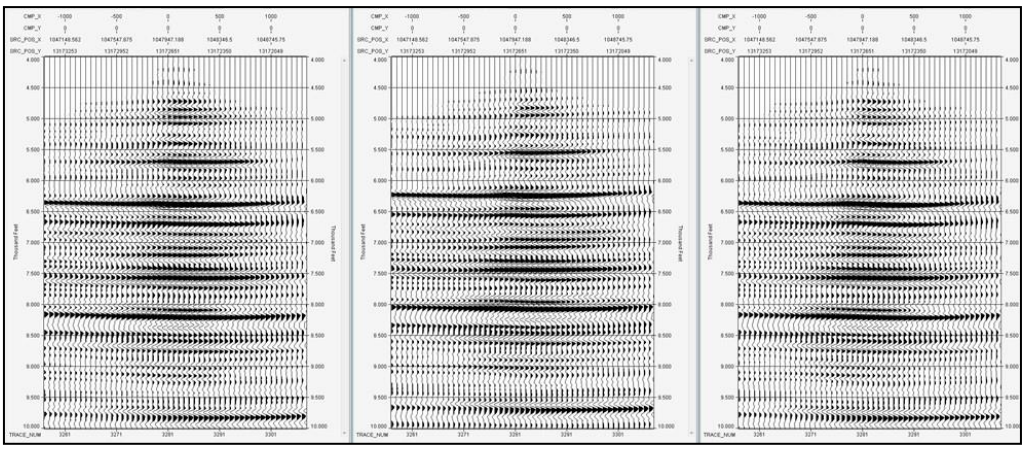

Figure 2.47: Baseline (left), monitor 1 (middle) and monitor 2 (right) migrated cross-sections.

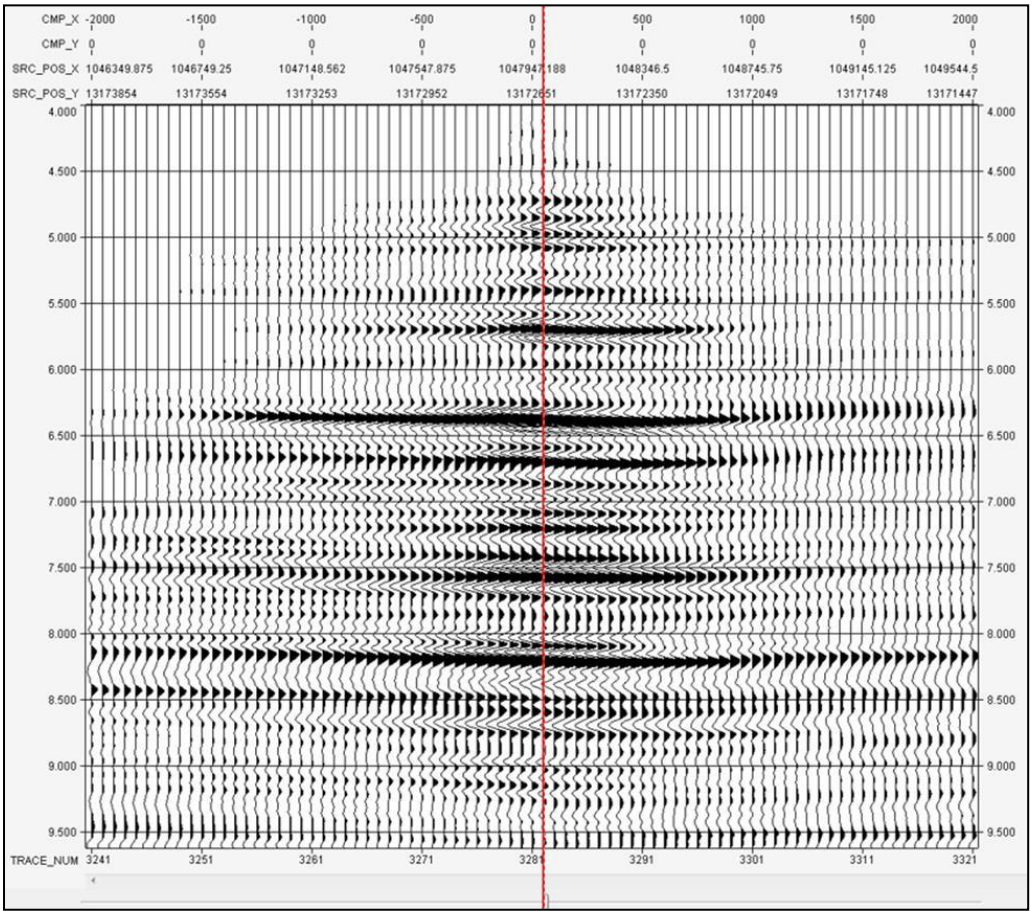

Figure 2.48: Comparison between baseline (left half) and monitor 2 (right half).

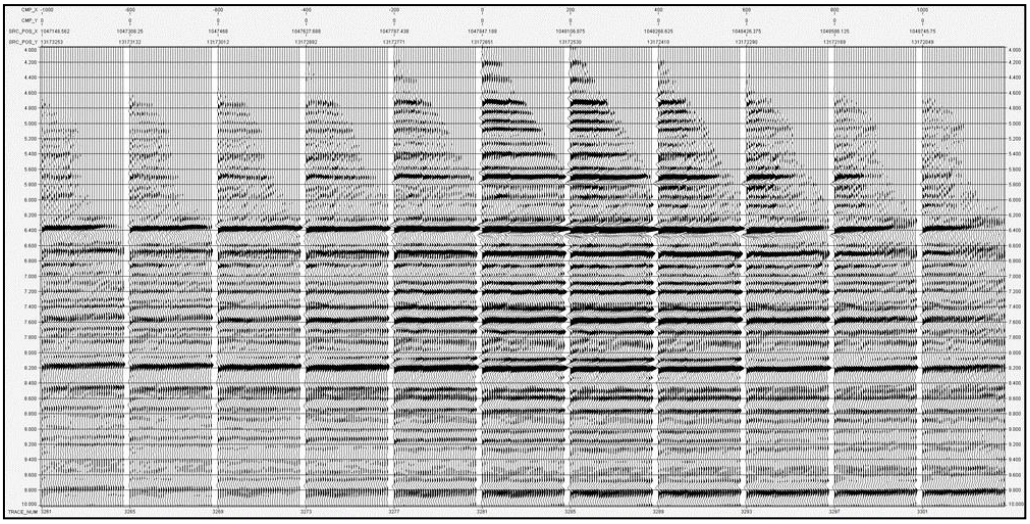

Figure 2.49: Baseline survey CIP gathers along NW-SE line.

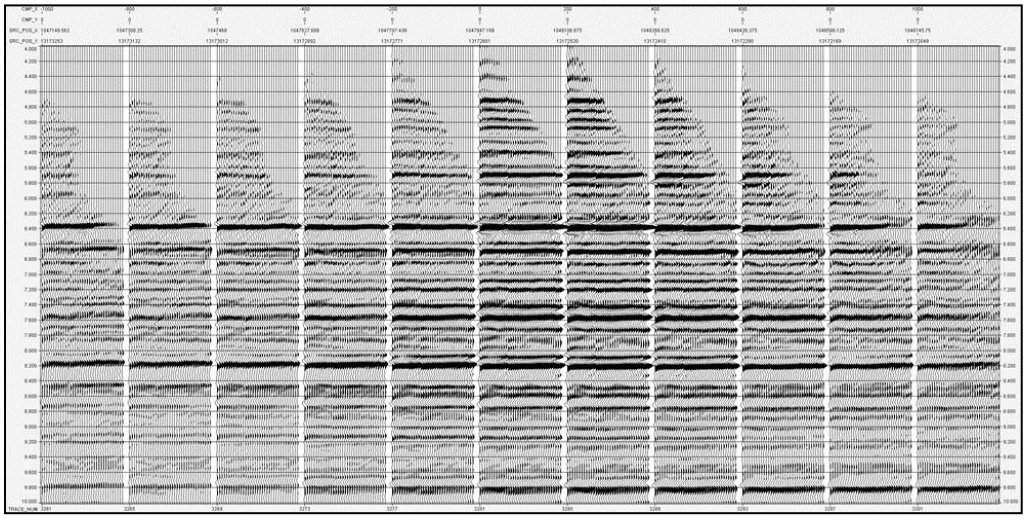

Figure 2.50: Monitor 1 survey CIP gathers along NW-SE line.

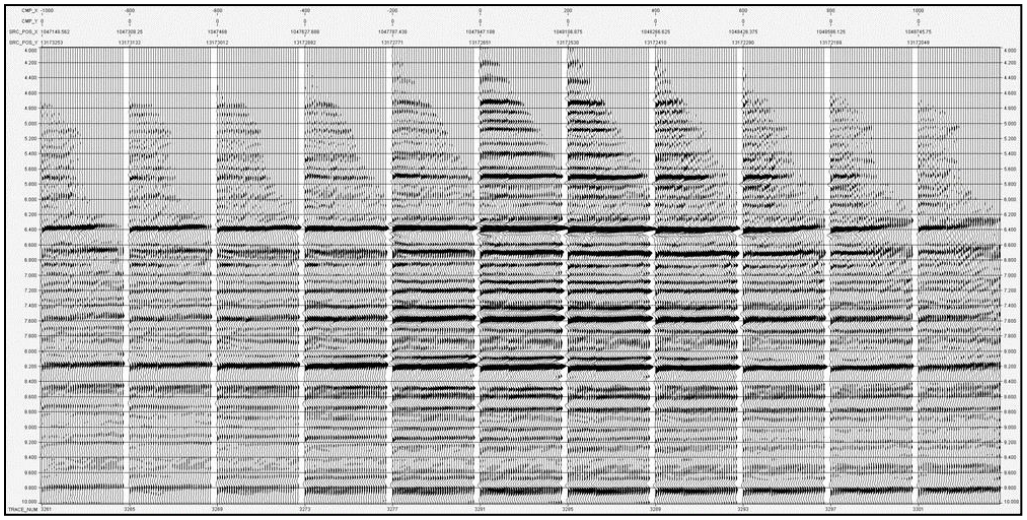

Figure 2.51: Monitor 2 survey CIP gathers along NW-SE line.

2.3.14 Post Depth Imaging Processing:

Cross Equalization:

It is common for residual "non-repeatable" energy to appear in the overburden in post imaged data. This energy is often termed "time-lapse noise". In order to minimize the noise, and preserve time-lapse signature caused by fluid changes in the reservoir, cross-equalization workflow, using baseline survey as target (reference), was applied to monitors 1 and 2 surveys. Time-lapse attributes were computed from cross-equalized datasets. Depth imaged datasets for all the surveys were converted to time domain, trace by trace. Time invariant match filter (operator) was obtained by the process of cross-equalization over a designed time window representing 6000 – 6500 feet window (1828.8 – 1981.2 meters) in depth domain. The operator was applied to the time converted datasets. Cross-equalized time domain stack volumes were then converted back to depth domain.

Cross-equalization workflow was implemented in several steps, figure 2.52:

1. Design time window for autocorrelation and cross-correlation.
2. Autocorrelations and cross-correlations are generated from traces of a source datasets (Monitors 1 and 2) and corresponding traces of a target dataset (baseline) with the designed window.
3. Spectral estimates of these autocorrelations and cross-correlations were used to generate cross-equalization filters.
4. The cross-equalization filter was used to transform amplitude and phase spectra of source datasets to match that of the target dataset.

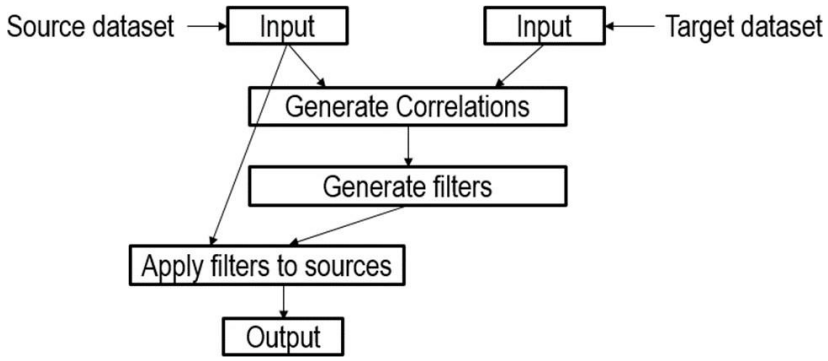

Figure 2.52: Cross-equalization workflow.

Quality control plots were generated, before and after cross equalization, to verify correct application of filters, figures 2.53 – 2.56. Undesired noise in the overburden can be seen in the difference plots before cross equalization. Cross equalization successfully minimized the noise above the reservoir (~7800 feet (2377.4 meters)), as observed in the post cross equalization plots. No artifacts were introduced by the process.

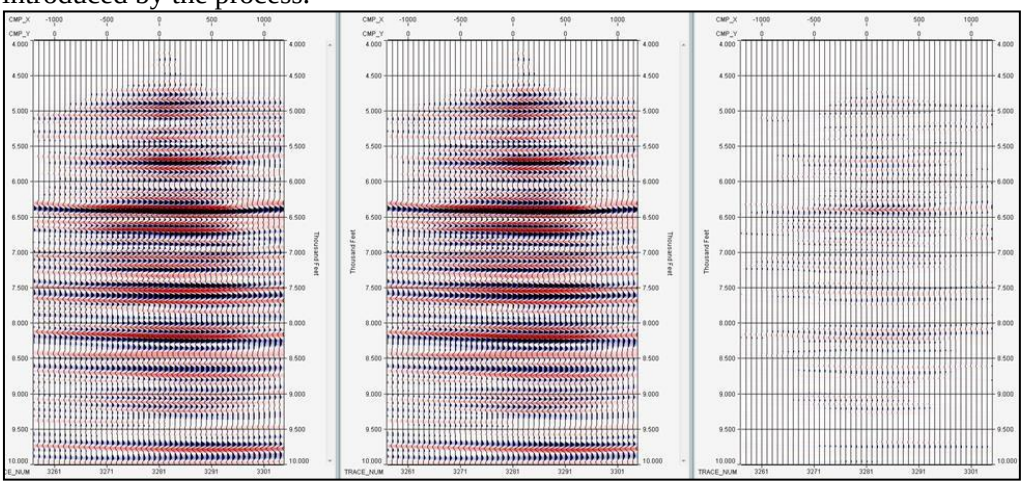

Figure 2.53: Baseline survey (left), monitor 1 survey before cross equalization (middle) and difference (right).

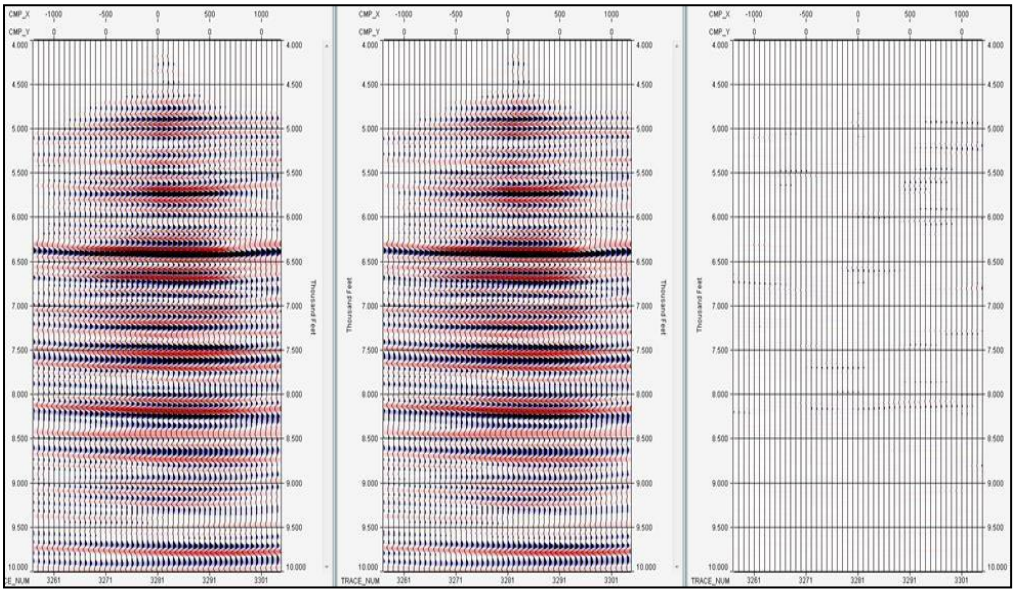

Figure 2.54: Baseline survey (left), monitor 1 survey after cross equalization (middle) and difference (right).

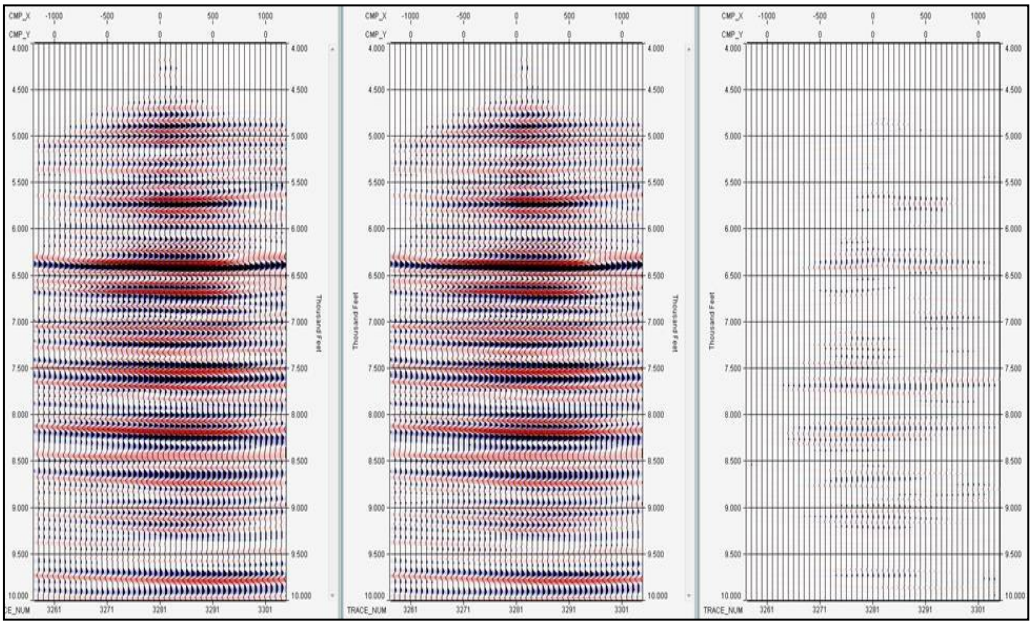

Figure 2.55: Baseline survey (left), monitor 2 survey before cross equalization (middle) and difference (right).

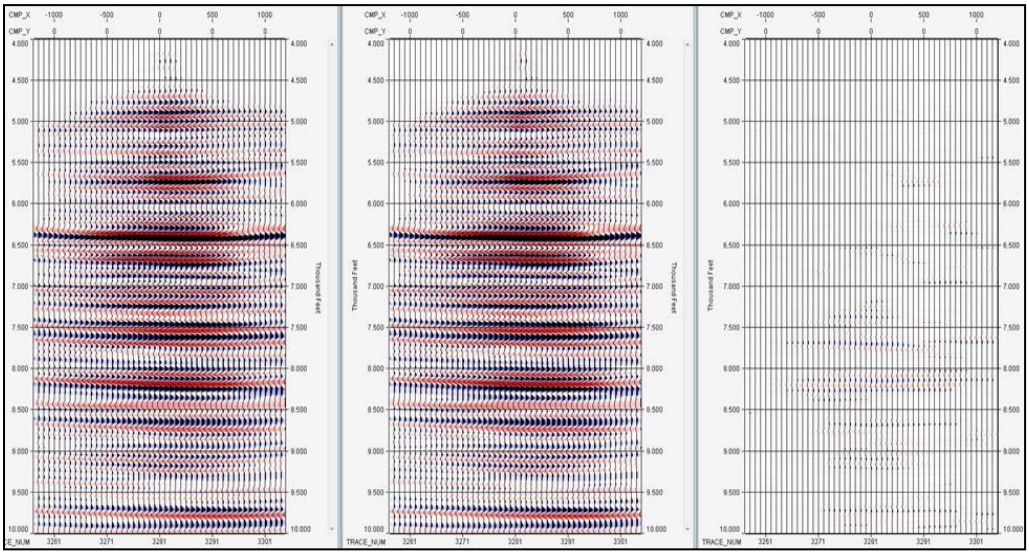

Figure 2.56: Baseline survey (left), monitor 2 survey after cross equalization (middle) and difference (right).

2.4 Gravity Data Analysis Summary

The top of the pre-Cambrian basement is not detectable on seismic lines from Farnsworth Field and surrounding areas, and because of poor data quality, the basement cannot be accurately defined based on changes in seismic character. Here we report on a study in which potential field data (Bouguer gravity and magnetic data) are used to find the top of the basement. Gravity data coverage in the Farnsworth Field area is very good.

We developed gravity models using bulk densities and layer tops derived from wells in the area (32-8 and CHK Hocking). With these constraints, our models predict a Bouguer gravity anomaly that is in excellent agreement with measurements (within 1 mGal error). However, the gravity models are not sensitive to assumed basement depth. Allowed basement depth variations range from 2973 m to 3973 m on the northernmost point of our model.

Densities of the deeper sedimentary layers are very close (or similar) to crystalline basement densities. As a result, the sedimentary cover does not provide constraints on the basement top depth. We also find that small variations in thickness of the shallowest formations (Wellington) control most of the anomaly fluctuations of our gravity model which allows us to make large variations in depth of the basement without increasing the misfit between data and models.

We have considered other geophysical methods that may be helpful in constraining the depth to basement, such as magnetics. Because of the lack of basement top structure, magnetic data do not provide additional constraints. Extending the modeled transects further south may provide better constraints on the basement depth.

2.4.1 Introduction: Depth to basement in Farnsworth Field

The Anadarko Basin is a deep continental basin (basement depth of ~12,000 m in its deepest part) within the North American craton (van Wijk et al., 2019). At the Farnsworth Field study area, the depth to basement is unknown. Aim of this study is to find the top basement in the Farnsworth Field area, which can then be used for interpretation of 3D seismic datasets. Models created for this project are located outside of the Farnsworth Field area and follow seismic lines DC-NEP-10 and DC-NEP-33. We chose this modeling approach to include constraints to formation tops from the seismic lines, as well as general subsurface structure (formations gently dipping southward). The models may help constrain depth of the basement on the Farnsworth Field 3D seismic data (Figure **2.57**).

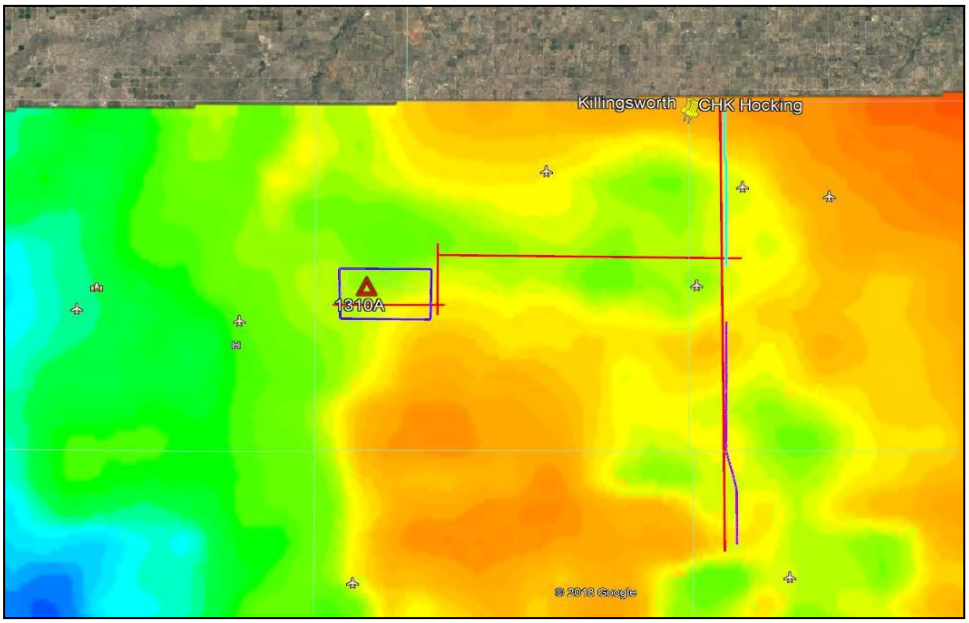

Figure 2.57: General setup for 2D gravity models along the red lines. The first transect is along NS seismic line DC-NEP-33 (north and south) to make use of previously interpreted formation tops. Other transects follow other 2D seismic lines in the Anadarko Basin to the 3D seismic data. The blue box indicates the location of the 3D seismic data set.

Despite decades of research in the Anadarko Basin and Farnsworth Field, there is no accurate estimate on the depth of the basement within Farnsworth Field. This is because the Anadarko Basin is a petroleum producing basin where bedrock is never a drilling target. To find the depth of the basement, we used interpretations of seismic lines DC-NEP-10 and DC-NEP-33 (**Figure 2.58**) (van Wijk et al., 2019) along with data from wells 32-8 and CHK Hocking in order to gather data for depths to horizons along with densities of respective formations. With these data, we can constrain depth to the top of the Mississippian formation, and densities to a depth of 3500 meters. Further, data from stratigraphic columns of the Anadarko Basin are considered in order to make assumptions of the formations between the Mississippian to the basement (Figure 2.59); densities are then applied to an assumed formation based on their lithology (Table 2.7).

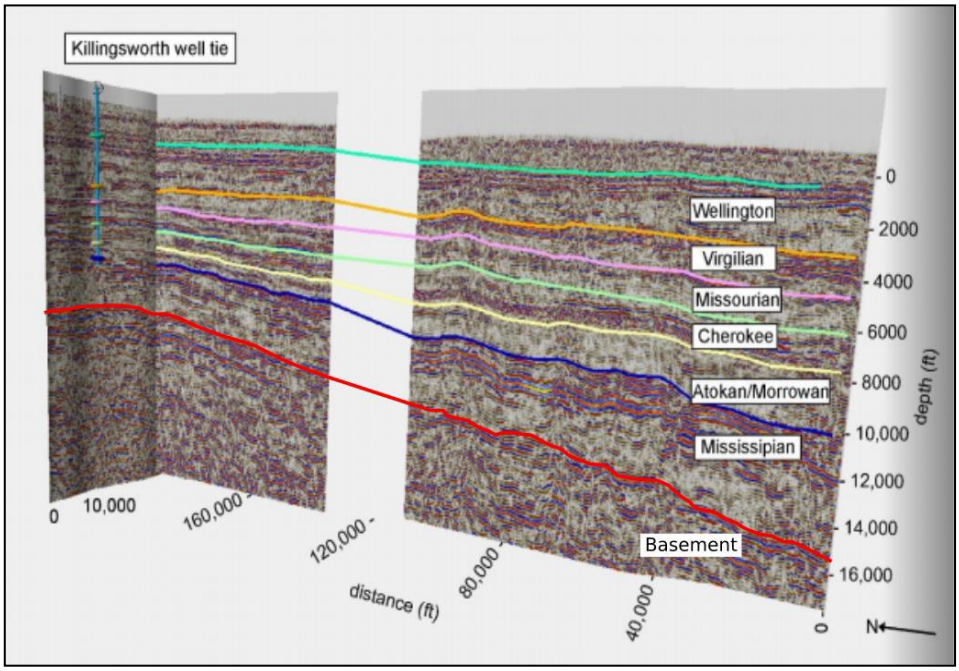

Figure 2.58: 2D seismic lines DC-NEP-10 (east-west intersecting with Killingsworth) and DC-NEP-33 (north-south). The red line on this seismic line indicates the depth to basement in the base gravity model. Basement in the south is assumed to be at ~15,500 ft (4742 m) below the surface.

Stratigraphy of the Northwest Shelf of the Permian Basin

PERIOD	EPOCH	FORMATION	GENERAL LITHOLOGY	APPROXIMATE THICKNESS (ft)
Permian	Ochoan	Dewey Lake	Redbeds/Anhydrite	200-400
		Rustler	Halite	100
		Salado	Halite/Anhydrite	1000
	Guadalupian	Tansil	Anhydrite/Dolomite	200
		Yates	Anhydrite/Dolomite Anhydrite	200
		Seven Rivers	Dolomite/Anhydrite	500
		Queen	Sandy Dolomite/ Anhydrite/Sandstone	200-500
		Grayburg	Dolomite/Anhydrite/ Shale/Sandstone	300
		San Andres	Dolomite/Anhydrite	1500
	Leonardian	Glorieta	Sandy Dolomite	100
		Yeso: Paddock, Blinebry, Tubb, Drinkard	Dolomite/Anhydrite/ Sandstone	1500
		Abo	Dolomite/Anhydrite/ Shale	1000
	Wolfcampian	Wolfcamp	Limestone/Dolomite	0-1500
Pennsylvanian	Virgilian	Cisco	Limestone/Sandstone	0-1250
	Missourian	Canyon	Limestone/Shale	
	Des Moinesian	Strawn	Limestone/Sandstone	0-750
	Atokan	Bend	Limestone/Sandstone /Shale	0-1250
	Morrowan	Morrow		
Mississippian		----	Limestone/Shale	0-800
Devonian		----	Dolomite/Chert	0-1200
Silurian		Fusselman		
Ordovician	Upper	Montoya	Dolomite/Chert	0-400
	Middle	Simpson	Limestone/Sandstone /Shale	0-200
	Lower	Ellenburger	Dolomite	0-400
Cambrian		----	Sandstone	----

Figure 2.59: Stratigraphic column from Pranter (2004) used to help determine formations and depths below Mississippian formation.

2.5 Methods

Geosoft's Oasis Montaj is used to make the gravity models for this project (Figure 2.60), and Google Earth to ensure the gravity model is spatially correct (Figure 2.61). Log data from wells 32-8 and CHK Hocking are used to constrain formation depth and densities used for the gravity model. Seismic lines DC-NEP-33 are used as guidelines to make a reasonable initial estimate for depth of the basement. Bouguer gravity anomaly data are collected from Bureau Gravimétrique International (BGI) (Figure 2.62) in the region from latitude 34° to 36.5° and longitude -102° to -100°. The Bouguer anomaly is a gravity correction that corrects for elevation.

Gravity modeling was chosen for this project as it is a geophysical method that is often sensitive to sediment/igneous/basement interfaces. The model created in Oasis Montaj shows us three curves: a dotted curve which is the Bouguer gravity anomaly downloaded from BGI, a mostly straight curve that follows the trend of the Bouguer gravity anomaly which is the curve created from adding layers with densities to our model, and a curve mirroring the Bouguer gravity anomaly which is the misfit (average difference between predicted Bouguer anomaly and observed Bouguer anomaly).

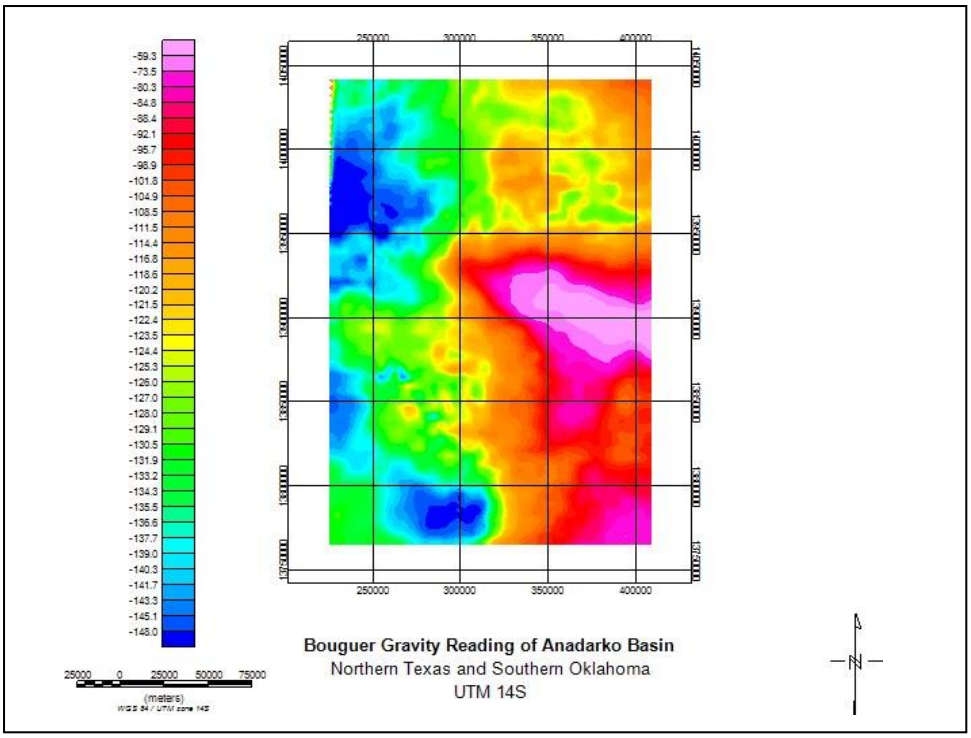

Figure 2.60: Bouguer gravity anomaly map of study area from Bureau Gravimétrique International (BGI).

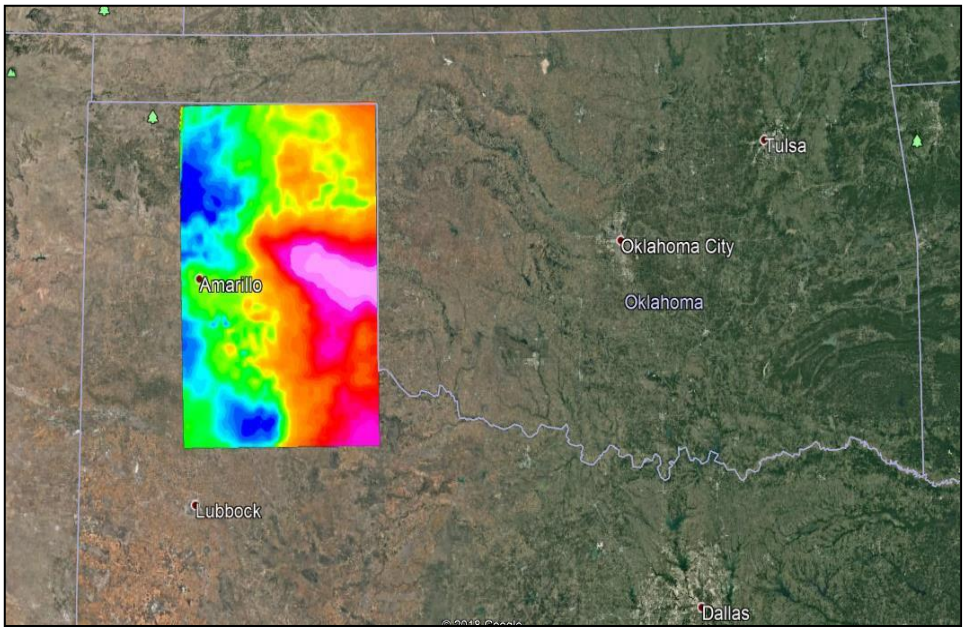

Figure 2.61: Google Earth was used to spatially reference data shown in Figure 4

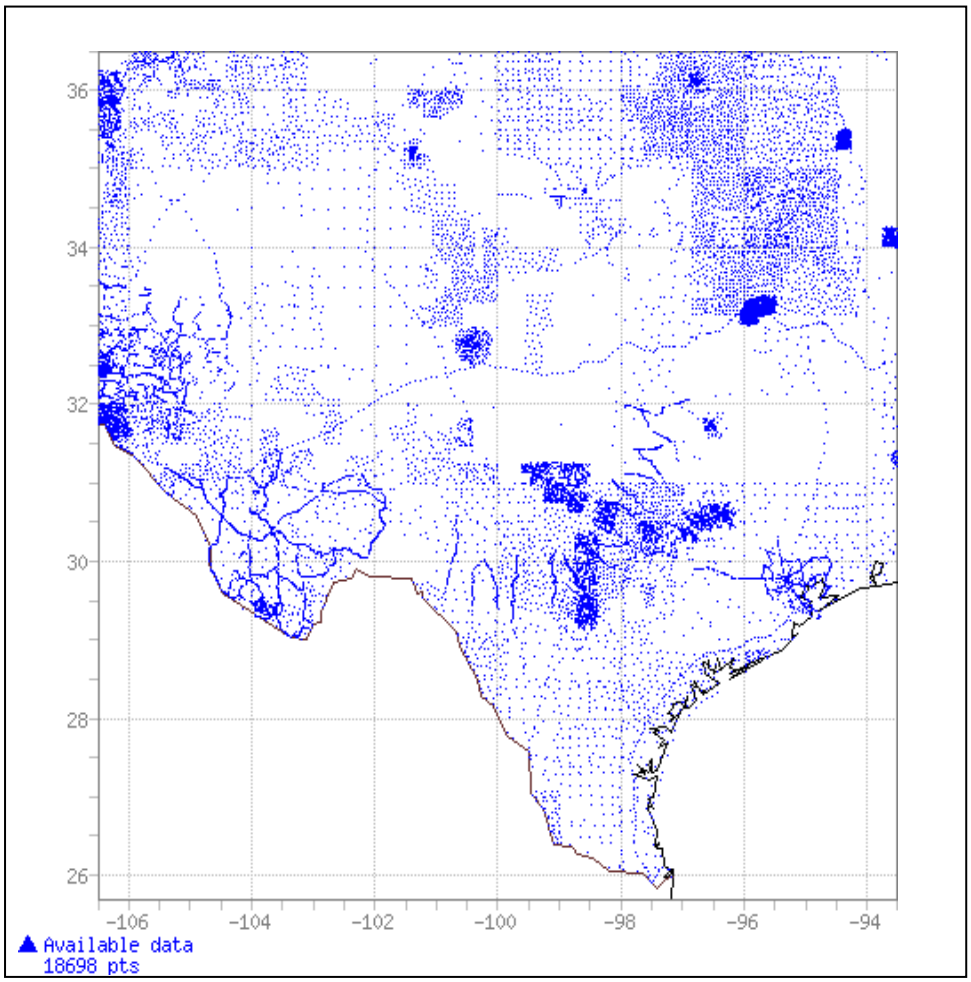

Figure 2.62: Available gravity data from Bureau Gravimétrique International (BGI). Data collected from this region were from latitude 34° to 36.5° and longitude -102° to -100°.

Table 2.7: Data used for models, from wells CHK Hocking and 32-8.

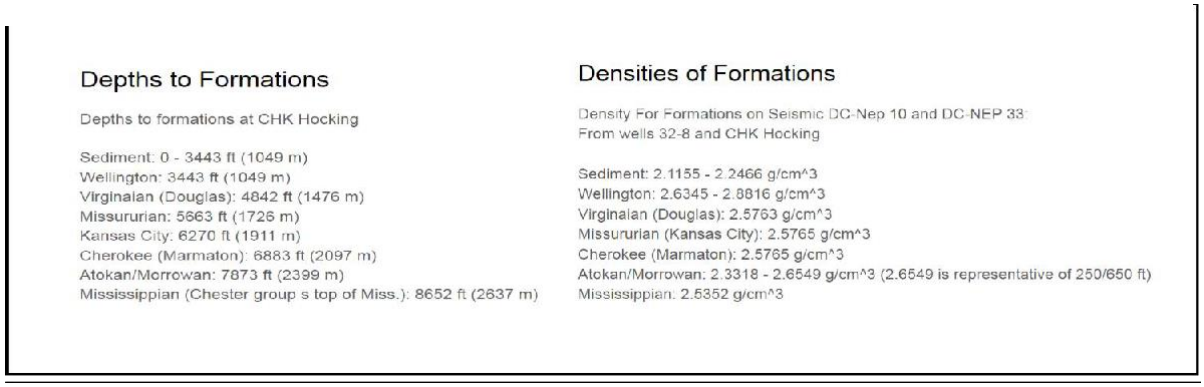

Depths to Formations

Depths to formations at CHK Hocking

Sediment: 0 - 3443 ft (1049 m)
Wellington: 3443 ft (1049 m)
Virginalan (Douglas): 4842 ft (1476 m)
Missururian: 5663 ft (1726 m)
Kansas City: 6270 ft (1911 m)
Cherokee (Marmaton): 6883 ft (2097 m)
Atokan/Morrowan: 7873 ft (2399 m)
Mississippian (Chester group s top of Miss.): 8652 ft (2637 m)

Densities of Formations

Density For Formations on Seismic DC-Nep 10 and DC-NEP 33
From wells 32-8 and CHK Hocking

Sediment: 2.1155 - 2.2466 g/cm^3
Wellington: 2.6345 - 2.8816 g/cm^3
Virginalan (Douglas): 2.5763 g/cm^3
Missururian (Kansas City): 2.5765 g/cm^3
Cherokee (Marmaton): 2.5765 g/cm^3
Atokan/Morrowan: 2.3318 - 2.6549 g/cm^3 (2.6549 is representative of 250/650 ft)
Mississippian: 2.6352 g/cm^3

Table 2.8: Depths with respective densities from well CHK Hocking.

CHK Hocking Density from Blocked Log	
Depth (m)	Density (kg/m^3)
2440-2548	2323
2548-2745	2569
2745-3359	2689
3359-3400	2641
3400-3500	2804

These depths are not assigned specific formation names as they are below the Mississippian. After using the constraints from Table 2.7 and Table 2.8 to add formations and densities to our gravity model, the next step is to change depth to basement.

2.6 Results

The initial model made with a near perfect fit of -124 mGals (Figure 2.63), gives us a basement depth of 3784 m at 35 56’ 38.97’’N 100 28’44.93’’ W, and 3473 m at 36 29’ 37.63’’N 100 29’45.49’’W. Our original plan from this point was to make another gravity model to the north of DC-NEP-33 that follows along DC-NEP-10 using the east side of the formations along the seismic line now constrained.

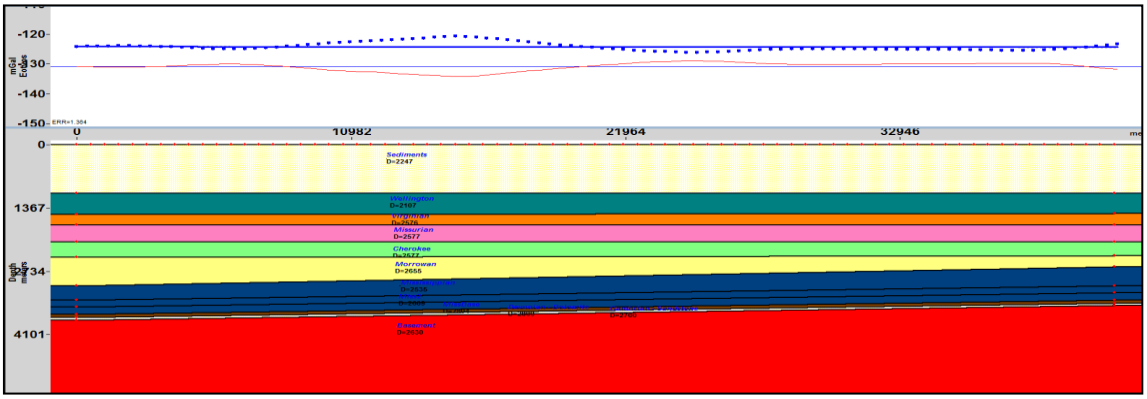

Figure 2.63: Initial constrained model with a misfit of ~1.3 mGal. There are noticeably higher amplitude anomalies from the measured gravity data (dotted line); these are due to minor variations formation thickness and were not modeled because the general trend of formations in this region is flat. Using a density of 2630 kg/m^3 (characteristic of granitic rhyolite), the basement depths are 3784 m in the south (left side of figure) and 3473 m in the north (right). This 2D model runs parallel with seismic line DC-NEP-33 (north-south).

2.7 Discussion Points

Aside from the first model that provided a good fit, two other models were tested for this project. In one model the basement was moved 500 meters deeper. This resulted in almost the same misfit (1.3 mGal) (**Figure 2.64**). In the next model tested, the Cambrian, Devonian, and assumed lower Mississippian formations were removed, and moving the basement up 500 meters resulted in a misfit of ~1.3 mGal (**Figure 2.65**). There are a couple of reasons why it is possible to move the basement in this area +/- 500 meters and still have the model fit the data:

1) The Wellington formation at the top dominates the gravity anomalies;
2) Most of the (deeper) formations within this area have similar densities, which are similar to the basement density. As a result, the calculated Bouguer gravity anomaly is not sensitive to basement depth.

Because of the old age and large depth of the Anadarko Basin, its formations are strongly compacted and do not vary much in density.

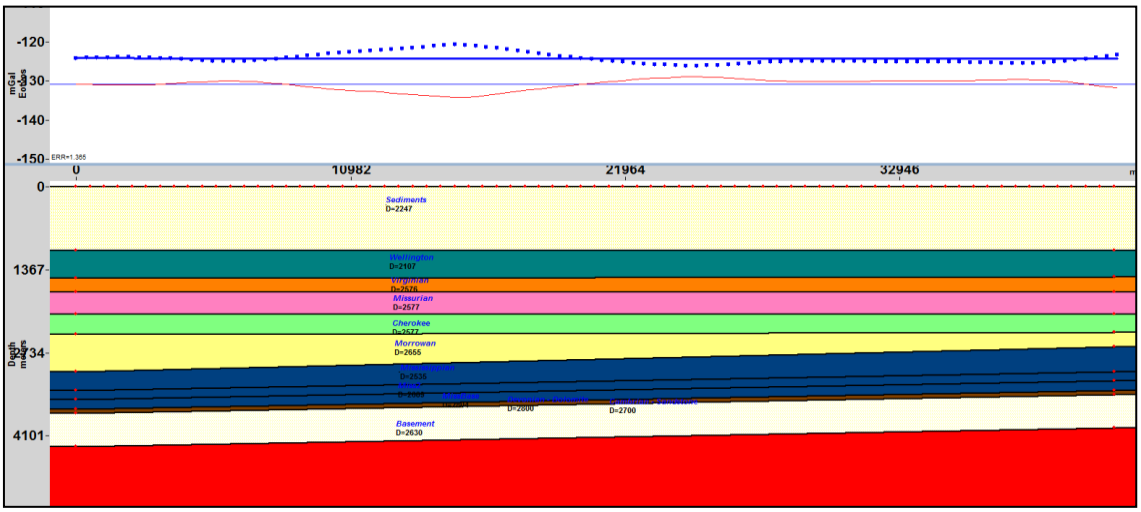

Figure 2.64: Model with basement depth 500 meters deeper results in a very small misfit (~1 mGal).

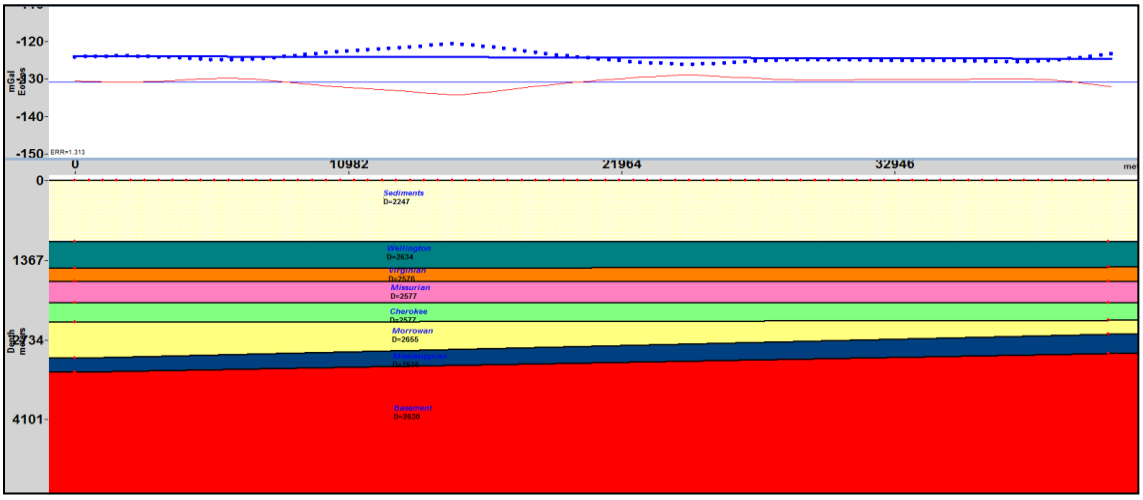

Figure 2.65: Model with Cambrian, Devonian, and lower Mississippian formations removed and basement raised 500 meters. Misfit is ~1.3 mGal.

We considered other geophysical methods to constrain the models:
Resistivity: Basement-sediment interface should show a high anomaly. Unfortunately, the basement is too deep, and there are too many formations that would complicate the apparent resistivity enough to not be able to show a clear anomaly.
Magnetics: Because the area is generally flat and both the sediments and basement are continuous in the region, the magnetic trend will follow that of the gravity anomaly not helping to constrain our gravity model. Longer transects that continue much farther south may cross igneous formations related to aulacogen formation.

2.8 Conclusions

We were not able to constrain depth to basement using gravity modeling. This is because densities of the sedimentary layers are very similar to each other and to the basement density. Extending the lines further southward where they may cross aulacogen basalt infill may yield more constraints on basement depth.

Chapter 3
Wellbore Geomechanics

Summary

This chapter presents the construction of a petrophysical model and a 1D Mechanical Earth Model (MEM) for the Farnsworth Unit 13-10A well. This technical memorandum discusses the core and log input data, the processing steps, and the interpretation of the results. This work provides a basis to interpret the time microseismic and time-lapse vertical seismic profile data required to quantify and monitor the in-situ stresses in the area surrounding the well. The laboratory testing of the recovered core was completed at TerraTek in Salt Lake City, and the measurements as provided in their digital files and report were utilized for analysis. An extensive logging suite was conducted on this well by Schlumberger and their measurements as provided in their digital files and reports for were employed for some analysis. The coring and final logging runs were completed by the first week in January of 2014.

We will discuss the wellbore geomechanics in six sections, 1) core analysis, 2) acoustical analysis, 3) petrophysics analysis, 4) rock physics analysis, 5) the construction of the 1D mechanical earth model (MEM), and 6) the geomechanical simulations based on the MEM. The core analysis quantified a variety of petrophysical and mechanical properties at the scale of the sample size. The acoustical analysis included the processing of the dipole sonic waveforms for multiple sonic velocities and the analysis of the ultrasonic borehole image (UBI) data. The sonic velocities were used to compute the dynamic elastic moduli and the UBI data was used to determine the borehole size and shape and quantify the type and orientation of the drilling induced fractures. The petrophysical analysis quantified the mineralogy, porosity, fluid saturation, and matrix permeability within the volume of investigation of the logging tools. Rock physics models were created to characterize and support the fluid substitution, stress sensitivity, and upscaling components of the MEM. The geomechanical analysis quantified the rock strength parameters and in-situ stress loads supported by the formations.

3.1 Methods

3.1.1 Core Analysis

Five cores, for a total of 240 feet, were recovered from the 13-10A well covering the interval from the Thirteen Fingers Lime to the Morrow Shale below the Morrow B Sand. The recovered core was tested for geochemistry, petrophysical, and geomechanical properties. A typical stress strain curve for a triaxial test for the Morrow B formation is shown in Figure 3.1.

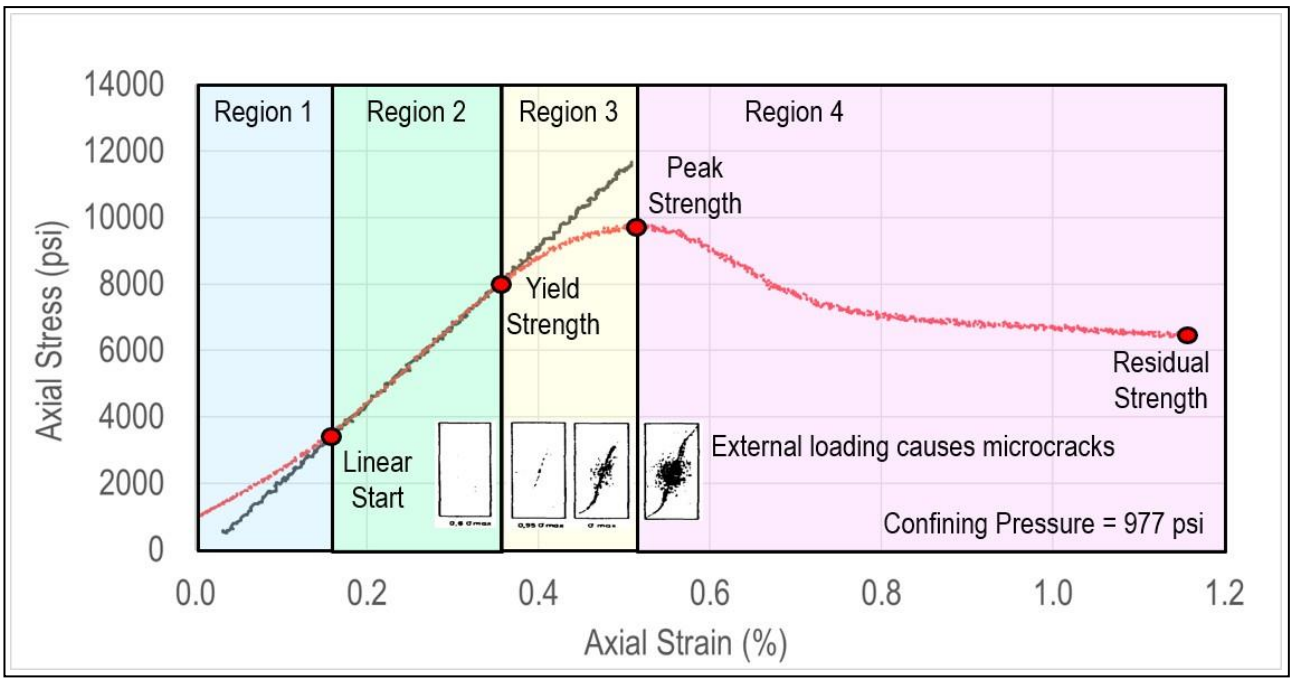

Figure 3.1: A triaxial test of the Morrow B Formation. The red curve shows the axial strain as a function of the axial loading at a confining pressure of 977 psi.

The stress strain curve in Figure 3.1 is divided into four regions of different mechanical behavior. The stress strain curve is concave upwards in region 1 indicating the closing of microcracks and a stiffening of the sandstone. The stress strain curve is linear in region 2 and this region is used to quantify the static properties of Young's modulus and Poisson's ratio. The formation's yield strength is defined as the elastic limit of the sample and defines the end of region 2. The stress strain curve is concave downwards in region 3 indicating the opening of microcracks. The peak strength defines the end of region 3. The stress strain curve decreases in region 4 exhibiting post failure behavior. The definition of residual strength is arbitrary in this example, but the testing shows that even though the sample has been failed, it can still support a reduced load. The four images shown at the bottom of the figure suggest the growth and coalescence of the microcracks due to the axial stress loading (Hallbauer et al., 1973).

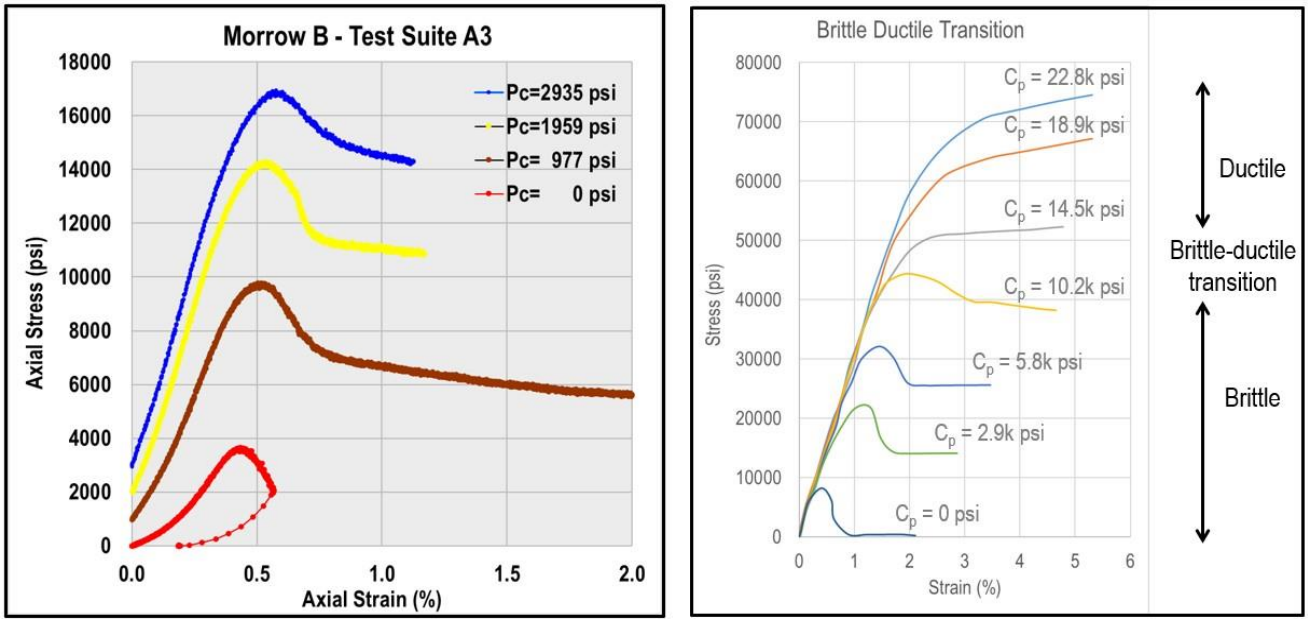

Figure 3.2: The left plot shows a series of triaxial tests at different confining pressures for the Morrow B Formation. The right plot shows the expected brittle to ductile transition for a porous sandstone from southwest Germany (Gowd and Rummel, 1980).

Brittle behavior is characterized by a stress strain curve that exhibits a yield strength, a peak strength, and a reduction in load bearing capacity after peak strength. Ductile behavior is characterized by a yield strength but without an observable peak strength. A series of triaxial tests at different confining pressure are required to observe the transition from brittle behavior to ductile behavior. The left plot in Figure 3.2 shows the A3 test suite of four confining pressures for the Morrow B Formation. The right plot shows a series of triaxial tests on a porous sandstone in southwest Germany (Gowd and Rummel, 1980). This example clearly shows the brittle to ductile transition that occurs between the confining pressures of 10,200 psi and 14,500 psi. The test suite A3 for the Morrow B Formation shows the confining pressure of 2,935 psi is close to, but below, the transition from brittle to ductile behavior. The Mohr's circles plot for the A3 test suite with a linear failure envelope is shown in the left plot of Figure 3.3. The right plot shows the failure envelope. The failure envelope is clearly non-linear over this set of confining pressures.

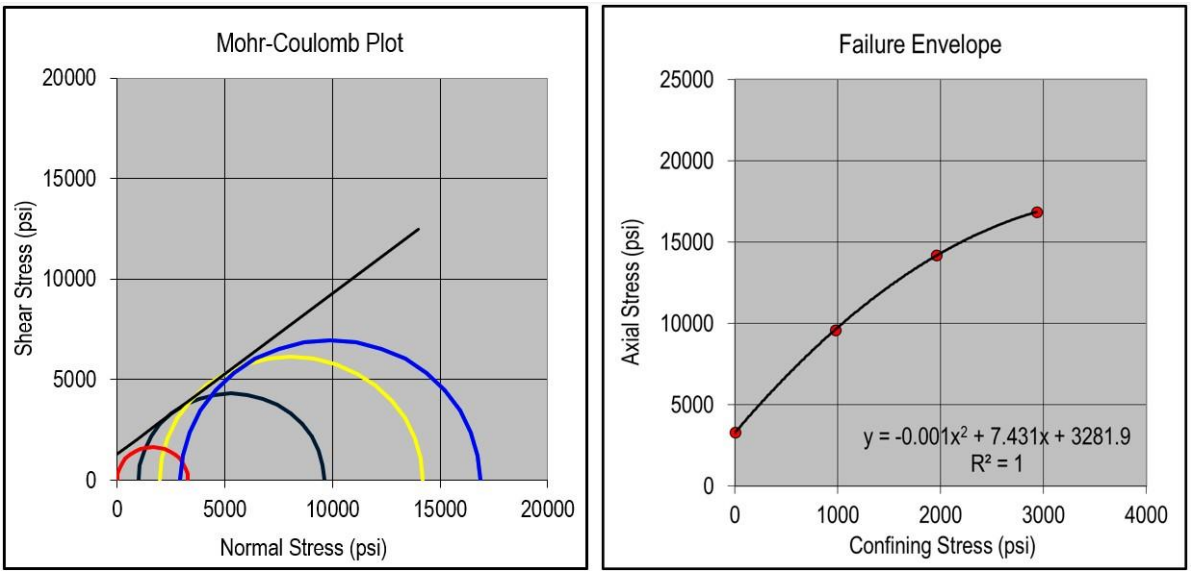

Figure 3.3: The left plot shows the Mohr's circles for the A3 test suite in the Morrow B Formation. The right plot shows the failure envelope.

The P-wave and S-wave ultrasonic velocities are strong functions of stress loading as shown in Figure 3.4. While it the velocities are expected to increase in region 1 prior to the linear portion of the stress strain curve (highlighted in green), it is not expected the velocities continue to increase in region 2. This indicates the micro fractures in the sample are still closing in the lower stress part of region 2. Both P-wave and S-wave velocities decrease in regions 3 and 4 due to the creation and opening of fractures when the stress loading exceeds the yield strength of the sample.

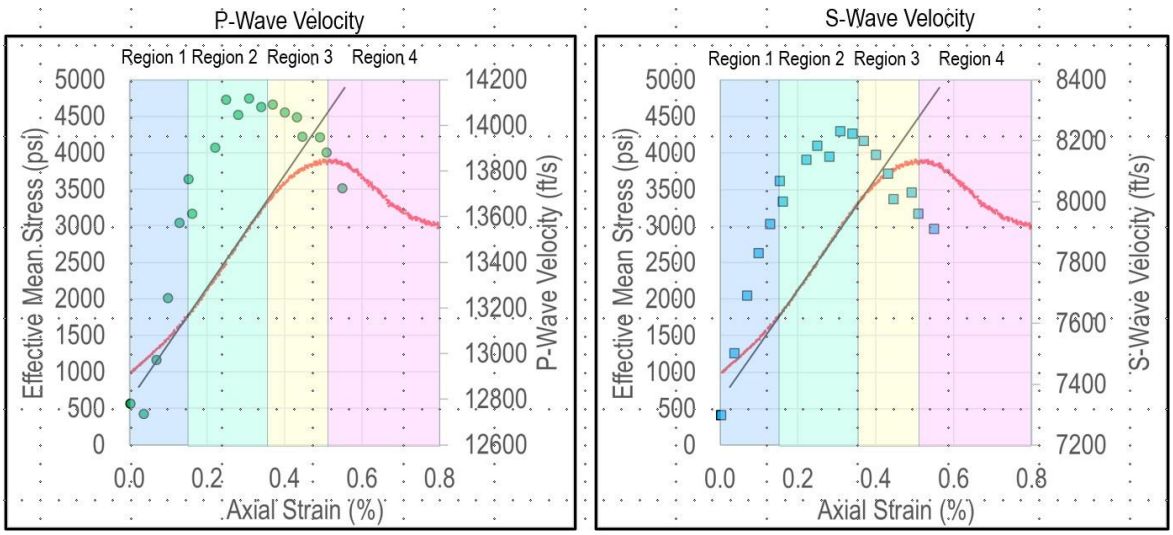

Figure 3.4: Ultrasonic velocities as a function of stress loading. The P-wave velocity is shown on the left and the S-wave velocity is shown on the right. The area highlighted in green is region 2 where the stress strain curve shows a linear response.

Eberhart-Phillips (Eberhart-Phillips et al., 1989) introduced a P-wave velocity model that acknowledged some of the variation of the P-wave velocity was due to composition, and some of the variation was due to effective stress.

$$V_P = A_O - A_1\phi - A_2\sqrt{V_{Cl}} - C_1\sigma' - C_2 e^{-C_3\sigma} \tag{3.1}$$

Porosity is given by ϕ, the volume of clay is given by V_{cl}, and effective stress is given by σ'. The A_i coefficients are fitting parameters for the compositional part of the model and the C_j coefficients are fitting parameters for the stress part of the model. These stress coefficients were determined by empirical fits to the data studied.

Shapiro (Shapiro, 2003) derives the stress dependence using a dual porosity concept based on a combination of stiff and compliant porosity. The derivation uses both theoretical and empirical considerations. The compliant porosity and high aspect ratio pores or fractures gives rise to the exponential increase in the P-wave velocity as the compliant porosity closes under the influence of increasing effective stress. The stiff porosity, arising from low aspect ratio pores, increases the P-wave velocity as the stiff pores resist deformation. The Shapiro model is given in Equation (3.2).

$$V_P = a_O + a_1\sigma' - a_2 e^{-a_3\sigma'} \tag{3.2}$$

This model does not explain the decrease in velocity due to the opening of microfractures after the stress loading exceeds the elastic limit. The ultrasonic velocity data was fit to the Shapiro model to quantify the stress sensitivity of the Morrow B Formation and is shown in Figure 3.5. The linear portion of the Shapiro model gave a P-wave stress sensitivity of 240 ft/sec per 1000 psi change in effective stress. The S-wave sensitivity was 104 ft/sec per 1000 psi change in effect stress.

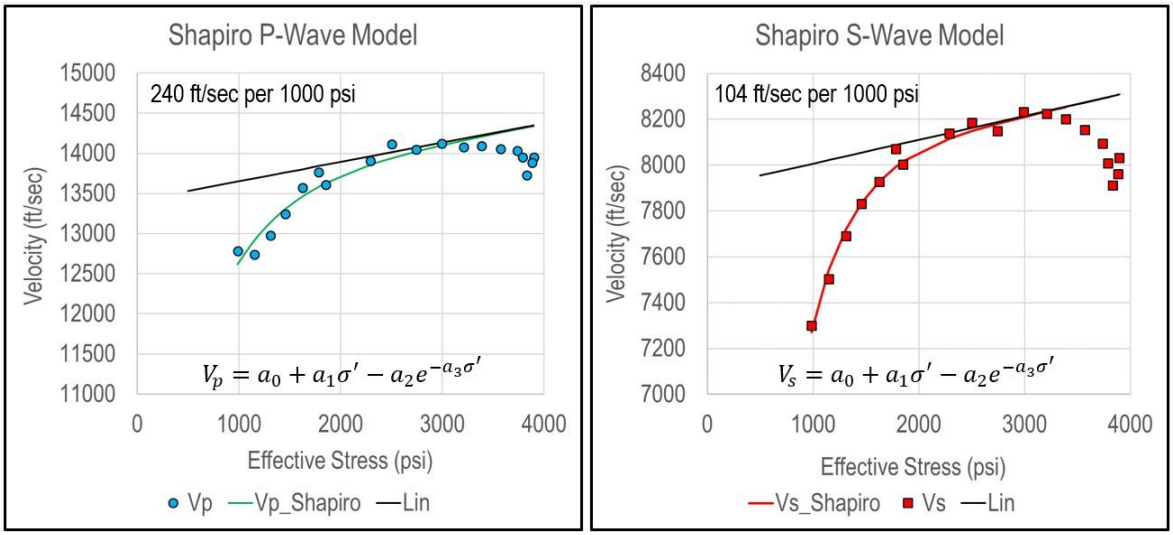

Figure 3.5: The left plot shows the P-wave velocity, and the right plot shows the S-wave velocity as a function of effective stress. The green and red lines are the best fit of the Shapiro model fit to the increasing ultrasonic velocities. The linear black lines represent the linear portion of the Shapiro model.

Figure 3.6 shows Young's modulus and the ultrasonic velocities as a function of effective mean stress. Young's modulus initially increases with loading (1000 to 2500 psi), becomes flat (2500 to 3000 psi), and then decreases. The ultrasonic velocities have the same character. The expected stress range during the water alternating gas (WAG) phase of the field development is highlighted in green. The initial effective mean stress, prior to the WAG, is about 2750 psi. However, with injection the effective mean stress will drop as the pore pressure increases. The stress sensitivity is likely larger under the in-situ stress changes than that estimated from the linear part of the Shapiro model.

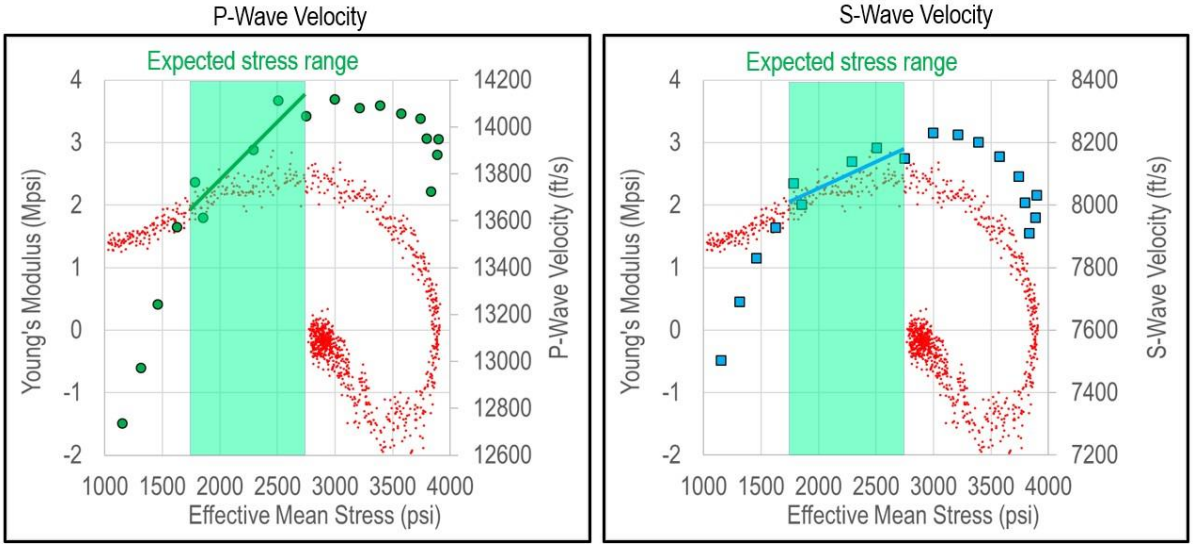

Figure 3.6: These plots show Young's modulus (in red) and the P-wave (left) and S-wave (right) stress sensitivity to the effective mean stress and the expected in-situ stress range, highlighted in green, during the water alternating gas (WAG) phase of the field development.

Fracture compliance depends on the scale of measurement. A laboratory measurement on a core sample with the dimensions of 1 inch in diameter by 2 inches in length can only sense the compliance of microfractures within the volume of the sample. Modern dipole sonic logs investigate a larger volume on the order of 30 cubic feet. The larger sample size allows the dipole sonic log to sense not only the microfractures observed in the core sample, but larger scale fractures within the larger volume of investigation. The same argument is made for the seismic scale. Prioul in (Prioul et al., 2007) reported on measurements taken from other papers and Worthington (Worthington, 2008) plotted the data reported by Prioul as shown in Figure 3.7. Thus, it is not anticipated that the stress sensitivity as measured in core accurately represents the stress sensitivity of the larger scale vertical seismic profile (VSP) measurements.

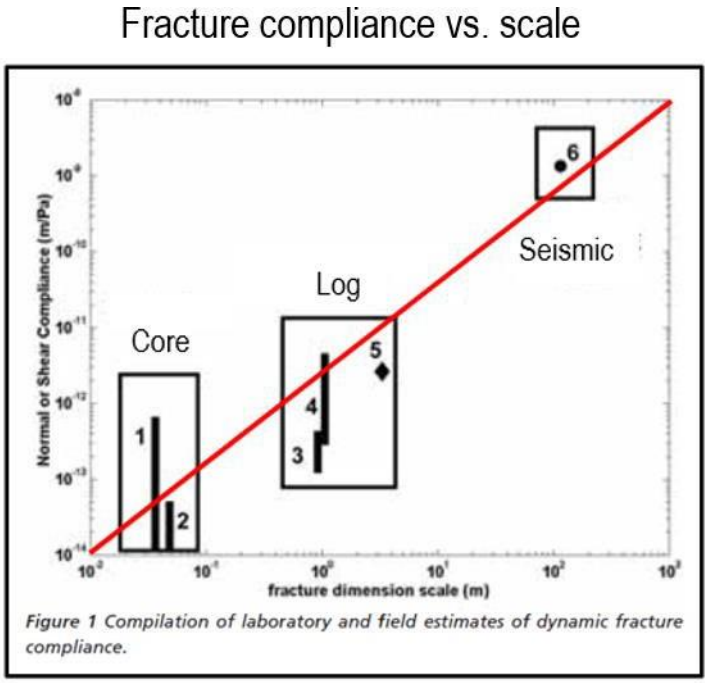

Figure 3.7: Fracture compliance as a function of scale from Worthington 2008. The red line just shows the qualitative increase in compliance with scale.

3.1.2 Acoustical Analysis

The processing of full waveform sonic logs is complicated and requires a special expertise. Acoustical anisotropy is classified into 5 major groups based on the three-shear velocity overlay. Using the bulk density, the three shear moduli are computed from the three shear velocities (Figure 3.8). If the three moduli agree within a threshold, the formation is classified as isotropic and shaded green. Transverse isotropy with a vertical axis of symmetry (VTI) is diagnosed when the horizontal shear is greater than the fast and slow shear (which overlay within the threshold). VTI is shaded yellow. Transverse isotropy with a horizontal axis of symmetry (HTI) is diagnosed when the fast and slow shear waves split, and the horizontal shear overlays with the slow shear. HTI is shaded light blue. Orthotropic formations are diagnosed when all three shears are different by more than a threshold. If the horizontal shear is greater than the average of the fast and slow shear, the anisotropy is diagnosed as VTI-like and is shaded red. Otherwise, the anisotropy is diagnosed HTI-like and is shaded dark blue. In addition, if the fast and slow shear are the same within the threshold, and the horizontal shear is slower than the average of the fast and slow shear, this special case is also called HTI-like and shaded dark blue. This reduction in velocity is generally a permeability effect on the Stoneley (Brie, 2000).

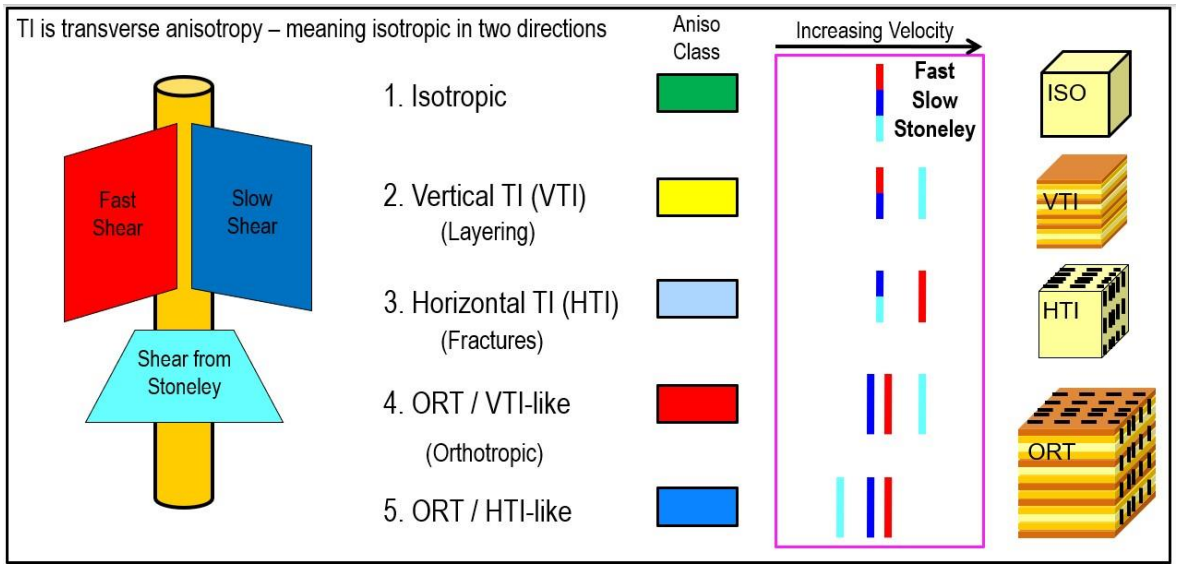

Figure 3.8: Anisotropy classification from dipole sonic logs. The three-shear velocity overlay is highlighted in the violet box.

Acoustical dispersion is the variation in slowness with frequency. Dispersion analysis is also critical to the accurate quantification of acoustical anisotropy (Plona, 2002; Plona, 2004). Figure 3.9 shows the five major groups of anisotropy classification together with their associated dispersion fingerprint for vertical wells.

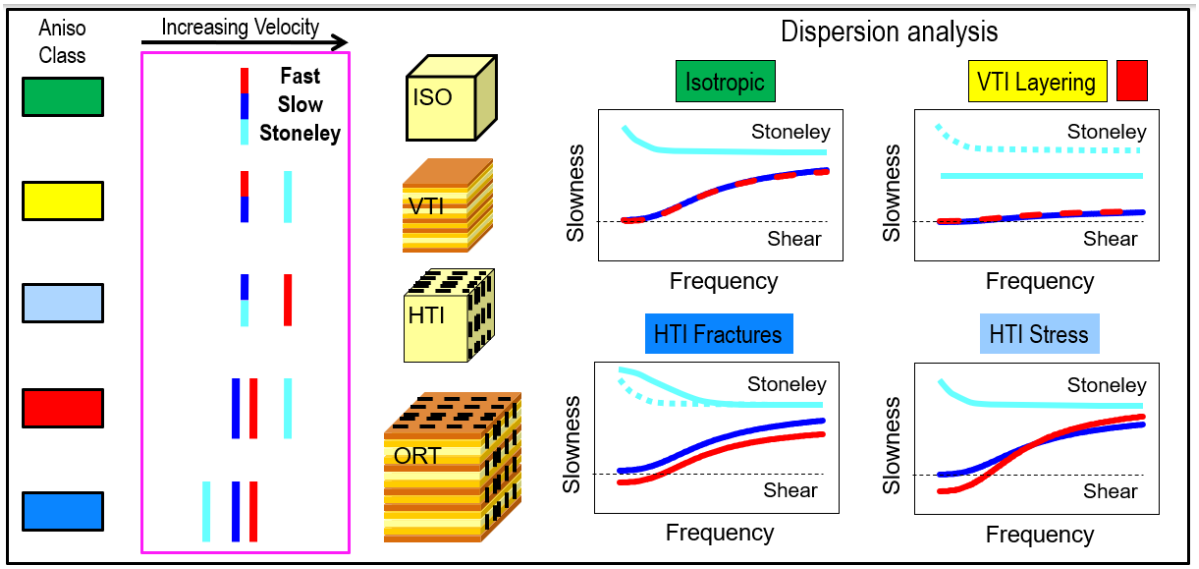

Figure 3.9: Anisotropy classification based on dispersion.

The dispersion curves for an isotropic formation are shown in the upper left plot labeled isotropic. The low frequency asymptote of the dipole shear wave, however more accurately described as a flexural wave, corresponds to the shear slowness of the formation. At high frequency, the flexural wave is strongly influenced by the mud slowness and does not reflect the shear slowness of the formation. Both dipoles overlay. The Stoneley wave is also dispersive. At low frequency, the Stoneley wave increases in slowness due to the presence of the logging tool in the borehole. At high frequency, the Stoneley wave decreases in slowness. These homogeneous and isotropic dispersion curves serve as a reference to help diagnose other forms of anisotropy.

The dispersion curves for a VTI formation are shown in the upper right plot labeled VTI Layering. Whereas the isotropic flexural dispersion has an increase in slowness with higher frequency, a VTI formation has a much lesser increase in slowness with the same increase in frequency. The Stoneley

response is more flattened and exhibits a lower slowness at all frequencies. The dispersion curves for an orthotropic formation that is classified at VTI-like shares the signature of a VTI formation albeit with a small amount of shear wave splitting.The dispersion curves for a fracture enhanced HTI formation are shown in the lower left plot labeled HTI Fractures. Here, the flexural dispersion has the same shape as the isotropic case, increasing slowness with frequency, but are offset in slowness due to the azimuthal difference in slowness caused by an aligned set of fractures. The fast shear is shown in red, and the slow shear is shown in dark blue. At low frequency, the Stoneley slowness increases due to the permeability of the fracture system. The permeability effect at high frequency is minor thus the high frequency response is identical to the isotropic Stoneley case.

The dispersion curves for a stress enhanced HTI formation are shown in the lower right plot labeled HTI Stress. Again, the flexural dispersion is quite different from all other cases. At low frequency, shear wave splitting is observable. However, the slow shear wave show less increase in slowness with frequency than the fast shear wave, causing a "cross-over" of dipole dispersion curves at an intermediate frequency. Because low frequencies probe deeper into the formation than higher frequencies, the low frequencies are sensitive to the far-field in-situ horizontal stresses, while the high frequencies are sensitive to the wellbore "hoop" stress which is perturbed by the existence of the fluid filled borehole. In fact, there is a 90-degree rotation in horizontal stress from the far-field to the wellbore, which cause the dispersion curves to cross over.

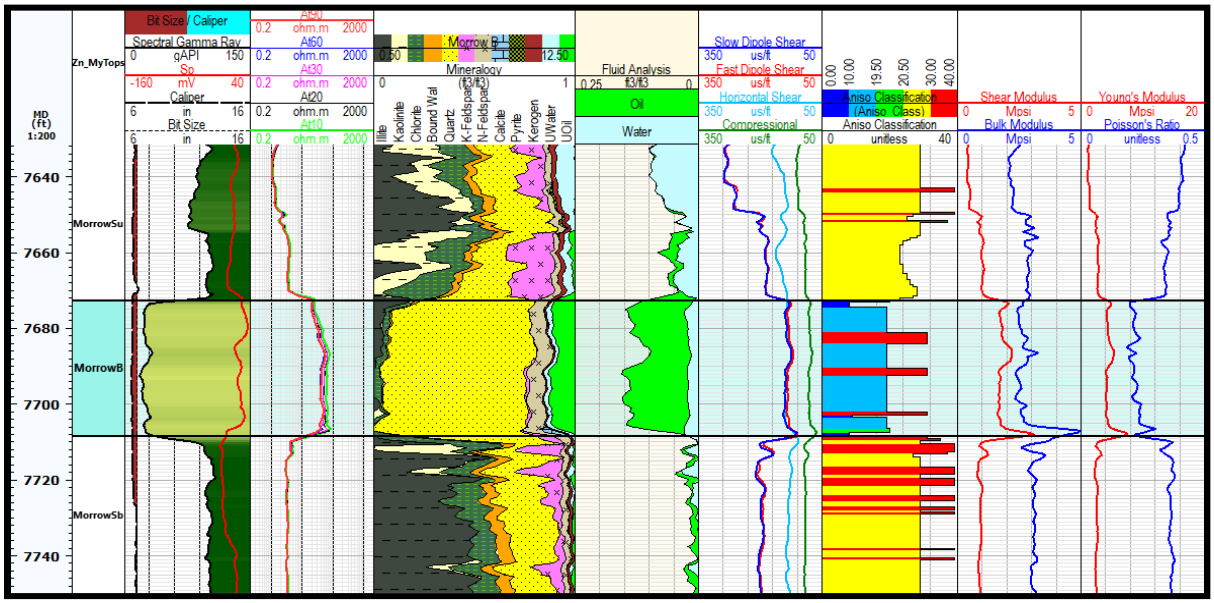

Figure 3.10: Anisotropy analysis for the Morrow B and Morrow Shale Formations. Track 1 shows the measured depth, track 2 shows the formation names, track 3 shows the bit size and caliper, spectral gamma ray and spontaneous potential, track 4 shows the induction resistivities, track 5 shows the fractional volumes, track 6 is the fluid analysis, track 7 shows the acoustical slownesses, track 8 shows the anisotropy classification, and tracks 9 and 10 show the isotropic dynamic elastic moduli.

The type and magnitude of anisotropy in the Morrow Formations is quite varied as shown in Figure 3.10. The Morrow B sandstone is slightly HTI. The magnitude of the HTI anisotropy is too small for the dispersion analysis to distinguish if the source of anisotropy is caused by fractures or stress. The Upper Morrow Shale is strongly VTI (yellow shading) with few orthotropic layers (red shading). The Lower Morrow Shale is also strongly VTI (yellow shading). However, the upper part of the Lower Morrow Shale shows several layers are orthotropic (red shading). Figure 3.11 shows the same analysis as Figure 3.10, but over a larger depth interval.

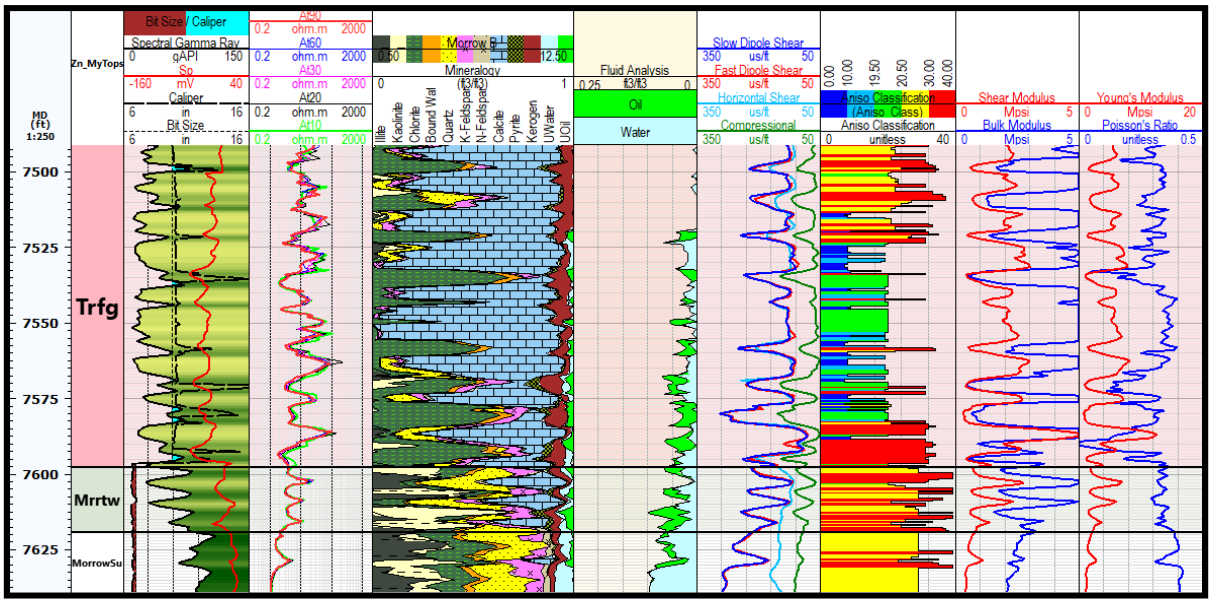

Figure 3.11: Anisotropy analysis for the Thirteen Finger Limestone Formation (Trfg) in comparison to the Morrow Formations. Track 1 shows the measured depth, track 2 shows the formation names, track 3 shows the bit size and caliper, spectral gamma ray and spontaneous potential, track 4 shows the induction resistivities, track 5 shows the fractional volumes, track 6 is the fluid analysis, track 7 shows the acoustical slownesses, track 8 shows the anisotropy classification, and tracks 9 and 10 show the isotropic dynamic elastic moduli.

The source rock for the Morrow B Formation is the Thirteen Finger Limestone formation. It has a large magnitude of organic carbon and is highly layered and fractured as shown by the anisotropy classification. Full waveform processing of sonic logs is complicated and requires special expertise to accurately determine the type and magnitude of anisotropy. Special diagnostic plots are required to ensure the full waveform data is processed correctly. Full sonic waveforms must be filtered appropriately to remove unwanted components as shown in Figure 3.12.

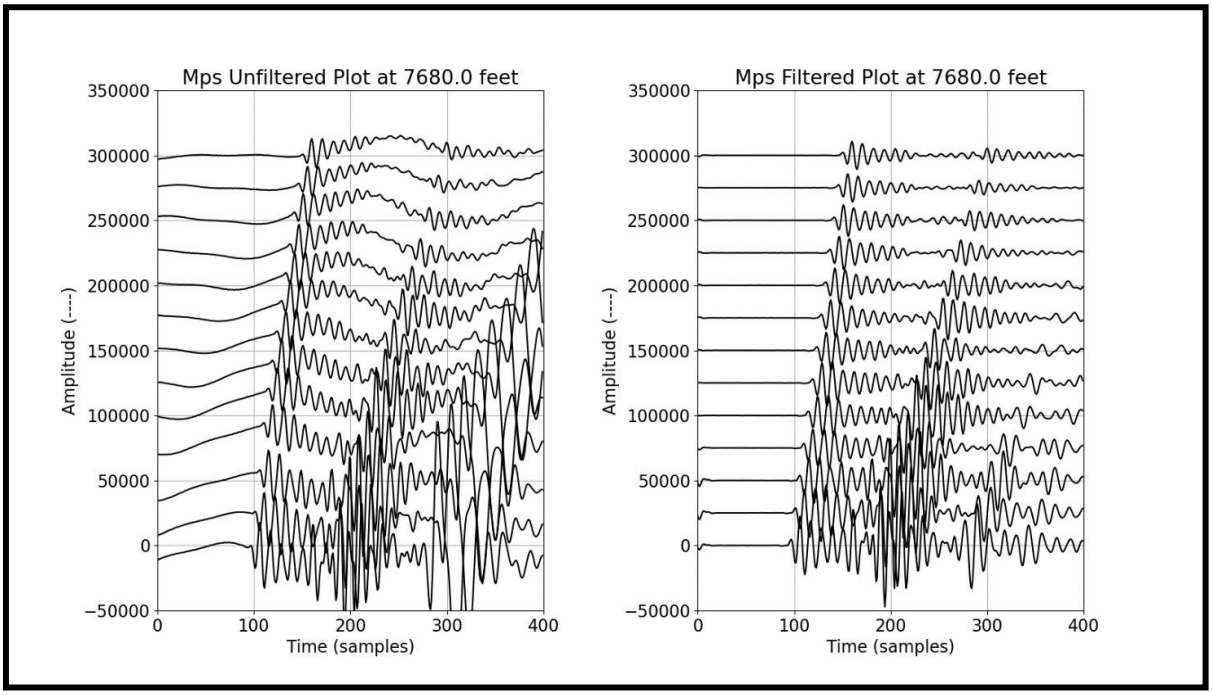

Figure 3.12: A comparison of the high frequency monopole waveforms, unfiltered on the left and filtered on the right.

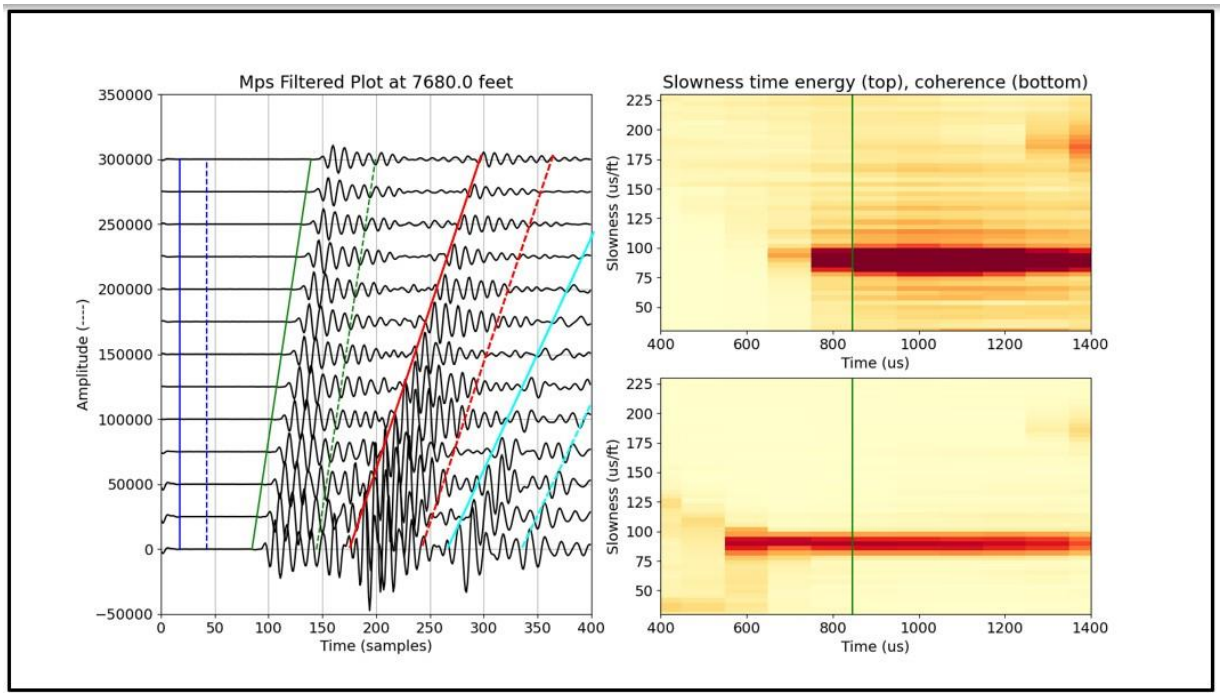

Figure 3.13: The left sonic waveform plot shows the location of energy windows in the time domain. The solid line shows the beginning of the energy window, and the dotted line shows the end of the energy window. The dark blue window measures noise, the green window measures the P-wave information, the red window measures the S-wave information, and the cyan window measures the Stoneley information. The plots on the right show the energy (top) and coherence (bottom) for the P- wave arrival. The vertical green line shows the time where the P-wave information is quantified. It is important to identify the propagating modes in the full waveform data to characterize the attributes, e.g., slowness, amplitude, and attenuation of each mode. Some waveform sets are complicated with noise, reflections, borehole size changes and tool artifacts.

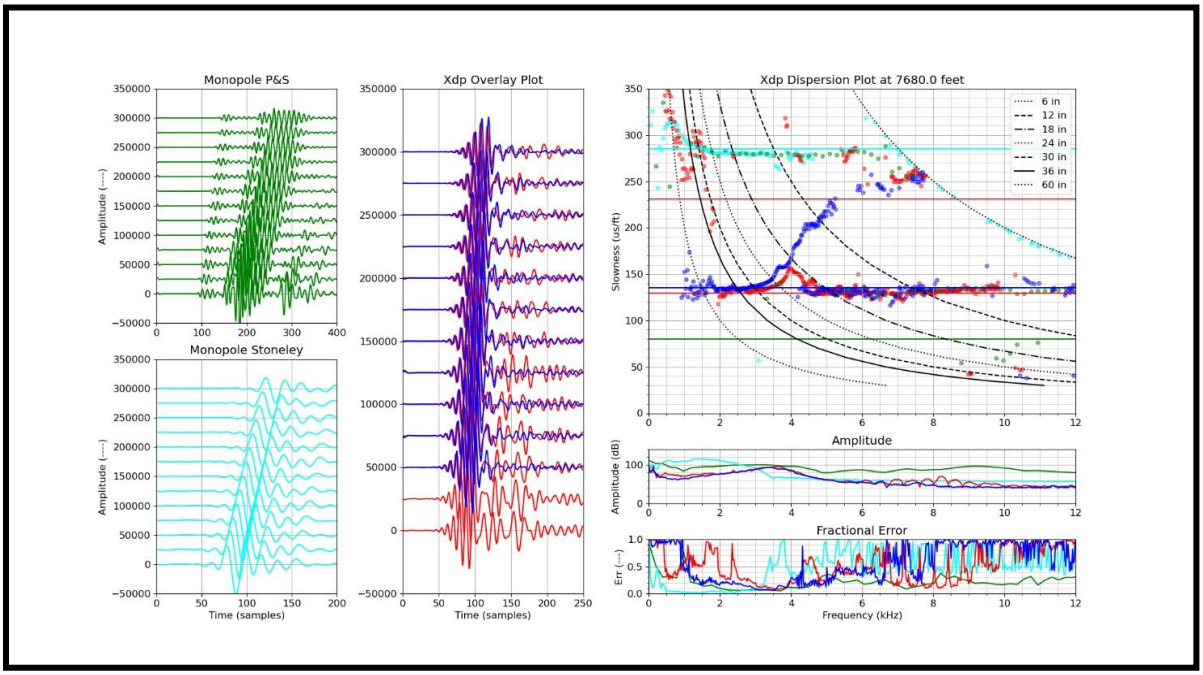

Figure 3.14: This is a collection of plots to analyze the dispersion in the waveform data. The plot in the top left corner shows the filtered high frequency monopole data in green. The P-wave, S-wave, and Stoneley arrivals are clearly visible. The plot in the bottom left shows the filtered low frequency monopole data in cyan. The low frequency Stoneley arrival is clearly visible. The central plot shows the filtered dipole waveforms. This overlay plot shows the "X" dipole waveform in blue and the "Y" dipole waveform in red. Shear wave splitting is seen by the offset of the two waveforms in time and moveout. The three plots on the right show the dispersion in the data (top), the amplitude of the signal (middle), and the fractional error (bottom). The curved black lines show the slowness frequency relationship for constant wavelengths of 6 to 60 inches.

Dispersion analysis is critical to analyze the acoustical behavior of the formation. This includes diagnostics for isotropic and homogeneous formations, but also anisotropic and heterogeneous formations. HTI anisotropy from full waveform data is quantified using Alford rotation (Alford, 1986 and Esmersoy, 1995). One assumption in the Alford rotation processing requires all hydrophones to be matched in absolute amplitude and the acquisition free from the complicating factors mentioned above. One diagnostic is plot shown in Figure 3.15. If a formation exhibits shear wave splitting, then one observes a time delay with the slow shear waveform. In addition, the slowness vs. angle plot, middle plot on the right, should have a two-theta dependence, or a complete cycle in 180 degrees. Also, the energy vs. angle plot, bottom plot on the right, should have a four-theta dependence, or two cycles in 180 degrees. If the hydrophones are matched, and the acquisition free from complications, the minimums in energy occur at the angles that define the fast and slow shear. High quality rotation results are not possible in bad borehole conditions.

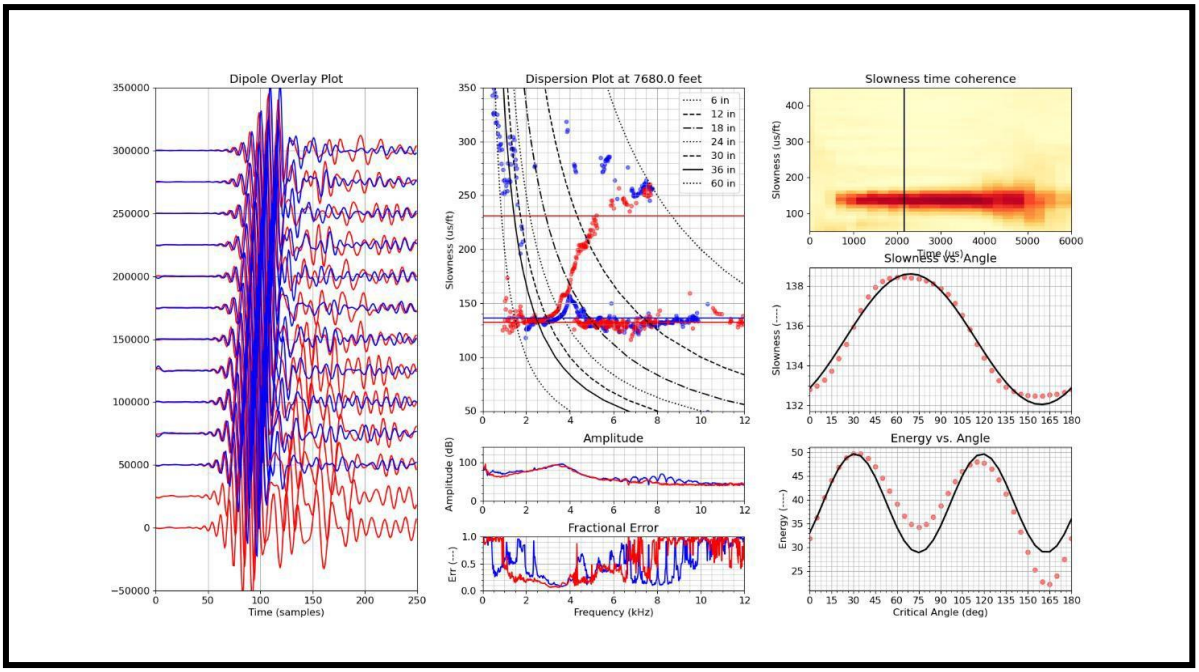

Figure 3.15: This is a collection of plots to understand shear wave splitting and quantify the fast-shear azimuth. The left plot shows the filtered dipole waveforms. This overlay plot shows the "X" dipole waveform in blue and the "Y" dipole waveform in red. Shear wave splitting is seen by the offset of the two waveforms in time and moveout. The three plots in the middle show the dispersion in the data (top), the amplitude of the signal (middle), and the fractional error (bottom). The curved black lines show the slowness frequency relationship for constant wavelengths of 6 to 60 inches. The three plots on the right show the slowness-time-coherence for the shear arrival (top), the slowness as a function of rotation angle (middle), and the crossline energy of the shear arrival.

3.2 Petrophysical Analysis

Three logging runs were made over different intervals of the well as shown in Table 3.1.

Table 3.9: Logging runs on Farnsworth 1310A. PeX – Platform Express (Triple combo), SS – Sonic Scanner (Full waveform Dipole Sonic), ECS (Elemental Capture Spectroscopy), CMR (Combinable Nuclear Magnetic Resonance), UBI (Ultrasonic Borehole Imager), and OBMI (Oil Based Mud Imager).

Logging Run	Depths (feet)	Logging Tools
Run 1	841 to 1990	Platform Express (PeX), Sonic Scanner (SS)
Run2	1914 to 7563	PeX, SS
Run3	7488 to 7863	PeX, SS, Spectral Gr, ECS, CMR, UBI, OBMI

To solve for the fractional volumes of minerals and fluids, the authors employed Schlumberger's elemental analysis (ELAN), a multi-mineral petrophysical solver (Quirein et al., 1986). A set of input logs are used to determine the fractional volumes by minimizing the difference between the measured and modeled logs.

Geologic knowledge, in the form of mineral and fluid volumetric relationships, can be honored in the weighted least squares inversion. Multiple models can be evaluated at every depth and the most appropriate model is selected for the final output. The input logs used for Run 3 include the bulk density, volumetric photoelectric factor, thermal neutron porosity, and deep and shallow resistivity curves from the Platform Express tool, the potassium curve from the spectral gamma ray tool, the total porosity from the nuclear magnetic resonance tool, the compressional and shear velocity from the dipole sonic tool, and the weight fractions of quartz-feldspar-mica (QFM), calcite, and clay, from the elemental capture spectroscopy tool, and total organic carbon from the uranium curve from the spectral gamma ray tool. The formation model for Run 3 solved for the fractional mineral volumes of illite, kaolinite, chlorite, quartz, potassium feldspar, sodium feldspar, calcite, pyrite, and kerogen, and the fractional fluid volumes of oil and water. The dual water model was used to interpret the resistivity measurements and a linear model was used for the dipole sonic velocities. Three models for total organic carbon were considered, the Passey model (Passey, 1990), a model based on uranium content, and the Schmoker model based on bulk density (Schmoker, 1983).

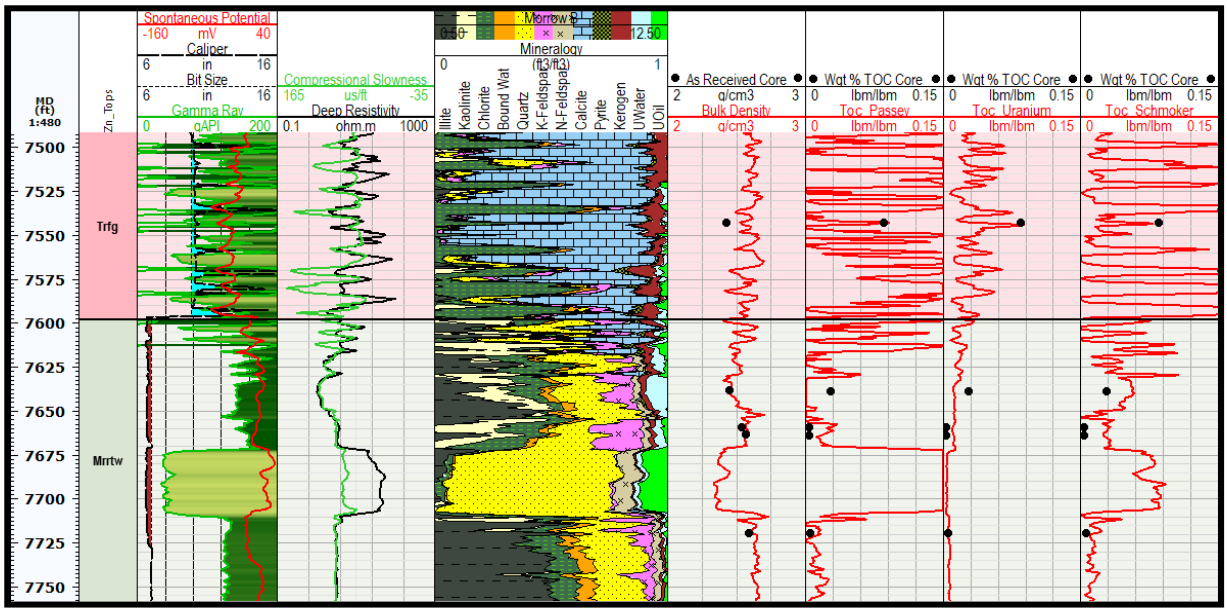

Figure 3.16: Calibration of the log models to the total organic carbon measure in the core.

All three models match the core data reasonably well, but the uranium model matches the core data the best. The Morrow Shale Formation above the Morrow B Sand Formation has more organic carbon than the Morrow Shale Formation below the Morrow B Sand Formation, but the Thirteen Fingers Lime has three times more organic carbon than the upper Morrow Shale Formation. The average R_o value from the core is 0.7. This value allowed the petrophysical properties of kerogen to be determined (Craddock, 2019). Once the organic carbon is quantified and combined with the nuclear spectroscopy logs, a full mineral based petrophysical analysis can be conducted.

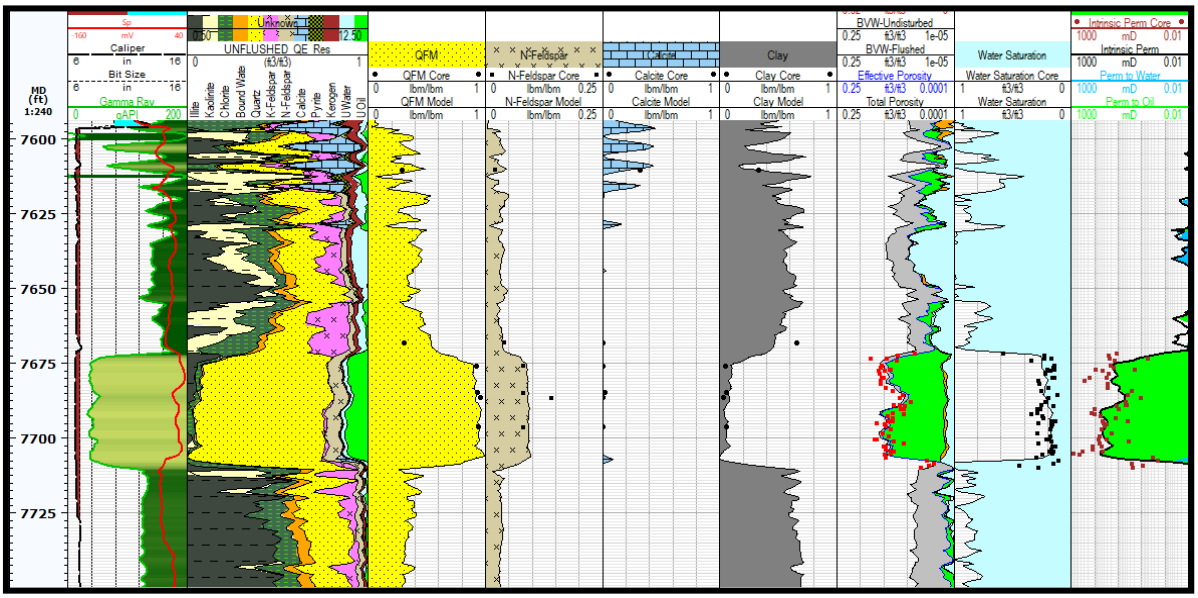

Figure 3.17: Calibration of the petrophysical parameters to the core data. Track 1 is the depth track, track2 shows the gamma ray, caliper, and spontaneous potential, track 3 shows the mineralogical model, track 4 through 7 show the comparison between the model and core for quartz-feldspar-mica, sodium feldspar, calcite and clay, track 8 shows the porosity, track 9 shows the water saturation, and track 10 shows the permeability.

This petrophysical model fits the compositional minerals determined from core quite well as does the porosity and water saturation. Matrix permeability was computed using Herron's geochemical algorithm (Herron, 1987), and the isotropic dynamic elastic moduli were computed using the measured P-wave and S-wave velocities.

3.3 Rock Physics Analysis

Rock physics models are required for fluid substitution and upscaling. The variation of the log derived shear modulus with porosity in the Morrow B Formation is shown in Figure 3.18. The left plot shows the isotropic shear modulus decreases with an increase in effective porosity. The least squares linear fit gives an R-squared value of 0.69. The corrected gamma ray (Cgr) is computed with the contributions of thorium and potassium but without the contribution of uranium, Thus, it is a good clay indicator and is shown in color. The higher volume of clay is correlated with a decrease in effective porosity. The right plot compares the log-derived shear modulus with established correlations given by Lev Vernik (Vernik, 1998). Vernik defined a clean arenite as a matrix-supported siliciclastic with the volume of clay less than 2%, an arenite with the volume of clay more than 2% but less than 12%, and a wacke as a clay-supported siliciclastic with the volume of clay more than 12% but less than 27%. These correlations based on ultrasonic velocities measured on recovered core were made with an effective stress of 5800 psi. The log-derived shear modulus was made with an effective stress of 3200 psi. It is interesting to note that whereas the Morrow B Formation is an arenite, the log-derived shear modulus corresponds to Vernik's wacke correlation. The lower modulus values observed could be due to lower cohesion or lower stress.

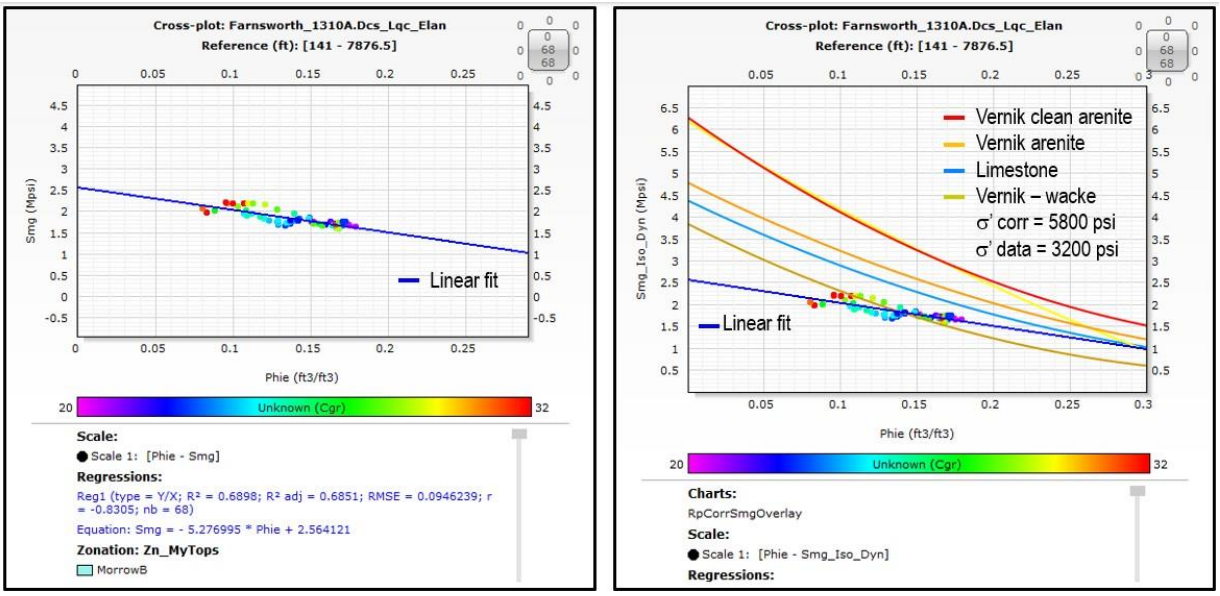

Figure 3.18: Variation of shear modulus with porosity in the Morrow B Formation. The left plot shows the relationship between the shear modulus (Smg) with effective porosity (Phie). The right plot compares the measured shear modulus with established correlations due to Vernik.

The variation of the log derived bulk modulus with effective porosity in the Morrow B Formation is shown in Figure 3.19. The left plot shows the isotropic bulk modulus decreases with an increase in effective porosity. The right plot compares the log-derived bulk modulus with established correlations given by Lev Vernik (Vernik, 1998). The dry rock-frame modulus, also known as the skeleton modulus, K_{skel}, is a primary input for fluid substitution modeling. It is a primary input because to a large extent it controls the impact of fluids on the wet-frame bulk modulus.

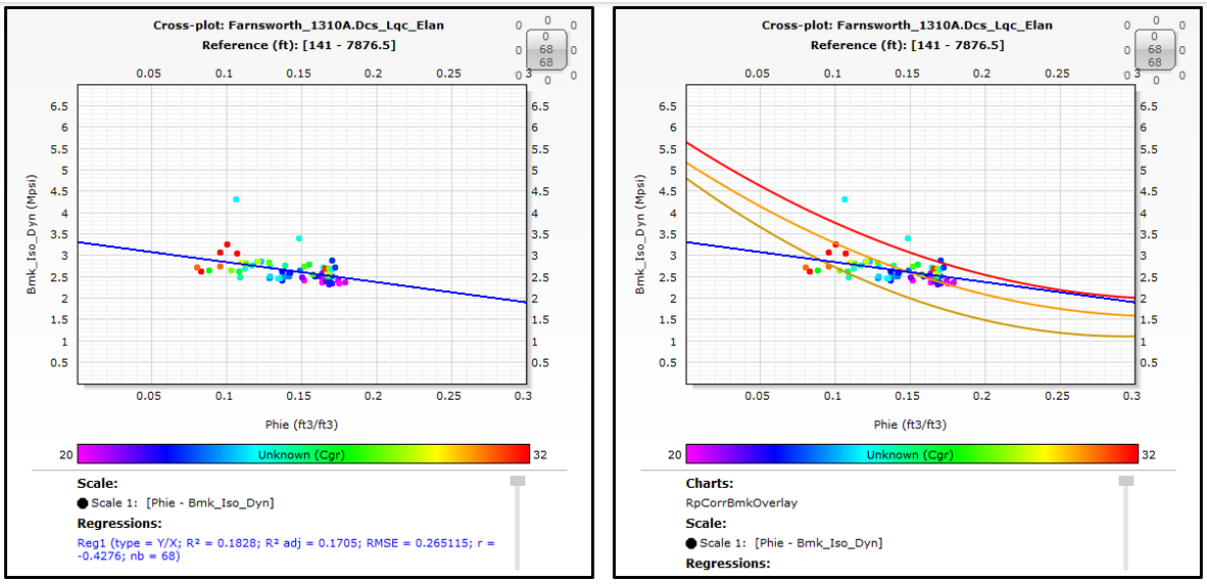

Figure 3.19: Variation of bulk modulus with porosity in the Morrow B Formation. The left plot shows the relationship between the bulk modulus (Bmk) with effective porosity (Phie). The right plot compares the measured bulk modulus with established correlations due to Vernik.

The skeleton modulus was modeled as a function of porosity using the model of Krief (Krief, 1990) but with fitting parameters based on the Morrow B Formation. Krief modeled the skeleton modulus as a function of porosity with the relationship given in Equation 3.3.

$$K_{skel} = K_{solid}[1-\phi]^{\left(\frac{3}{1-\phi}\right)} \tag{3.3}$$

K_{solid} is the zero-porosity limit of K_{skel} and ∅ is the effective porosity. The value of 3 in the numerator of the exponent can be adjusted to fit the measured data. An identical equation was utilized for the shear modulus by substituting the shear modulus for the bulk modulus as given in Equation 3.4.

$$G_{skel} = G_{solid}[1-\phi]^{\left(\frac{3}{1-\phi}\right)} \tag{3.4}$$

Biot's coefficient is given by Equation 3.5.

$$\alpha = 1 - \frac{K_{skel}}{K_{solid}} \tag{3.5}$$

The pore modulus is defined by Equation 3.6.

$$K_{pore} = \frac{\alpha^2}{\frac{\phi}{K_{fluid}} - \frac{(\alpha-\phi)}{K_{solid}}} \tag{3.6}$$

The wet-frame, or saturated, bulk modulus is given by Equation 3.7.

$$K_{sat} = K_{skel} + K_{pore} \tag{3.7}$$

The variation of the shear modulus with effective porosity for the Morrow B Formation is shown in the left plot of Figure 3.20. The solid shear modulus used was 2.70 Mpsi and the fitting coefficient used was 1.44. The variation of the dry-frame bulk modulus with effective porosity for the Morrow B Formation is shown in the right plot of Figure 3.20. The solid bulk modulus used was 3.40 Mpsi and the fitting coefficient used was 2.20. The fluid effect is given by Equation 3.6 and the wet-frame, or saturated, bulk modulus is given by Equation 3.7. It should be noted that the much of the variability in the shear and bulk moduli is caused by variations in the solid modulus due to mineralogy or fabric.

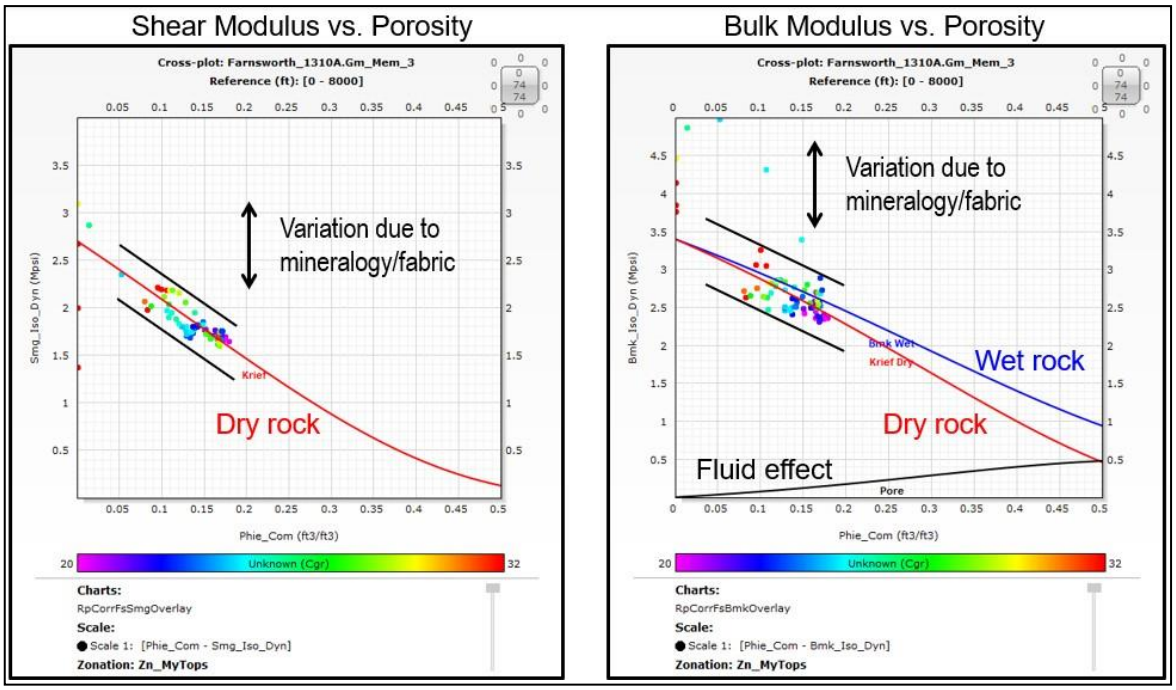

Figure 3.20: The isotropic shear (Smg) and bulk modulus (Bmk) as a function of effective porosity for the Morrow B Formation.

Upscaling from the log scale to the VSP scale is needed to provide an appropriate velocity model for the full waveform inversion of the VSP data. Backus upscaling is appropriate for isotropic or VTI layers (Backus, 1962). However, there exists a significant amount of HTI in the layers above the Morrow B Formation which cannot be upscaled with the conventional Backus upscaling. Schoenberg-Muir upscaling can account for isotropic, both VTI and HTI, and orthotropic layers (Schoenberg, 1989).

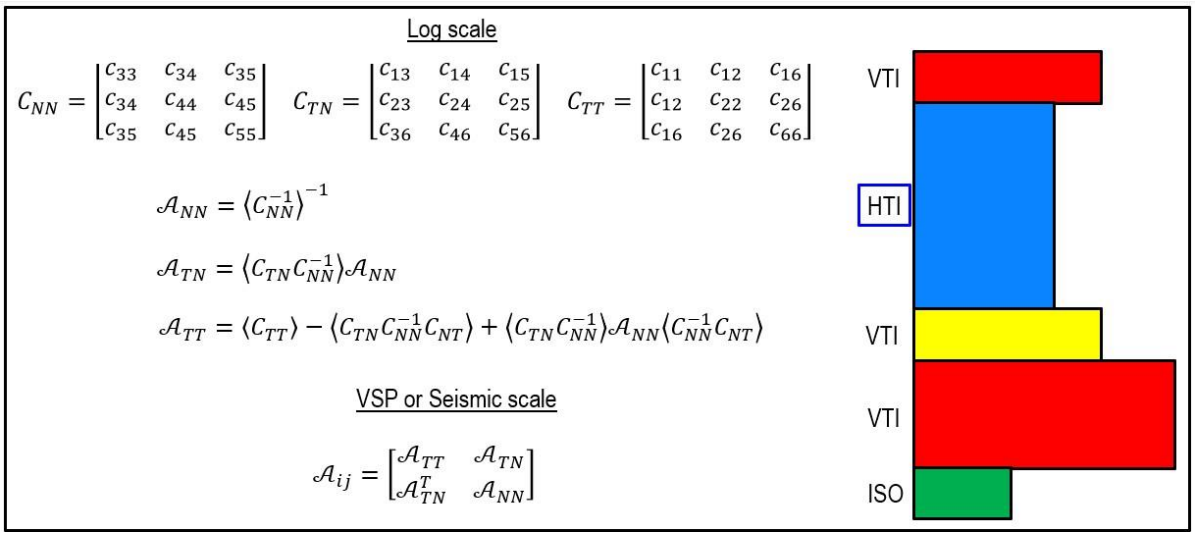

Figure 3.21: Schoenberg-Muir upscaling to account for HTI layers.

3.4 Geomechanics

The purpose of a mechanical earth model (MEM) is to provide a complete collection of input data required to run a geomechanical simulation. While the components of the earth model vary with the requirements of the geomechanical simulation, in general there are eight components to the MEM: 1) a framework model to characterize the structure of the formation including formation horizons and major faults, 2) a petrophysical model to quantify the lithology, porosity, water saturation, matrix permeability, and dynamic elastic moduli, 3) a mechanical stratigraphy model to characterize the stratigraphic column, load bearing facies, and natural and drilling induced fracture attributes, 4) a rock property model to characterize the static moduli, deformation, yield, and failure properties of the formation, 5) an overburden model to characterize the vertical loading, 6) a pore pressure model to quantify the pore pressure, 7) a stress orientation model to characterize the dip and azimuth of the far-field stresses, and finally 8) a stress magnitude model to quantify the horizontal loading on the formations. Figure 3.22 shows the eight components of the MEM and the typical sources of data to construct the individual models.

Seismic, Wellbore images	**Triple-combo, Sonic, Core**	**Wellbore images, Sonic, Core**	**Petrophysics, Sonic, Core**
Framework Structure Faults Horizons	**Petrophysics** Lithology, Vcl Porosity, Sw Matrix Perm Elastic Moduli	**Mechanical** Strat Column Facies Support Fracture Attributes	**Rock Strength** Compressive & Tensile Strength Friction Angle
Vertical Stress Overburden	**Pore Pressure** Pore Pressure	**Stress Direction** Maximum Horizontal Stress Direction	**Stress Magnitude** Minimum & Maximum Horizontal Stress
Density log, Petrophysics	**Formation testing, Petrophysics, Mud logs**	**Wellbore images, Sonic, 4-Arm calipers**	**In-situ stress tests, Sonic**

Figure 3.22: The components of a mechanical earth model and typical sources of data to quantify the components.

.

The area of interest covers a five-spot pattern in the Farnsworth Field in the Texas panhandle. A petrophysical model was built and discussed in a preceding section. A mechanical stratigraphy model was constructed using petrophysical cross plot methods (Herron et al., 1992). A rock properties model was built using standard geomechanical correlations. The static Young's modulus was derived from the Morales correlation (Morales, 1993), the unconfined compressive strength was derived from the Coates-Denoo correlation (Coates, 1981), and the friction angle was derived from the Plumb correlation (Plumb, 1994).

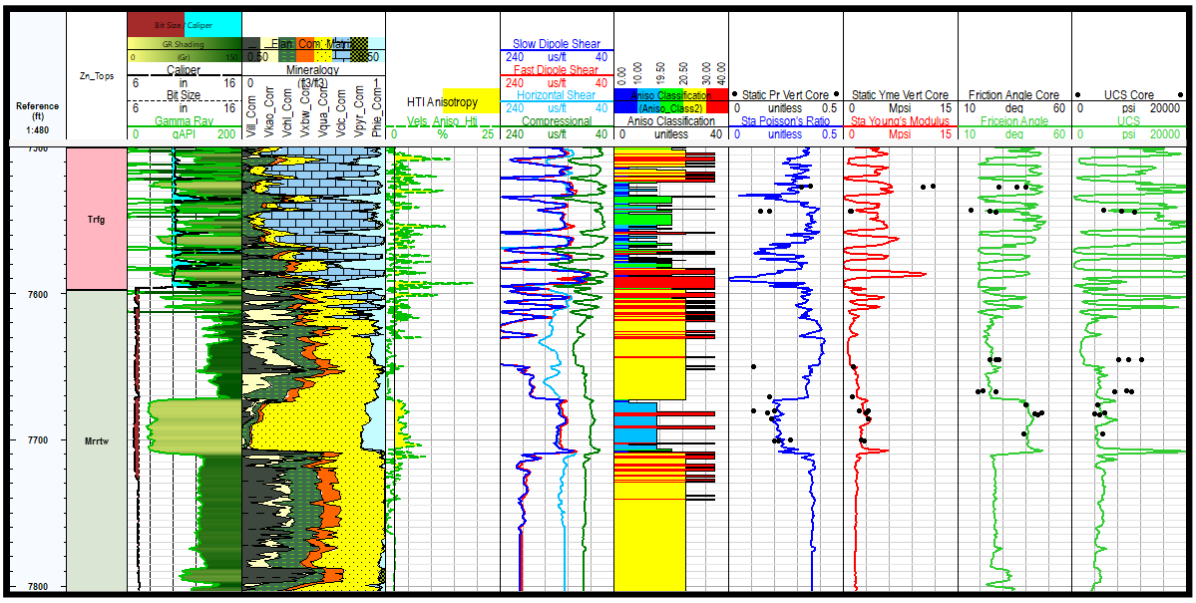

Figure 3.23: Static moduli and rock strength parameters.

An overburden model was constructed by integrating the measured bulk density from the surface to below the Morrow Formation.

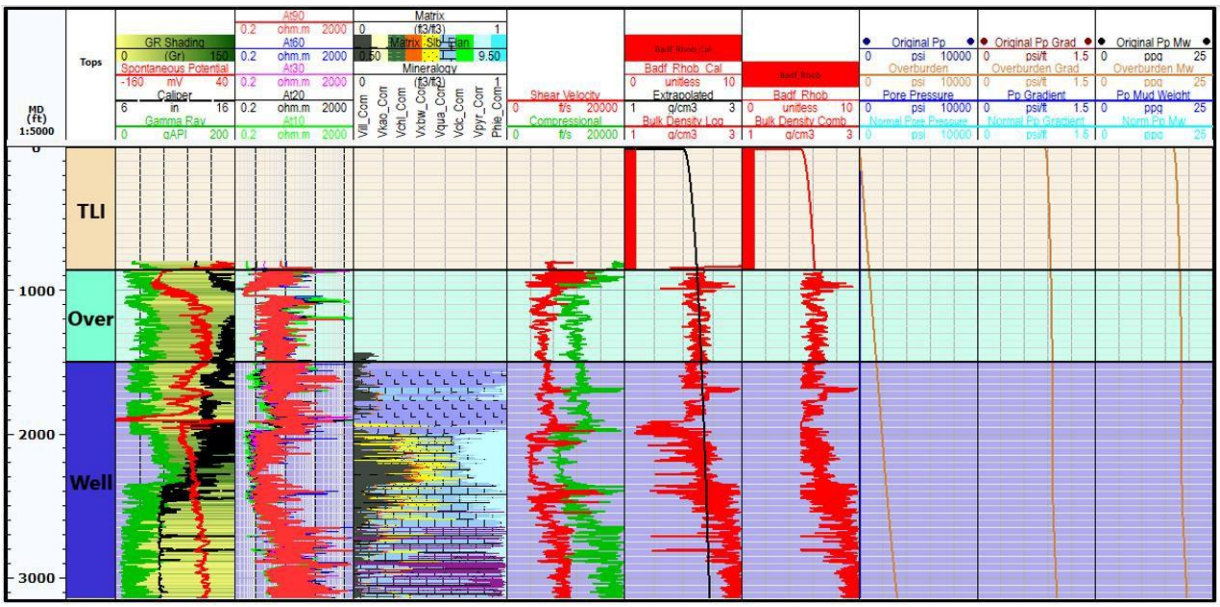

Figure 3.24: The overburden and pore pressure model. Track 1 is the depth track, track 2 shows the stratigraphic column, track 3 shows the correlation curves, track 4 shows the resistivity curves, track 5 shows the fractional volumes, track 6 shows the vertical sonic velocities, track 7 shows the measured density in red and an exponential model in black, track 8 shows the combination model where the exponential model was spliced to the measured density, tracks 9, 10 and 11 show the resulting pore pressure and overburden stresses in pressure, pressure gradient, and mud density.

An exponential bulk density model was used in the top 900 feet where no bulk density measurement was acquired. In addition, a bulk density curve based on the petrophysical model is used in place of the measured bulk density in intervals of enlarged and rugose borehole where the measured bulk density is invalid. The Morrow B Formation was significantly underpressured when the Farnsworth Field was discovered. The pore pressure was reported to be 2130 psi (0.28 psi/ft). Interestingly, there are many salt and anhydrite layers in the Wellington Formation which extends from 1500 feet to 3300 feet.

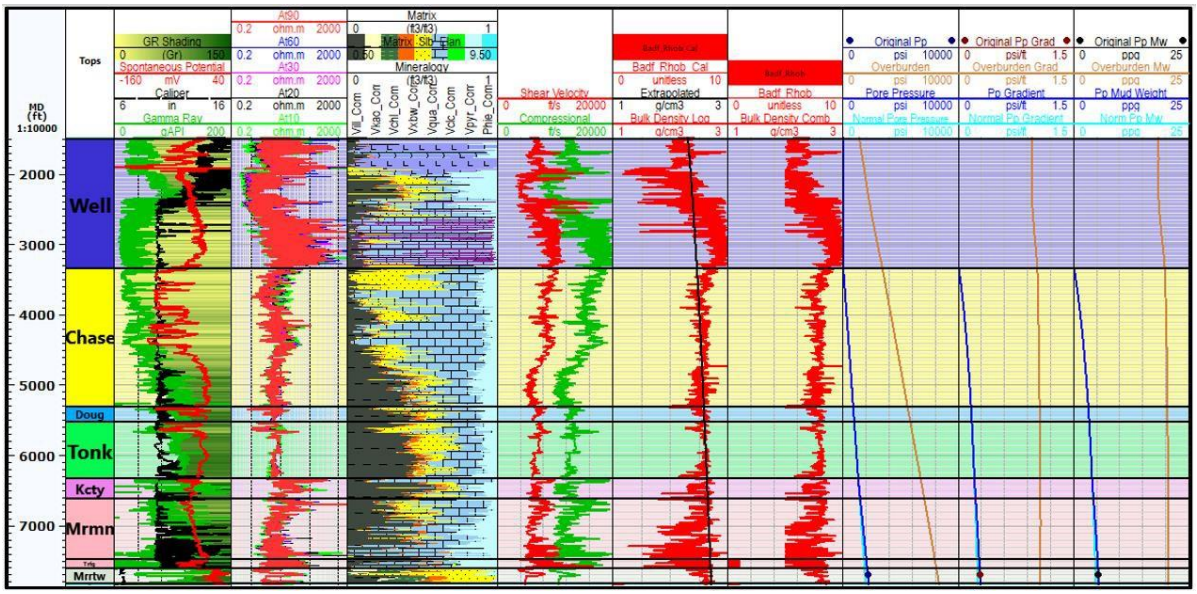

Figure 3.25: Overburden and pore pressure model from the Wellington Formation to below the Morrow Formation. Track 1 is the depth track, track 2 shows the stratigraphic column, track 3 shows the correlation curves, track 4 shows the resistivity curves, track 5 shows the fractional volumes, track 6 shows the vertical sonic velocities, track 7 shows the measured density in red and an exponential model in black, track 8 shows the combination model where the exponential model was spliced to the measured density, tracks 9, 10 and 11 show the resulting pore pressure and overburden stresses in pressure, pressure gradient, and mud density.

On a hunch, the fluid density from the bottom of the Wellington Formation was integrated into the Morrow B Formation, resulting in a calculated normal pore pressure of 1976 psi. Thus, the Morrow B Formation appears 154 psi overpressured, likely due to the maturation of the organic carbon. It appears there is no hydraulic continuity to the surface due to the salt and anhydrite layers in the Wellington Formation. In addition, these logs were acquired prior to the injection of the EOR CO_2 flood, so the slight overpressure is not likely due to the injection of fluids.

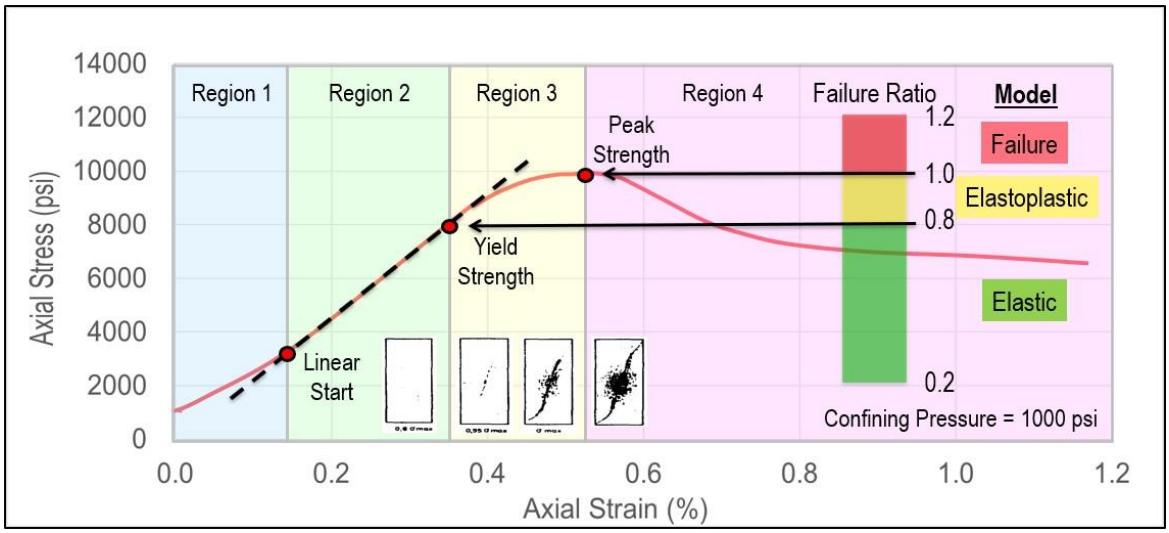

Figure 3.26: An elastic model is appropriate for Region 2, an elastoplastic model is appropriate for Region 3, and a failure model is appropriate for Region 4.

The stress magnitude model was constructed based on an estimate of the mechanical behavior of each layer as shown in Figure 3.26 (Bratton, 2018). In higher strength layers, where the in-situ stresses are estimated to be less than the elastic limit of the layer, the standard linear poroelastic horizontal strain model was selected (Green-Elastic). In lower strength layers, where the standard linear elastic model estimates the in-situ stresses to be greater than the confined compressive strength, the standard Mohr-Coulomb model was selected for these critically stressed layers (Red-Failure). An interpolated elastoplastic model was used for layers that are estimated to be greater than the elastic limit but less than the confined compressive strength of the critically stressed layers (Yellow-Elastoplastic). The right plot shows the stress polygon including impossible states of stress and differentiates elastic behavior from elastoplastic behavior.

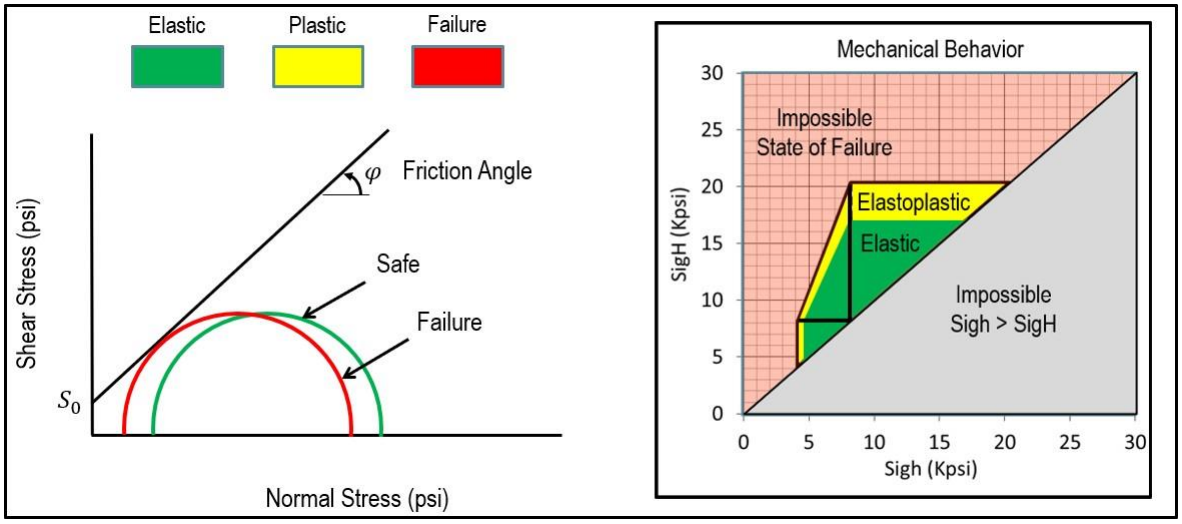

Figure 3.27: A stress polygon analysis. The left plot shows the standard Mohr-Coulomb plot. A linear failure envelope is shown by the black line defined by the cohesion (So) and the friction angle. When the Mohr half-circle is plotted using minimum and maximum normal effective stresses and half-circle touches the failure envelope.

.

Plotting data on a stress polygon is a good method to analyze in-situ far-field stresses. The left plot of Figure 3.27 shows a linear failure envelope in black that is defined by the cohesion (S_0), and the friction angle. When the Mohr half-circle shown in red touches the failure envelope, the formation is at failure defined by the peak strength. When the Mohr half-circle shown in green is right of the failure envelope, it is thought to be safe. But this can be a bit misleading. The right plot of Figure 3.27 shows the stress polygon for brittle formations. This is a plot of the maximum horizontal stress versus the minimum horizontal stress. By definition, the maximum horizontal stress is always equal to or greater than the minimum horizontal stress, so the area highlighted in grey represents an impossible situation. The three linear lines shown in black on the outside of the polygon represents the peak strength for the three stress regimes, normal faulting, strike-slip faulting, and thrust faulting. The vertical segment is the bound for normal faulting, the horizontal segment is for thrust faulting, and the diagonal segment is for strike slip faulting. Enclosed in the polygon are two areas shaded yellow for elastoplastic behavior and green for elastic behavior. The outer edge of the green shading represents the elastic limit of the stress state and is equivalent to the yield strength of the formation. Stress polygons that do now show the elastoplastic stress state are misleading because microcracks form and coalesce in this area which precedes failure. It is this more detailed mechanical analysis that is used in this study. The far-field in-situ stress orientation is assumed perfectly vertical and horizontal.

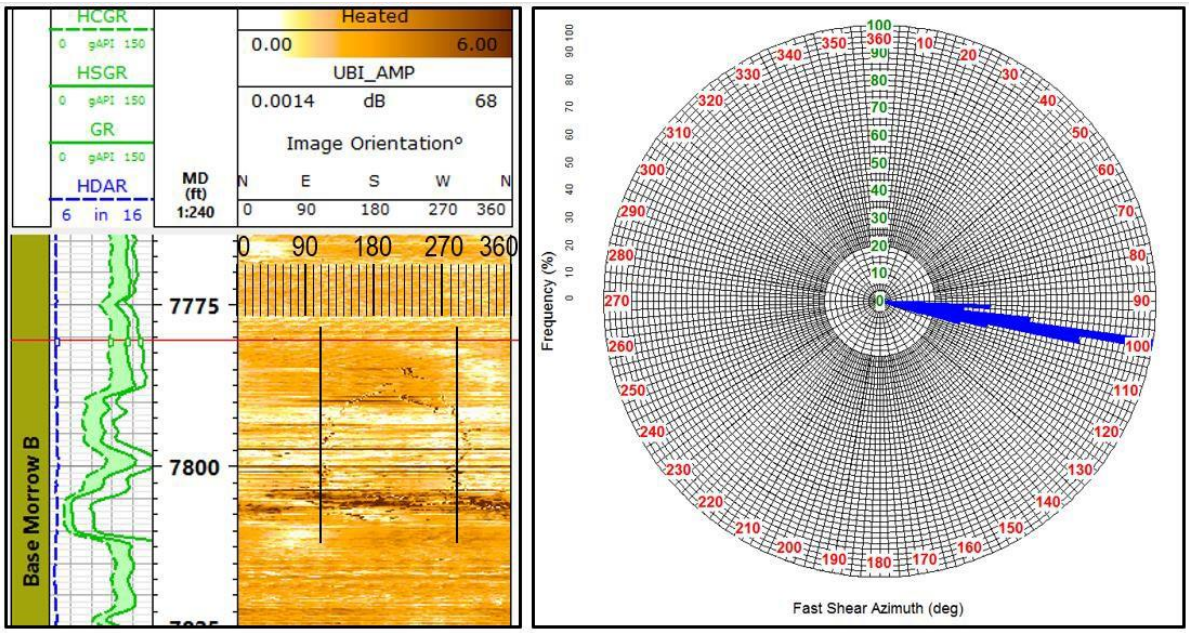

Figure 3.28: The far-field maximum horizontal stress azimuth defined by the ultrasonic images (left plot) and the acoustical azimuthal anisotropy (right plot).

The azimuth of the maximum horizontal stress is determined to be 108 (+- 4) degrees from the ultrasonic wellbore images based on the drilling induced fractures in the Morrow Shale Formation just below the Morrow B Formation. The drilling induced fracture is a combination of shear and tensile failure, leading to a greater uncertainty than a pure tensile failure. The fast shear azimuth from the azimuthal acoustical anisotropy yields 98 (+-2) degrees (Figure 3.28). These two measurements are independent from each other and represent consistency of the interpretation. The standard poroelastic horizontal strain equations were used in the layers diagnosed to be in the elastic domain. The minimum horizontal stress equation is shown in Equation 3.8 and the maximum horizontal stress is show in Equation 3.9.

$$\sigma_h = \left(\frac{\upsilon}{1-\upsilon}\right)(\sigma_V - \alpha P_P) + \left(\frac{E}{1-\upsilon^2}\right)\epsilon_h + \left(\frac{E_\upsilon}{1-\upsilon^2}\right)\epsilon_H + \alpha P_P \tag{3.8}$$

$$\sigma_H = \left(\frac{\upsilon}{1-\upsilon}\right)(\sigma_V - \alpha P_P) + \left(\frac{E_\upsilon}{1-\upsilon^2}\right)\epsilon_h + \left(\frac{E}{1-\upsilon^2}\right)\epsilon_H + \alpha P_P \tag{3.9}$$

The static values were used for the elastic moduli and Biot's alpha was set to one. The strain values

used was 0.00 for the minimum horizontal strain and 0.15 for the maximum horizontal strain. The standard Mohr-Coulomb failure model was used in the layers diagnosed to be critically stressed and in a state of failure. The Mohr-Coulomb equation is shown in Equation 3.10 and the confinement multiplier (N), which is a function of the friction angle, is shown in Equation 3.11.

$$\sigma_h = \frac{\sigma_V + (N+1)P_P}{N} \tag{3.10}$$

$$N = \frac{1 + sin\varphi}{1 - sin\varphi} \tag{3.11}$$

The maximum horizontal stress for the Mohr-Coulomb failure model was chosen to be 1.15 times the minimum horizontal stress, a value similar to that computed in the elastic model. An interpolated modelbased on failure ratio was used to estimate the stresses in the elastoplastic layers. Figure 3.29 shows the results of this analysis.

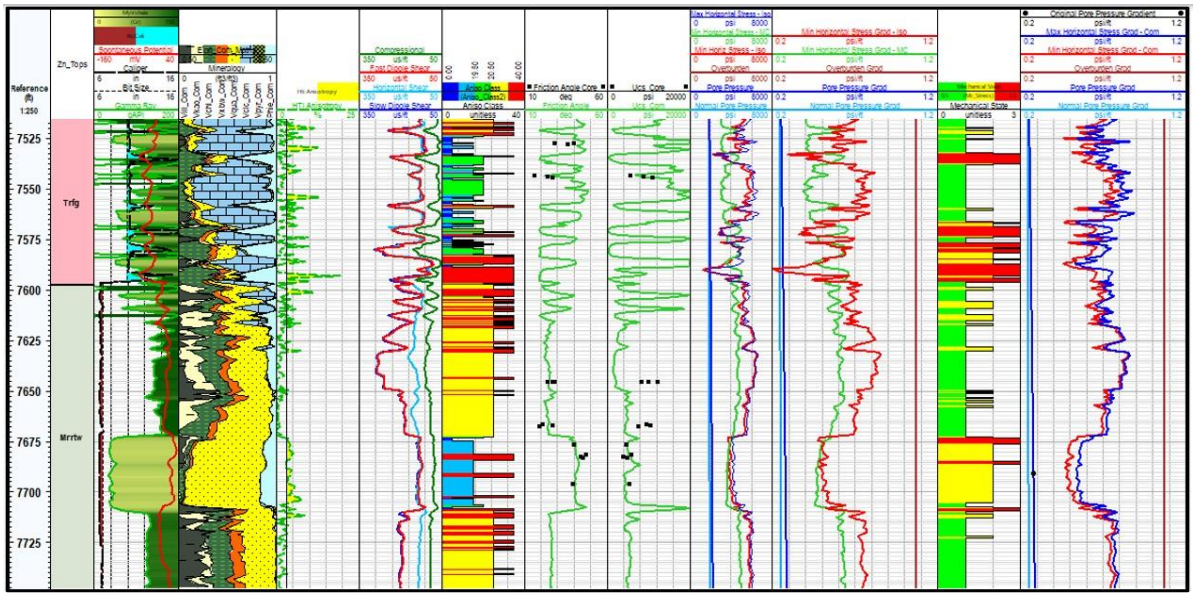

Figure 3.29: Horizontal stress magnitude analysis. Track 1 shows the measured depth, track 2 shows the formation names, track 3 shows the standard correlation curves, track 4 shows the mineralogical fractional volumes, track 5 shows the azimuthal HTI anisotropy, track 6 shows the dipole sonic slownesses, track 7 shows the anisotropy classification, track 8 shows the comparison between the log and core values for the friction angle, track 9 shows the comparison between the log and core values for the unconfined compressive strength, track 10 shows the pore pressure and stress curves, track 11 shows the pore pressure and stress gradients, track 12 shows the mechanical state, green shading for the elastic model, red shading for the Mohr-Coulomb Failure model and yellow shading for the elastoplastic model, and track 13 shows the stress gradients for the combined model.

It is interesting to note that the mechanical state for the Morrow B Formation from 7675 to 7710 feet is diagnosed as elastoplastic (shown in yellow). It is also interesting to note the mechanical state for the lower section of the Thirteen Finger Lime is diagnosed critically stressed and in a state of failure. However, mechanical state of the Morrow Shale both above and below the Morrow B Formation is diagnosed as elastic. Figure 3.30 shows the stress analysis in the Kansas City Formation. The mechanical state for the shaly interval starting at 6400 feet is critically stressed and in a state of failure.

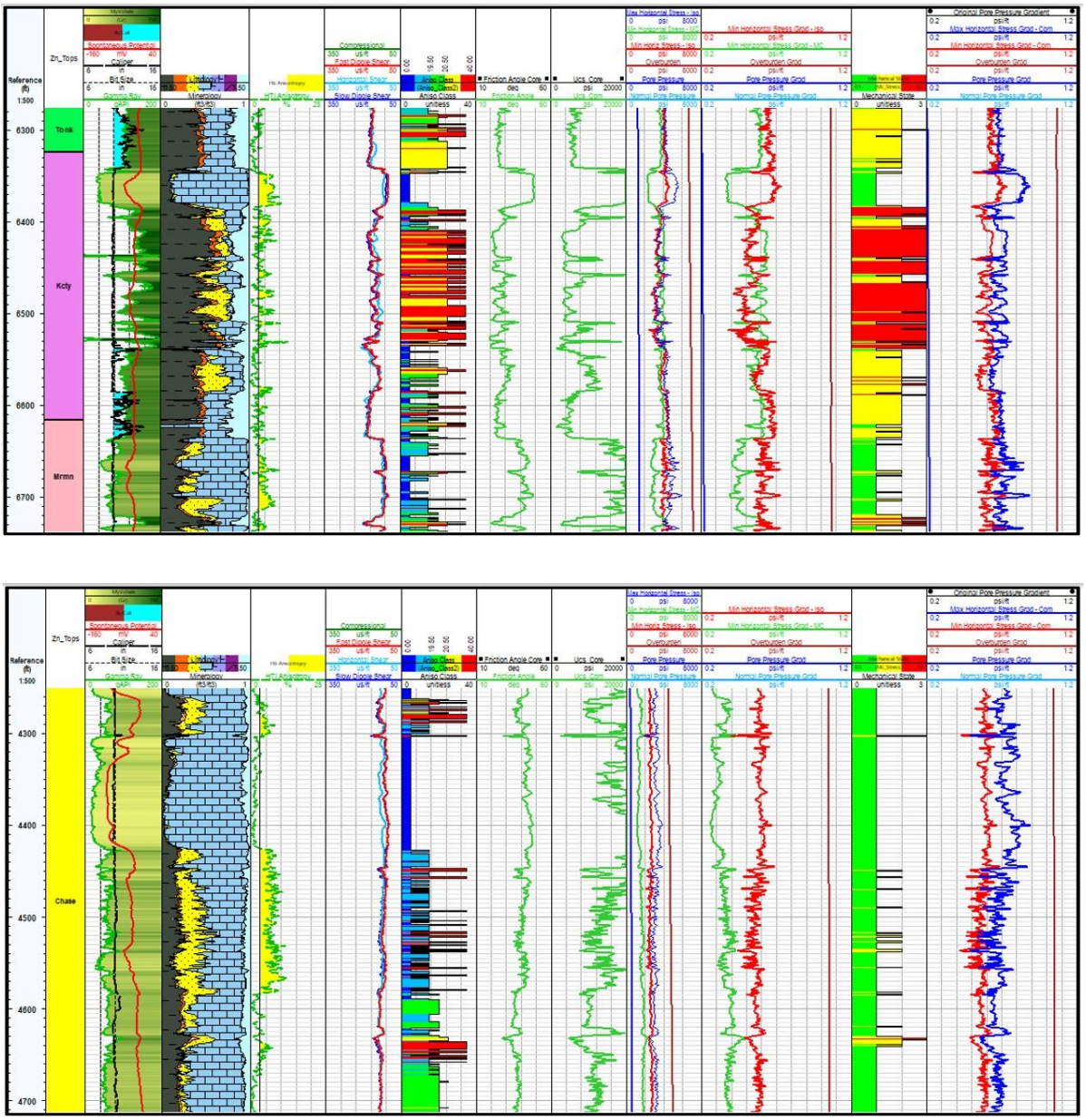

Figure 3.30: Horizontal stress magnitude analysis. Track 1 shows the measured depth, track 2 shows the formation names, track 3 shows the standard correlation curves, track 4 shows the mineralogical fractional volumes, track 5 shows the azimuthal HTI anisotropy, track 6 shows the dipole sonic slownesses, track 7 shows the anisotropy classification, track 8 shows the comparison between the log and core values for the friction angle, track 9 shows the comparison between the log and core values for the unconfined compressive strength, track 10 shows the pore pressure and stress curves, track 11 shows the pore pressure and stress gradients, track 12 shows the mechanical state, green shading for the elastic model, red shading for the Mohr-Coulomb Failure model and yellow shading for the elastoplastic model, and track 13 shows the stress gradients for the combined model.

Figure 3.31 shows the stress analysis in the Chase Formation. The interval just below the clean limestone shows considerable HTI azimuthal anisotropy.

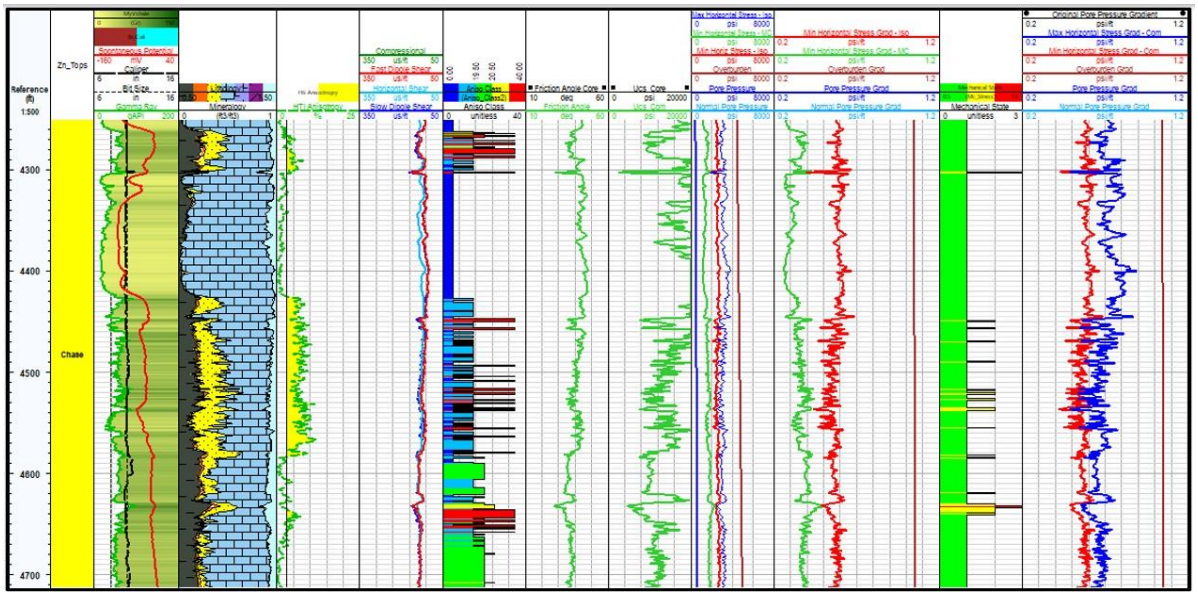

Figure 3.31: Horizontal stress magnitude analysis. Track 1 shows the measured depth, track 2 shows the formation names, track 3 shows the standard correlation curves, track 4 shows the mineralogical fractional volumes, track 5 shows the azimuthal HTI anisotropy, track 6 shows the dipole sonic slownesses, track 7 shows the anisotropy classification, track 8 shows the comparison between the log and core values for the friction angle, track 9 shows the comparison between the log and core values for the unconfined compressive strength, track 10 shows the pore pressure and stress curves, track 11 shows the pore pressure and stress gradients, track 12 shows the mechanical state, green shading for the elastic model, red shading for the Mohr-Coulomb Failure model and yellow shading for the elastoplastic model, and track 13 shows the stress gradients for the combined model.

Schlumberger's ultrasonic borehole imager (UBI) was run for wellbore images and hole shape analysis.

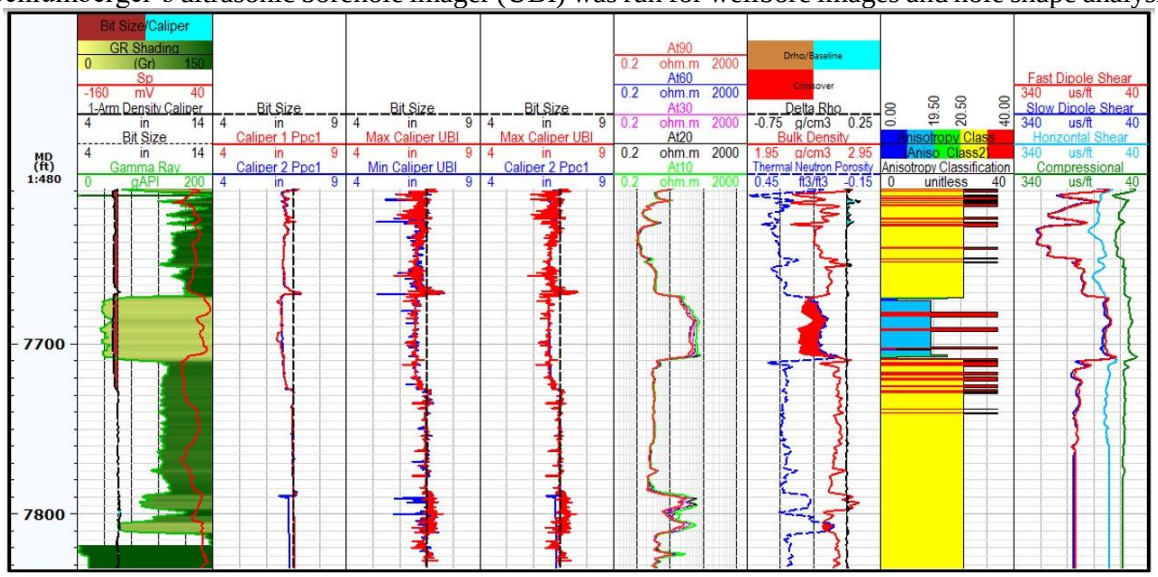

Figure 3.32: Hole size comparison between a 1-arm density caliper, two sets of 4-arm calipers, and a high-resolution ultrasonic caliper with 180 azimuthal measurements. Track 1 shows the measured depth, track 2 shows the correlation curves, the one-arm density caliper, gamma ray and spontaneous potential, track 3 shows the 4-arm caliper data, track 4 shows the minimum and maximum UBI caliper, track 5 shows a comparison between the 4-arm mechanical caliper and the high resolution UBI caliper, track 6 shows the resistivity curves, track 7 shows the thermal neutron porosity and density curves, track 8 shows the anisotropy classification, and track 9 shows the sonic slownesses.

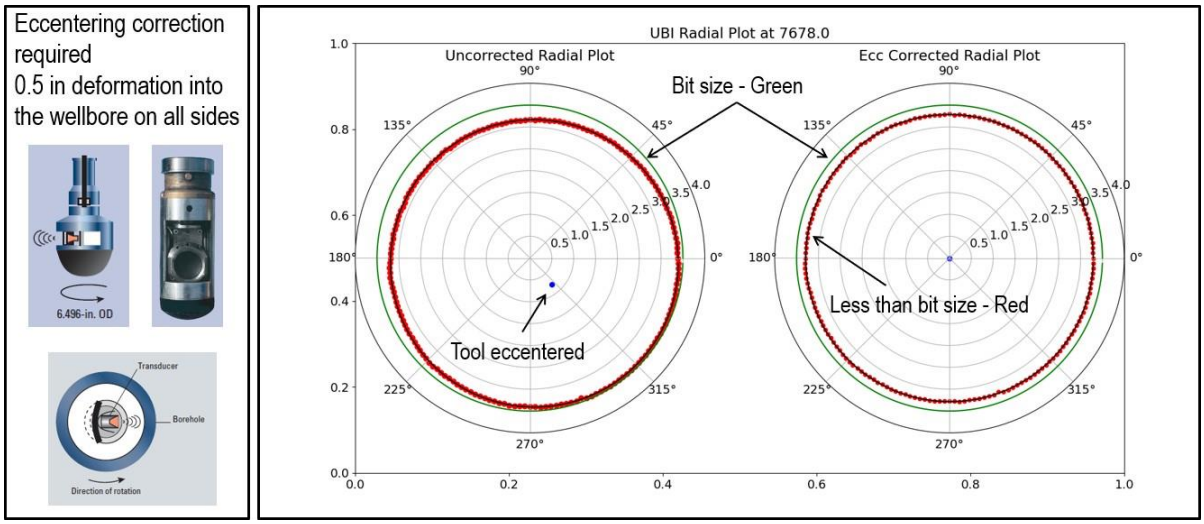

Figure 3.33: Ultrasonic Borehole Image data eccentering correction. The left plot shows the UBI sensor. The right plot shows a comparison on the uncorrected radial data and the eccentering corrected data in the Morrow B Formation. The green curve shows the expect hole size based on the bit size. The red dots are the 180-radial pulse-echo measurements.

Even though the UBI tool string had centralizers, the acquired data required an eccentering correction. The blue dot shows the central axis of the tool, but the position is exaggerated by a factor of five to provide a better comparison level to level. The measurements show deformation of the Morrow B Sand into the wellbore and an equal deformation on all sides of the borehole. Figure 3.34 shows the UBI data in the Morrow Shale Formation below the Morrow B Formation at a depth where the hole size is equal to the bit size.

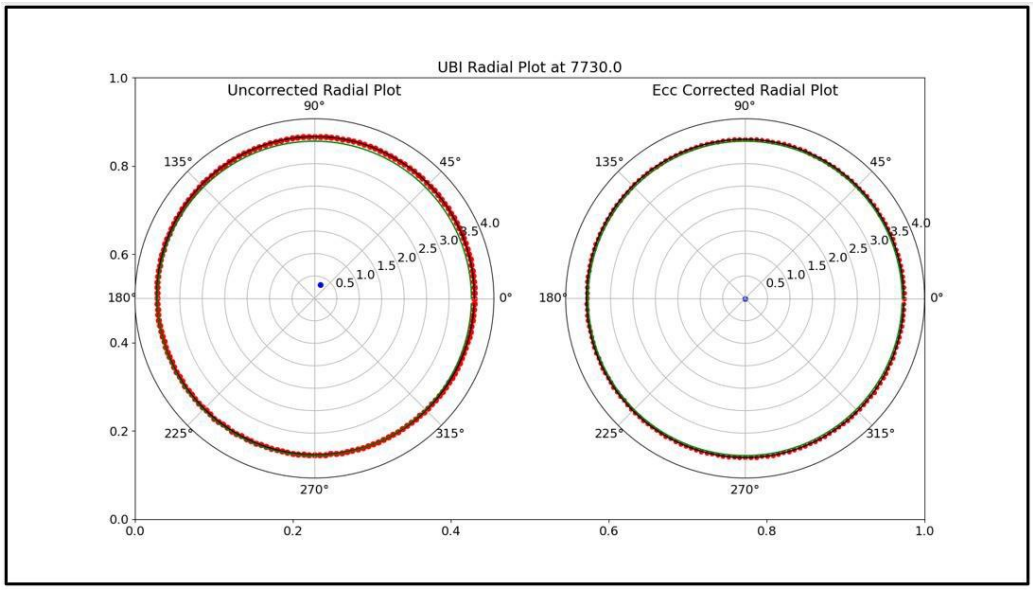

Figure 3.34: The right plot shows a comparison on the uncorrected radial data and the eccentering corrected data in the Lower Morrow Shale Formation. The green curve shows the expect hole size based on the bit size. The red dots are the 180-radial pulse-echo measurements.

It is interesting to observe the same magnitude of radial deformation into the wellbore in both the Morrow B Sand Formation and the Morrow Shale Formation both above and below the sand. This is surprising since the static mechanical properties shown in Figure 3.23 are different. Figure 3.35 shows the same radial deformation into the wellbore is observed in both the 13-10A well and the 13-14 well.

However, the depth where the deformation begins is different.

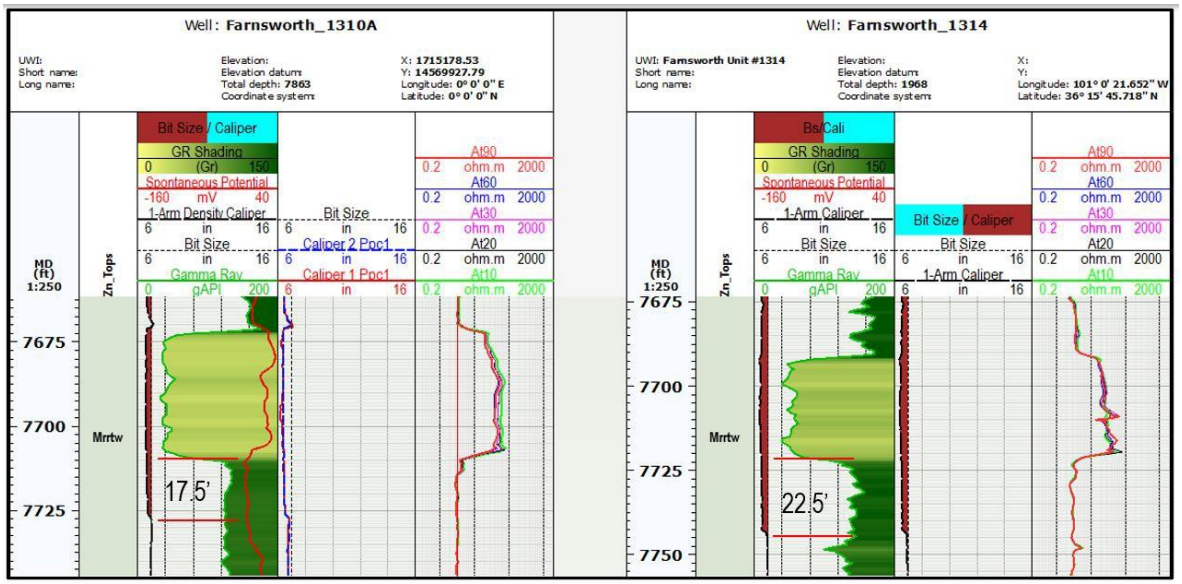

Figure 3.35: The same radial deformation is observed in two wells separated by 1500 feet. Track 1 shows the measured depth, track 2 shows the Formation names, track 3 shows the caliper, gamma ray, and spontaneous potential curves, track 4 also shows the caliper information, and track 5 shows the resistivity logs.

In the 13-10A well, the deformation begins 17.5 feet below the base of the Morrow B Sand while in the 13-14 well the deformation begins 22.5 feet below the base of the Morrow B Sand. These wells are separated by about 1500 feet. It is worth considering whether there has been any movement along a weak bedding plane that extends between the two wells.

3.4.1 Geomechanics simulations

The purpose of a mechanical earth model is to provide all the data needed to run a geomechanical or engineering simulator. Figure 3.36 shows a simulation of the stress response to the withdrawal and injection of fluids.

F

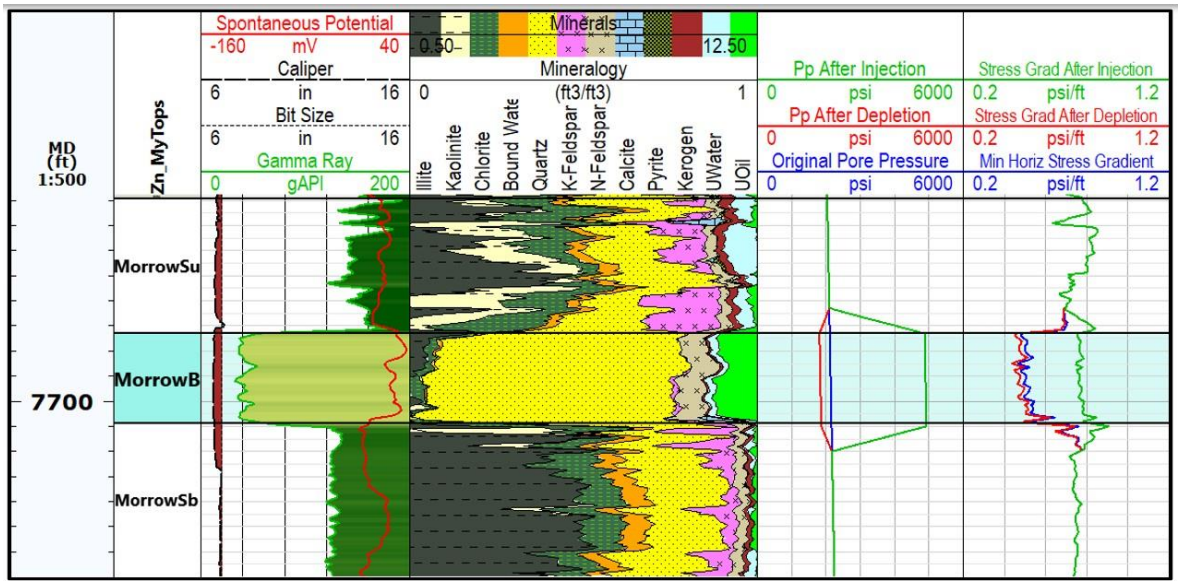

Figure 3.36: Impact of changes in pore pressure due to withdrawal and injection of fluids on the minimum horizontal stress. Track 1 show the measured depth, track 2 shows the formation names, track 3 shows the correlation curves, track 4 shows the mineralogy, track 5 shows the original pore pressure in blue, a lower pore pressure due to the initial production of oil, and a higher pore pressure simulating the WAG injection.

During the early years of production, prior to the water flood, the pore pressure decreased which also decreased the minimum horizontal stress. There are strong barriers to fracture height growth when the pore pressure is low. The bounding shales have a 0.7-0.8 psi/ft. stress gradient while the Morrow B Formation has a 0.5 psi/ft. stress gradient. That represents a 1,925 psi contrast in stress. However, with the injection of fluids, the stress contrast goes to zero. Figure 3.37 shows the results of the Schoenberg-Muir upscaling and the VSP time-lapse differences in the monitor surveys.

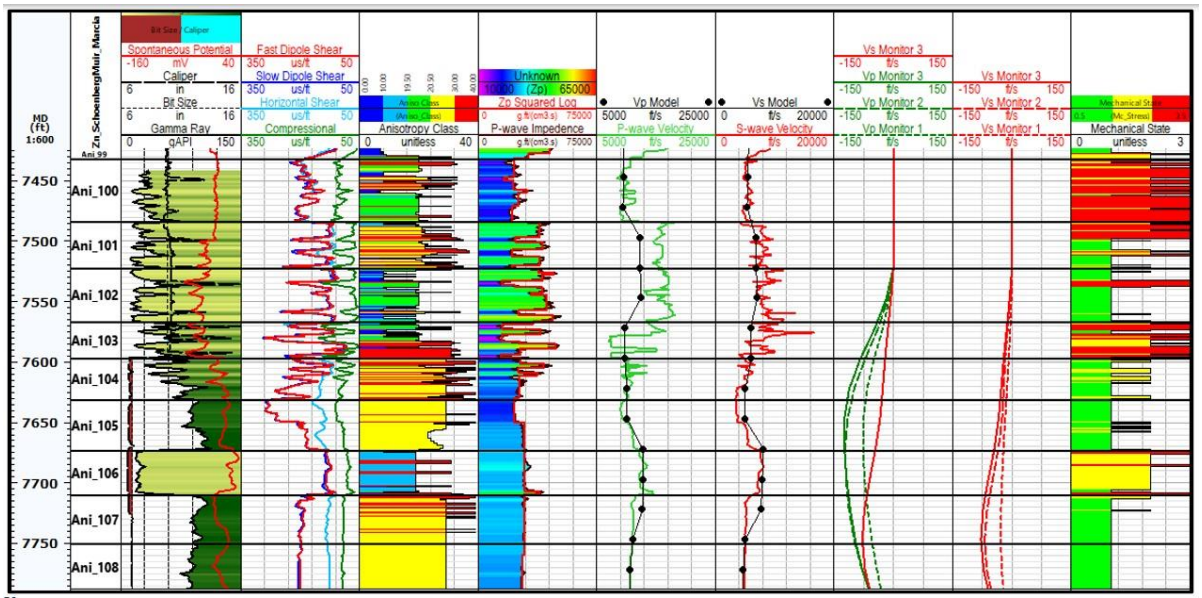

Figure 3.37: Results of the time-lapse VSP in relation to the MEM. Track 1 shows the measured depth, track 2 shows the layers used for the upscaling of the log data to the VSP scale, track 3 shows the correlation curves, track 4 shows the dipole acoustical slowness, track 5 shows the anisotropy classification, track 6 shows the P-wave impedence used to define the layers, track 7 shows the upscaled Vp model in black and the P-wave log velocity in green, track 8 shows the upscaled Vs model in black and the S-wave log velocity in red, track 9 shows the change in P-wave velocity for the three monitor surveys in green and the third time-lapse S-wave monitor in red, track 10 shows the change in S-wave velocity for the three monitor surveys in red, and track 11 shows the mechanical behavior.

There is a very good correlation between the Schoenberg-Muir upscaled velocity model shown in tracks 7 and 8 with the dipole sonic log velocities. And as previously noted, the Schoenberg-Muir algorithm accounts for the different classes of anisotropy observed in the dipole sonic logs. While the compressibility of a fluid depends on both the fluid's density and the velocity, either property can change the compressibility. If a more compressible fluid replaces a less compressible fluid, in the fractional volume of the solid, the fluid modulus decreases. If the density of the two fluids is constant, then the P-wave velocity of the formation will decrease. It is interesting to observe the differences in time lapse behavior between the P-wave and S-wave monitor surveys. The maximum reduction in P-wave velocity in monitor 3 occurs just above the Morrow B sand while the maximum reduction in the S-wave velocity in monitor 3 occurs well below the Morrow B sand. Since the carbon dioxide gas is more buoyant than the water, it is expected to reduce the P-wave velocity at shallower depths. Slippage on a weak bedding plane below the Morrow B Sand would reduce the horizontal stress below the sand. And due to the negligible fluid effect on the S-wave velocity, that would explain the reduction in shear velocity at a lower depth.

3.5 Results

3.5.1 Core Analysis

1. The mechanical of the Morrow B Formation is described as brittle. The failure envelope is non-linear. The ultrasonic velocities show increasing velocities in regions 1 and 2 and decreasing velocities in regions 3 and 4. This indicates that microcracks exist in the tested samples and change in compliance with loading. The stress sensitivity of the tested samples was quantified using the Shapiro model. The P-wave stress sensitivity is 240 ft/sec per 1000 psi change in effective stress while the S-Wave stress sensitivity is 104 ft/sec per 1000 psi change in effective stress. The stress sensitivity increases with a decrease in effective mean stress.
2. The geochemical analysis on the recovered core shows the total organic carbon content is low in the Morrow B Shale Formation but much higher in the Thirteen Finger Limestone Formation.
3. The mineralogy, porosity, and permeability were quantified on the recovered core.

3.5.2 Acoustical Analysis

1. The acoustical anisotropy at every depth was classified into one of five categories, 1) isotropic-ISO, 2) transverse isotropic with a vertical axis of symmetry-VTI, 3) transverse isotropic with a horizontal axis of symmetry-HTI, 4 orthotropic but more like VTI, and 5 orthotropic but more like HTI. Dispersion analysis was used to diagnosis the source of anisotropy.
2. The Morrow B Formation has a small amount of HTI anisotropy. The anisotropy was too small to differentiate the source as dominated by fractures or dominated by stress.
3. The Morrow Shale is highly VTI.

3.5.3 Petrophysical Analysis

1. A petrophysical model was built to honor the mineralogy, porosity, and permeability as determined by the geochemical measurements on the recovered core.
2. The triple combo, spectral gamma ray, geochemical and nuclear magnetic resonance logs were used in the petrophysical interpretation. No adjustments were needed in the petrophysical outputs to match the core derived values.

3.5.4 Rock Physics Analysis

1. A modified Krief model was used to construct the fluid substitution rock physics model. The average shear modulus model was defined by a solid modulus of 2.7 Mpsi with the porosity coefficient of 1.44. The average bulk modulus model was defined by a solid modulus of 3.4 Mspi with a porosity coefficient of 2.20.
2. Because of the number of layers diagnosed as HTI, the Schoenberg Muir upscaling model was implemented and used. The more traditional Backus upscaling model only supports isotropic or VTI formations.

3.5.5 Geomechanics

1. The modified Morales correlation was used to determine the static Young's modulus. The static Poisson's ratio was assumed the same as the dynamic Poisson's ratio. Plumb's grain volume model was used for the friction angle and the Coates-Denoo model was used for the unconfined compressive strength. These correlations provided a reasonable match to the core derived results. No further adjustments were made.
2. The vertical stress gradient was determined to be 1.066 psi/ft by integrating the formation's bulk density from the surface to the Morrow B Formation. The original pore pressure of 2150 psi, determined shortly after the discovery of the field in 1955, was used for the Morrow B Formation. This represents a normal pore pressure gradient starting at 3300 feet at the base of the Wellington Formation. Using this datum, the top of pressure was determined to be 7450 feet corresponding the top of the Thirteen Finger Limestone Formation, the likely source rock for the Morrow B Formation.
3. The maximum horizontal stress direction was determined to be 108 degrees southeast from the drilling induced fractures observed in the ultrasonic borehole images. The fast shear azimuth from the acoustical anisotropy yielded 98 degrees. These two measurements are independent from each other and represent consistency in the interpretation.
4. Two models based on different assumptions were combined to estimate the minimum horizontal stress. The linear elastic poroelastic horizontal strain model was found to be valid in the higher strength formations. However, some of the layers in the overburden are critically stressed and better described by the Mohr-Coulomb failure model. Some zones are beyond the elastic limit of the poroelastic horizontal strain model but not yet critically stress as determined by the Mohr-Coulomb failure model. An average of the two models was used in these elastic plastic layers. The minimum horizontal stress gradient in the Morrow B Formation was determined to be 0.5 psi/ft (assuming the original pore pressure).
5. The shale intervals of the Kansas City Formation are either elastoplastic or critically stressed. Small perturbations in the stress field are likely to cause microseismicity. A clastic interval in the Chase Formation exhibits strong stress induced anisotropy and could also be a source of microseismicity.
6. The ultrasonic borehole images show unusual behavior in the Morrow B Shale and the Morrow B Sand. A 0.5-inch circular deformation into the wellbore is observed. This abrupt change from bit size is observed 17.5 foot below the base of the Morrow B Formation in the Farnsworth 13-10A well and 22.5 foot below the base of the Morrow B Formation in the 13-14 well.

3.5.6 Geomechanics simulations

1. The linear elastic poroelastic horizontal strain model was used to model the change in minimum horizontal stress with the change in pore pressure. When discovered, the minimum horizontal stress gradient was determined to be 0.5 psi/ft in the Morrow B Formation and 0.7 psi/ft in the Morrow B Shale. However, with an elevated pore pressure of 5000 psi due to the injection of water and/or CO_2, the minimum horizontal stress gradient in the Morrow B Formation increases to 0.8 psi/ft while the Morrow B Shale formations remain at 0.7 psi/ft.
2. An asymmetry in the VSP derived time-lapse P-wave velocity and the time-lapse S-wave velocity. The maximum negative P-wave velocity is observed at 7672 feet while the maximum negative S-Wave velocity is observed at 7747 feet.

3.6 Conclusion

1. The Morrow B Formation as well as many of the layers in the overburden show stress sensitivity at both the core and log scale. While no calibration data exists for the in-situ stresses, the current log derived MEM gives stress sensitivities five to six times greater than the core data.
2. The reduction in hole size in the Morrow B Formation and Morrow B Shale is perplexing. The reduction is observed in multiple independent caliper measurements. The hypothesis that it was an eccentering effect was investigated and dismissed. The reduction is also seen in two wells separated by 1500 feet. Whatever mechanism is controlling this behavior, it might explain the reduction in the shear velocity below the Morrow B formation.

Chapter 4
Seismic Monitoring at the Farnsworth CO_2-EOR Field using Time-lapse Elastic Waveform Inversion of 3D-3C VSP Data

Summary

During the Development Phase of the U.S. Southwest Regional Partnership on Carbon Sequestration, supercritical CO_2 was continuously injected into the deep oil-bearing Morrow B formation of the Farnsworth Unit in Texas for Enhanced Oil Recovery (EOR). The project injected approximately 94 Kilotons of CO_2 to study geologic carbon storage during CO_2-EOR. A three-dimensional (3D) surface seismic dataset was acquired in 2013 for characterizing subsurface structures of the Farnsworth site. Then the baseline and three time-lapse three- dimensional, three-component (3D-3C) vertical seismic profiling (VSP) data were acquired at a narrower area surrounding the CO_2 injection and oil/gas production wells from 2014 to 2017 for monitoring CO_2 injection and migration. With these VSP datasets, we invert for subsurface velocity models to quantitatively monitor the CO_2 plume within the Morrow B formation. We first build 1D initial P-wave (Vp) and S-wave (Vs) velocity models by upscaling the sonic logs. We improve the deep region of Vp and Vs models by incorporating the deep part of a migration velocity model derived from the 3D surface seismic data. We improve the shallow region of 3D Vp and Vs models using 3D traveltime tomography of first arrivals of VSP downgoing waves. We further improve the 3D baseline velocity models using elastic-waveform inversion (EWI) of the 3D baseline VSP upgoing data. Our advanced EWI method employs alternative tomographic and conventional gradients and total-variation-based regularization to ensure the high-fidelity updates of the 3D baseline Vp and Vs models. We then sequentially apply our 3D EWI method to the three time-lapse datasets to invert for spatiotemporal changes of Vp and Vs in the reservoir. Our inversion results reveal the volumetric changes of the time-lapse Vp and Vs models, showing the evolution of the CO_2 plume from the CO_2 injection well to the oil/gas production wells.

Keywords: CO_2 monitoring, elastic-waveform inversion, enhanced oil recovery, Farnsworth, geologic carbon storage, time-lapse seismic monitoring, Vertical Seismic Profiling (VSP).

4.1 Introduction

Time-lapse seismic data contain information about subsurface reservoir changes and can be inverted for reservoir imaging and monitoring (Lumley et al., 2003). Time-lapse seismic surveys have been widely used for monitoring geologic carbon storage (Huang, 2022). Various time-lapse inversion methods have been developed during the last decade (e.g. Ajo-Franklin et al., 2007; Daley et al., 2008, Zhang and Huang, 2013). Because of the advantages of full- waveform inversion (FWI) that uses the complete information of seismic waveforms to invert for high-resolution distributions of subsurface elastic parameters (Virieux and Operto, 2009), time-lapse FWI (TLFWI) or time-lapse EWI (TLEWI) has been used for time-lapse seismic monitoring (Zhang and Huang, 2013; Asnaashari et al., 2015; Raknes and Arntsen, 2015; Egorov et al., 2017; Kamei, and Lumley, 2017; deRidder et al., 2019). The velocity changes are inverted using time-lapse FWI in a two-step procedure: (1) construct the baseline velocity models; (2) invert for the time-lapse changes of velocity models. Generally, there are two

effective strategies for the implementation of the second step (Asnaashari et al., 2015): (1) sequential inversion; (2) double-difference inversion. The latter one has theoretically better performance by removing the negative influence of not matched baseline data (Asnaashari et al., 2015; Raknes and Arntsen, 2015), but is less robust as it requires that time-lapse seismic data have excellent repeatability between surveys (Kamei and Lumley, 2017). However, most TLFWI experiments still utilize the acoustic assumption because of the limit of computational capability. As the Earth is elastic, the acoustic assumption possibly results in incorrect estimations of subsurface models (Raknes and Arntsen, 2014). Elastic- waveform inversion can more accurately determine underground geophysical properties than acoustic-waveform inversion (Virieux and Operto, 2009). With the exponentially increasing of computing power, it is becoming practical to implement elastic TLFWI (Raknes and Arntsen, 2015). However, the previous studies were limited to synthetic data.

We apply 3D elastic TLEWI to time-lapse 3D VSP data acquired at the Farnsworth unit, Texas (Figure 4.1)to invert for spatiotemporal changes of seismic velocities during CO_2 injection and migration. To our knowledge, this is the first application of TLEWI to time-lapse 3D field data. Before the time-lapse VSP surveys, a 3D surface seismic dataset was first acquired in 2013 around a wide area at the Farnsworth unit for site characterization. Next, a 3D baseline VSP dataset was acquired in 2014 before CO_2 injection. The VSP data are 3C data as displayed in (Figure 4.2).

Tons of anthropogenic CO_2 were continuously injected to drive subsurface fluids containing oil and gas into production wells. For monitoring the development of CO_2 plume, three repeat 3D-3C VSP datasets were acquired in 2015, 2016, and 2017, respectively. Comparing with the surface seismic survey, VSP has the following advantages: (1) allowing more convenient time-lapse acquisition with fixed 3C geophones in a well, and (2) containing fewer noises such as free of contaminations of surface waves. Additionally, comparing with cross-well seismic monitoring (Daley et al., 2008), VSP surveys provider broader subsurface monitoring. However, the VSP downgoing free-surface multiples are strong events and can cover most late arrivals after the first-arrival P-waves (Liu et al., 2018), which can also be observed from (Figure 4.2a). By contrast, the VSP upgoing free- surface multiples are much weaker and located at later time and therefore, their negative effects for velocity inversion can be neglected using a time window for inversion. We use the separated upgoing waves for EWI to update the deep region of the 3D baseline Vp and Vs models and for TLEWI of the time-lapse 3D VSP data.
We organize the paper as follows. We first present the practical workflow for 3D Vp and Vs inversion, and then apply our workflow to the baseline 3D VSP data and three repeat 3D VSP data. Our results reveal the volumetric evolution of time-lapse velocity changes with the increasing injection of CO_2.

4.2 Method

4.2.1 Building the baseline velocity models

We build the initial Vp and Vs models by combining information from the sonic logs, the 3D surface seismic survey, and the baseline 3D VSP survey. First, we upscale the sonic logs using the Schoenberg-Muir method (Carcione et al., 2012) within layers divided according to P-wave impedance. We compute the 1D initial Vp and Vs models (Figure 4.3) using the upscaled elastic moduli and densities. Beneath the maximum depth of the sonic logs, we improve the initial Vp velocity model by appending in the inverted velocities from Schlumberger's state-of-art reflection tomography of the 3D surface seismic data. As displayed in (Figure 4.8), the surface seismic survey covers a much larger surface area than the VSP survey. Some reflection events with large-reflection angles are recorded by surface seismic data. Reflection tomography of surface seismic data (Woodward et al., 2008) provides long-wavelength velocity updates for the deep subsurface. We update for the initial Vs velocity model in the deep region according to the Vp/Vs ratio at the lower boundary of the sonic log (Figure 4.4). Above the well head of logging, we improve the initial Vp velocity model using tomography of picked first-arrivals:

$$f\left(V_p\right) = \iint \left(t_{cal}\left(V_p\right) - T_{obs}\right) d\mathbf{x}_r d\mathbf{x}_s \tag{4.1}$$

,

where t_{cal} is the computed traveltime using the updated Vp model, and T_{obs} is the observed first- arrival traveltime. We employ adjoint-state first-arrival traveltime tomography (FATT) (Taillander et al., 2009), which calculates the velocity gradient using the adjoint-state method and is more suitable for 3D velocity building with much reduced memory-storage requirement than classic traveltime tomography. We update the shallow region of the Vs velocity model using the FATT Vp updates according to the Vp/Vs ratios at the upper boundary of the sonic logs (Figure 4.5).

4.2.2 Elastic-waveform inversion of 3D-3C VSP data

We use EWI of 3C VSP upgoing data as shown in Figure 4.2b to improve Vp and Vs models with both tomographic parts and high-resolution details, especially for the deep region beneath the reservoir. For EWI implementation, the conventional L2-norm-based misfit measures differences between observed and synthetic seismic data with both amplitudes and phases. However, there usually exist unreliable amplitudes in seismic data because unknown source/receiver coupling and seismic processing procedures without preserving amplitudes, and unknown exact subsurface physics (e.g. density and attenuation are not fully considered in forward modeling for synthetic data). All above issues can make the L2-norm-based misfit fails to converge. In our EWI, we employ a cross-correlation-based misfit (Routh et al., 2011):

$$f(m) = \iint \left(1 - \frac{\int d_m(X_r, t; X_s) d_{obs}(X_r, t; X_s) d_t}{\sqrt{d_m^2(X_r, t; X_s) d_t} \sqrt{\int d_{obs}^2(X_r, t; X_s) d_t}}\right) dX_r dX_s \tag{4.2}$$

which measures the global phase closeness between the synthetic data $\mathbf{d}_m$ and the observed seismic data $\mathbf{d}_{obs}$. In equation 4.2, t, $\mathbf{x}_r$, $\mathbf{x_S}$, and $\mathbf{m}$ represent recording time, receiver position, source position, and the models including Vp and Vs to be inverted, respectively. The gradient in EWI inversion is computed using the adjoint-state method to the first-order velocity-stress elastic-wave equations as follows:

$$\frac{\partial f}{\partial \lambda} = -\iint \left(\frac{\partial V_x}{\partial x} + \frac{\partial V_y}{\partial y} + \frac{\partial V_z}{\partial z}\right)\left(\frac{\partial \tilde{u}_x}{\partial x} + \frac{\partial \tilde{u}_y}{\partial y} + \frac{\partial \tilde{u}_z}{\partial z}\right) d_t dX_s$$

$$\frac{\partial f}{\partial \mu} = -\iint \begin{pmatrix} \left(\frac{\partial V_x}{\partial z} + \frac{\partial V_z}{\partial x}\right) & \left(\frac{\partial \tilde{u}_x}{\partial z} + \frac{\partial \tilde{u}_z}{\partial x}\right) + \\ \left(\frac{\partial V_x}{\partial y} + \frac{\partial V_y}{\partial x}\right) & \left(\frac{\partial \tilde{u}_x}{\partial y} + \frac{\partial \tilde{u}_y}{\partial x}\right) + \\ \left(\frac{\partial V_y}{\partial z} + \frac{\partial V_z}{\partial y}\right) & \left(\frac{\partial \tilde{u}_y}{\partial z} + \frac{\partial \tilde{u}_z}{\partial y}\right) + \\ 2\left(\frac{\partial V_x}{\partial x}\frac{\partial \tilde{u}_x}{\partial x} + \frac{\partial V_y}{\partial y}\frac{\partial \tilde{u}_y}{\partial y} + \frac{\partial V_z}{\partial z}\frac{\partial \tilde{u}_z}{\partial z}\right) & \end{pmatrix} d_t dX_s \tag{4.3a}$$

where λ and μ are Lamé moduli, (v_x, v_y, v_z) represents particle velocity components of source wavefields and $(\tilde{u}_x, \tilde{u}_y, \tilde{u}_z)$ represents the displacement components of adjoint receiver wavefields. To reduce inter-parameter cross talks, we further rewrite gradients with respect to Vp and Vs as

$$\frac{\partial f}{\partial v_p} = \frac{\partial f}{\partial \lambda}\frac{\partial \lambda}{\partial v_p} = 2\rho_O v_p \frac{\partial f}{\partial \lambda},$$

$$\frac{\partial f}{\partial v_s} = \frac{\partial f}{\partial \lambda}\frac{\partial \lambda}{\partial v_s} + \frac{\partial f}{\partial \mu}\frac{\partial \mu}{\partial v_s} \tag{4.3b}$$

$$= 4\rho_O v_s \frac{\partial f}{\partial \lambda} + 2\rho_O v_s \frac{\partial f}{\partial \mu},$$

We first improve the entire models along seismic wavepaths (tomographic updates) and then invert for high-resolution details of the models, particularly in the region beneath the reservoir (conventional updates). We manipulate the gradient to extract tomographic parts or keep the conventional format with the operation (Fei et al., 2015; Chi et al., 2017) as,

$$G_{\text{tomo/conventional}} = W_S W_r + \alpha H_z(W_S) H_z(W_r), \tag{4.4}$$

where $\alpha = 1 \, or \, 0$ produces tomographic or conventional kernel, respectively, H_z represents the Hilbert transform along the depth direction, and W_S and W_r denote any combination pair of source and adjoint wavefield components in equation 4.3, which are applied to all the combination pairs. Furthermore, during the inversion, we use an alternating Tikhonov and total-variation (TV) regularization schemes to penalize possible inversion noise (Gao and Huang, 2019):

$$m^{(i)} = \underset{m}{argmin}\left\{f(m) + \frac{\varepsilon_1}{2}\left\|m - u^{(i-1)}\right\|_2^2\right\} \tag{5a}$$

and

$$u^{(i)} = \underset{u}{argmin}\left\{\left\|m^{(i)} - u\right\|_2^2 + \varepsilon_2\|u\|_{TV}\right\} \tag{5b}$$

where the superscript ***i*** represents the iteration number, **u** denotes TV de-noised auxiliary models with an initial guess of $u^{(O)} = m^{(O)}$, and $\varepsilon_1 \wedge \varepsilon_2$ are regularization weighting coefficients. The TV-denoised auxiliary term serves as the prior model in the Tikhonov regularization term, which remove noise and stabilize the inversion procedure. We employ generalized TV de-noising by incorporating a second-order derivative term in equation 5b, which produces more reliable results than conventional TV -de-noising/regularization with assumption of piece-wise smoothing.

4.3 Time-lapse inversion strategies

With the updated baseline Vp and Vs models, we can use a sequential method or a double-difference method to invert for time-lapse velocity changes (Asnaashari et al., 2015). The time- lapse 3D VSP data contains a lot of inconsistent source positions, and the inconsistency increases for the data acquired later. Thus, the repeatability of seismic data becomes worse for the VSP data acquired later. Additionally, the double-difference method requires an additional processing step that time-lapse difference of observed data is summed together with the synthesized data modeled with inverted baseline velocity models, which can be challenging if the amplitudes of synthetic data do not match well with those of the field data. Therefore, we use the sequential inversion strategy to obtain the time-lapse velocity changes considering its less repeatability requirement during inversion of time-lapse VSP data.

We implement the sequential strategy in our EWI of time-lapse 3D-3C VSP data using 3D EWI-

updated baseline Vp and Vs models as the initial models of TLEWI. The time-lapse changes because of CO_2 injection and migration are expected to be bounded within a thin reservoir layer called Morrow B (Czoski P., 2014). Such a change does not generate cycle- skipping effects in the frequency band of the inversion. We invert the upgoing data of the time- lapse VSP datasets using the frequency band used in EWI of the baseline VSP data. The misfit function in equation 4.2 is solved for velocity models in monitoring stages. We obtain the time- lapse changes of seismic velocities by subtracting the baseline velocity models from the velocity models at monitoring stages.

To obtain high-quality time-lapse inversion results, we employ cross-equalization (Rickett and Lumley, 2001) to balance the VSP data between the baseline survey and repeat surveys within the time window of less than 1s. This procedure is particularly useful when there exist waveform distortions between the datasets of the repeat surveys and that of the baseline survey. Because the Morrow B reservoir formation is a thin layer and the radius of CO_2 plume is predicted to be less than 457.2 m (1500 feet) away from the CO_2 injection well according to prior information, and we use a spatial mask enclosing the possible range of velocity changes as a spatial prior in EWI to increase the robustness of WEI and reduce inversion uncertainty.

4.4 Results

The Farnsworth CO_2-EOR field in Ochiltree, Texas (Figure 4.1a) is a site for a field demonstration of geologic carbon storage. The Farnsworth Unit (FWU) is the largest Morrowan oil field in the western part of the Anadarko Basin. The uppermost sandstone, "Morrow B," is the reservoir for CO_2-EOR. The thickness of the Morrow B formation ranges from 0 to 54 feet (Czoski P., 2014). One million tons of supercritical CO_2 produced from an Ethanol Plant and a Fertilizer Plant nearby was planned to be injected into the Morrow B formation. Well 13-10A was used for CO_2 injection and 3D-3C VSP data acquisition (Figure 4.1b) shows seismic sources of the baseline VSP survey surround Well 13-10A. In the velocity models, the well is at the distance of 1403 m along South-West (SW)-North-East (NE) direction and at distance of 1642 m along North- West (NW)-South-East (SE) direction.

(a)

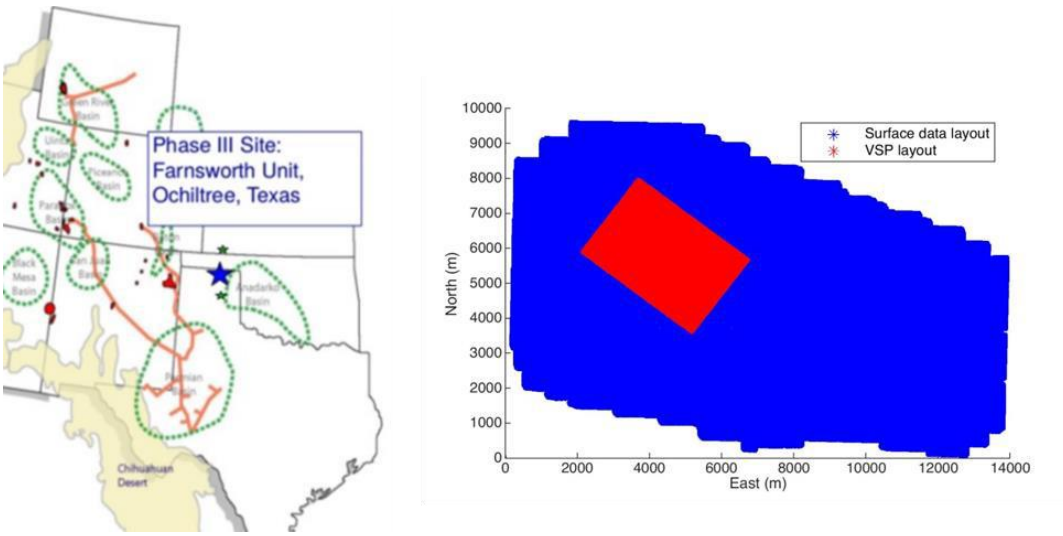

(b)

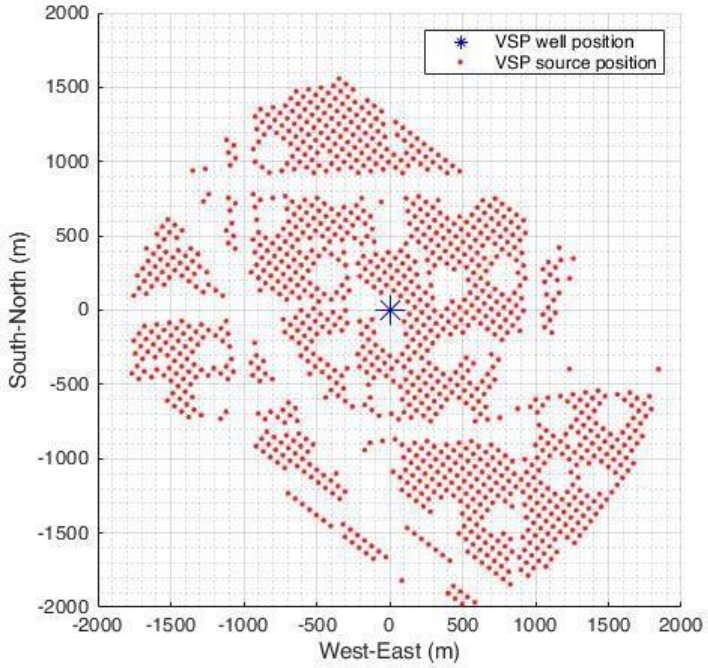

Figure 4.1: (a) Location of the Farnsworth CO_2-EOR field and seismic acquisition geometry, and (b) VSP acquisition geometry for the baseline 3D-3C VSP survey.

A baseline 3D-3C VSP dataset was acquired in November 2014, and then repeat 3D-3C VSP datasets were acquired in January 2015 (Monitor 1), November 2016 (Monitor 2), December 2017 (Monitor 3), respectively, for monitoring CO_2 injection and migration. A total of 33,070.25, 43,526.89, and 17,689.24 tons of CO_2 were injected between the baseline and Monitor 1 survey, between Monitor 1 and Monitor 2 survey, and between Monitor 2 and Monitor 3 survey, respectively. The 3D-3C VSP seismic datasets are processed in workflows as follows: first break picking, 3C geophone orientation, noise attenuation, surface consistent amplitude compensation, and wavefield separation for upgoing data. The processing datum is at 3100 feet above sea surface. The processed VSP data, as shown in Figure 4.2, contains 35 geophones within the depth between 1140 m and 1688 m.

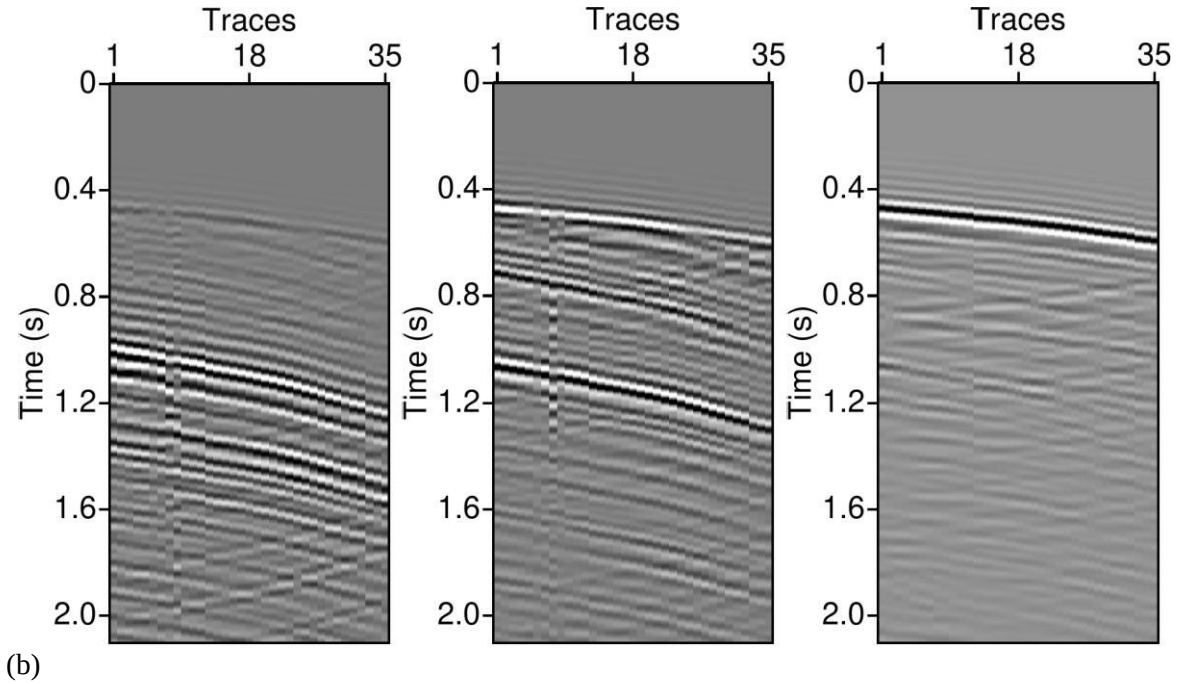

(b)

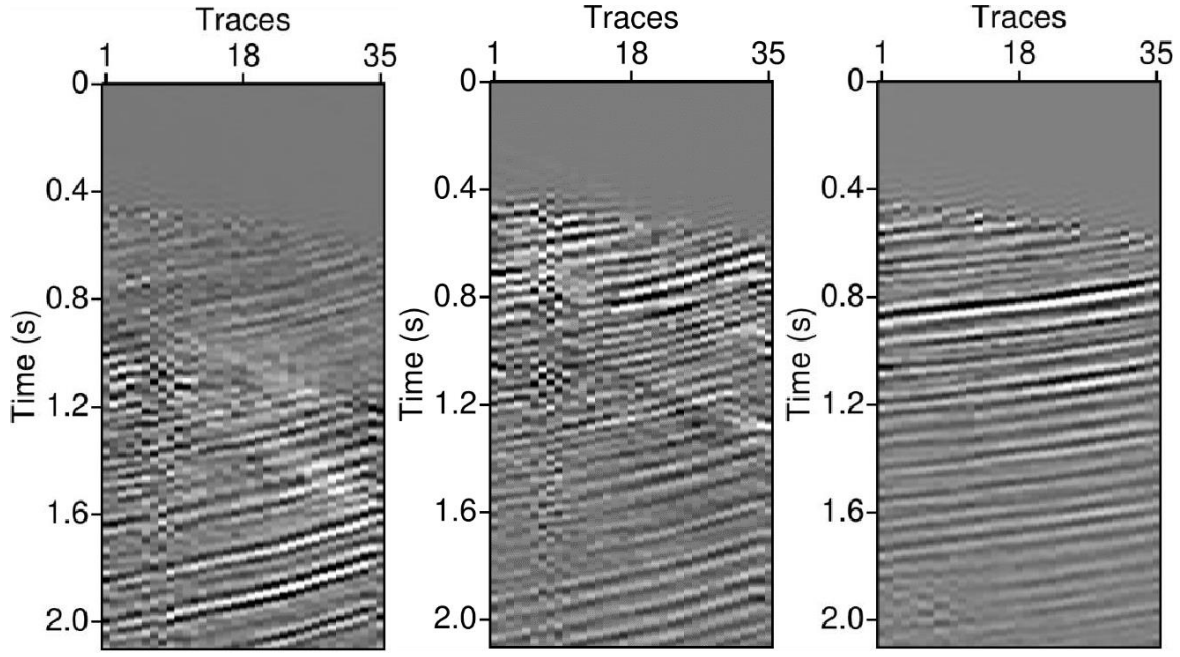

Figure 4.2: Left, middle, and right panels show X (East), Y (North) and Z (Vertical) components, respectively, of (a) full wavefield data and (b) the separated upgoing data of the baseline 3D-3C VSP survey.

We build the baseline velocity models using the processed 3D-3C VSP data and the workflow described in Section 2.1. All models are discretized with a grid interval of 7.62 m (25 feet) along three axes. (Figure 4.3) shows the initial Vp and Vs baseline velocity models built after upscaling the sonic logs.

(a)

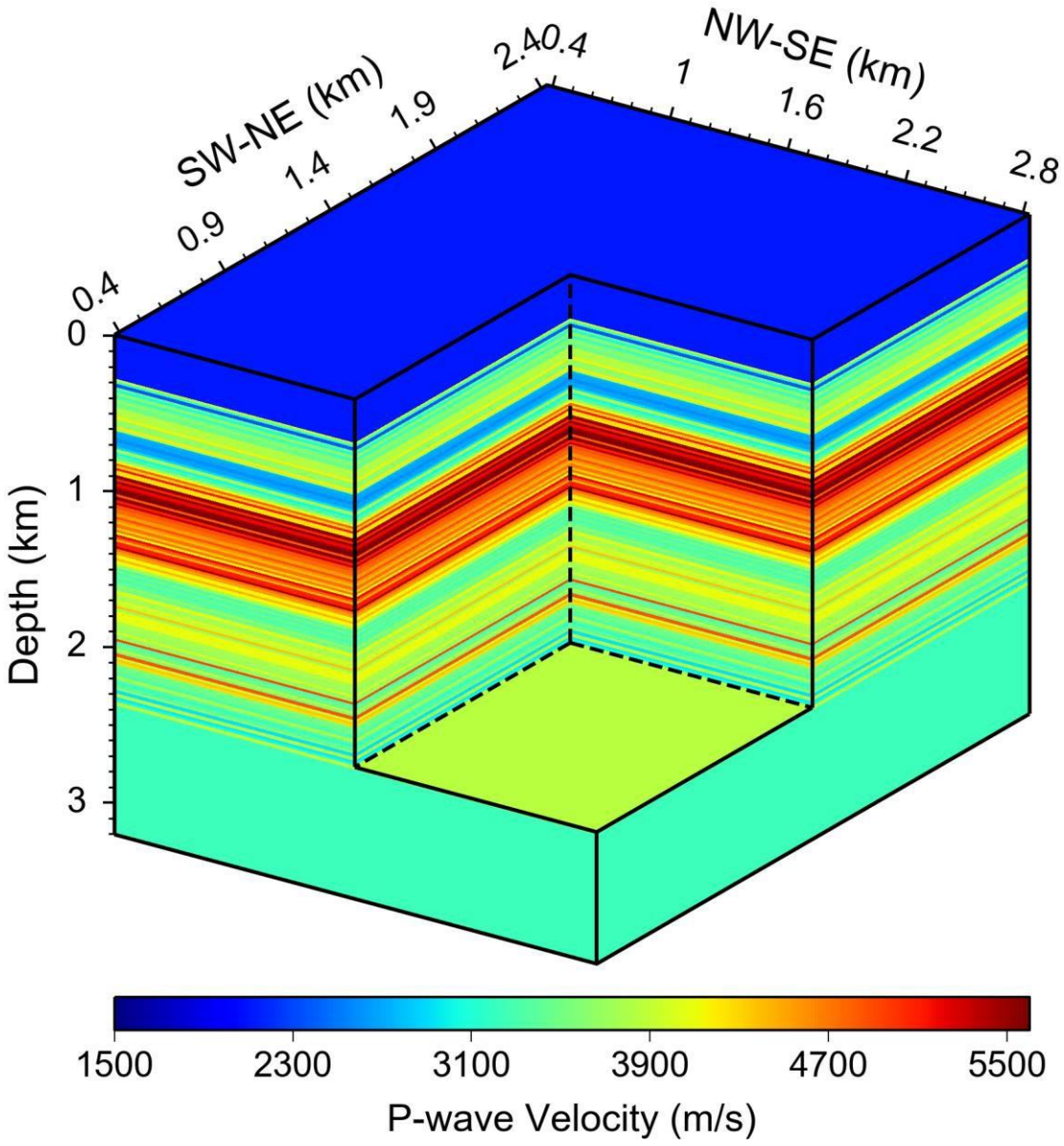
SW-NE (km)
0.4
0.9
1.4
1.9
2.4
NW-SE (km)
0.4
1
1.6
2.2
2.8
Depth (km)
0
1
2
3
1500
2300
3100
3900
4700
5500
P-wave Velocity (m/s)

(b)

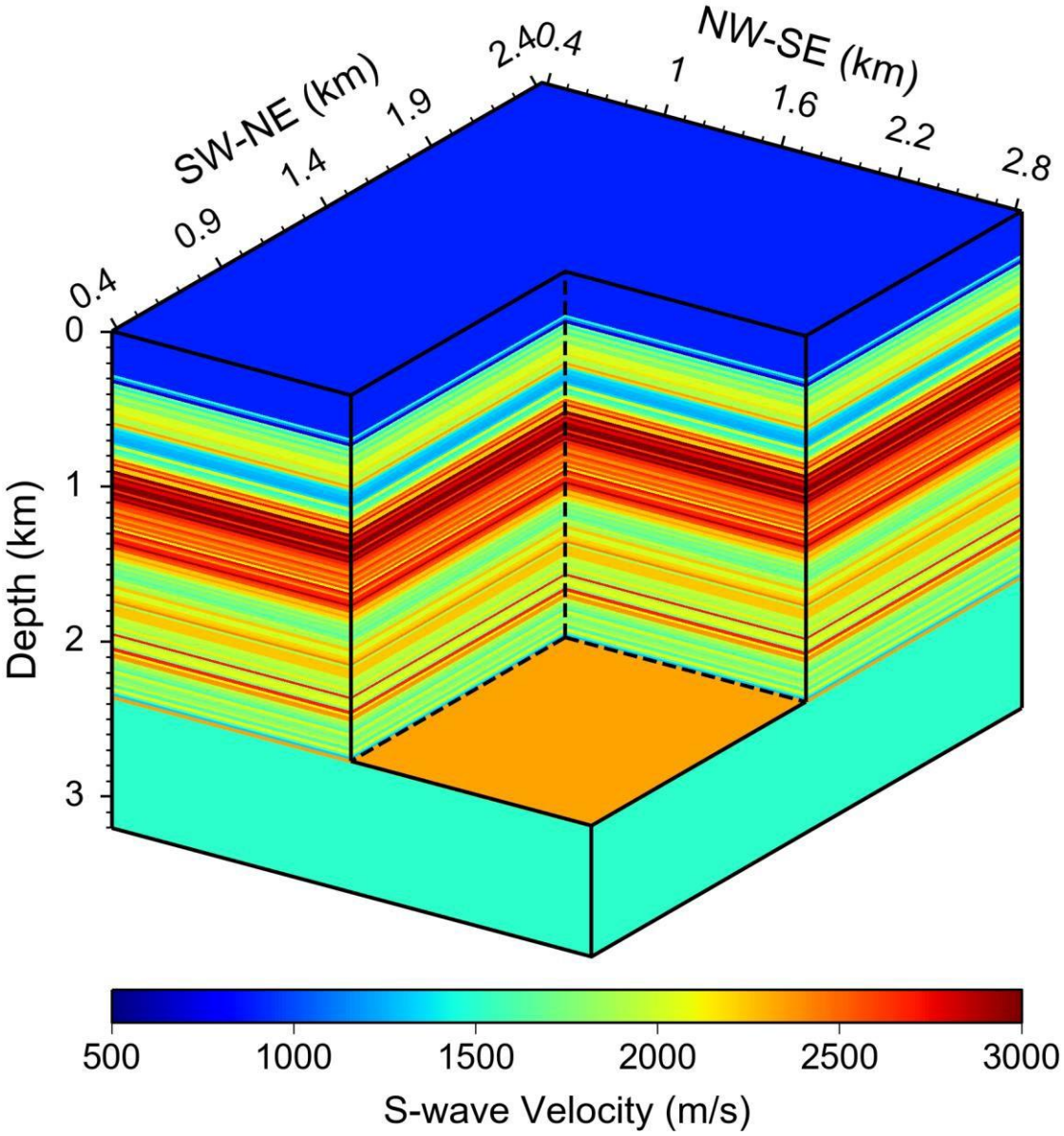

Figure 4.3: Initial baseline P-wave (Vp) and S-wave (Vs) velocity models obtained by upscaling the sonic logs.

With the seismic datum as the zero-depth position, well recording starts from the depth of 260.5 m (854.5 feet), and seismic velocities Vp and Vs at this depth are extended to the entire shallower space. Figure 4.4 depicts the updated baseline velocity model after appending the deep region of the velocity model derived from the 3D surface seismic data.

(a)

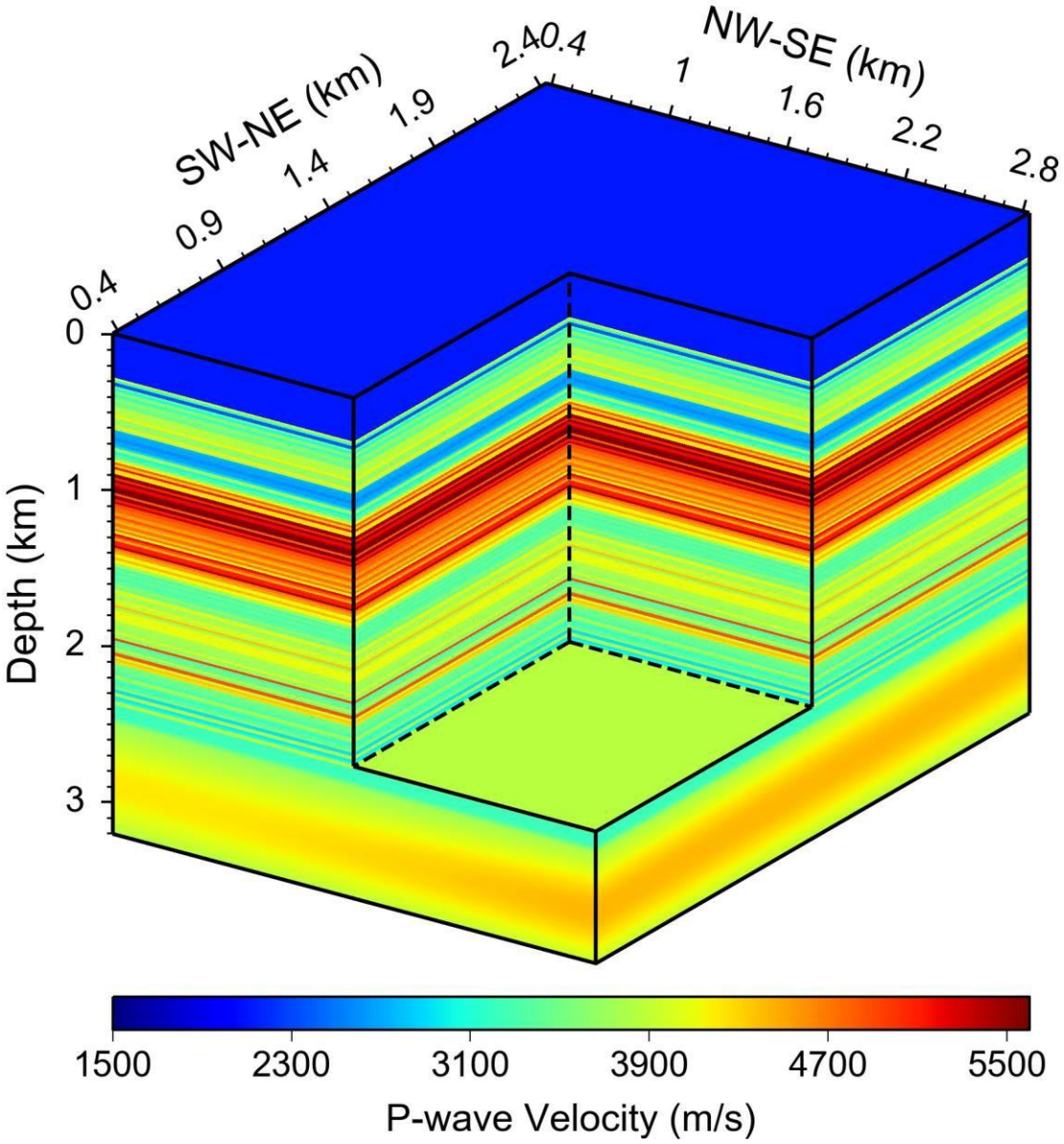

(b)

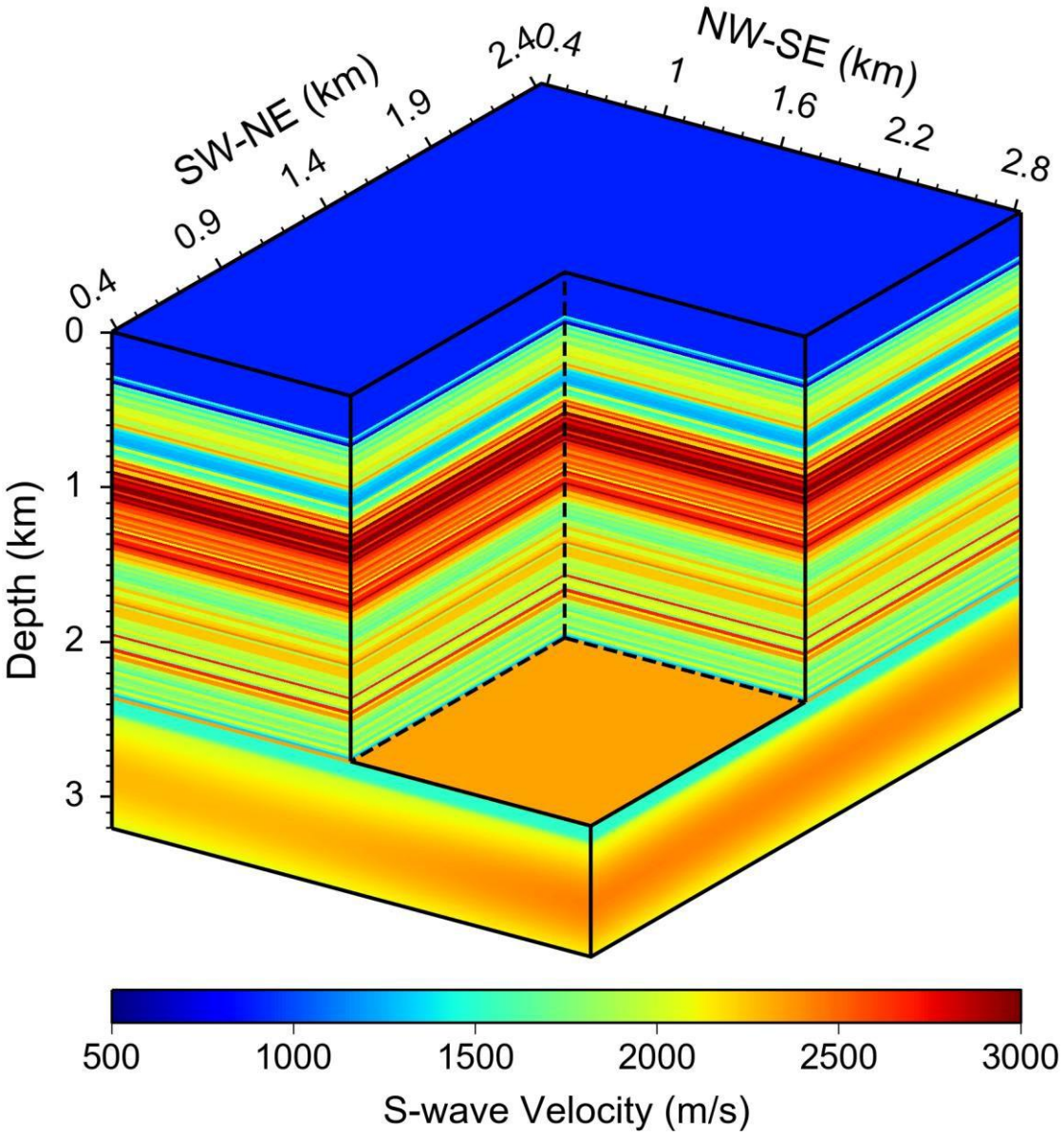

Figure 4.4: Updated baseline Vp model by incorporating the deep region of the velocity model derived from the 3D surface seismic data and Vs model with the deep region updated according to the Vp/Vs ratio at the lower boundary of the sonic logs.

We then improve the shallow region of the baseline Vp model using 3D tomography of the first arrivals of the baseline VSP downgoing waves, as displayed in Figure 4.5.
(a)

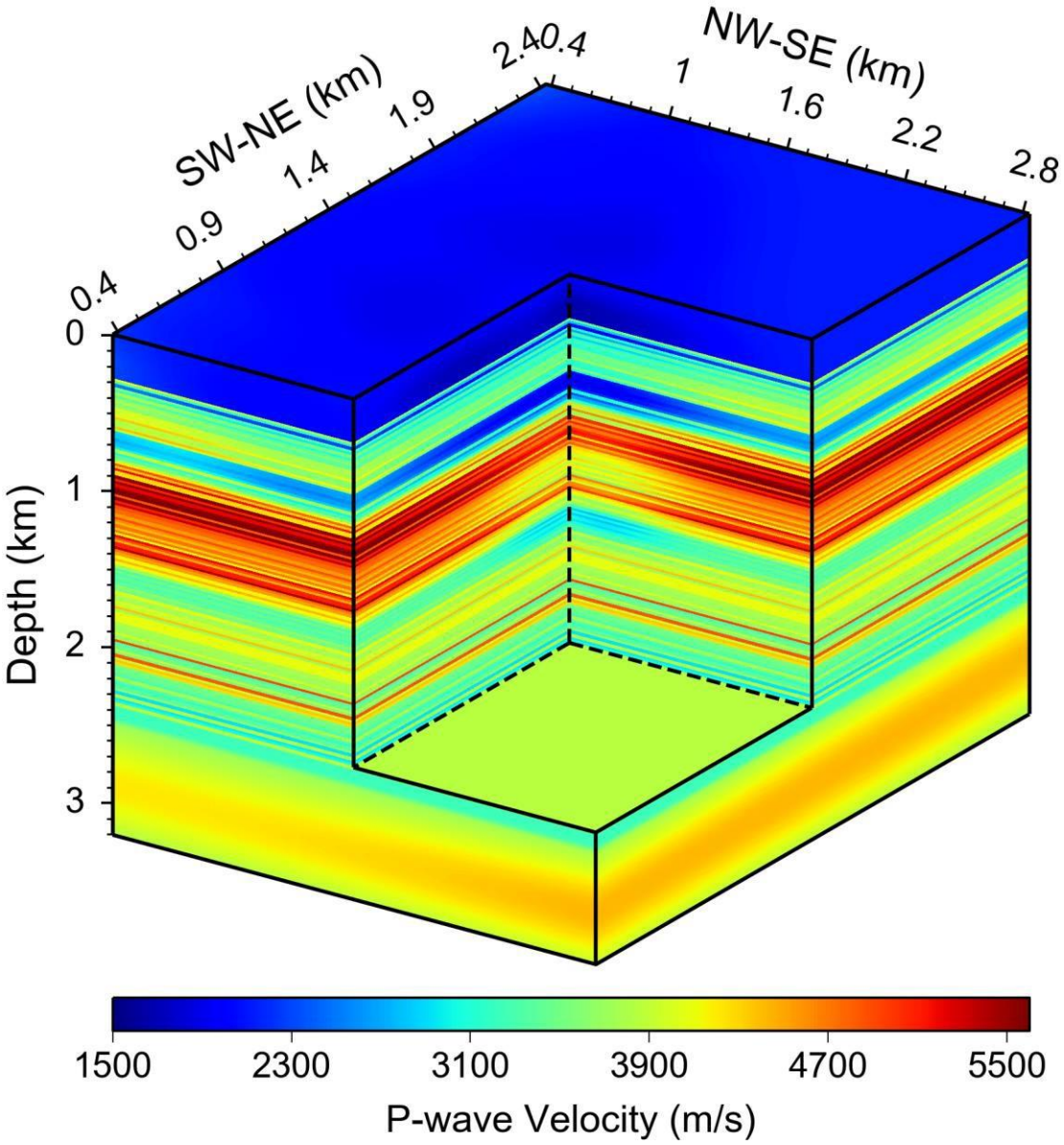

(b)

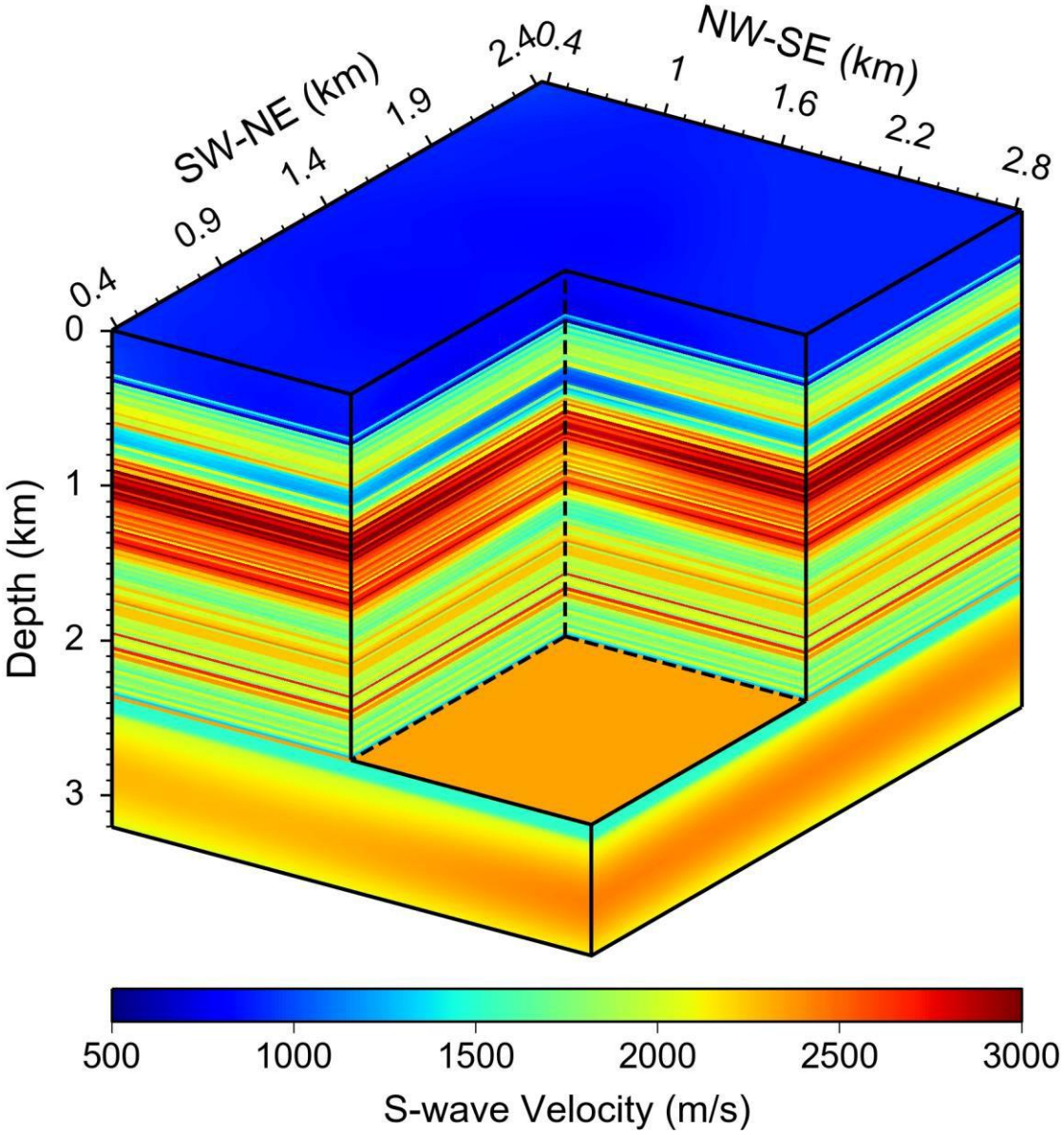

Figure 4.5: Improving the shallow regions of the baseline Vp model using first-arrival tomography of the downgoing waves of the baseline VSP data, together with Vs model with estimated updates for the shallow region according to the Vp/Vs ratios at the upper boundary of the sonic logs.

In Figures 4.4 and 4.5, we estimate updates for the initial Vs velocity model below and above the depth range of the sonic logs from Vp updates according to the Vp/Vs ratios at the lower and the upper boundaries of the sonic logs. We improve the baseline velocity models using 3D elastic-waveform inversion of the baseline 3D-3C VSP upgoing data. We filter the data with a maximum frequency of 30 Hz. We estimate the source wavelets by stacking the first-arrivals of vertical components. We perform multi-scale EWI of VSP upgoing data to improve the baseline velocity models using three bandpass frequency scales of 3-5-9-12 Hz, 3-5-17-20 Hz, and 3-5-27-30 Hz. Figure 4.6 depicts the final updated baseline velocity models, and Figure 4.7 displays the velocity updates. EWI of VSP upgoing data provides low-wavenumber tomographic update and high-resolution updates

for the deep region of the baseline velocity models. The convergence curves shown in Figure 4.8 demonstrate robust velocity inversions at three frequency scales.

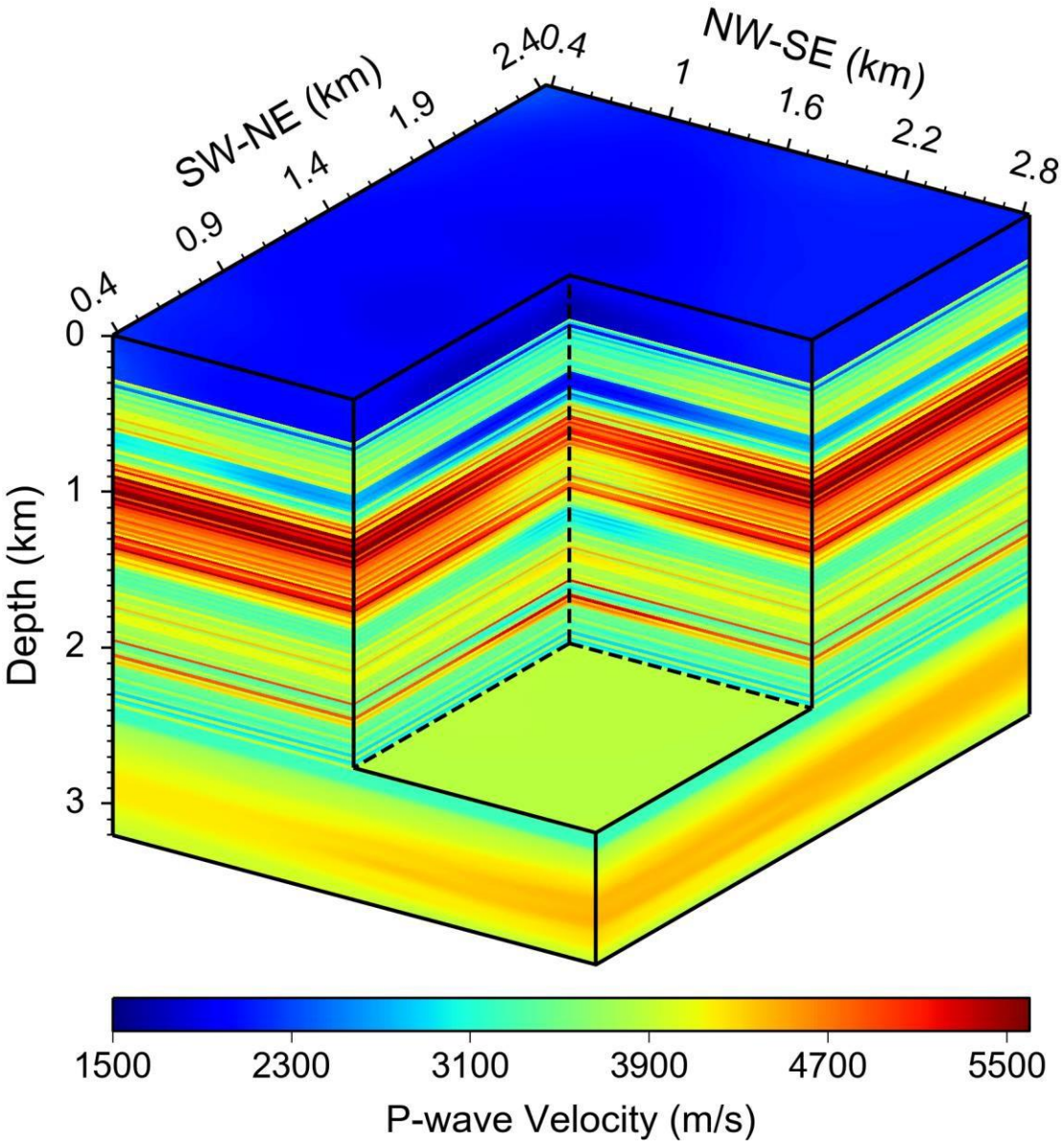

(b)

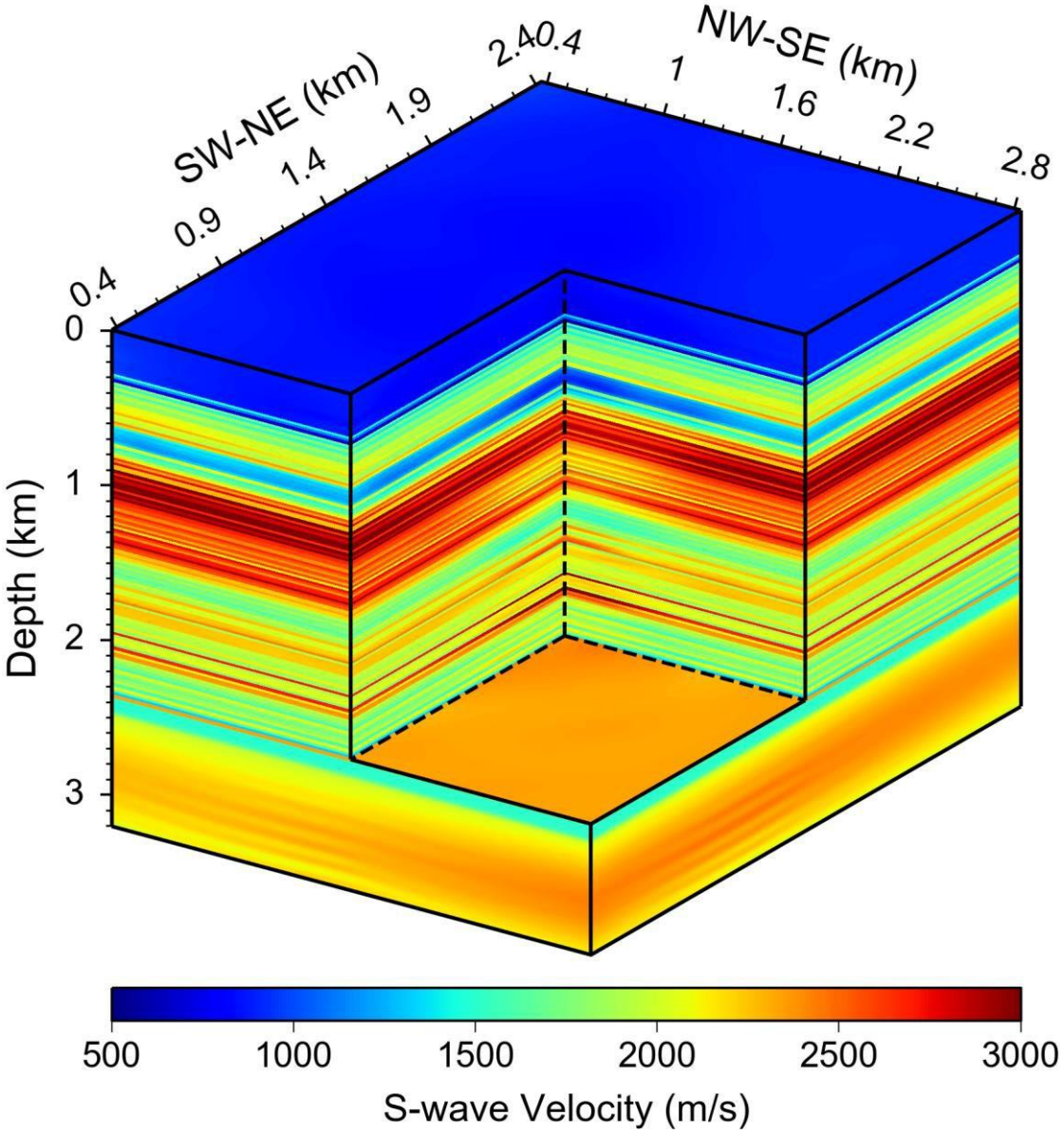

Figure 4.6: Final updated baseline velocity models obtained using 3D elastic-waveform inversion of 3C VSP upgoing waves of the baseline VSP data.

(a)

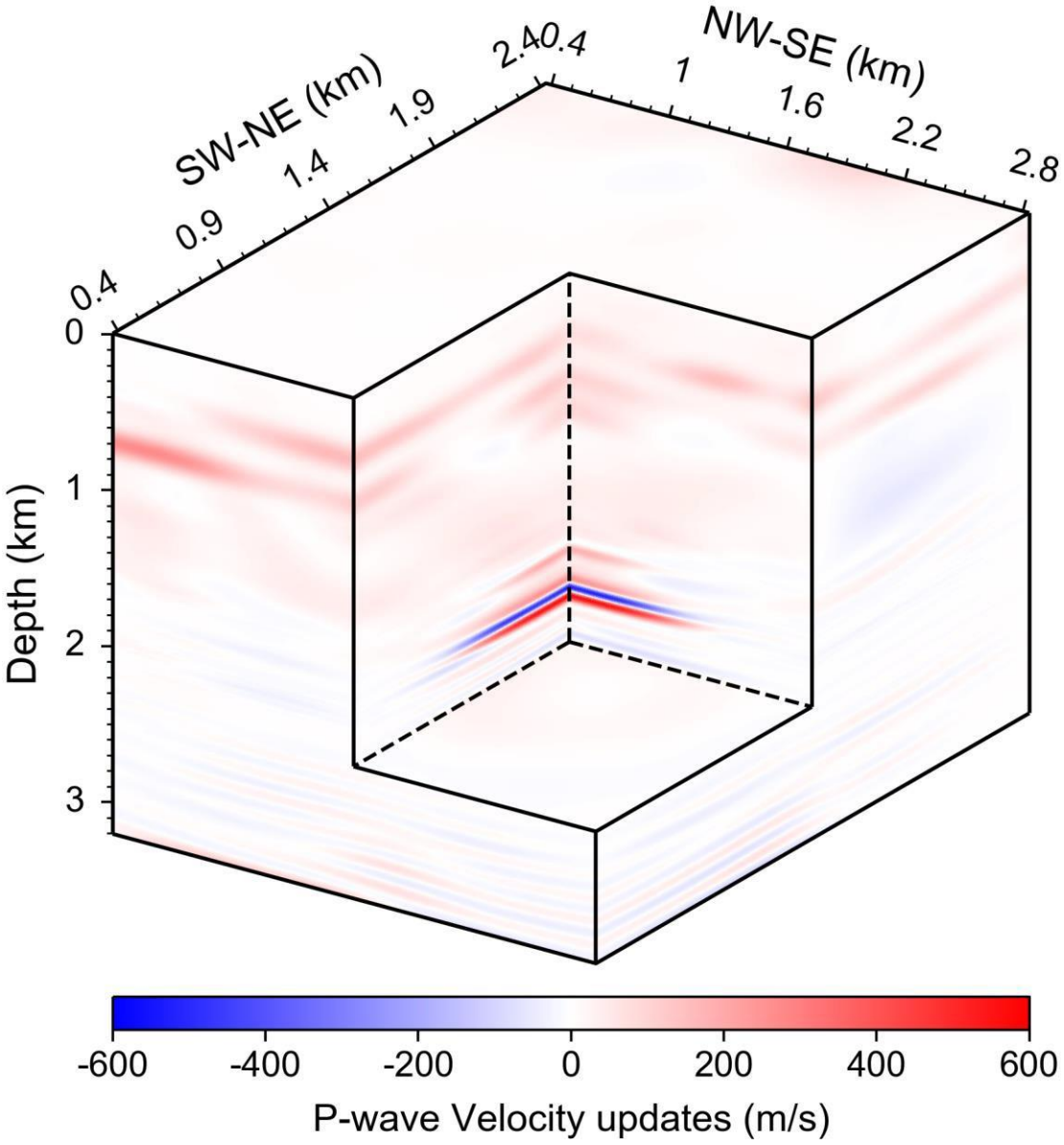
SW-NE (km)
0.4
0.9
1.4
1.9
2.4
NW-SE (km)
0.4
1
1.6
2.2
2.8
Depth (km)
0
1
2
3
-600
-400
-200
0
200
400
600
P-wave Velocity updates (m/s)

(b)

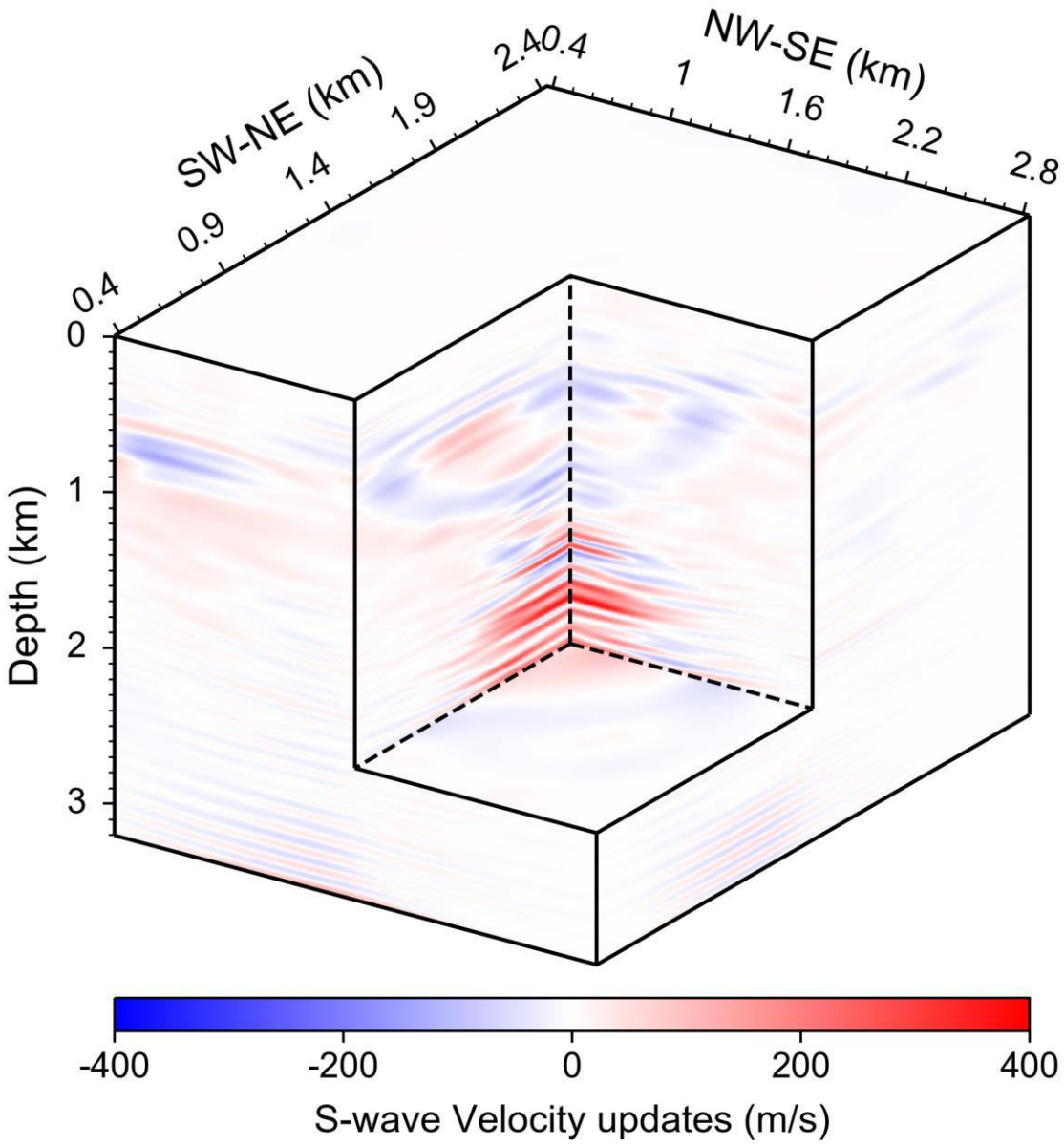

Figure 4.7: Velocity updates obtained using 3D elastic-waveform inversion of 3C VSP upgoing waves of the baseline VSP data (i.e. differences by subtracting models in Figure 5 from those in Figure 6), with both low-wavenumber tomographic and high-resolution detailed updates.

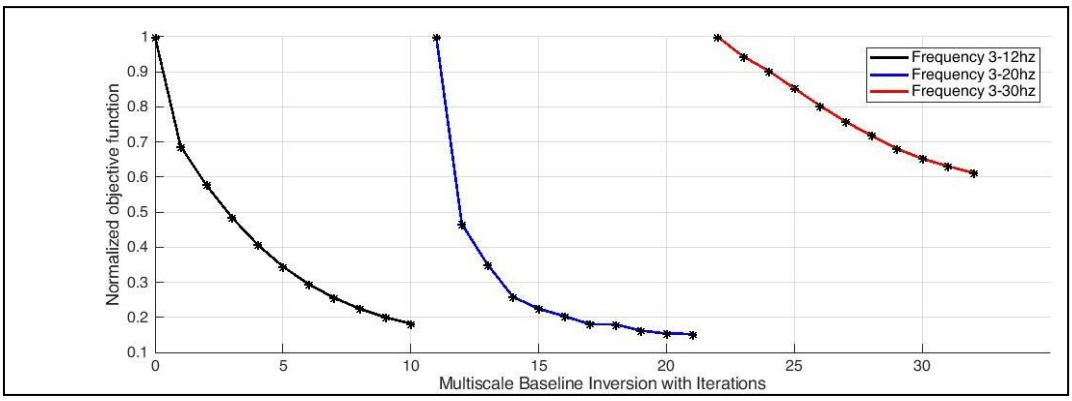

Figure 4.8: Convergence curves of 3D multi-scale elastic-waveform inversion of the baseline VSP data at three frequency scales.

After obtaining the baseline velocity models, we perform TLWEI of the time-lapse 3D- 3C VSP data to quantitatively measure time-lapse velocity changes that indicate evolution of the CO_2 plume. We compute the time-lapse velocity changes by subtracting the baseline velocity models from the sequentially inverted velocity models at monitoring stages. Figure 4.9, Figure 4.10, and Figure 4.11 show the velocity changes between baseline and Monitor 1, between baseline and Monitor 2, and between baseline and Monitor 3, respectively, at the center depth of Morrow B.

(a)

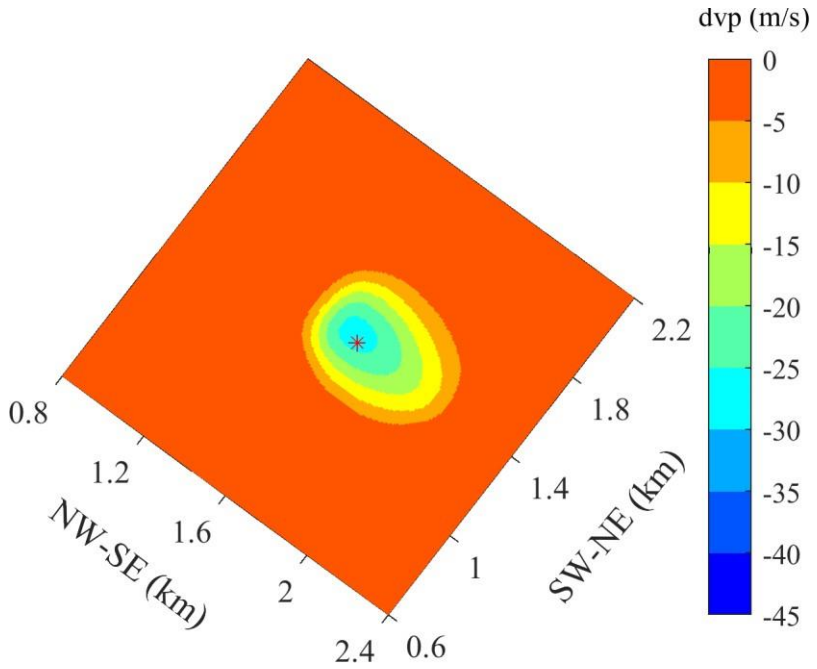

(b)

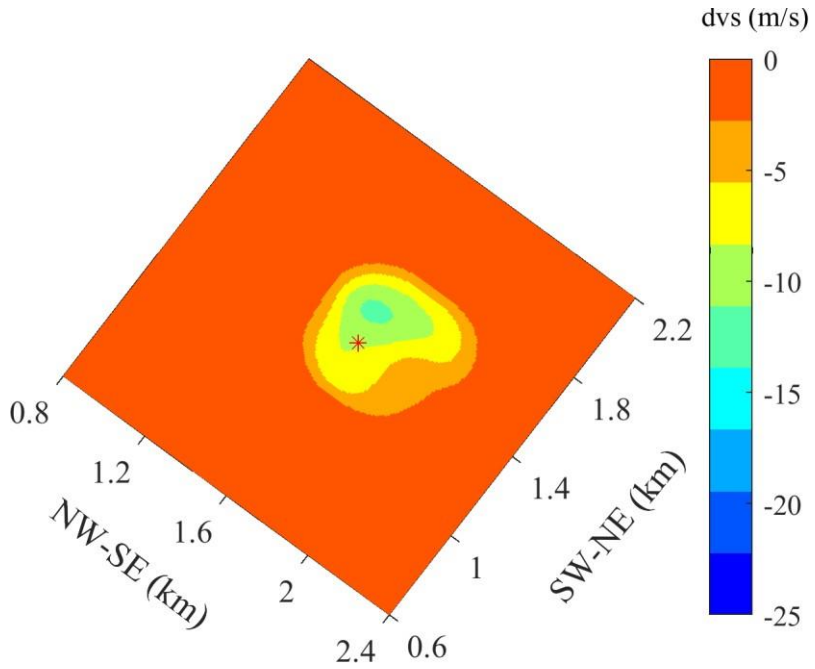

Figure 4.9: Inverted time-lapse velocity changes between baseline and Monitor 1 VSP surveys at the center depth of Morrow B.

(a)

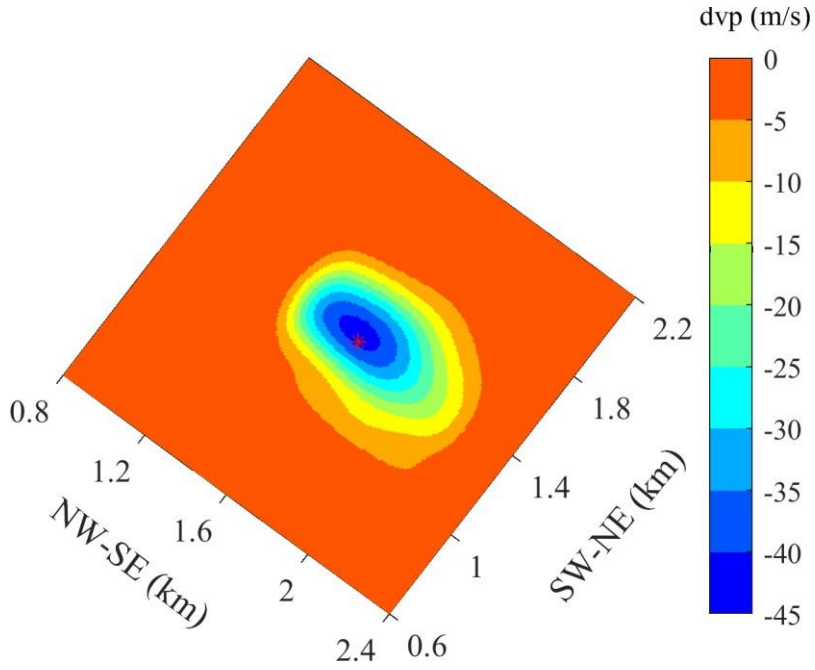

(b)

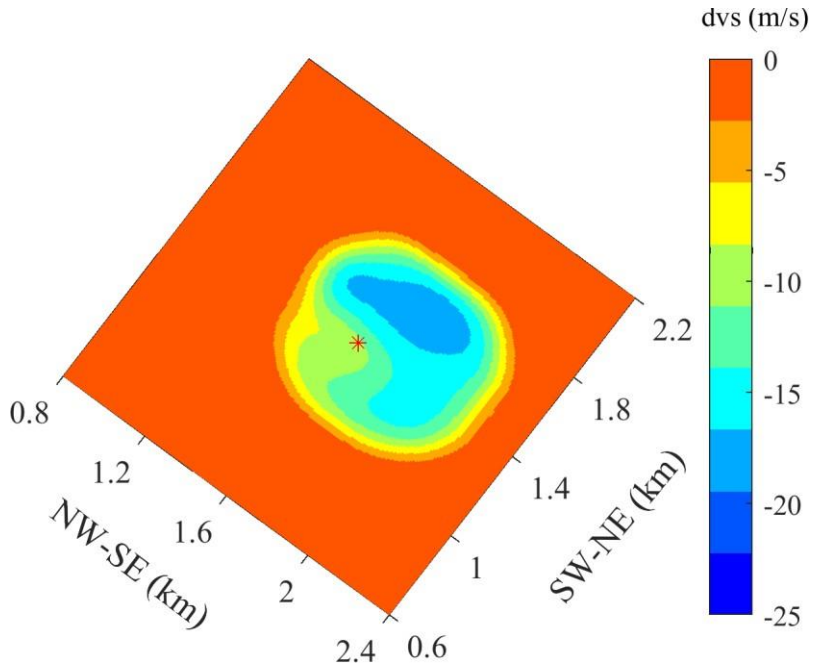

Figure 4.10: Inverted time-lapse velocity changes between baseline and Monitor 2 VSP surveys at the center depth of Morrow B.

(a)

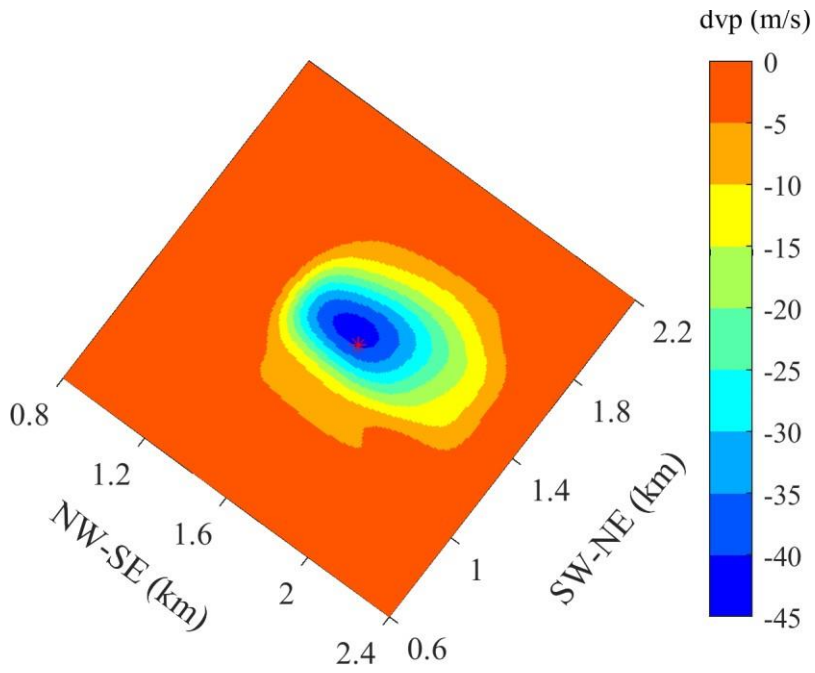

(b)

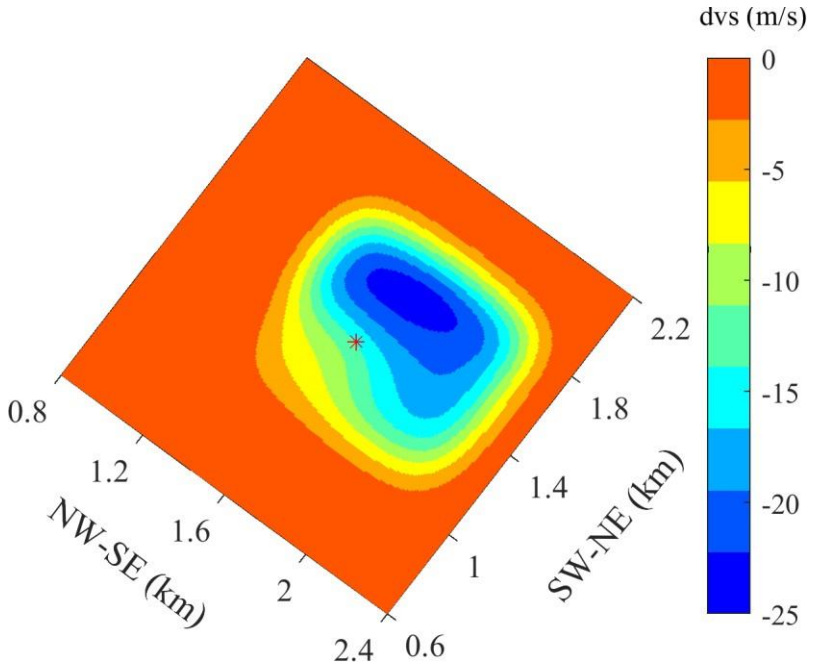

Figure 4.11: Inverted time-lapse velocity changes between baseline and Monitor 3 VSP surveys at the center depth of Morrow B.

The steadily dropped convergence curves in Figure 4.12 demonstrate the robustness of time-lapse inversion. Additionally, time-lapse Vp changes show large values near the CO_2 injection well (the red star in those figures).

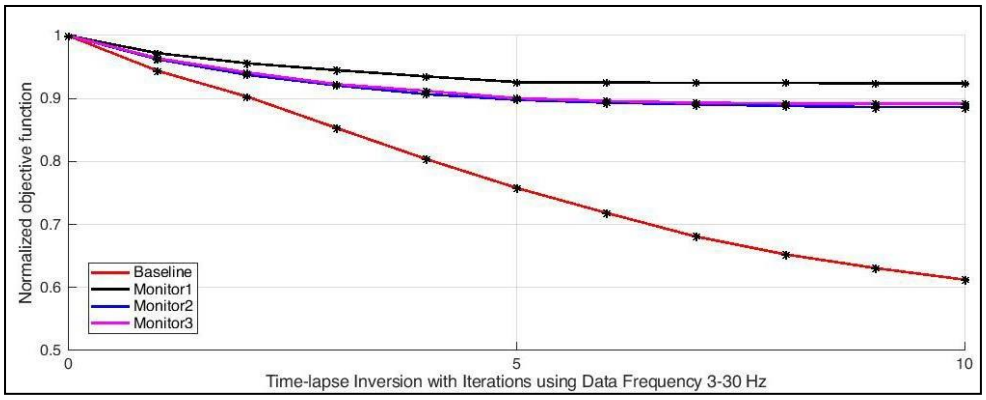

Figure 4.12: Comparison of convergence curves of baseline and three monitoring datasets at the final frequency scale.

Figure 4.13 is a comparison of inversion results with the well logs

.

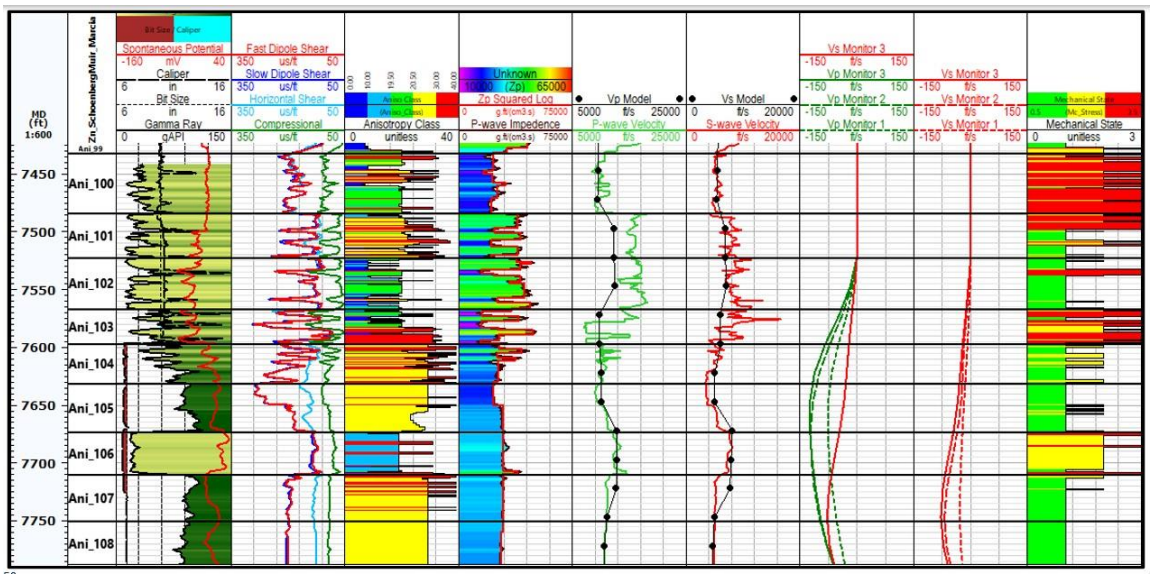

Figure 4.13: Results of the time-lapse VSP inversion in relation to the Mechanical Earth Model (MEM). Track 1 shows the measured depth, track 2 shows the layers used for the upscaling of the log data to the VSP scale, track 3 shows the correlation curves, track 4 shows the dipole acoustical slownesses, track 5 shows the anisotropy classification, track 6 shows the P-wave impedance used to define the layers, track 7 shows the upscaled Vp model in black and the P-wave log velocity in green, track 8 shows the upscaled Vs model in black and the S-wave log velocity in red, track 9 shows the change in P-wave velocity for the three monitor surveys in green and the third time-lapse S-wave monitor in red, track 10 shows the change in S-wave velocity for the three monitor surveys in red, and track 11 shows the mechanical behavior.

Note that the depths are measured with the reference of the well head, which is 16.2 m (53 feet) lower than the seismic processing datum. The maximum reduction in Vp in Monitor 3 occurs just above the Morrow B sand while the maximum reduction in Vs in Monitor 3 occurs well below the Morrow B sand. If there is slippage on a weak bedding plane below the Morrow B sand, it would reduce the horizontal stress below the sand. Because of the negligible fluid effect on the S-wave velocity, the reduction in shear-wave velocity occurs at a lower depth. The Vp is dependent on both changes in stress and fluids. Since carbon dioxide is more buoyant than the water, it is expected to reduce the P-wave velocity at shallower depths. Note that the inverted time-lapse Vp and Vs changes for this CO_2-EOR field are significantly smaller than those of petrophysical prediction for CO_2 flooding (Wang et al., 1998).

We plot the volumetric contour of our inverted velocity changes to visualize the spatiotemporal evolution of the CO_2 plume. We plot the velocity contours of -5 m/s as shown in Figure 4.14, Figure 4.15 and Figure 4.16, which vividly display the evolution of the CO_2 plume between baseline and Monitor 1, between baseline and Monitor 2, and between baseline and Monitor 3, respectively. They show how the CO_2 plume drives the oil and gas from the CO_2 injection well to the oil/gas production wells.

(a)

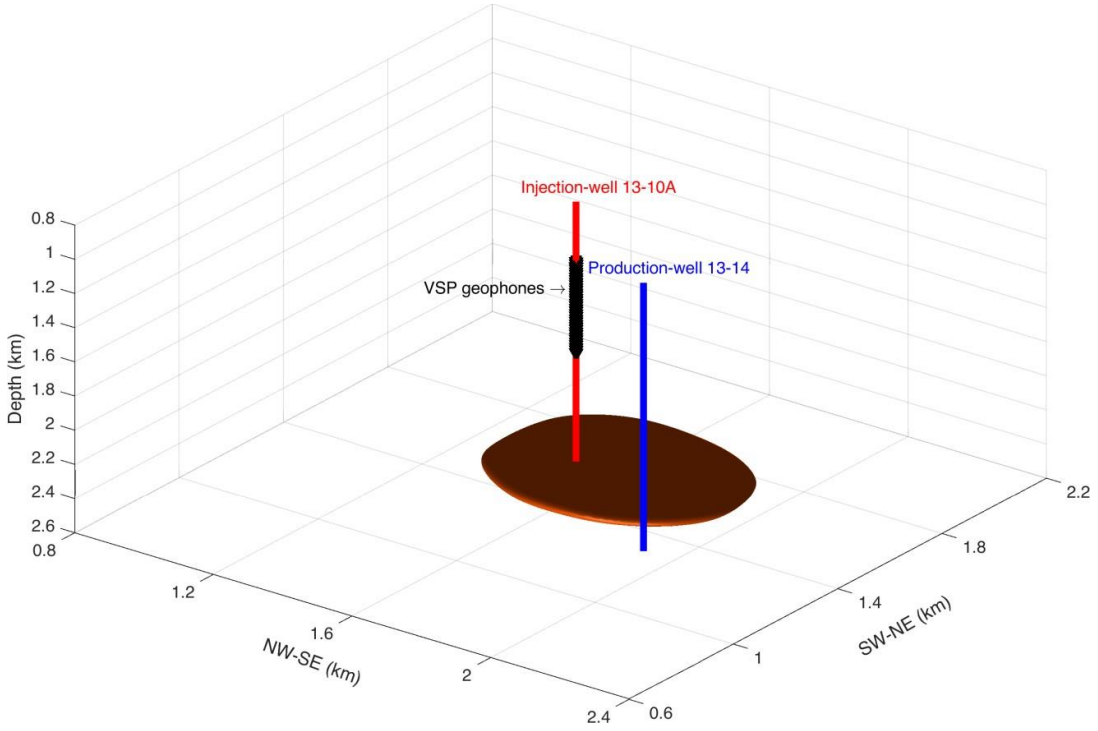

(b)

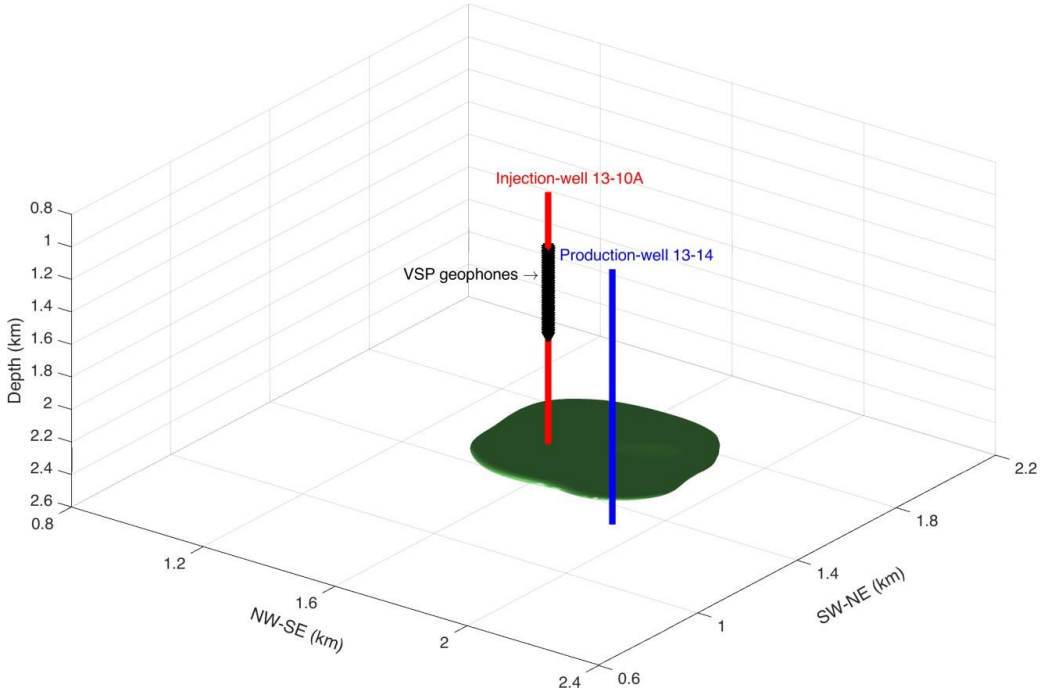

Figure 4.14: The volumetric contours of inverted time-lapse velocity changes between baseline and Monitor 1 VSP surveys.

.

(a)

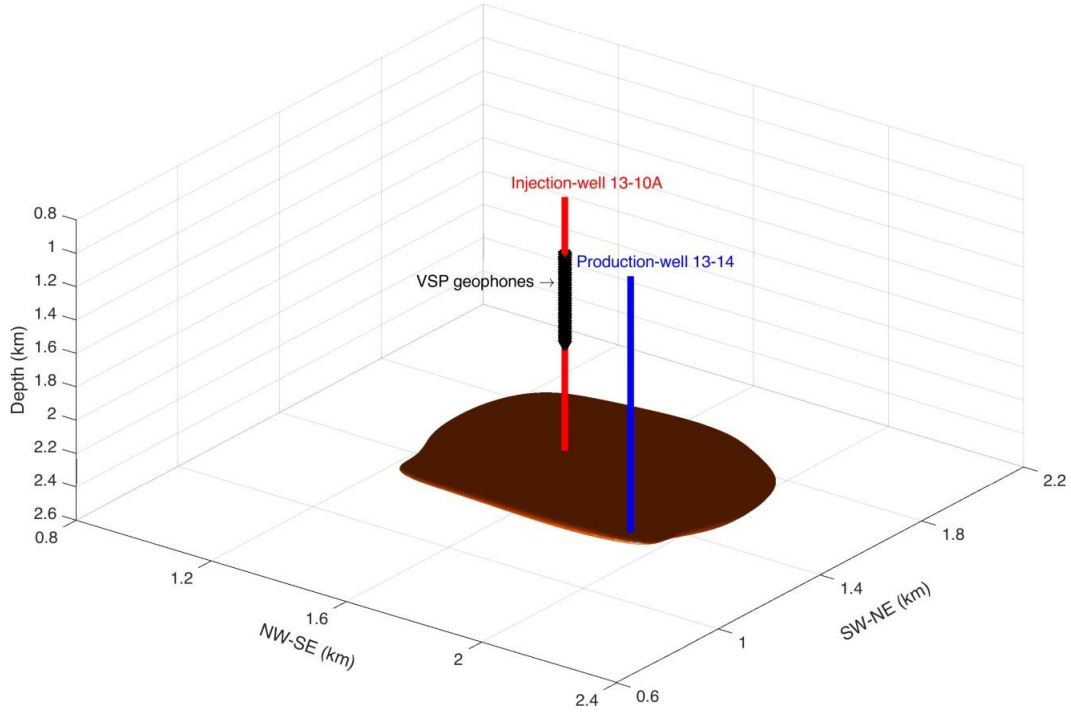

(b)

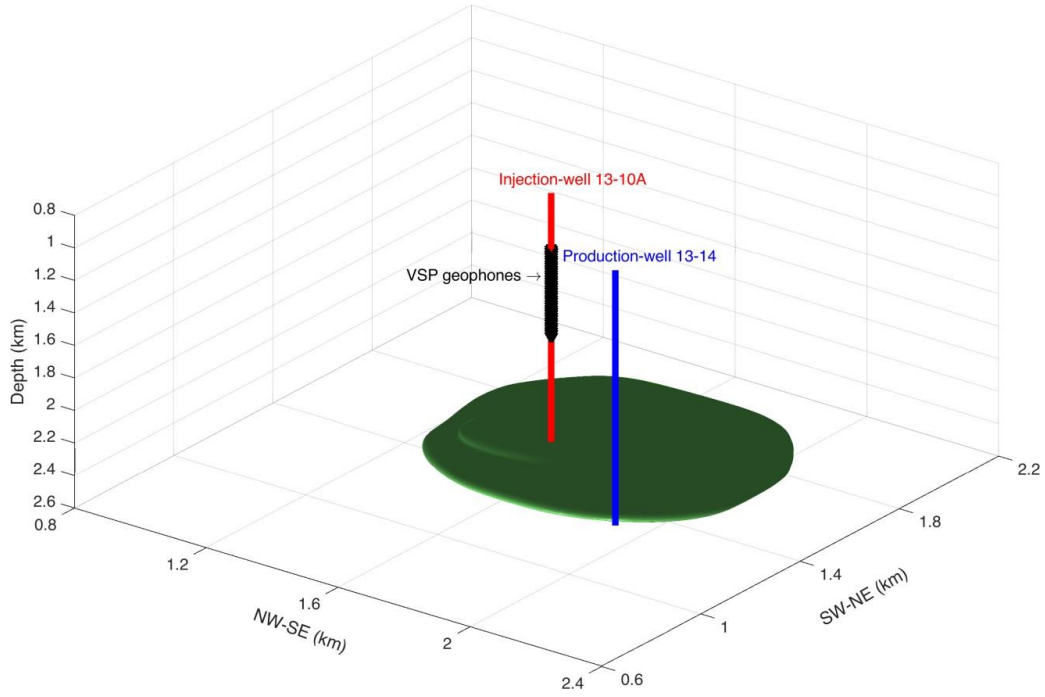

Figure 4.15: The volumetric contours of inverted time-lapse velocity changes between baseline and Monitor 2 VSP surveys.

(a)

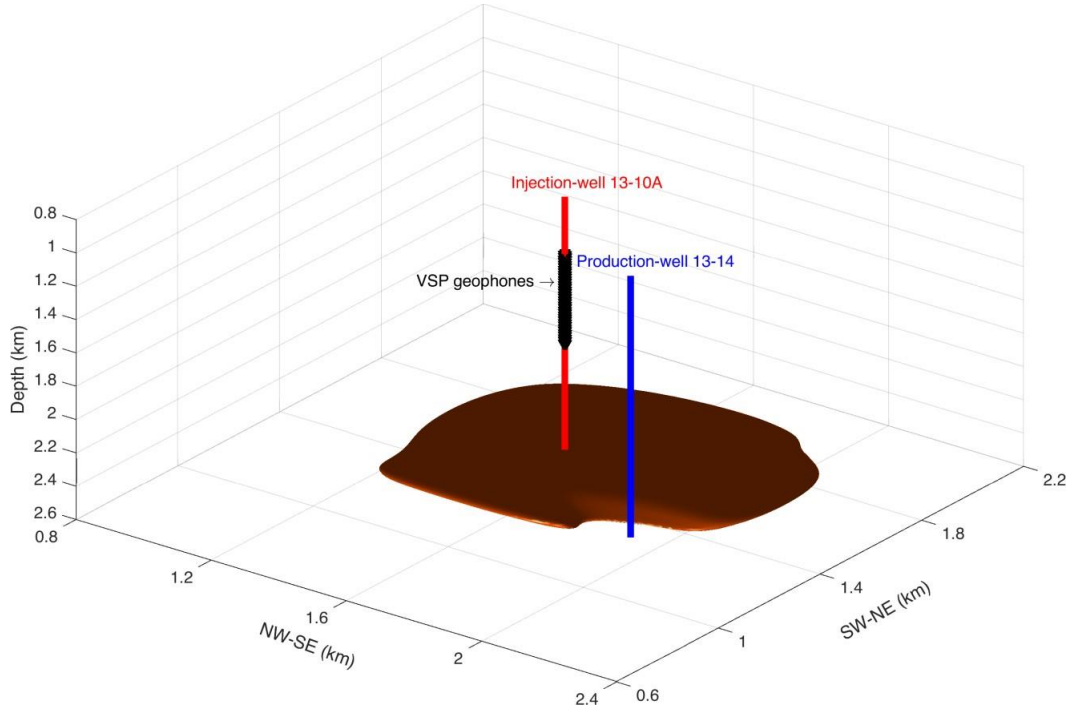

(b)

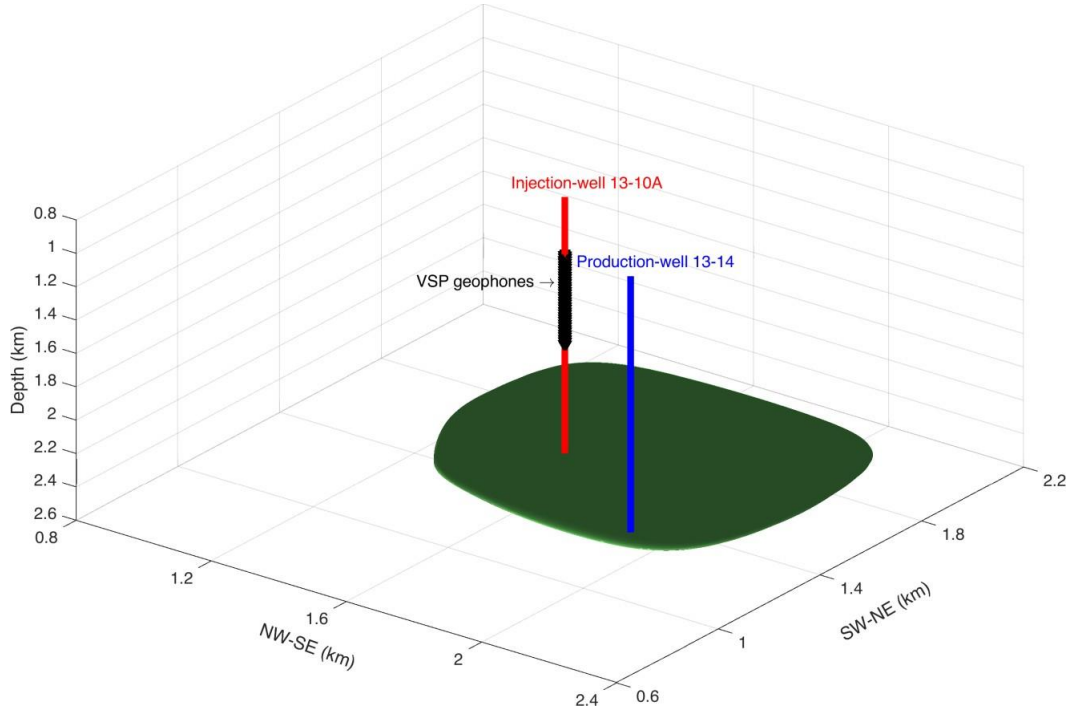

Figure 4.16: The volumetric contours of inverted time-lapse velocity changes between baseline and Monitor 3 VSP surveys.

.

4.5 Conclusions

We have performed 3D elastic-waveform inversion of the time-lapse 3D-3C VSP data acquired at the Farnsworth CO_2-EOR field for monitoring the spatiotemporal evolution of the CO_2 plume. We have built the baseline velocity models for time-lapse inversion using sonic logs, the velocity model derived from the 3D surface seismic data, 3D tomography of first arrivals of the baseline VSP downgoing waves, and elastic-waveform inversion of the upgoing waves of the baseline VSP data. We employ the spatial prior information in elastic-waveform inversion of time-lapse 3D-3C VSP data to improve the inversion robustness. Our results of time-lapse elastic-waveform inversion show the decreasing time-lapse velocities with the increasing of CO_2 injection, which are validated through comparison with borehole sonic logging and petrophysical prior information. The volumetric contour plots of the time-lapse velocity changes reveal the spatiotemporal evolution of the CO_2 plume, driving oil and gas from the CO_2 injection well to the oil/gas production wells.

4.6 Acknowledgments

This work was supported by the U.S. Department of Energy (DOE) through the National Energy Technology Laboratory to the Los Alamos National Laboratory (LANL), which is operated by Triad National Security, LLC, for the National Nuclear Security Administration (NNSA) of U.S. DOE under Contract No. 89233218CNA000001. This research used resources provided by the LANL Institutional Computing Program, which is supported by the U.S. DOE NNSA under Contract No. 89233218CNA000001. The 3D surface seismic data and time-lapse VSP data from Farnsworth were provided by the Southwest Regional Partnership on Carbon Sequestration (SWP) funded under DOE Award No. DE-FC26-05NT42591.

.

Chapter 5
Microseismic Analysis

Summary
The Farnsworth Unit in northern Texas is a field site for studying geologic carbon storage during enhanced oil recovery (EOR) using CO2. Microseismic monitoring is essential for risk assessment by detecting fluid leakage and fractures. We use well-established and newly developed seismic methods to analyze borehole microseismic data acquired during CO2 injection and migration, including data denoising, event detection, location, magnitude estimation, moment tensor inversion, and stress field inversion. We detect and locate two shallow clusters, which occurred during increasing injection pressure and feature large b values and tensile cracking moment tensors. The inverted stress fields at the two clusters show large deviations from the regional stress field. The results provide evidence for microseismic response to CO_2/fluid injection and migration.

5.1 Introduction

The Southwest Regional Partnership on Carbon Sequestration (SWP) is one of seven regional partnerships established in 2003 by the U.S. Department of Energy (DOE) to study carbon management strategies. The SWP is conducting Phase III field demonstration in northern Texas using carbon dioxide (CO_2) for enhanced oil recovery (EOR) within the Farnsworth Unit (FWU) in Ochiltree County, Texas. The CO_2-EOR project injects CO_2 from 100% anthropogenic CO_2 sources from the Arkalon Ethanol Plant in Kansas and the Agrium Fertilizer Plant in Texas. The primary goals of the project are the option of geologic carbon storage during CO_2-EOR, quantifying storage capacity, and optimizing the balance between enhanced oil recovery and CO_2 storage (Balch & McPherson, 2022).

In geologic carbon storage projects, the reservoir is subject to an increased pore- pressure regime because of continuous CO_2 injection, which increases the potential for induced seismicity and the risk of reactivating faults or fracture zones in the underlying crystalline basement. Monitoring for induced microseismicity is essential to map the pressure front, detect CO_2 leakage, and avoid damage to the storage facility or surface infrastructures, particularly when no seismically resolvable faults can be mapped on 2D/3D seismic data (van Wijk et al., 2021). Microseismicity has been recorded at multiple CO_2 injection sites. At the Weyburn Field, Saskatchewan, Canada, approximately 100 microseismic events with magnitudes ranging from -3 to -1 were recorded during five years of monitoring and event occurrence seemed to be associated with injection or production rate changes (D. White, 2009). At the Aneth CO_2-EOR field in Utah, 3800 microearthquakes were detected and the magnitude ranged from -1 to 1. These events correlated with fracture zones on opposite flanks of the reservoir but not with CO_2 injection or production activities (Rutledge, 2009; Zhou et al., 2010). At the In Salah Carbon Capture and Storage site, over 9000 events were recorded with maximum magnitude of 1.7, and the microseismicity occurrence correlated well with CO_2 injection rate (Stork et al., 2014).

The microseismicity provides valuable information about the underground, including location and orientation of the activated fracture plane, fracturing mode, and perturbed local stress field. Microseismic monitoring in combination with the injection rate and pressure data can improve understanding of the subsurface injection, storage, and fracturing processes.

We analyze microseismic data recorded within a vertical borehole using well-established and newly developed seismic methods. We first describe the data used in this study, introduce the methodology, and then show results of microseismic event locations, magnitude distribution, moment tensor inversion, and inverted stress field. Finally, we compare the microseismic events to the injection rate and pressure to study their relationship.

5.2 Data

At the Farnsworth field, we have one vertical borehole (Figure 5.1) to monitor induced microseismicity during CO_2 injection and migration. The well is located in the middle of the project study area. The borehole geophone array consists of 16 three-component (3C) receivers at depths from 1345 to 1795 m with a vertical spacing of 30 m. We analyze continuously-recorded borehole microseismic data from August 2019 to February 2022.

The project also deployed 20 surface seismic stations to monitor the microseismicity. Compared to borehole monitoring, the surface stations cover a large aperture of the study area (about 3 by 3 $km2$). However, the signals recorded by these surface seismic stations are much noisier than borehole data, and the data are not completely continuous. We only observe clear phase arrivals for a few regional events, where the time difference between P and S phase arrivals is larger than one second. Since we are mainly interested in the local events within the CO_2 injection area, only borehole data are used in our analysis.

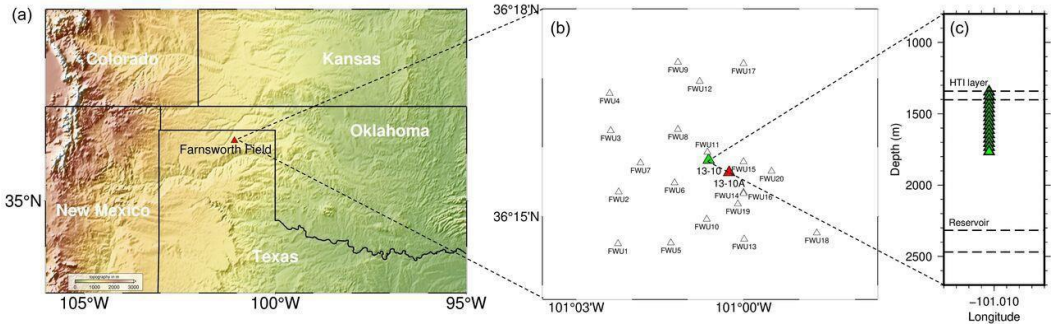

Figure 5.1: (a) Location of the Farnsworth CO_2-EOR field. (b) Microseismic monitoring network, including 16 geophones in the vertical borehole 13-10 (green triangle) and 20 surface seismic stations (white triangles). Well 13-10A (red triangle) is the primary CO_2 injection well. (c) Depth view of the borehole geophones (green triangles). The Morrow B reservoir and one horizontal transversely isotropic (HTI) layer at shallow depth are highlighted.

5.3 Methodology

5.3.1 Geophone Orientation Calibration

Inside the borehole, the horizontal channels of the geophones are usually misoriented, that is, the two horizontal components are not necessarily aligned in the north and east direction. Following the method from (Gaiser et al., 1982) and (DiSiena & Gaiser, 1983), we use the offset vertical-seismic-profiling (VSP) check shots with known source locations to calculate the rotation angles. We first rotate the two horizontal components to the radial (maximum P wave amplitude) and transverse directions. Since the azimuth of radial and transverse directions are known for a check shot, we calculate the azimuth of the horizontal channels. Figure 5.2 shows the computed rotation angles of the first horizontal components ($H1$) for each geophone. The rotation angles are randomly distributed, which makes the rotation correction essential for the following analyses of borehole microseismic data. After correcting the geophone orientations, we also remove the instrument response from the waveform to convert the digital counts recorded to physical displacement.

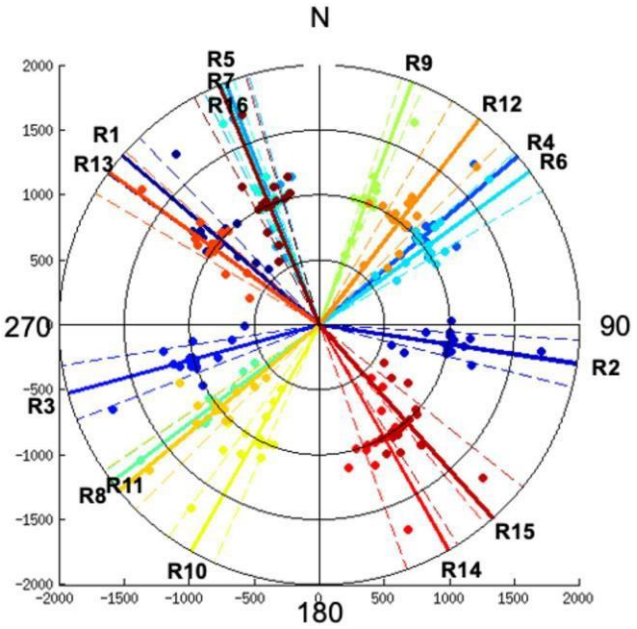

Figure 5.2: The orientations of the first horizontal channel (H1) of the borehole geophones used at the Farnsworth CO_2-EOR field. Each color represents a different geophone. The solid lines are the rotation angles, and the dashed lines show the 95% uncertainty.

5.3.2 Event Detection

We examine the spectrograms of the waveform data and find signals in two different frequency ranges, 5 to 50 Hz and 150 to 350 Hz. For each frequency range, we apply bandpass filtering to the continuously-recorded borehole microseismic data and use the short-term average/long-term average (STA/LTA) method (Allen, 1978) to automatically detect microseismic events on the continuous waveforms. For low-frequency signals, we use 0.1 s and 2 s for short and long term windows, respectively, and detect 13, 398 events from August 2019 to June 2021. Figure 5.3 shows all the detections from 2020 to 2022 with their signal-to-noise ratio (SNR). Of all the detected events, we remove the borehole events that have apparent velocity around 1500 m/s and select 932 events with SNR larger than 2.0 for event location. For high-frequency signals, since it is difficult to obtain the accurate location and moment tensors, we only run detection for a short period of time from July 2019 to February 2020 and detect 278 events.

5.3.3 Waveform Denoising

We denoise microseismic data using a denoising algorithm from (Mousavi et al., 2016) that is based on synchrosqueezed continuous wavelet transform (SS-CWT) and custom thresholding of single-channel data. The SS-CWT allows for the adaptive filtering for frequency-varying noise and offers improvement in resolution over the conventional wavelet transform. The method has been successfully applied to field microseismic data and proves effective to enhance SNR (Mousavi et al., 2016). Figure 5.4 shows an example of waveform comparison before and after denoising for our borehole microseismic data. The result shows that the algorithm successfully removes the background noise and keeps the signal. We apply the algorithm to all detected events and compare the SNRs in Figure 5.5. The median SNRs for denoised waveform is improved from 2.5 to 8.

5.3.4 Event Location

After waveform denoising, we use the 2D Kirchhoff migration (Baker et al., 2005) to locate the microseismic events. First, we compute a traveltime table using the resulting velocity models from elastic-waveform inversion (EWI) of the 3D VSP data. Then, the microseismic waveforms are migrated and stacked for different event locations and origin times based on the pre-computed traveltime table. The mesh point with the maximum value of the stacked image is the location of the microseismic event. The method does not require explicit phase picks and works well for borehole microseismic data. Since we have only one vertical borehole array, we can only determine the event location in 2D plane (depth and offset). Next, we perform hodogram analysis of three- component microseismic data to determine the event azimuth, where we cross plot the waveform of two horizontal channels and its slope represents the azimuth of ray path (Han et al., 2009). For a homogeneous layered model, the receivers in the vertical well should have the same azimuth angle for one event. We take the average direction of 16 receivers as the azimuth of an event. Finally, based on the 2D location and azimuth angle, we calculate the 3D locations for all microseismic events.

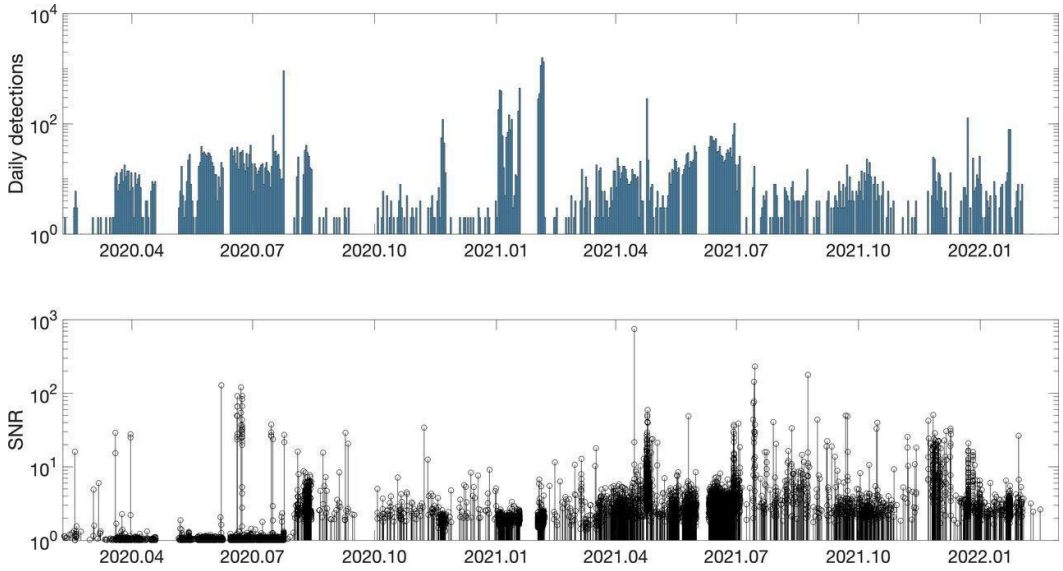

Figure 5.3: STA/LTA detection results on borehole microseismic data from the Farnsworth CO_2-EOR field.

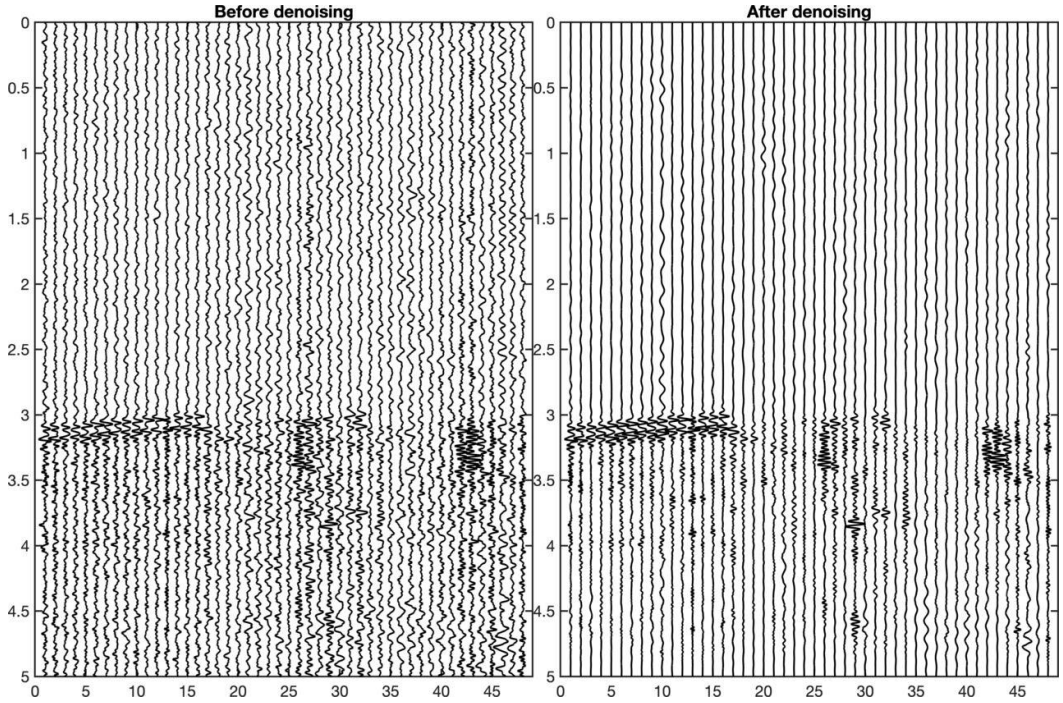

Figure 5.4: Comparison of borehole microseismic waveforms before and after denoising

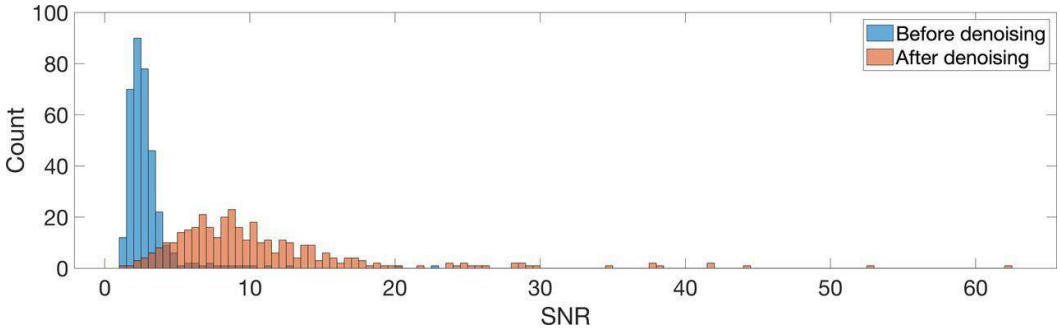

Figure 5.5: Comparison of SNRs before and after waveform denoising for detected microseismic events.

5.3.5 Magnitude Estimation

To estimate the moment magnitude of the located microseismic events, we first remove the effect of radiation pattern and geometric spreading (Yue & Xiao-Fei, 2005) from microseismic waveform. Then we compute the source spectrum using Fourier transform and calculate the least- squares fits of the scalar seismic moment ($M0$) and the corner frequency for Brune's model (Brune, 1970). The moment magnitude (Mw) is then calculated using (Kanamori & Brodsky, 2004),

$$Mw = 2/3log10\ M0 - 6.07 \qquad (5.1)$$

Based on the magnitude, we calculate the b value and magnitude of completeness using the maximum likelihood estimator (Bender, 1983) in seismicity analyzing package ZMAP (Wiemer, 2001).

5.3.6 Moment Tensor Inversion

We use a full-waveform inversion method (Gao et al., 2021) to invert for moment tensors of the microseismic events. The method utilizes a weighted, normalized deconvolution misfit function and a zero-lag cross-correlation misfit function. It also simultaneously estimates the event origin time and moment tensor in the inversion. Synthetic tests have shown that the method can accurately estimate moment tensors using microseismic data recorded with a single-borehole geophone array. After we obtain the full moment tensor for each event, we decompose it into isotropic (ISO), double-couple (DC), and compensated linear vector dipole (CLVD) components (Dziewonski et al., 1981). The DC component represents the shear faulting. The CLVD component has no simply physical meaning itself but combined with the ISO component, it can be interpreted as tensile faulting. For a pure tensile crack, the major dipole of the CLVD component is aligned with the normal to the crack surface, and the ISO component represents the volume change associated with the opening crack (Vavryčuk, 2015). We use Hudson plot (Hudson et al., 1989) to visualize the decomposition results. The origin of coordinates represents pure shear faulting. The margins of the diamond represent pure tensile and compressive cracks. Points along the CLVD axis correspond to faulting on non-planar faults and points in the second and fourth quadrants of the diamond correspond to shear-tensile sources.

5.3.7 Stress Inversion

After obtaining moment tensor, we use the MSATSI software package (Martínez-Garzón et al., 2014) to invert for stress field. The MSATSI software is based on the inversion method from (Michael, 1984), which minimizes the difference between the slip vector and the resolved shear stress vector on each fault plane,

$$Gm = d \qquad (5.2)$$

where G is the data kernel matrix derived from the fault normal vector of each focal mechanism, d is the slip vector of each focal mechanism, and m is the model vector of stress tensor. The program generates the orientations of three principal stresses (σ_1, σ_2, σ_3) and a relative stress magnitude (R) among σ_1, σ_2, σ_3. The inversion process requires a minimum of 20 focal mechanisms at each grid point to obtain reliable results.

5.4 Results

5.4.1 High-Frequency Events

For high-frequency microseismic events, which are detected in the frequency range of [150, 250] Hz, we are only able to obtain the 2D location because the hodogram analysis does not work well for high-frequency signals. Figure 5.6 shows the depth distribution of the events and comparison with the petrophysical logs. The events mainly occurred in the horizontal transversely isotropic (HTI) layer (4400–4600 ft in depth). It is possible that the vertical fractures in the HTI layer are reactivated during injection. Figure 5.7 shows the magnitude distribution for high-frequency events. Most events have magnitudes from -1.5 to 0.5. The b value and the magnitude completeness is 1.47 and -1.2, respectively.

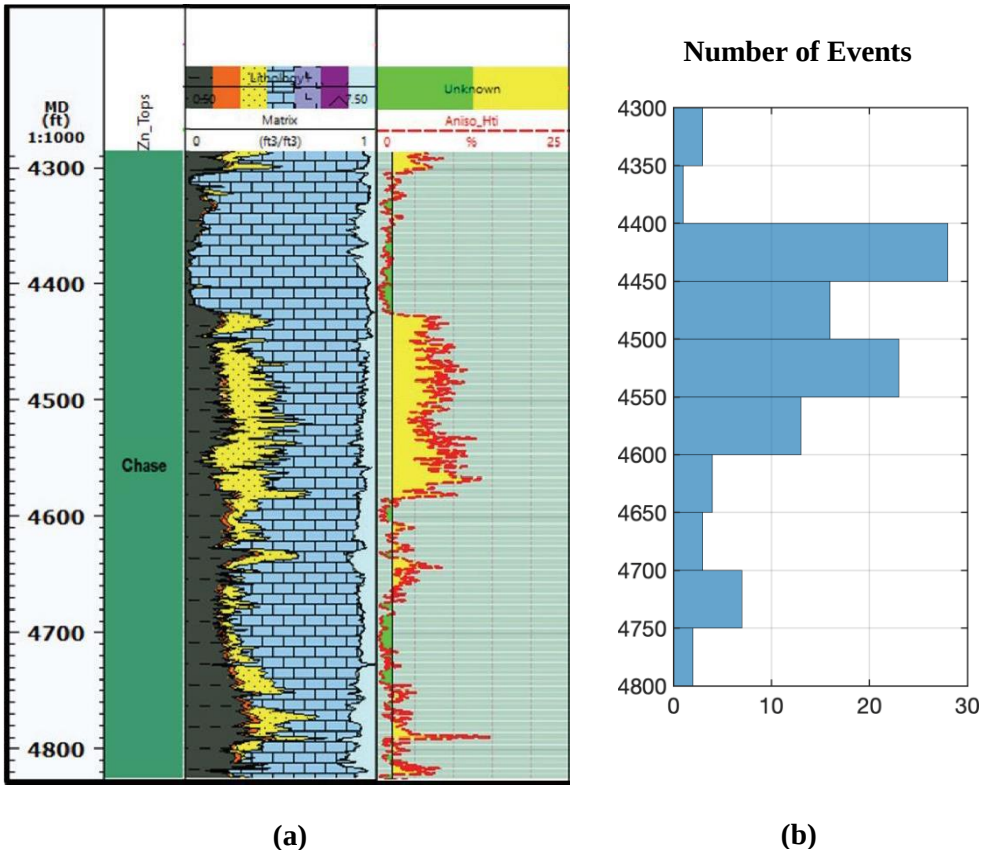

Figure 5.6: (a) Petrophysical logs for lithology and HTI anisotropy. (b) Depth distribution of high- frequency microseismicity. The depth are aligned for (a) and (b).

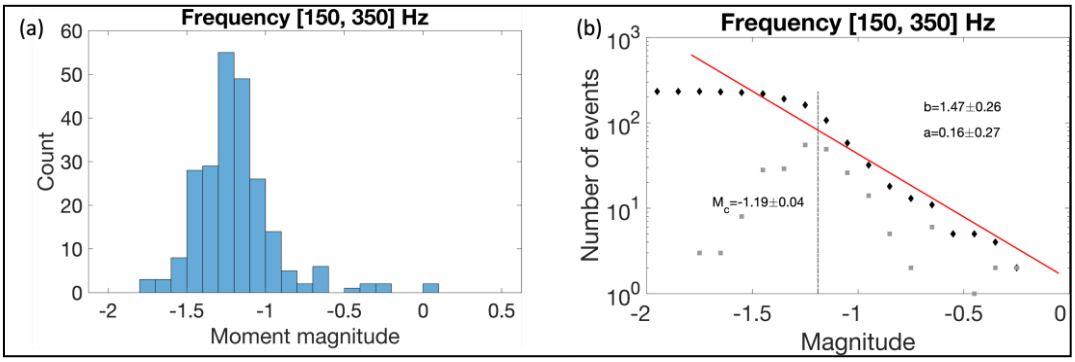

Figure 5.7: (a) Magnitude histogram and (b) magnitude-frequency distribution for high-frequency microseismic events from July 2019 to February 2020.

5.4.2 Low-Frequency Events

Figure 5.8 shows the location results for low-frequency microseismic events (5–50 Hz). We observe two shallow clusters activated in February 2021 and January 2022, respectively. The first cluster depicts a NW trending (-57◦) and subvertical (dip angle 83◦) fault plane. The events are mainly distributed on the path from injection well 13-10A to the monitoring well. The second cluster in January 2022 is oriented in the NS direction and forms a horizontal plane. Similar to the high-frequency events, the depth of the events is consistent with the HTI layer. In depth (>2000 m), the events are scattered. The deeper events have larger magnitude than shallow events. The diffusion migration pattern is not evident, and only a few events occurred in the Morrow B reservoir.

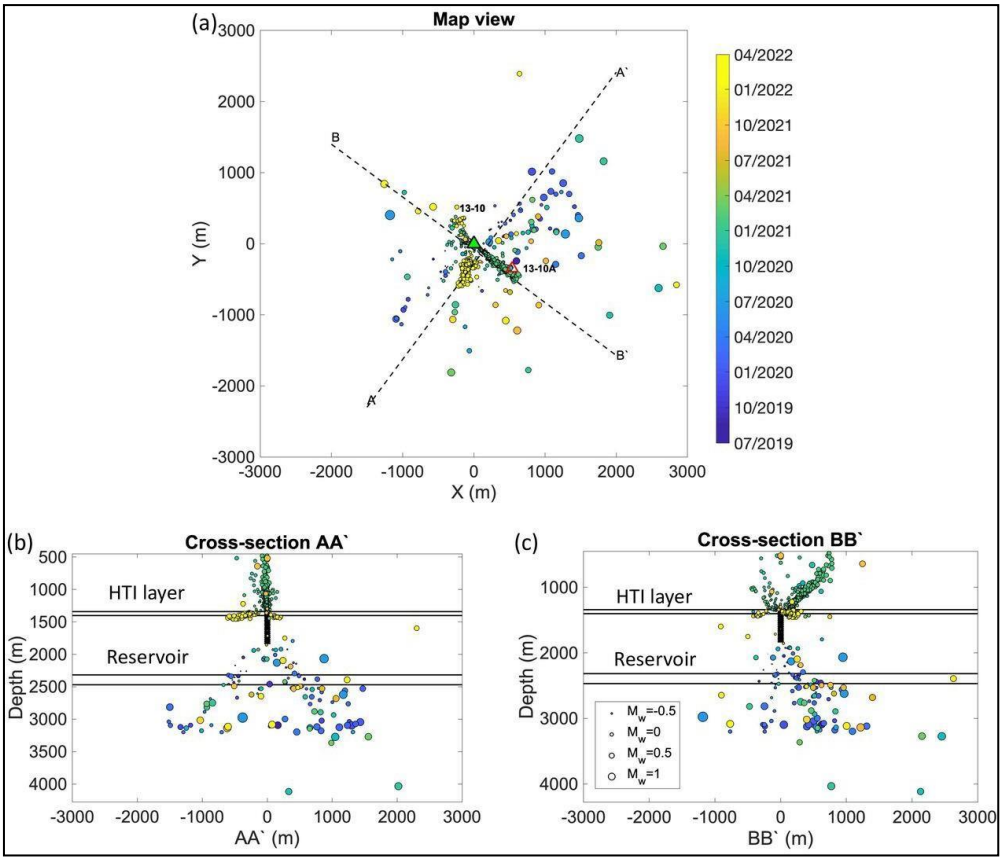

Figure 5.8: Location results in (a) map view, (b) cross-section view AA', and (c) cross-section view BB' for low-frequency microseismic events from August 2019 to January 2022). The events are colored by event time. Reservoir layer and a shallow HIT layer are highlighted.

Figure 5.9 shows the magnitude distribution for low-frequency microseismic events (5–50 Hz). The majority of the low-frequency events are within the magnitude range of [-1, 0.5]. The estimated b value is 2.07, and the magnitude of completeness is 0.33. Compared to high-frequency events, the magnitude of low-frequency events is slightly larger, and b value is much higher. To explore the spatial variations of b values, we separate the shallow and deep microseismicity at depth of 2000 m. For deeper events, the b value is 1.38, and the magnitude of completeness is 0.2 (Figure 5.10a). Since we have more events at shallow depth (< 2000 m), we compute the b value variations over time. The results show that the two temporal clusters in February 2021 and January 2022 have b values significantly larger than 1.0 (Figure 5.10a), suggesting the influence of injection on microseismicity.

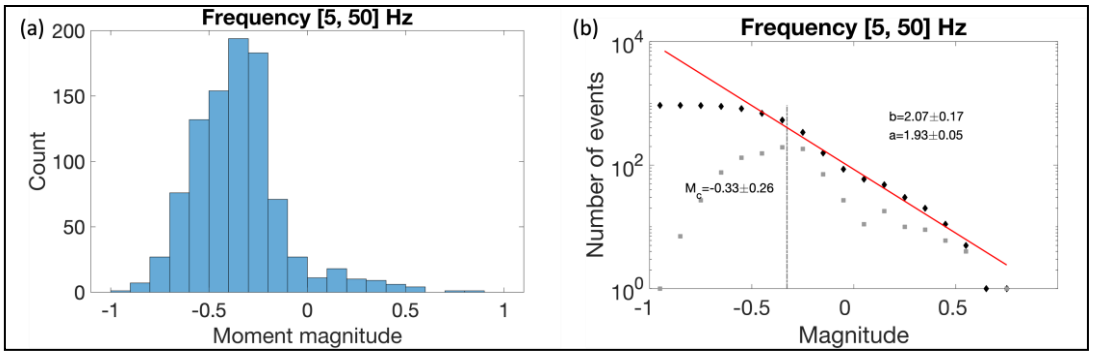

Figure 5.9: (a) Magnitude histogram and (b) magnitude-frequency distribution for low-frequency microseismic events from August 2019 to January 2022).

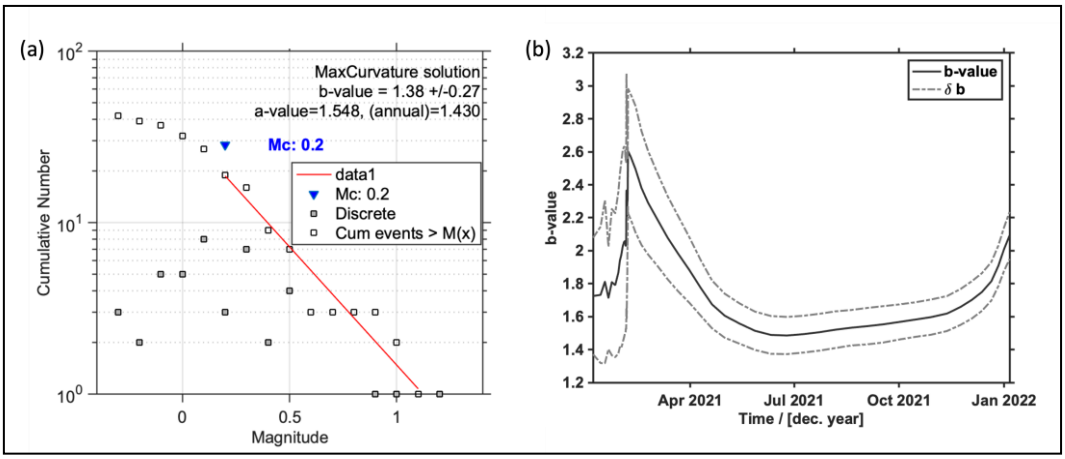

Figure 5.10: (a) Magnitude-frequency distribution for deep (depth>2000 m), low-frequency microseismic events. (b) b-value variations over time for shallow (depth<2000 m), low-frequency microseismic events. The solid line shows the b value, and the dashed lines show the 95% uncertainty.

5.4.3 Moment Tensors

Using the method from (Gao et al., 2021), we are able to compute the moment tensors for 125 microseismic events. As shown in Figure 5.11, the events at depth (>2000 m) show a variety of mechanisms. Within the two shallow clusters, the moment tensors are similar to one another. The inverted full moment tensor is decomposed into isotropic (ISO), double-couple (DC), and compensated linear vector dipole (CLVD) component. As shown on the Hudson plot in Figure 5.12, moment tensors at deeper depth are mainly shear slip events, possibly induced by reactivating existing fractures. Moment tensors at shallow depths have a larger CLVD and ISO component, suggesting fracture opening and closing under injection.

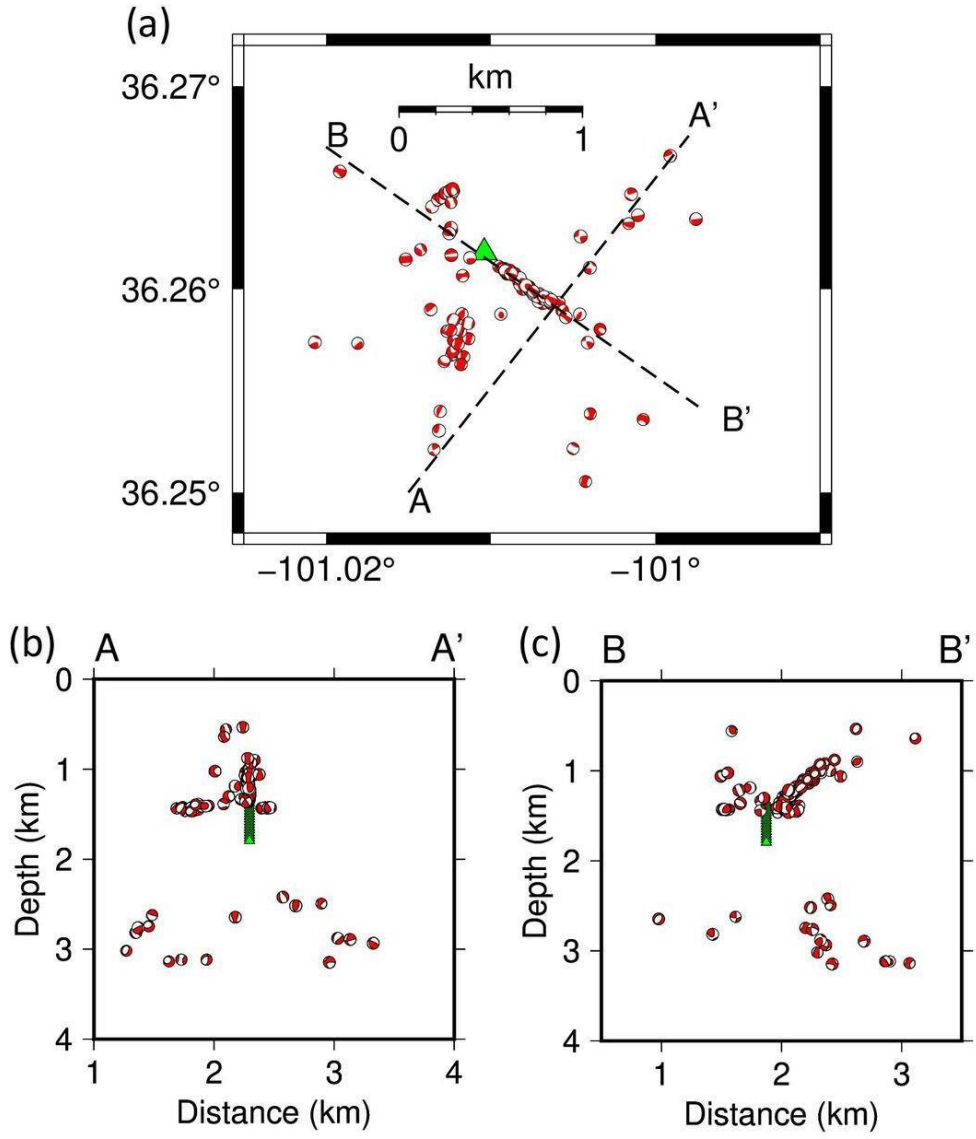

Figure 5.11: Moment tensor inversion results shown in map view and cross-section views (AA‘ and BB’). The green triangles are boreholes geophones.

5.4.4 Stress Inversions

We obtain 21 moment tensors at depth deeper than 2000 m (grid 1), and 67 events in the NS trending shallow cluster (grid 2), and 20 events in the NW trending shallow cluster (grid 3). We invert for stress field separately for the three grids.

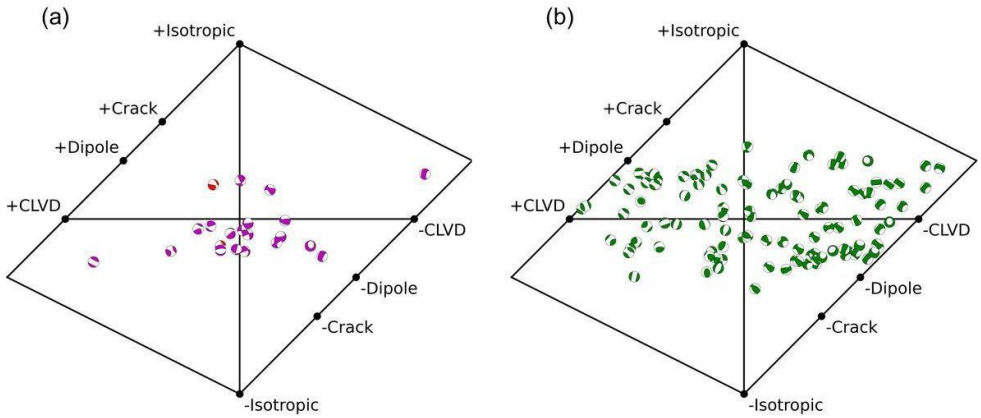

Figure 5.12: Figure 5.12. Hudson plot for moment tensors at (a) deeper depths (> 2000 m) and (a) shallow depths (< 2000 m). Microseismic events in the reservoir are highlighted in red.

Figure 5.13 depicts the stress inversion results. The deeper events result in an oblique normal faulting regime, and the maximum horizontal stress orientation is 97◦. The inversion results are consistent with the regional stress field from (Snee & Zoback, 2022). The NS trending cluster shows an oblique faulting regime, and the results are better constrained than the first grid. The NW trending cluster shows a reverse faulting regime with a maximum horizontal stress orientation of 143◦.

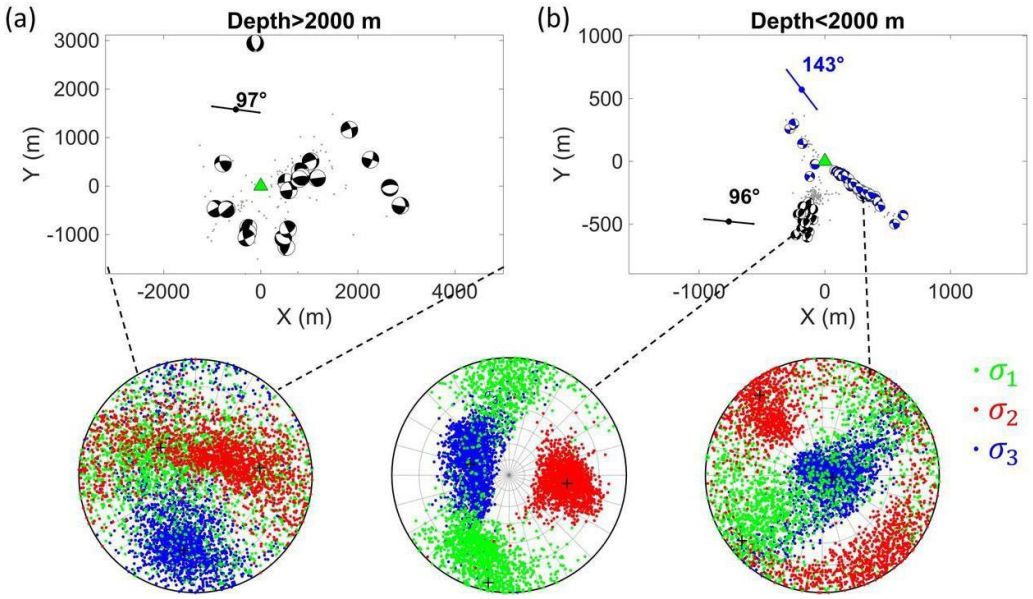

Figure 5.13: Stress inversion results for (a) deeper events (depth>2000 m) and (b) two shallow clusters (depth < 2000 m). Green triangle is the vertical borehole. Black color represents oblique faulting regime, and blue color represents reverse faulting regime. The stereonet plots show the inverted stress field for each grid. Green, red, and blue dots show the orientations of the maximum, intermediate, and minimum principal stresses.

5.5 Discussion

Figure 5.14a shows the five-spot well patterns, where four injection wells at the corners and a production well at the center. The CO_2 injection depth is within the Morrow B reservoir (2300–2500 m in depth). The CO_2-EOR operations started in 2010, and the field is operated on a water-alternating-gas (WAG) cycle (Figure 5.15). The average CO_2 injection rate from 2014 to 2020 is around 16000 thousand standard cubic feet per day (Mscf/d). At the peak time, there are 14 active injection wells operating at the same time. In Figure 5.15, we compare the microseismic analysis results to the injection data from the primary CO_2 injection well 13-10A. Figure 5.15a shows the WAG injection cycle, and Figure 5.15b shows the injection pressure measured in 13-10A. The pressure during CO_2 injection is higher than that of water injection. The microseismic event occurrence does not show significant difference for CO_2 and water injections, similar to the findings in (Verdon et al., 2010). One striking feature is that a temporal microseismic event cluster occurred when CO_2 injection pressure increased in February 2021. The moment tensors of the cluster have larger portions of CLVD components compared with the other events. The evidences suggest that the sudden pore pressure change in February 2021 possibly created a new fracture, and the moment tensors of the induced microseismic events record the fracture opening and closing.

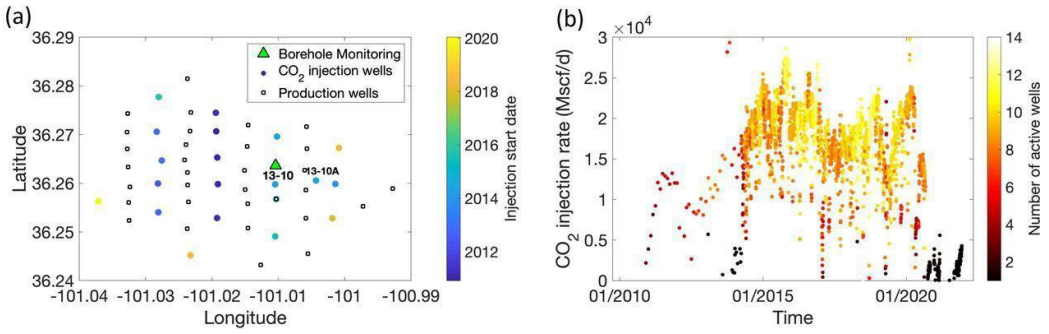

Figure 5.14: (a) Spatial distribution of injection and production shows the five-spot well patterns. The injection wells are colored by injection start date. 13-10 is the monitoring well, and 13-10A is the primary CO_2 injection well. (b) CO_2 injection rate. The plot is colored by the number of active injection wells at every timestamp.

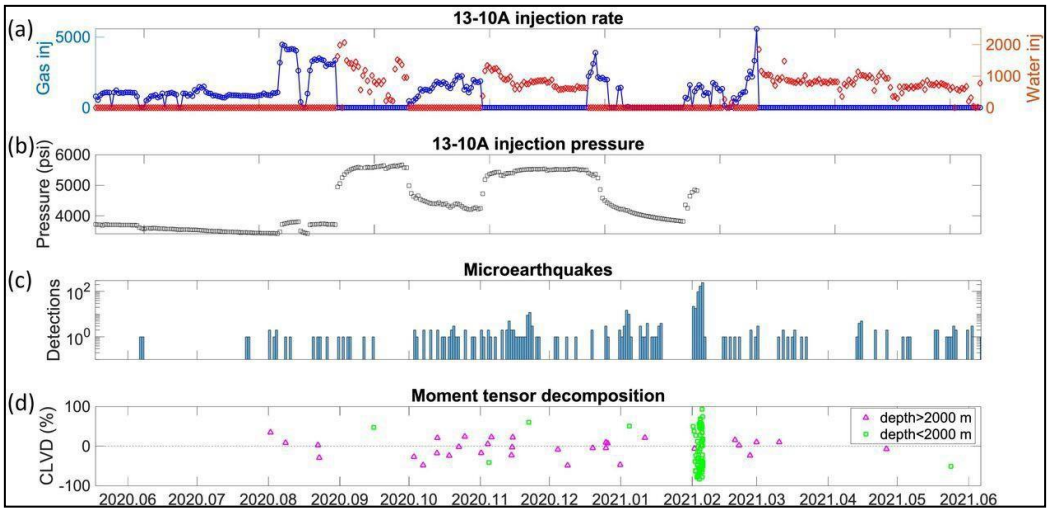

Figure 5.15: (a) Alternating CO_2 and water injection rate. (b) Injection pressure for well 13-10A. (3) Located microearthquake distribution over time. (4) CLVD component for moment tensors.

Our microseismic data analysis results reflect microseismic response of *CO2*/water injection. First, the temporal correlation between microseismicity burst and injection pressure increase (Figure 5.15) provides direct evidence of induced microseismicity. Second, consistent with the findings at other induced seismicity areas, e.g., geothermal field, fluid injection influences the magnitude distribution of microseismicity and usually results in higher b values compared with tectonically originated value of one. The b values of the two shallow clusters are significantly larger than 1.0. Next, moment tensors of the shallow events show large portion of CLVD component, which corresponds to tensile cracking. Finally, the inverted stress field at deeper depths is consistent with regional stress field. However, the stress field at shallow depths displays large deviations from the regional stress field. The above evidences suggest that the shallow clusters are probably induced by fluid injection.

5.6 Conclusions

We have analyzed the borehole microseismic data from the Farnsworth CO_2-EOR field using both well- established and newly-developed seismic methods. Our analyses include microseismic data denoising, event detection, location, magnitude estimation, moment tensor inversion, and stress field inversion. The results, for example, large b values, tensile cracking mechanism from moment tensor, and local variations of stress field, provide evidences of microseismic response to CO_2/fluid injection.

Chapter 6
Coupled Geomechanical Models: Construction, Initialization and Dynamic Testing

6.1 Introduction

Geomechanical modeling is an integral aspect of the VSP integration project. The VSP integration project uses acoustic measurements such as time-lapse VSP to calibrate the hydromechanical simulation model. The selected study site is a CO_2-EOR process, and as such substantial impacts on time-lapse VSP changes are due to the combined effects of fluid substitution and influx-induced changes in the stress. This chapter documents the "best practices" for geomechanical modeling within the FWU and presents full-field geomechanical results during the CO_2-EOR operations, as this is the time for the VSP integration study.

Hydromechanical models integrate the coupled effects of fluid and mechanics. For a free-flowing fluid within a deformable porous solid matrix (Biot, 1941), increases in fluid pressure cause dilation of the matrix while loads imposed on the rock induce fluid pressure increase if the matrix is undrained (Detournay et al., 1993). The coupling procedure implemented depends on the relative impact of the stress on the fluid flow. Several methods: Fully coupled, two-way iterative coupling, and one-way coupling provides options based on the effect of stress on the fluid flow.

The first published record of geomechanical simulation modeling is the work of (Heffer et al., 1994), who coupled thermal, mechanical and hydraulic considerations that explained the deviations to breakthrough pathways during waterflooding operations. The late 1990's exploitation of stress-sensitive North Sea reservoirs highlighted the potentially costly impacts of inappropriately accounting for poroelastic effects with rock compressibility. Many North Sea fields encountered issues with reservoir compaction (Nagel, 2001), seafloor subsidence jeopardizing the safety of platforms (Pattillo et al., 1998), and the wellbore failures (Da Silva et al., 1990). The 2010's boom in oil production from unconventional resources has also spurred additional interest in geomechanics. A sound understanding of stress orientations and minimum horizontal stress is essential for appropriate well planning (Britt & Schoeffler, 2009; Jin et al., 2015). Additionally, the current drive to safely and securely store CO_2 in the subsurface has raised concerns about the containment assurance, assessing and avoiding leakage pathways (Li et al., 2016).

The validity of numerical geomechanical simulation outputs is inextricably linked to the appropriate construction of the geomechanical models. The geomechanical property population extends from the surface to the underburden and is constructed with judicious utilization of all available datasets. This chapter addresses the building, stress initialization and dynamic testing of the coupled hydrodynamic geomechanical simulation model for the FWU.

6.2 Workflow Overview of Mechanical Earth Model Construction

The workflow for the MEM construction is shown in Figure 6.1. The three-dimensional ***geologic framework*** is constructed from the 3D seismic, interpreted faults and all available well logs and cores, capturing the petrophysical heterogeneity, structure, and stratigraphy of the FWU. The geologic framework provides geologic consistency and feeds both the reservoir simulation and the geomechanical model. Figure 6.1 also indicates differences in coupling methodologies. Several coupling procedures exist, including fully coupled, which involves the simultaneous flow and

mechanical equations solutions. Although rigorous and accurate, fully coupled solutions are expensive and time-consuming and thus rarely utilized. More commonly applied are the two-way iterative coupling and the one-way coupling indicated in Figure 6.1.

In two-way coupling, the reservoir simulation model communicates the pressure, saturation (and temperature) to the initialized geomechanical module. The geomechanical model sends permeability updates back to the hydrodynamic model. When the pressure (and temperature) perturbations from the reservoir simulation are small, there is a negligible effect on the permeability, and a one-way couple, in which there is no communication from the geomechanical model back to reservoir simulation, can be implemented. Both Coupling methodologies have been applied to the FWU.

6.3 Geologic Model

The SWP FWU geological model was first created and presented by Ampomah et al. (Ampomah et al., 2015). Various researchers have used this full-field model to conduct research in hydrogeology, reactive transport and risk assessments (Ahmmed et al., 2016; Ampomah et al., 2015; Dai et al., 2014; Pan et al., 2016). (Gallagher, 2014) work, examining cores, identified critical depositional and diagenetic controls on reservoir heterogeneity for the initial geologic model. The model has been updated periodically to incorporate additional well log and 3D seismic data interpretations (Hutton, 2015; Rose-Coss et al., 2015). Hutton, (2015) presented a description of faults in the study area that were interpreted from 3D seismic data analysis but have not been included in this current model.

6.4 Hydrodynamic Properties and Reservoir Simulation

Fifty-one wells with core porosity and permeability measurements defined eight distinct porosity/permeability relationships based on depositional/diagenetic facies described from core and thin section analysis. Recent experimental work (Rasmussen et al., 2019) has confirmed differing three- phase relative permeability relationships for respective HFU's and progressive wettability evolution triggered by exposure to CO_2.

Naturally, the HFU discretization have been incorporated into the hydrodynamic properties and affect the reservoir simulation outputs. The reservoir simulation model covers the Western FWU, which is gridded at 100 ft. x 100 ft. in the x and y directions and is rotated to -18^o to match the stress orientation of the FWU. The active cells for the Morrow B interval are 190 x 180 x 4**.**

Figure 2.3 shows a version of the simulated pore pressure and production history for the Morrow B formation. As discussed in chapter 2, the development of the Morrow B at FWU commenced with primary depletion in 1955. The field was unitized in 1964, at which time production methodology was switched progressively from west to east across the field from depletion to 5-spot waterflood patterns (McKay & Noah, 1996; Munson, 1989). The water flood extended from 1964 to December 2010, a period of 46 years. Water-flooding is followed by tertiary CO_2-EOR. CO_2 EOR began in 2010 with selected water injectors being converted to CO_2 WAG injectors, again successively moving from the western side of the field eastward. The calibrated reservoir simulation model is an integral component of hydromechanical coupling; however, only a cursory review is presented here as the primary focus is on constructing the geomechanical modeling.

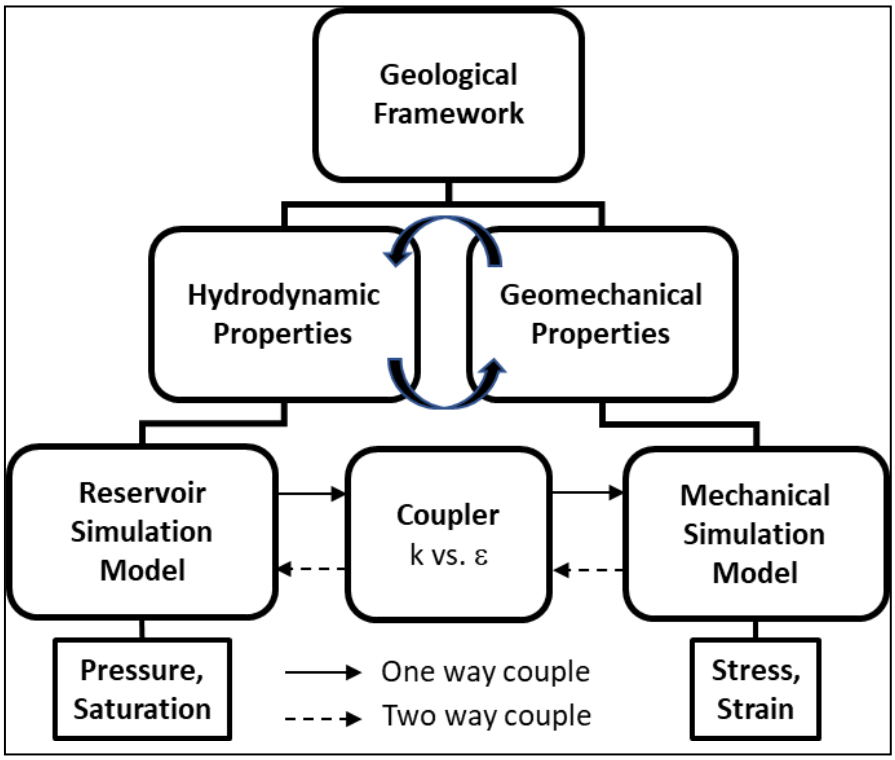

Figure 6.1: Block diagram of Mechanical Earth Modeling workflow applied at FWU

6.5 Geomechanical Model Construction

The geologic framework is similarly integrated into the geomechanical property population. The geomechanical property population extends from the surface to the underburden model and is a tartan style grid extending beyond the reservoir simulation grid and containing 204 x 194 x 87 cells in x, y and z-direction, respectively. Figure 6.2 shows the main zones and the sub-layers that comprise the geomechanical model. The mechanical properties population's primary "hard" data support is derived primarily from the 2014 1D MEM conducted on the 13-10A well (Figure 6.5). A one-dimensional Mechanical Earth Model (1D MEM) is a numerical representation of all geomechanical knowledge available for a field or basin along the analyzed well trajectory. The property population for the elastic parameters, including Young's modulus and Poisson ratio distributions (Figure 6.3), is achieved through integration with 3D seismic elastic inversion data acoustic impedance and subsequent co- simulation with porosity.

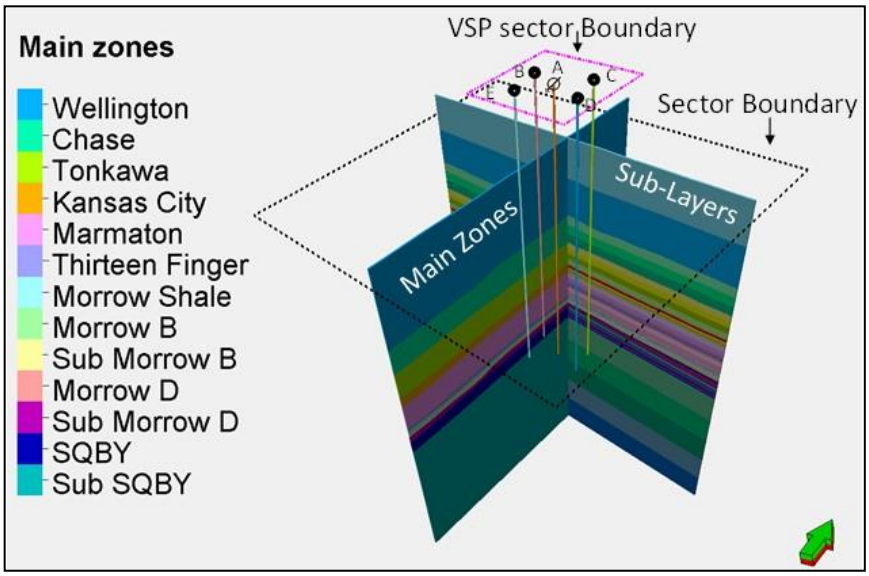

Figure 6.2: Constructed geological framework within the sector boundary. X and Y direction slices through the model showing main zones and sub-layers for each zone (left).

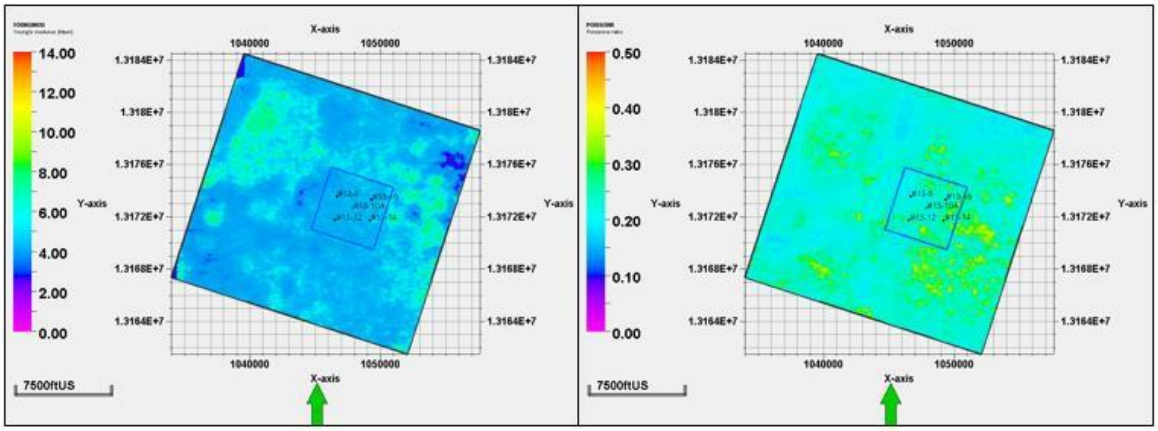

Figure 6.3: Seismic inversion derived estimate of Young Modulus in the Morrow B and (b) Distribution-adjusted and co-kriged Morrow B Young Modulus in the geomechanical grid.

(Herwanger, 2014) provide an exhaustive treatment of building geomechanical models using seismic data. Output univariate distributions were adjusted to match well data on a zone-by-zone basis accounting for the mechanical facies' distribution. Appropriate measures for the conversion from dynamic to static elastic moduli were undertaken. Dr. Robert Will supplied the geomechanical property distributions for the geomechanical modeling, which are summarized in (Ampomah et al., 2021). Figure 6.4 shows the reservoir simulation grid embedded with the geomechanical grid and displays the supporting segments: overburden, sideburden and underburden formations required to impose mechanical boundary conditions.

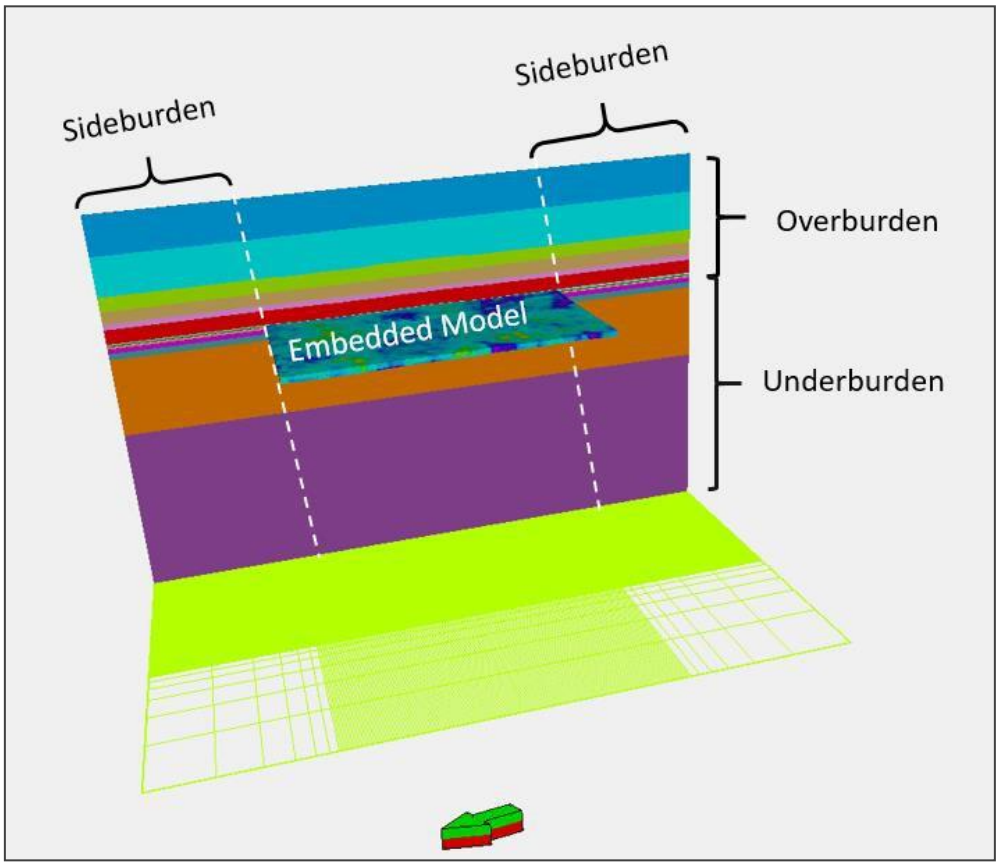

Figure 6.4: Visualization of Embedded Reservoir Simulation Grid within the Geomechanical Grid

Prior geomechanical simulation modeling work for the FWU had confirmed that the (McMillan et al., 2019a, 2019b) Morrow B formation, the primary target of this investigation is far from the line (Mohr- Coulomb Failure criteria is utilized). Consequently, our approach to the geomechanical modeling excludes the failure properties: Unconfined Compressive Strength; Friction Angle; Dilation Angle and Tensile Strength Cutoff. The resulting static MEM is the computational framework for transient computations using coupled fluid flow and mechanical solvers.

6.6 Coupling Procedures

One-way and two-way coupled simulations were performed using a compositional hydrodynamic flow model and geomechanical solvers. Stresses in the static MEM were initialized from wellbore stress estimates and reservoir simulation pore pressures. Coupled simulations were performed using history- matched primary and secondary (waterflood) recovery, tertiary (CO_2-WAG) recovery, and an optimized WAG prediction period. Simulation runs included two-way coupling for stress-dependent permeability updating using Kozeny-Carman. Essentially, Kozeny-Carman relates porosity to permeability and the application to two-way geomechanical coupling is based on the equivalence of changes in porosity to volumetric strain. Volumetric strain along with stresses are updated by geomechanical computations. In turn, changes in porosity then impact the fluid flow (reservoir simulation model)

$$K_O = \begin{bmatrix} K_x & \\ K_y & K_z \end{bmatrix} \tag{6.1}$$

$$\phi = (\phi_0 - \Delta\phi)/(1 - \Delta\phi) \tag{6.2}$$

$$\Delta\phi = \Delta\varepsilon_v \tag{6.3}$$

where K_O initial permeability, ϕ - current porosity, ϕ_O-initial porosity, $\Delta\phi$ - change in porosity, $\Delta\varepsilon v$ - change in volumetric strain from initialization.

Given the current porosity at each pressure update step as computed by Eq. 6.5, permeability was updated using the Kozeny-Carman relation:

$$k = \emptyset^3/cS^2 2(1 - \emptyset)^2 \tag{6.4}$$

where k = current permeability, c = constant, S = specific surface.

$$[K] = [K_O]\left(\frac{\frac{\phi^3}{(1-\phi)^2}}{\frac{{\phi_O}^3}{(1-\phi_O)^2}}\right) \tag{6.5a}$$

$$K_{KC} = \left(\frac{1}{f_g \tau S_{vgr}^2}\right)\left(\frac{\phi^3}{(1-\phi)^2}\right) \tag{6.5b}$$

Where k_{KC} is the Kozeny-Carman permeability in μm^2, f_g is the shape factor, τ is the tortuosity, S_v specific surface area of the grains in μm^{-1}. Note that equation 5.5a and 5.5b both represent the Kozeny- carman relationship.

The Morrow B does not have the required volumetric strain- permeability relationships and as a result, the default within Petrel have been utilized.

6.7 Stress Initialization

6.7.1 Horizontal Stress Magnitude and Orientation.

The technical memorandum (Bratton, 2021) summarizing the 1D-MEM data (Swager, 2017b) provided measured wellbore data of pressure, stress magnitudes and stress orientations estimates. This dataset was also used in the evaluation of failure states along the 13-10A wellbore. Two types of analytical models exist: Linear elasticity utilized Hooke's law and remain valid until the yield point where various failure models ought to be applied. The Mohr-Coulomb failure model is applied. Despite vastly varying assumptions both models result in similar vertical stress profile (Bratton et al., 2018; Thiercelin & Plumb, 1994). Considering these similarities in vertical stress profile, a simplified analytical approach is adopted. The stress magnitudes are modeled after based on their estimated mechanical behavior (Bratton, 2021). The findings are that the Thirteen Finger is categorized as critically stressed, the overlying and underlying Morrow shales as elastic and Morrow B formation as elasto-plastic. In formations categorized as elastic, the Poro-elastic Horizontal Strain model is applied. The Mohr- Coulomb failure model is applied to critically stressed zones and elastoplastic regions, and the average of the two models is used. The poroelastic horizontal strain model computes the minimum and maximum horizontal stresses (equations 6.6, 6.7) and considers anisotropic tectonic stress by applying a pair of constant strains, εx and εy, to the formation in the directions of minimum and maximum stress, respectively.

The Poro-elastic Horizontal Strain model is:

$$\sigma_h = \frac{\nu}{(1-\nu)}\sigma_v - \frac{\nu}{(1-\nu)}\alpha P_P + \frac{E}{(1-\nu^2)}E_x + \frac{Ev}{(1-\nu^2)}\varepsilon_y \tag{6.6}$$

$$\sigma_H = \frac{\nu}{(1-\nu)}\sigma_v - \frac{\nu}{(1-\nu)}\alpha P_P + \frac{Ev}{(1-\nu^2)}\varepsilon_x + \frac{E}{(1-\nu^2)}\varepsilon_y \tag{6.7}$$

where ν - Poisson ratio
σ_h - Minimum horizontal stress
σ_H - Maximum horizontal stress
σ_x - Strain in the direction of minimum horizontal stress
σy - Strain in the direction of maximum horizontal stress
Pp - Pore pressure

Mohr-Coulomb failure model applied in critically stressed zones is computed as,

$$\sigma_h = \frac{\sigma_v + (N+1)P_P}{N} \tag{6.8}$$

$$N = \frac{1+sin(\varphi)}{1-sin(\varphi)} \tag{6.9}$$

where,
σ_h - Minimum Horizontal Stress
σ_v - Overburden Stress
φ - Friction Angle
N - Confinement multiplier, which is a function of the friction angle.

The elastoplastic diagnosis of the Morrow B was not initially ascertained, and as such, the geomechanical models were run without yield criteria. Potentially impactful differences in

geomechanical modeling, such as vertical pressure profile utilized, impact the computed stresses. More importantly, the overlying and underlying Morrow Shale caprock and base-seal are adjudged to be an elastic stress state and as such, failure and potential leakage are not predicted. Nonetheless, computed principal stress profiles were utilized in the stress initialization of the geomechanical model.

6.7.2 Geomechanical Stress Boundary Condition

The computed minimum and maximum horizontal stresses are utilized for the stress initialization boundary conditions. Relationships for minimum and maximum horizontal stresses are developed as a function of depth.

$$S_{hmin} = 0.53\text{Depth} - 503.132 \tag{6.10}$$

$$S_{hmax} = 0.59\text{Depth} - 102.325 \tag{6.11}$$

Oil-Based MicroImager (OBMI) and Ultrasonic Borehole Imager (UBI) logs indicated that the minimum horizontal stress direction was 115-120 degrees. Thus, the finalized stress initialization incorporates a minimum horizontal stress azimuth of 20 degrees. Pore Pressures measured in the Morrow B had significant variation (from 4500-5400 psi) due to the cyclic water–alternating-gas production methodology. The pore pressure utilized in the building of the MEM was equivalent to 10.8 ppg and was measured in December 2014. Figure 6.5 shows the Geomechanical Stress Initialization. Naturally, the objective of the stress initialization is to create a model that replicates the stress and elastic parameter trajectories.

6.7.3 Stress State Diagram

As a verification of the stress initialization, the Stress State Diagram concept combines Coulomb Frictional Failure (Jaeger et al., 1979) criteria with Andersonian fault mechanics (Anderson, 1905) for specific depth and pore pressure. The coefficient of static friction is assumed to be 0.63 (Byerlee, 1978). The overburden stress is determined by integrating the density log and the extrapolation at shallow depths where the density log does not exist. Relationships representing the various faulting regimes are presented below.

Normal Faulting Regime:

$$\frac{\sigma_1}{\sigma_3} = \frac{S_v - P_P}{S_{hmin} - P_P} \leq \left[(\mu^2 + 1)^{\frac{1}{2}} + \mu\right]^2 \tag{6.12}$$

Strike-Slip Faulting Regime:

$$\frac{\sigma_1}{\sigma_3} = \frac{S_{Hmax} - P_P}{S_{hmin} - P_P} \leq \left[(\mu^2 + 1)^{\frac{1}{2}} + \mu\right]^2 \tag{6.13}$$

Reverse Faulting Regime:

$$\frac{\sigma_1}{\sigma_3} = \frac{S_{Hmax} - P_P}{S_v - P_P} \leq \left[(\mu^2 + 1)^{\frac{1}{2}} + \mu\right]^2 \tag{6.13}$$

ThThe stress state diagram is further constrained by combining knowledge of any wellbore failure, specifically shear-induced borehole breakout and drilling induced tensile fractures (Zoback et al., 1985; Zoback et al., 2003). Relevant equations are:

Drilling Induced Tensile Fracture:

$$S_{Hmax} = 3S_{hmin} - 2Pp - \Delta P - T_o - \sigma^{\Delta T} \tag{6.15}$$

Borehole Break Outs:

$$S_{Hmax} = \frac{\left(C_{eff} + 2P_P + \Delta P + \sigma^{\Delta T}\right) - S_{hmin}(1 + 2cos2\emptyset_b)}{1 - 2cos2\emptyset_b} \tag{6.16}$$

$$2\emptyset_b = \pi - w_{bo} \tag{6.17}$$

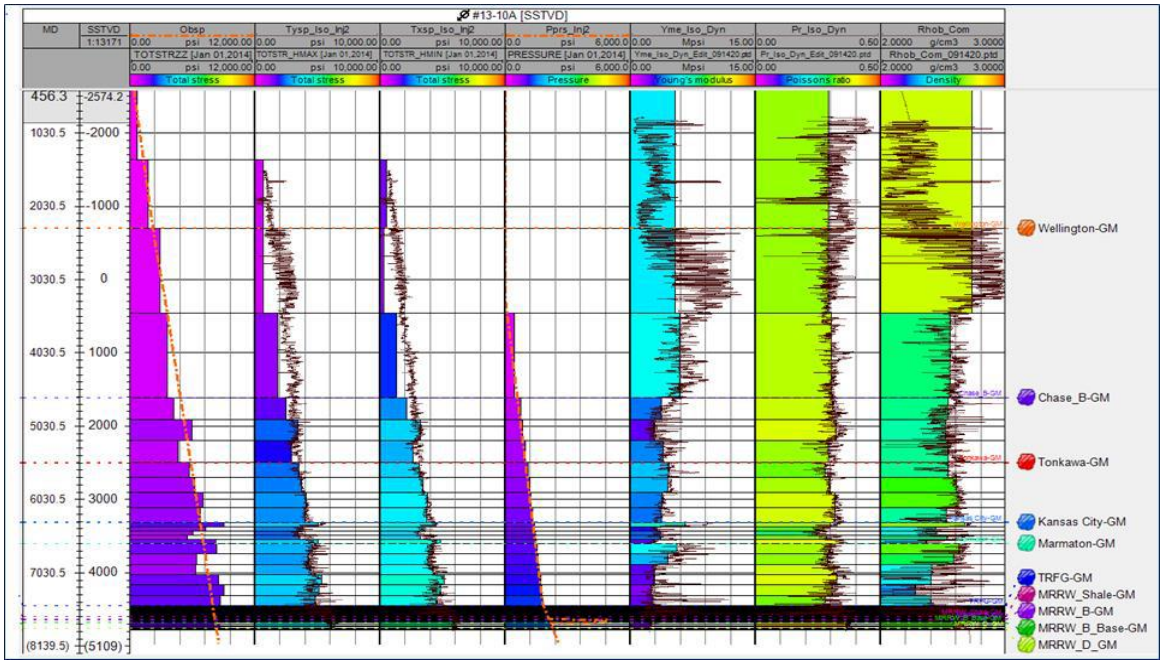

Figure 6.5 shows the computed Stress State Diagram indicating that Morrow B formation falls within the Normal Faulting region as indicated by the yellow diamond.

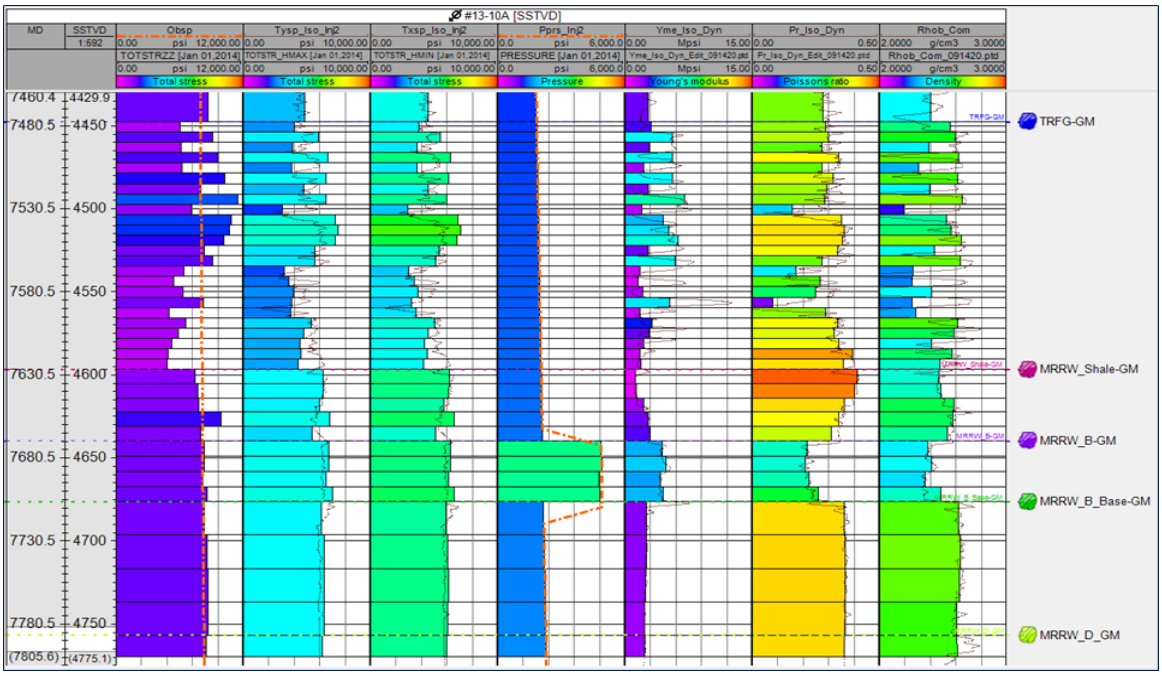

Figure 6.6: a) Full Wellbore Stress Initialization and b) zoomed-in assessment of Thirteen Finger to Morrow D. Both diagrams show a good comparison between modeled stress initialization (multi- colored solid bars) and the 1D MEM parameters (multi-colored lines) that inform the geomechanical modeling

.

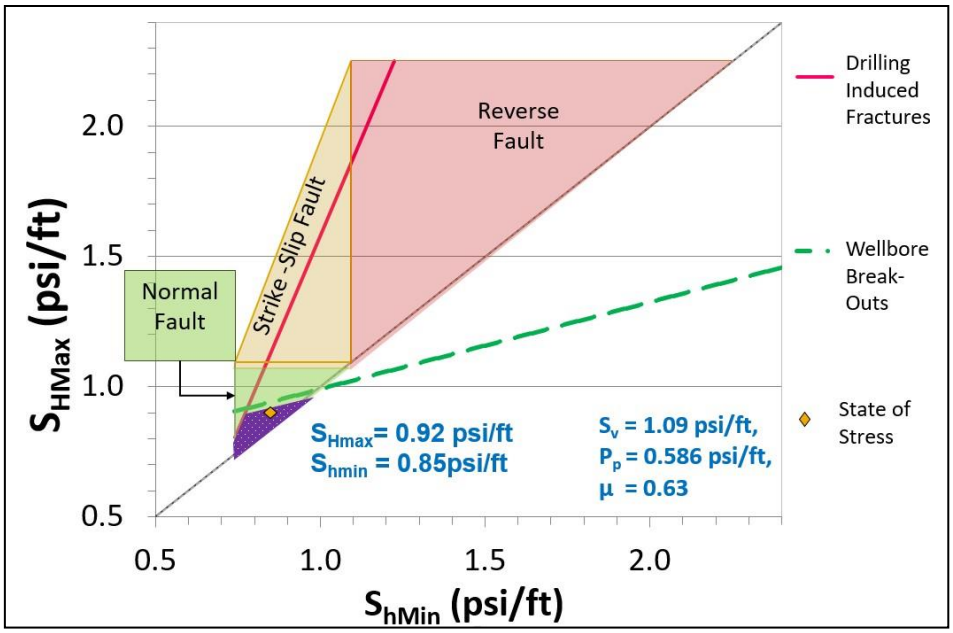

Figure 6.7: Stress State Diagram illustrates all possible stress states for depth and pore pressure. Allowable stress states are further constrained by Drilling Induced Tensile Fractures and Borehole breakouts leaving only the purple hashed area. Geomechanical model is initialized (red diamond) at overburden gradient of 1.093 psi/ft, Shmin = 0.85 psi/ft, ShMax = 0.92 psi/ft and a pore pressure gradient of 0.586 psi/ft, which falls in the normal faulting region.

6.7.4 Mohr-Coulomb Stress State Evaluation

Assessing the stress states predicted from dynamic hydromechanical evaluations can be achieved using the Mohr Circle analysis. Mohr circles are a two-dimensional semi-circular graphical representation of a stress transformation. The stress transformation is given by equations 6.18 and 6.19, first presented by Otto –Mohr in 1882.

$$\tau = 0.5(\sigma_1 - \sigma_3) \sin 2\theta \quad (6.18)$$

$$\sigma_n = 0.5(\sigma_1 + \sigma_3) + 0.5(\sigma_1 - \sigma_3)\cos 2\theta \quad (6.19)$$

Mohr circles indicate the stress state. The intersections of the semi-circle with the abscissa are the minimum and maximum stresses. Differences in minimum and maximum stress can be interpreted from the semi-circular diameter, and trends in Mohr-Circles changes illustrate operation-induced stress effects.

Typically, the Mohr Circles analysis is accompanied by failure criteria: the linearized Mohr-Coulomb failure criteria indicating shear failure, tensile failure either at tensile strength cut-off or when the minimum effective stress touches the shear stress axis. The yield criteria are not considered in further analysis as prior work indicates that the prevailing stress states are far from failure.

6.8 Dynamic Modeling

6.8.1 Permeability updates

The constructed static 3D MEM, when coupled with the calibrated reservoir simulation, allows for interpreting the impacts of two-way coupling, the effects of varying the coupling intervals and the characterization of Morrow B mechanical responses. Figure 3.3 shows a version of the calibrated reservoir simulation model utilized in this coupling workflow. One-way and two-way coupled simulations were performed. In two-way coupling, permeability was periodically updated as a function of volumetric strain using the Kozeny-Carmen porosity-permeability relationship. Our coupling analysis emphasizes the assessment of the impact of stress-dependent permeabilities on reservoir simulation-based production forecasting. Field pressure and cumulative oil production were analyzed using various pressure coupling and stress-dependent permeability update intervals for the primary and WAG recovery periods. At present, the required relationship linking permeability changes with strain are unavailable for the Morrow B. As such two-way coupling is approximated with Kozeny-Carman relationship. Figure 5.7 shows three porosity –permeability combinations and indicates very small permeability changes. (Only positive strains are shown). Figures 5.8 and 5.9 show the results of selected simulations illustrating some of the critical characteristic behaviors.

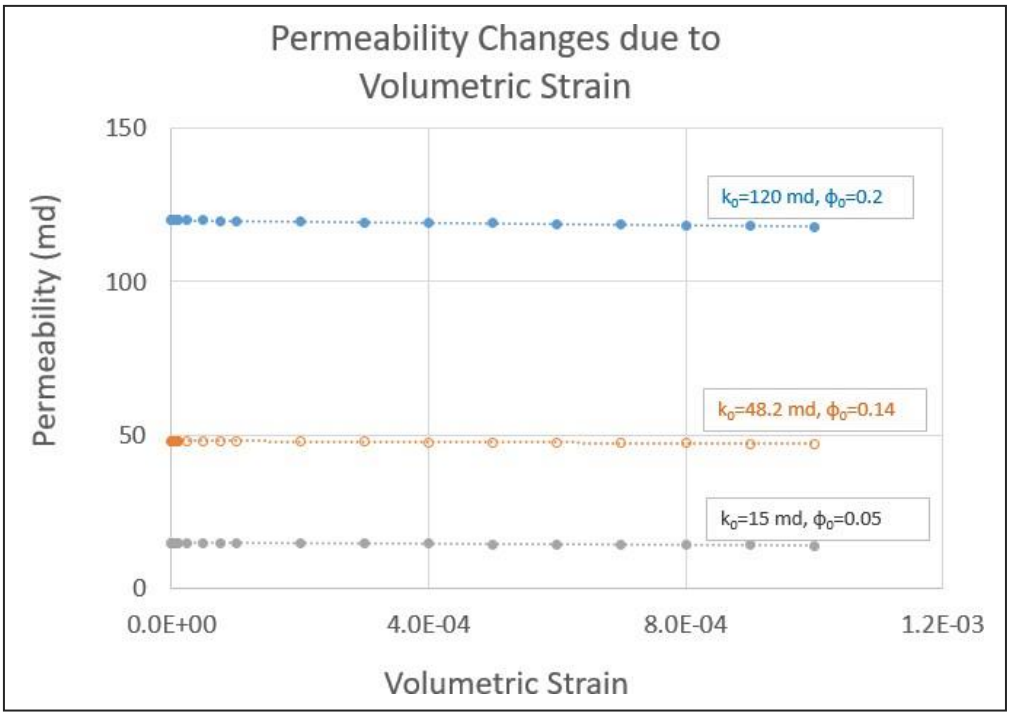

Figure 6.8: Permeability Changes due to Volumetric Strain, Computed Using Kozeny-Carman Relationship for three different Porosity -Permeability Combinations.

Figure 6.8 shows field pressure and cumulative oil production for the primary and waterflood recovery periods. Results are shown for ten years, five years, 1-year updates, and no permeability updating, essentially one-way coupling. Vast differences are seen in reservoir pressure and cumulative production behavior (dashed lines) between no updating and 1-year updating

simulation results, suggesting that uncoupled reservoir simulations without permeability updating may significantly underestimate potential recovery for this scenario. This result is likely due to a combination of the long recovery period (~55 years) and significant pore pressure increase (~3200 psi), which would significantly reduce volumetric strain, thus increasing the porosity and permeability computed with the computed pore pressure Eq. 6.5.

Figure 6.9 shows field pressure and cumulative oil production for the CO_2 WAG recovery period. Results are shown for one-year and three-month updates, and no permeability updating. Only minor differences are observed. In contrast to the primary and waterflood period, the WAG period sees a much smaller pressure change.

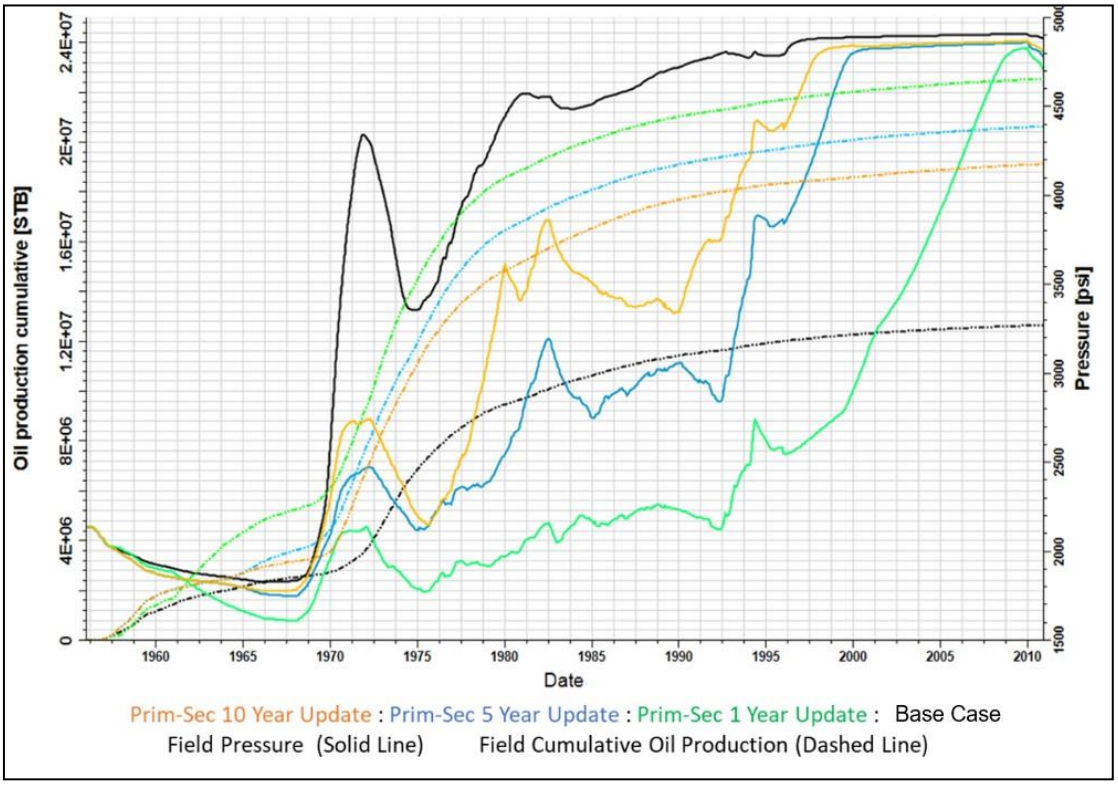

Figure 6.9: Comparison of field pressure (solid line) and cumulative oil production (dashed line) during the primary and waterflood recovery period for no-permeability update (black), one year permeability update (green), five-year permeability update (blue), and ten year permeability update (orange).

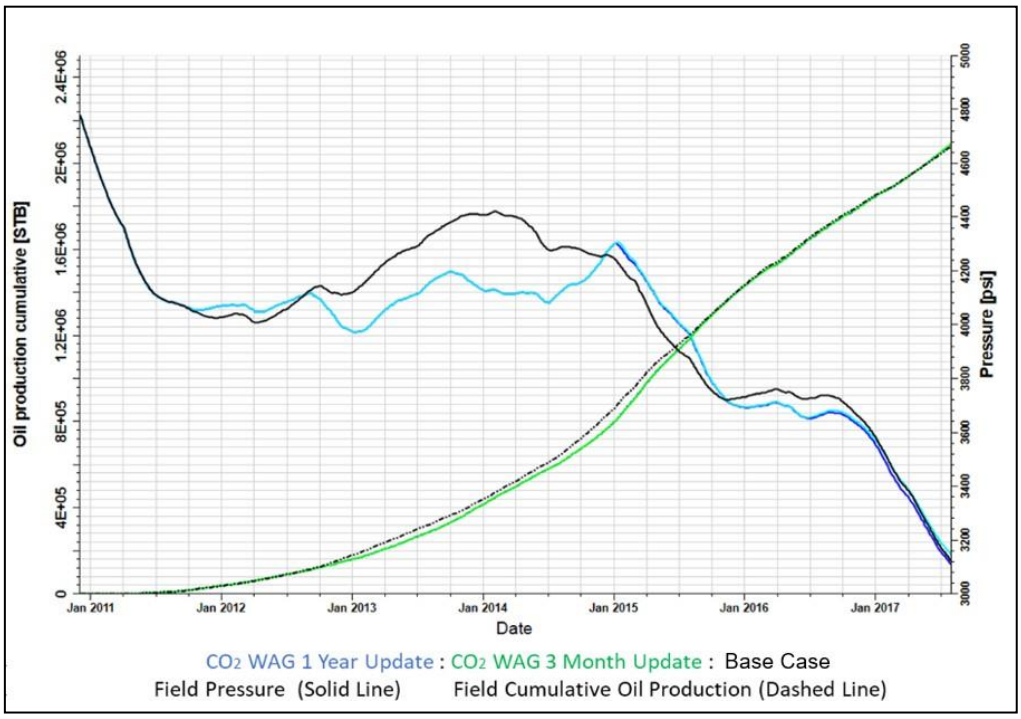

Figure 6.10: Comparison of field pressure (solid line) and cumulative oil production during the CO_2-WAG period for no-permeability update (black), three-month permeability update (green), and one-year permeability update (blue).

6.8.2 Coupled Primary & Secondary Production Stress Changes.

Geomechanical evaluations of coupled simulation model response is also evaluated using the Mohr Circle analysis. The coupled simulations covered the primary and secondary recovery periods and the permeability updates are performed at approximately 5 year intervals. Primary depletion started in 1955, continuing until 1964, after which a water-flood was implemented until 2010. The stress changes were evaluated using the Mohr Circles concept presented in section 4.4.4. Figure 6.10 illustrates the stress changes tracked at the center of the Western Morrow B (cell 102, 97, 51).

Figure 6.10a shows the stress changes during primary recovery. The large black Mohr circle represents the initial time step (1/1/1956). By 1960, the effective stresses increased (pore pressure decrease), and the grey dashed semi-circle illustrates the stress state. Figure 6.10a also shows a solid green Mohr circle representing the stress state in 1965. Nineteen sixty-five is one year after the phased introduction of waterflooding. By 1965 the injected water began to increase the pore pressure, decreasing the effective stress.

Also apparent in Figure 6.10a is the increasing size of the Mohr circle as it moves to the right. The maximum principal stress increases by more than the minimum principal stress, suggesting that pore pressure reduction is not impacting the principal stresses equally. (Streit et al., 2004) and (Hawkes et al., 2004) report that changes in minimum horizontal stress are approximately 50% of pore pressure change. (Streit et al., 2004) arrived at this number by examining databases, while (Hawkes et al., 2004) present an equation for an idealized thin, laterally extensive reservoir, and the

relationship is dependent on Poisson ratio and Biot coefficient. From 1955 to 1964, the reservoir pressure declined from 2150 psi to 1850 psi. Considering Figure 6.10a, the impact of the pressure decline has comparatively less effect on the minimum horizontal stress than the maximum horizontal stress. The result is enlarging the Mohr Circle during primary production (Lynch et al., 2013) instead of the simple translation of the Mohr Circle along the abscissa and may indicate pore pressure-stress coupling.

Figure 6.10b illustrates selected time steps for the water-flood period and shows decreasing effective stresses due to increased pore pressure. At the start of the WAG, the reservoir pressure is estimated at 4900 psi. As injection continues, the anticipated response of decreasing effective stresses is observed. However, between the start of field life in 1955 to 1985, there is relatively little change in the minimum principal stress. However, small changes in minimum effective stress are accompanied by larger changes in the maximum principal stresses. From 1985 to 1995 and 1995 to 2005, there was a marked decline in the minimum and maximum principal stresses.

6.8.3 CO_2-WAG Stress Changes, (December 2010 to July 2017)

Effective stress changes during the WAG period are tracked at an injector. Injection increases pore pressure, thereby reducing effective stresses. Further, the stress perturbations at injectors will induce the most significant stress changes. Injector 8-3 (cell, 60, 84, 50) has injected 3 Bscf of CO_2 and 360 Mstb of water between 2010 and July 2017. This cell has been chosen for tracking CO_2-WAG-induced stress changes in the Morrow B. Figure 6.11 shows Mohr Circles for selected time steps during the WAG production period. The black dashed line for 12/1/2010 is the start of WAG, which coincides with the end of water-flood and the point of peak field pore pressure. This high field pressure is concomitant with low effective stress and the relatively small Mohr circle in December 2010. Subsequent changes in stress state all indicate a lower pore pressure experienced at the end of the waterflood.

(a)

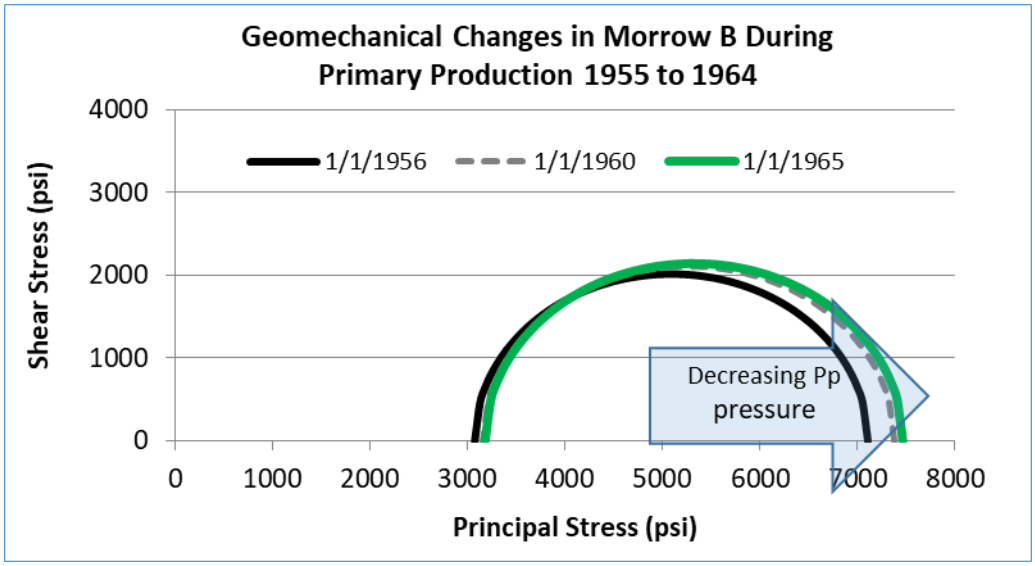

(b)

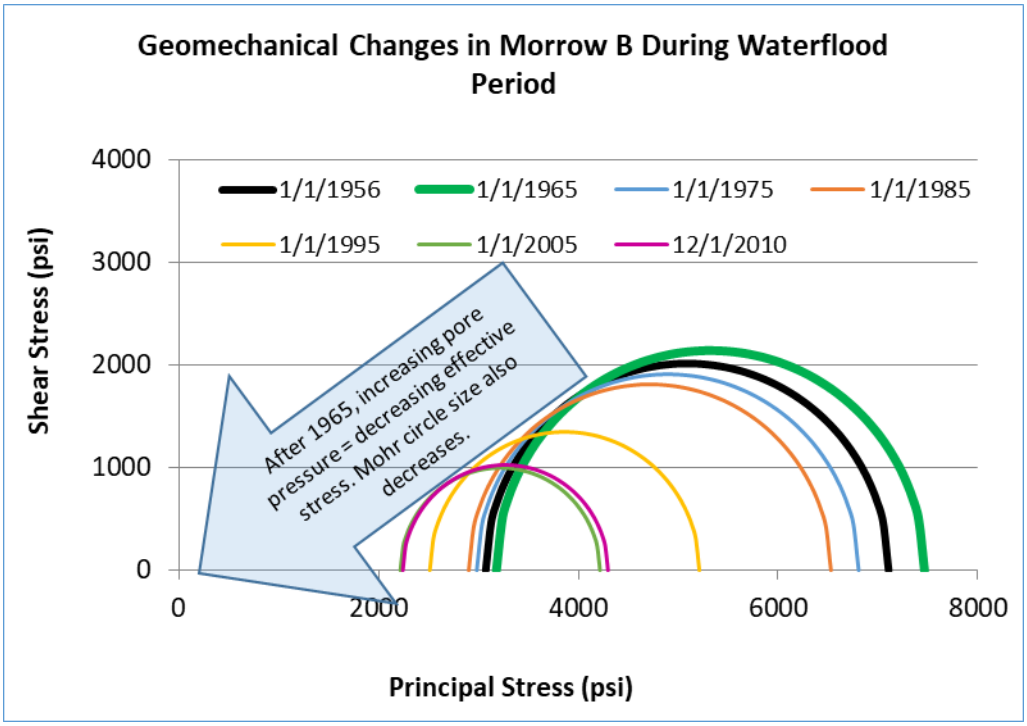

Figure 6.11: Figure 6.10: a) Stress changes during primary production indicate increased pore pressure and a slight increase in Mohr circle size. Figure 6.10b) illustrates the stress effects during the secondary recovery- waterflood period: effective stresses and Mohr circle size decrease due to the increasing pore pressure

(c)

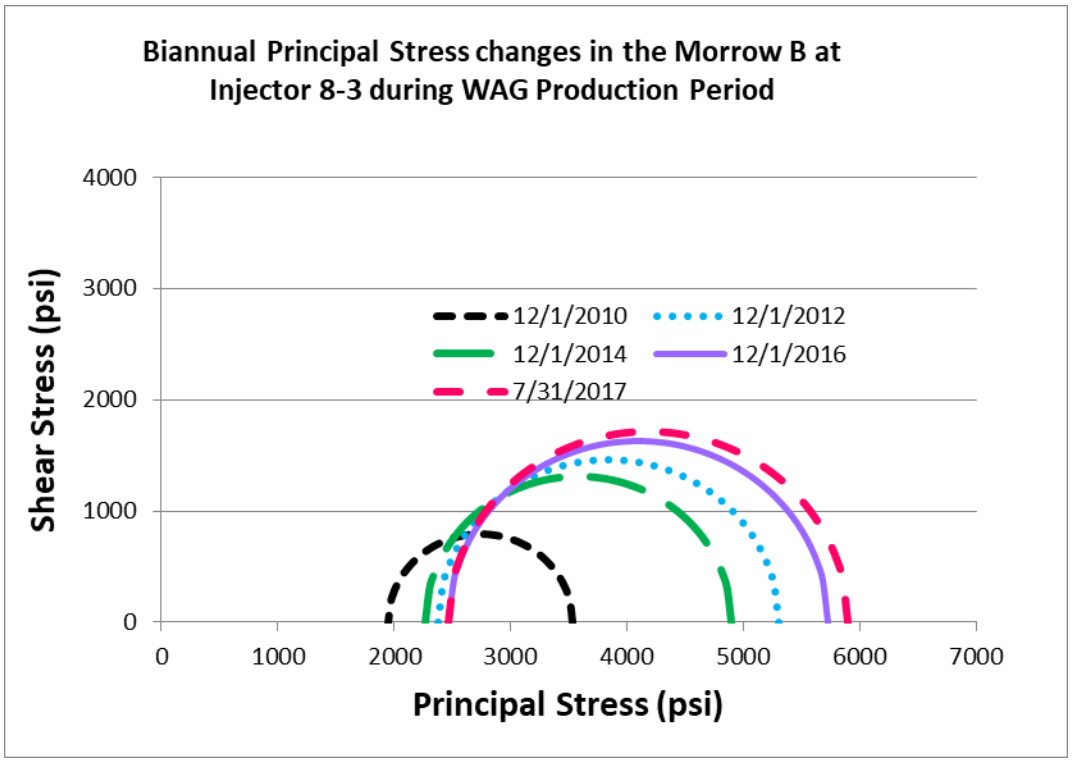

Figure 6.12: Mohr Circles shows stress changes in the Morrow B throughout the WAG cycles

Chapter 7
Vertical Seismic Profile Stress Calibration

7.1 Introduction

This study calibrates hydrodynamic-geomechanical input parameters by formulating an objective function between modeled and observed time-lapse seismic velocities. The method adopted is identical to industry-accepted approaches for the calibration of reservoir simulation models in that inverse methods are applied to converge on the optimized parameter set which most closely matches the observed datasets.

This study is conducted in the active CO_2-EOR operations at FWU. Inherently the time-lapse VSP carries the combined effects of fluid substitution and mean effective stress changes. The impacts on seismic velocity due to fluid substitution are driven by the elastic moduli (K_{smean}, μ_{smean}) at zero porosity which are derived from the site-specific rock physics relationship. Lumley (Lumley, 2001) states that for high porosity, unconsolidated, brine saturated sandstones, time-lapse measurements are extremely reliable but become less so in reservoirs with dead oil, such as the FWU. The VSP integration workflow and calibration are dependent on both fluid substitution and mean effective stress changes.

Relationships between seismic velocity change and stress change introduce even greater ambiguity. This work uses ultrasonic seismic velocity measurements on the core as the starting point for the seismic velocity-stress derivatives. (Nes et al., 2002) has presented reasons why core measured ultrasonic seismic velocities overestimate in situ velocity-stress derivatives. In actuality, in situ VSP measurements capture a saturated reservoir condition measured at frequencies of several orders of magnitudes lower than the ultrasonic seismic velocity measurement. It is also recognized that pore pressures impact seismic velocity. The standard industry practice of measuring the dry core mitigates the frequency-related velocity dispersion, and the fluid and pressure effects are added numerically. Several researchers have studied these ultrasonic tests and provide insights into seismic velocity dependence on confining stress (Amini & MacBeth, 2015; Eberhart-Phillips et al., 1989; Freund, 1992; Khaksar et al., 1999). In this study, the uncertain nature of velocity-stress derivatives is investigated using both stochastic and deterministic methods. The design of experiment is meant to explore the geomechanical solution space fully. Independent and impactful fluid substitution parameters, shear modulus at zero porosity, μ_{smean}, and bulk modulus at zero porosity, K_{smean} are perturbed and generate differing saturated bulk and shear moduli distributions.

Applying the linear elastic assumption to the saturated bulk and shear moduli distributions leads directly to the Young's Modulus and Poisson ratio distributions, necessary for geomechanical modeling. Time- lapse seismic velocities due to stress are generated by the shear and compressional seismic velocities- stress derivatives and the geomechanical outputs. The linear summation of time-lapse seismic velocity due to stress and fluid substitution form the modeled seismic velocity.

The objective function is formulated between the modeled and observed seismic velocity datasets to create models. Mapping the input parameters to the objective function using Linear and Second Order and Artificial Neural Networks (ANN) relationships is pursued. The ANN generated the smallest mean square error (MSE). The optimization is achieved using a Machine Learning Assisted Workflow comprised of ann and Particle Swarm Optimizer. We successfully

implemented and perturbed the variables of the VSP integration workflow. The optimal geomechanical parameters for the FWU VSP integration study are shear modulus at zero porosity, μ_{smean} of 3.0 Mpsi, bulk modulus at zero porosity K_{smean} of 3.0 Mpsi, dVp/dσ of 56.48 m/s per 1000 psi change in mean effective stress (185 m/s per 1000 psi change in mean effective stress), and dVs/dσ of 31.26 m/s per 1000 psi change in mean effective stress (102.5 m/s per 1000 psi change in mean effective stress).

7.2 Results and Discussion

7.2.1 Calibrated Reservoir Simulation Model

The VSP integration workflow assumes a single calibrated reservoir simulation model, and as such, only one set of pore pressure distributions are utilized. The calibrated reservoir model does not simulate the impact on the overlying and underlying formations but concentrates only on the Morrow B. A sector model covering the study area (Figure 7.2) is utilized for the VSP Integration study. The sector is a square of 5000 ft. centered on the 13-10 A well. The objective function is computed within only a 1000 ft. radius of the 13-10A well, where the validity of the VSP dataset is highest.

The forward modeling workflow begins with the compositional reservoir simulation. The time-lapse VSP study spans January 2014 to December 2017. The relevant segment of the production history match is captured in Figure 7.1. The production methodology implemented during this period is the CO_2-WAG process. The operation seeks to enhance oil recovery by swelling the in-situ oil and mobilizing production while simultaneously storing injected CO_2. Alternating water and CO_2 injection at predetermined intervals provide pressure maintenance. These production and injection patterns cause the mixing of pore fluids, changing saturation conditions with time, and inherently impact the measured time-lapse shear and compressional seismic velocities.

The sector model is built from the calibrated full-field simulation model by applying a constant flux boundary to the 5000 ft. square around the 13-10A. One of the advantages of applying Petrel's sector modelling is the ability to improve the calibrated simulation model within the boundary of a sector without affecting the remainder of the simulation model. This method can be applied in a region with a poor production and fluid influx mismatches, achieving reduced computation time due updating only within a reduced region. Essentially, the sector model updates the influxes within the prescribed (sector region) and combines the sector results with the full-field result making the sector model and full field model comparable.

Figure 7.1 compares the sector models' pressure and production history with the calibrated full field model and observed historical production, showing impeccable matches for oil production rate and cumulative oil production. The simulated average pressure for the sector model is shown as a solid blue line and is slightly higher than that for the full-field shown as a dashed purple line. Figure 7.1 also demarcates the baseline and monitor measurements where the fluid saturation and total compressibility are extracted to compute seismic velocities attributed to fluid substitution.

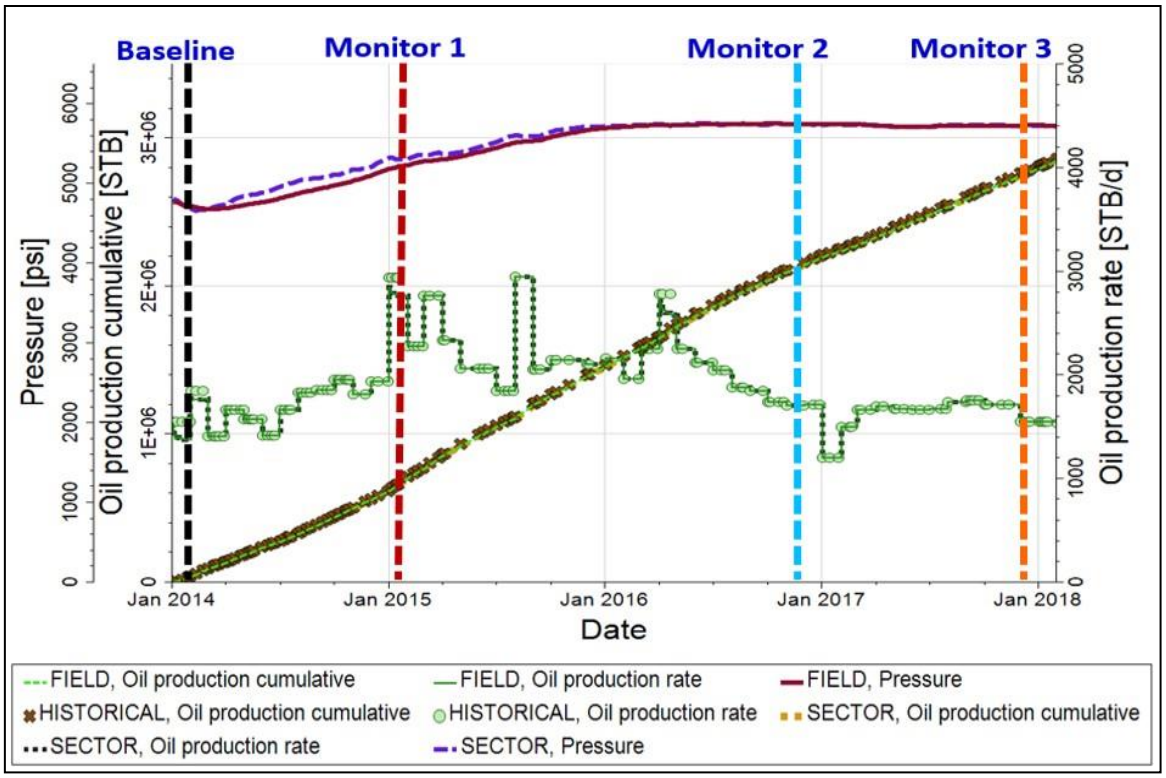

Figure 7.1: Calibrated reservoir simulation covering the time-lapse VSP study period

7.2.2 Modeled Time-Lapse Seismic Velocity due to Stress

Numerous geomechanical models, each with varying property populations, are generated for geomechanical optimization. The approach uses the linear elastic assumption and generates Young's Modulus (E) and Poisson ratio (ν) distribution from the Bulk Modulus (K_{sat}) and Shear Modulus (μ_{sat}). The modeling approach uses a geomechanical sector model covering the same 5000 ft. square centered on the 13-10A well shown in Figure 7.2. The geomechanical sector imposes a boundary condition constructed from the full-field geomechanical model. The objective function is formulated within the 1000 ft. radius of the 13-10A well. Variations of property distributions computed using the linear elastic assumption are applied to the sector models. Figure 7.2 shows identical matches for total vertical stresses, maximum horizontal stresses, and minimum horizontal stresses for the base case full-field and the geomechanical sector models. The strong agreement validates the sector model approach.

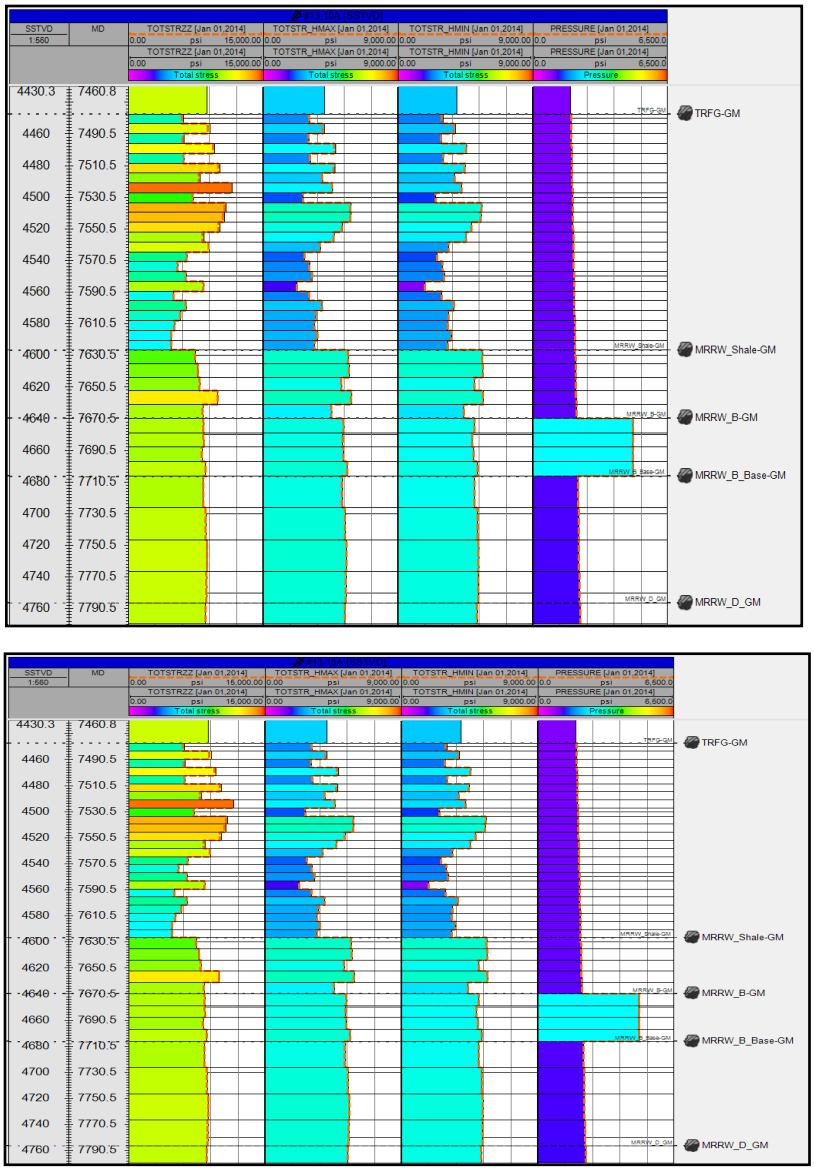

Figure 7.2: Identical Stress Distribution for Full Field (solid colored bars) and the sector model (dashed orange outline)

7.2.3 Comparison of Base Case and Observed Dataset

The base case utilizes μ_{smean} and K_{smean} elastic parameter values similar to that of the original Stochastic Gaussian Simulation (SGS) property population along with the seismic velocity-stress derivatives measured on the core. Base case parameters are captured in Table 7.1.

Table 7.10: Base Case Properties for Sensitivity Analysis.

	Shear Modulus at Zero Porosity (Mpsi)	Bulk Modulus at Zero Porosity (Mpsi)	Derivative of Compressional Seismic Velocity to Mean Effective Stress (m/s per 1000 psi Eff. Stress change)	Derivative of Shear Seismic Velocity to Mean Effective Stress (m/s per 1000 psi Eff. Stress change)
Base	2.55	3.225	152	70

Comparison of the observed dataset with the base-case modeled seismic velocity outputs establish the need for optimization. Figures 7.4 and 7.5 compare the time-lapse modeled shear and compressional seismic velocities versus the observed for a 1000 ft. radius around the 13-10A well as this is considered the limits of the accurate observed seismic velocity. Figures 7.4 and 7.5 show significant differences indicating a need to optimize the input parameters for the modeled seismic velocities in a bid to more closely compare with the observed. Figure 7.4 indicates the mean square error for the time-lapse compressional seismic velocities are 767 $\left(\frac{m}{s}\right)^2$, 2293 $\left(\frac{m}{s}\right)^2$ and 2164 $\left(\frac{m}{s}\right)^2$ at the monitors 1, 2 and 3 respectively. The differences are so large that differing scales are utilized to illustrate the areal patterns. The error margins for the time-lapse shear seismic velocity are smaller at 91 $\left(\frac{m}{s}\right)^2$, 209 $\left(\frac{m}{s}\right)^2$ and 155 $\left(\frac{m}{s}\right)^2$ at monitor 1, 2 and 3 respectively but also require improvement.

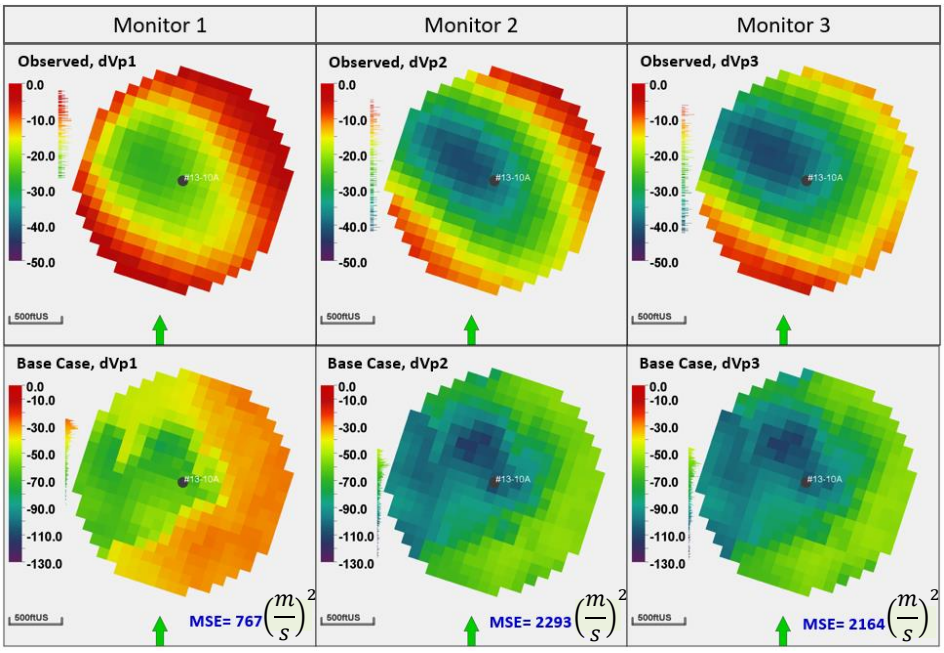

Figure 7.3: Time-Lapse Compressional Seismic Velocities, Large Mean Square Differences between Observed (top) and Modeled (bottom) indicate the need for Optimization. Monitor 1, 2 and 3 are shown.

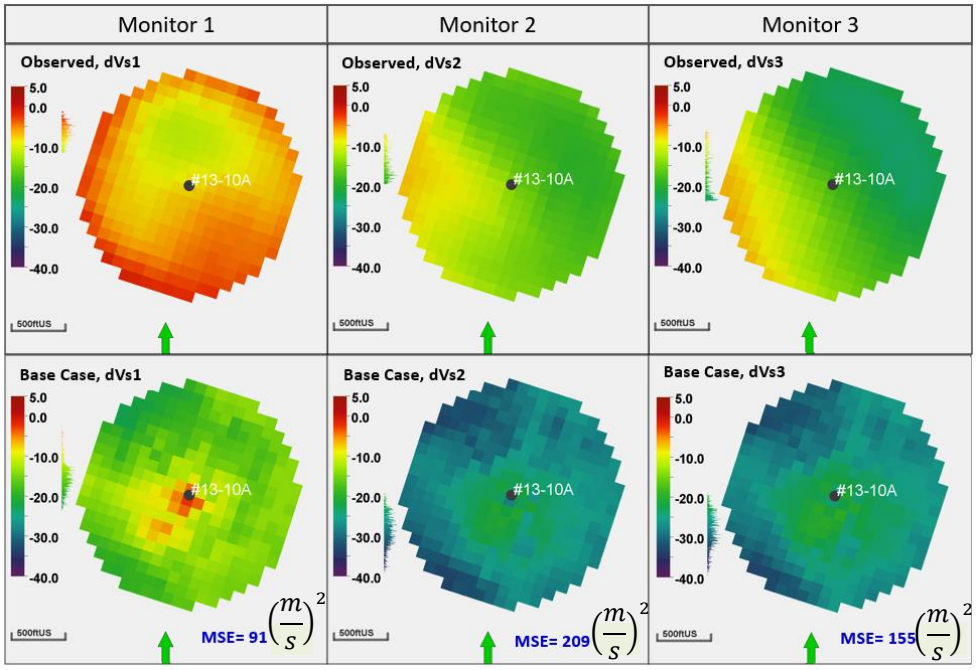

Figure 7.4: Time-Lapse Shear Seismic Velocities, Large Mean Square Differences between Observed (top) and Modeled (bottom) indicate the need for Optimization. Monitor 1, 2 and 3 are shown.

7.2.4 Geomechanical Optimization: Deterministic Analysis: Sensitivity Analysis

Optimization begins with a sensitivity analysis which considers one-at-a-time property modifications within the property ranges while all other parameters remain unchanged. Note however, that for the seismic velocity-stress derivatives, the smallest error (objective function) occurs at the intermediate parameter value which most closely matches the seismic velocity due to stress. Table 7.2 shows the maximum and minimum objective functions for each of the four independent parameters along with the parameter level.

Table 7.11: Tabulated Parameter Objective Function Extremes for Sensitivity Analysis.

	Parameter Values		Sensitivity Case Objective Function minus Base Case Objective Function	
	Value at Low	Value High	Low	High
Shear Modulus at Zero Porosity (Mpsi)	3.00	2.40	-1537	665
Bulk Modulus at Zero Porosity (Mpsi)	3.00	3.90	-27.52	156.1
Derivative of Shear Seismic Velocity to Mean Effective Stress (m/s per 1000 psi Δ in mean effective stress)	52	80.00	-301	287.2
Derivative of Compressional Seismic Velocity to Mean Effective Stress (m/s per 1000 psi Δ in mean effective stress)	61	152.0	-4763	2300

Figure 7.5 shows that the most impactful parameter on the total objective function is the derivative of the compressional seismic velocity - mean effective stress.Surprisingly, the least impactful is the K_{smean}. K_{smean} is the bulk modulus at zero porosity and is the independent parameter used to update the saturated bulk modulus. One would expect significant changes due to K_{smean} as the injected fluids change the fluid distribution, impact the bulk modulus of the fluid and therefore modeled compressional seismic velocity.

The modelling of this CO_2-EOR operation, with high injection pressures places the injected CO_2 in the supercritical region. Injected CO_2 had a density similar to that of oil and also has relatively small impacts on the total fluid compressibility. This result is also surprising because the range of the K_{smean} (3.0 - 3.9 Mpsi) is larger than that of the μ_{smean} (2.4 - 3.0 Mpsi). μ_{smean} is used to generate the shear modulus distribution but remains unchanged by fluid substitution. Shear modulus is the resistance to changes in shape due to applied shear stresses. The impact of the μ_{smean} parameter is driven by its' inclusion in both the shear seismic velocity and compressional seismic velocity relationships and is the second most impactful parameter. The derivatives of shear and compressional seismic velocity - mean effective stress are impacted by the same changes in mean effective stress. The velocity-stress derivatives are computed based on the same time-lapse changes in mean effective stress. The stark differences in the impact on the total objective function are partly due to the observed seismic velocity volumes- the compressional is approximately twice that of the shear seismic velocity changes.

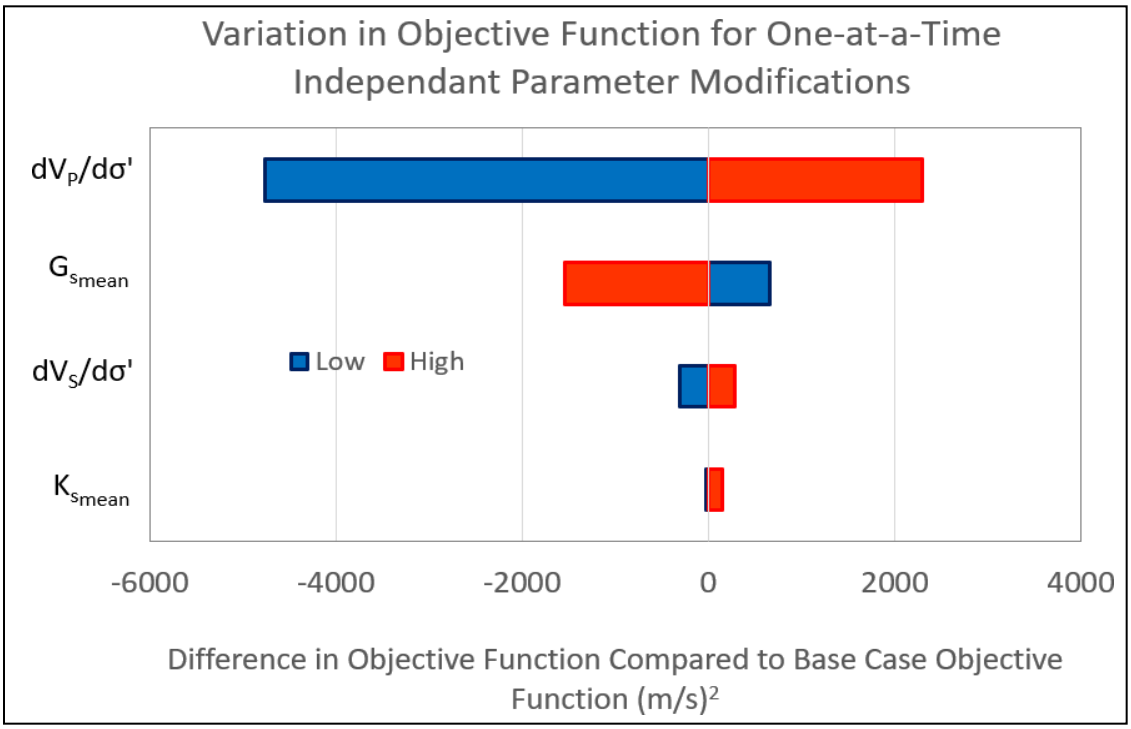

Figure 7.6: Sensitivity Analysis for Impactful and Independent geomechanical parameters. The compressional seismic velocity to stress derivative is the most impactful parameter, followed by the G_{smean}, the dVs/dσ' and lastly the K_{smean}.

7.2.5 Deterministic Solution Surfaces

Relationships between the objective function and the independent input parameters have been studied by holding two variables constant and plotting the result of varying the remaining two variables. Several solution surfaces are generated to deepen our understanding of the trends in the objective function. In particular, Figure 7.6a show the variations in μ_{smean} and K_{smean} with the shear seismic velocity to stress derivative held at 52 m/s per 1000 psi effective stress and the compressional seismic velocity to mean stress derivative held at 61 m/s per 1000 psi change in stress. The graphic 7.6a is bowl shaped with the plotted minimum occurs at μ_{smean} equal to 3.0 Mpsi and K_{smean} equal to 3.3474 Mpsi.

Similarly, Figure 7.6b shows the relationship between dVp/dσ' and dVs/dσ' for with the μ_{smean} equal to 2.55 Mpsi and K_{smean} equal to 3.45 Mpsi. Figure 7.6b shows a steep decline in the derivative of the compressional seismic velocity and very gentle changes associated with the derivative for the shear seismic velocity objective function, a phenomenon due to the large magnitude of the dVp/dσ' relative to dVs/dσ'. For the stated parameter selection, Figure 7.6b identifies a minimum of 283 $(m/s)^2$ for dVp/dσ' equal to 57.1m/s per 1000 psi change in mean effective stress and dVs/dσ' equal to 53.1 m/s per 1000 psi change in mean effective stress. Figure 7.6: Solution surface for variations in μsmean and Ksmean Plot shows a minimum value at μsmean = 3.0 Mpsi and Ksmean = 3.474 Mpsi. b) Solution surface for variations in dVp/dσ' and dVs/dσ'. Minima apparent at dVp/dσ' = 57.1 m/s and dVs/dσ' = 53.1 m/s per 1000 psi change in Mean Effective Stress.

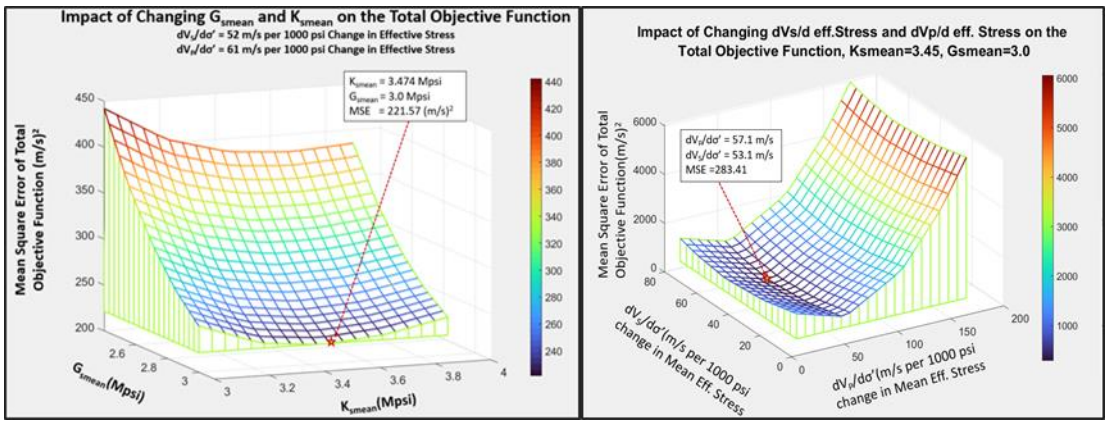

Figure 7.7: Solution surface for variations in μsmean and Ksmean Plot shows a minimum value at μsmean = 3.0 Mpsi and Ksmean = 3.474 Mpsi. b) Solution surface for variations in dVp/dσ' and dVs/dσ'. Minima apparent at dVp/dσ' = 57.1 m/s and dVs/dσ' = 53.1 m/s per 1000 psi change in Mean Effective Stress.

7.2.6 Stochastic Evaluation

A stochastic analysis is also conducted. Two hundred and fifty cases each with varying μ_{smean}, K_{smean}, dVp/dσ' and dVs/dσ' are generated. The goal is to develop mathematical relationships between the input parameters and the objective function computed within the Petrel interface.
The starting point is the simplest possible linear model, followed by the second-order mapping and an Artificial Neural Network. Figure 7.7 captures each of these relationships along with a compilation plot. Each mapping applies weights to the input parameters to replicate the Objective Function computed in Petrel. The objective of each mapping model is to find the weight coefficient for each input parameter which predicts the minimum MSE.

A proxy line x=y is superimposed on all subfigures within Figure 7.7 to identify the deviation of the "mapped" objective function from that computed within Petrel. The linear model deviates significantly from the proxy line, and the mapped linear relationship has a coefficient of determination (R^2) of only 82.1%. The second order provides an improved fit with an R^2 of 97.93%. At the lower and higher magnitudes of the Petrel computed Objective Functions, the second-order model indicates a small degree of scatter. Equation 7.1 and 7.2 show the relationships for the Linear and Second-Order mappings, respectively.

$$OBJ_{linear} = -2670.1 - 1489.9G_{S_{mean}} + 1256.5K_{S_{mean}} + 55.153\frac{dV_P}{d\sigma} + 15.3385\frac{dV_S}{d\sigma} \quad (7.1)$$

$$OBJ_{Second} = -2996.5 + 4967.4G_{S_{mean}} - 577.2649K_{S_{mean}} - 65.6362\frac{dV_P}{d\sigma} - 51.5807\frac{dV_S}{d\sigma} - 1310.5{G_{S_{mean}}}^2 + 311.87{K_{S_{mean}}}^2 + 0.731\left(\frac{dV_P}{d\sigma}\right)^2 + 0.844\left(\frac{dV_S}{d\sigma}\right)^2 \quad (7.2)$$

Figure 7.7 also displays the objective function mapping using an Artificial Neural Network. In this current ANN algorithm, a single hidden layer with 15 neurons is utilized, and the tangent sigmoid

is used as the activation function. A system of weights and biases applied to an independent and impactful property matrix links the inputs to outputs. These weights and biases are updated using backpropagation. The dataset is normalized and subdivided randomly, with 70% used for training the ANN and 15% for the validation dataset, which is also used to avoid over-training the data. The blind test dataset (remaining 15%) assesses the model by mapping previously unused data. This stochastic approach generates a unique solution for every specific subdivision of the ANN datasets (Training, Validation and Blind Test). The ANN Regression gives the best coefficient determination and the smallest MSE, indicating that the ANN match is optimal for all mapping methods implemented. The relationship for the normalized ANN output is shown in equation 7.3. Naturally, the normalization is revised to achieve the computed total objective function.

$$OBJ_{ANN\_Normalized} = \boldsymbol{w_2}(b_2, tanh(\boldsymbol{w_1}[b_1, \boldsymbol{Inputs}])) \quad (7.3)$$

Where ***Inputs*** refers to the input matrix, b1 is the bias associated with the input layer, and $\mathbf{w_1}$ is the matrix of weights applied to at the input layer. Similarly, b2 and **w2** are the biases and weights applied to the hidden layer.

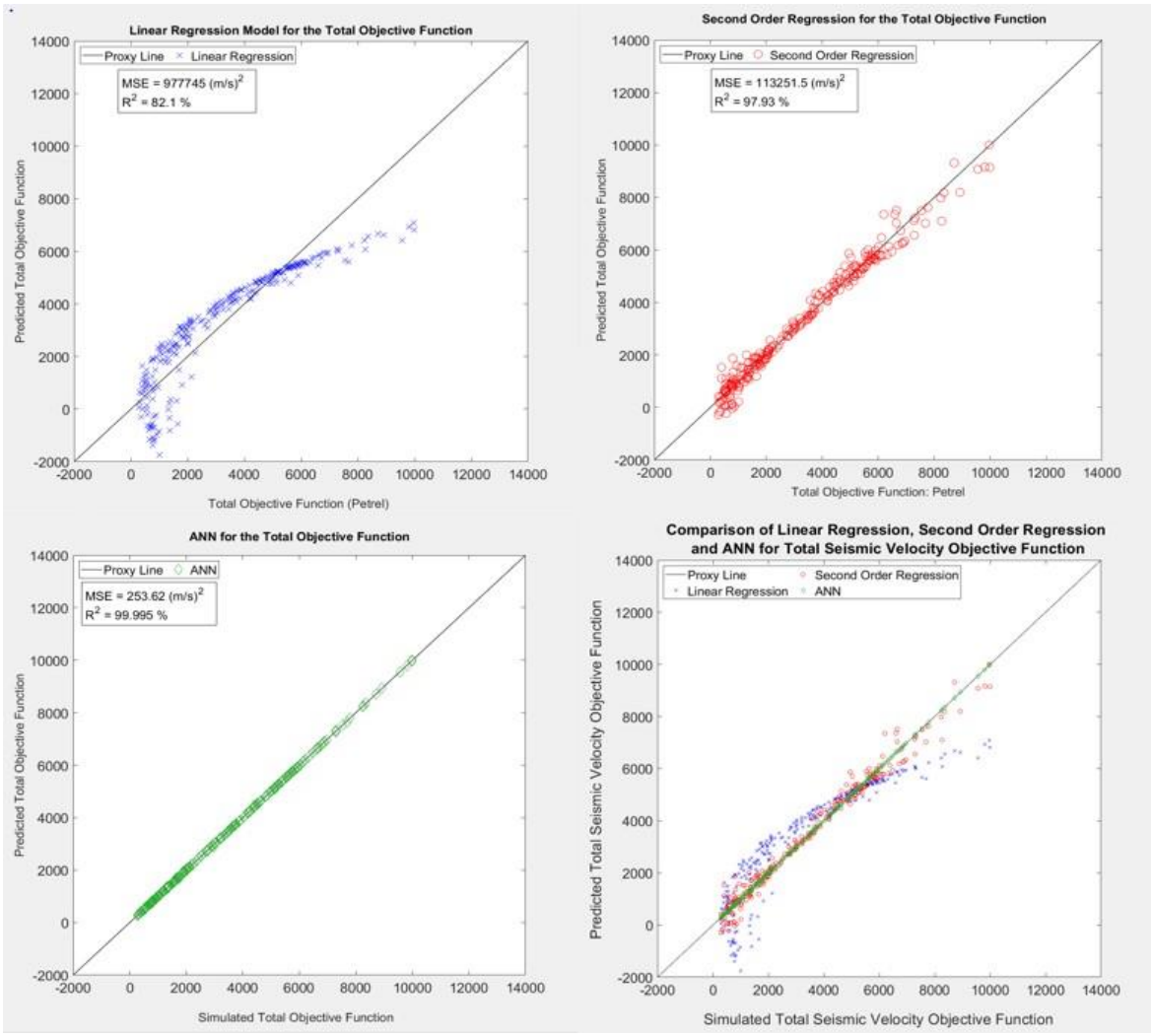

Figure 7.8: Top-left: First Order, top-right: Second Order, bottom left: Artificial Neural Network and bottom right: Compilation plot for the Total Objective Function. Each graph indicates the Mean Square Error (MSE) and the R2 (Coefficient of Determination) as measures of the goodness of fit. The ANN provides the best correlation.

7.3 Optimization

Section 2.4.5 reviews the application of hybrid machine learning algorithms to solve various petroleum engineering problems. The machine learning-assisted workflow implemented in this study is composed of an Artificial Neural Network embedded within a Particle Swarm Optimizer. The ANN has an identical setup to that addressed in section 2.5.4. Essentially, the ANN provides the mapping relationship, and the Particle Swarm Optimizer seeks to determine input parameters to minimize the Total Objective function computed from the ANN mapping. The hybrid workflow implements a similar population size as the 250 stochastic cases, initializes the particle velocity at zero for the initial iteration, and randomly initializes individual particle values. Based on this initial set of populated particles, global best is determined. After the second iteration, the best

position for every particle is determined. The algorithm runs for a predetermined number of iterations and converges to the optimal geomechanical parameters.
The optimal geomechanical parameters determined from the machine learning assisted workflow are μ_{smean} of 3.0 Mpsi, K_{smean} of 3.0 Mpsi, dVp/dσ' of 56.48 m/s per 1000 psi change in mean effective stress (185 m/s per 1000 psi change in mean effective stress), and dVs/dσ' of 31.26 m/s per 1000 psi change in mean effective stress (102.5 m/s per 1000 psi change in mean effective stress). Typically, the PSO seeks to generate an improved dataset by ensuring that the MSE of the PSO population is smaller than that of the original ANN. The ANN gave an exceptionally good match with an MSE of 253 m/s and a coefficient of determination of 99.995%, an almost perfect match, leaving little room for improvement by the PSO.

Even apart from the typical questions about the applicability of measurements taken on small core samples to the in-situ conditions, ultrasonic core seismic velocities measurements are not representative of in-situ conditions. In line with accepted industry practices, ultrasonic measurements are taken in the dry core, and the impacts of the fluid effects modulus are added numerically. The approach accounts for the well-known effects of frequency-dependent seismic velocity measured on saturated cores (Batzle et al., 2006; Mayr & Burkhardt, 2006). Additional factors impacting/limiting the use of acoustic, and rock mechanical measurements include the core damage when extracted from its native subsurface environment. Extraction leads to the breakage of intergranular bonds and the development of microcracks. Upon reloading, these cracks may be filled with debris and may not close completely, leading to lower measured seismic velocities. The orientation of the induced cracks relative to the measurement angle (vertical, 45^o or horizontal) also impacts the measured velocities. With further loading increase, a linear velocity-stress relationship emerges until the stress-velocity plateaus or decreases as continued loading also leads to the formation of new microcracks and seismic velocities decrease.

(Nes et al., 2000) discussed the use of core for seismic studies, presented experimental data on extracted and synthetic cores concluding that stress sensitivity measured on extracted core exceeds that of the in- situ rocks. Ultrasonic measurements of seismic velocities on the core significantly overestimate the velocity to stress derivative. Ultrasonic seismic velocity measurements on core serve as an absolute maximum limit and do not apply to in-situ conditions.

The stress dependency of seismic velocities has been studied by many researchers (Eberhart-Phillips et al., 1989; Freund, 1992; Khaksar et al., 1999; Winkler, 1986) while (MacBeth, 2004) and (Dvorkin et al., 1996) explore stress sensitivity more directly by assessing the related elastic moduli. (Shapiro, 2003) presented a derivation of seismic velocity as a function of differential stress (equation 7.4) by applying poroelasticity principles to the compressibility and stress dependency of stiff and compliant pores and the stress dependencies of the elastic moduli. Meaningful comparisons could be derived from comparison with the stress-velocity relationship presented by Shapiro (2003).

$$V(P) = A + KP - Bexp(-PD) \tag{7.4}$$

where P represents the differential stress, V(P) is the velocity variation with changing differential pressure and A, B, K, and D, are fitting parameters.

The linear portion of the velocity-stress relationship is akin to the linear relationships for stress-dependent elasticity and is our region of interest. The project rock physicist Dr. Tom Bratton

applied Shapiro's relationship. The gradient computed derivatives for Morrow B were 240 ft/sec per 1000 psi change in effective stress in compressional seismic velocity stress, while shear seismic velocity is 104 ft/sec per 1000 psi change in effective stress.

The shear seismic velocity derivative is larger than that from empirical measures as it compensates for the positive seismic velocity changes due to fluid substitution. The positive changes in shear seismic velocity are due to the changes in bulk density and the VSP integration workflow may benefit from a simplification of the EOS of fluid system. The percentage difference for the shear seismic velocity is - 43%. The optimized compressional seismic velocity derivative compares pretty well with that obtained through the VSP integration workflow with a percentage difference of 22%. This result begins to serve as confirmation that for this current FWU project, the VSP integration workflow can credibly be used to assess stress changes. Table 7.3 summarizes the optimized result.

Table 7.12: Summary of Optimized Geomechanical Parameters and Associated Error.

μ_{smean} (Mpsi)	Vs-Stress Derivative (m/s per 1000 psi change in mean effective stress)	Monitor 1: Average Sum of Square Error in dVs1 (m/s)2	Monitor 2: Average Sum of Square Error in dVs2 (m/s)2	Monitor 3: Average Sum of Square Error in dVs3 (m/s)2	All_dVs (m/s)2
3	45.5	24.6	19.8	47.7	92.1
K_{smean} (Mpsi)	Vp-Stress Derivative (m/s per 1000 psi change in mean effective stress)	Monitor 1: Average Sum of Square Error in dVp1 (m/s)2	Monitor 2: Average Sum of Square Error in dVp2 (m/s)2	Monitor 3: Average Sum of Square Error in dVp3 (m/s)2	All_dVp (m/s)2
3.35	57.5	2.5	44.6	40.6	107.7

7.3.1 Examination of Optimized Result

This workflow calibrates the stress change within the Morrow B interval by minimizing the mismatch between observed and modeled time-lapse seismic velocities and converges on optimum values for Ksmean, μ_{smean}, dVp/dσ and dVs/dσ. The K_{smean} and μ_{smean} characterize the fluid substitution contribution to seismic velocity change discussed in section 6.3.2 and generate Young's Modulus and Poisson ratio for the geomechanical analysis.

7.3.2 Modeled Seismic Velocity Attributed to Fluid substitution.

The ongoing CO_2-WAG operations within the Morrow B inevitably induce changes in fluid saturation as a mixture of water and CO_2 sweeps the in-situ oil to the producers. Figure 7.8 shows composite plots that illustrate the saturation evolution within the sector model at the baseline and the monitor measurements. Red indicates gas saturation, blue indicates water saturation, and green shows oil. The baseline measurement shows no CO_2 saturation near to the 13-10A as it was drilled in January 2014; however, every subsequent monitor measurement shows regions of higher gas saturations in the 13-10A near-wellbore region. This general pattern coincides with the evolution

of observed shear and compressional seismic velocity.

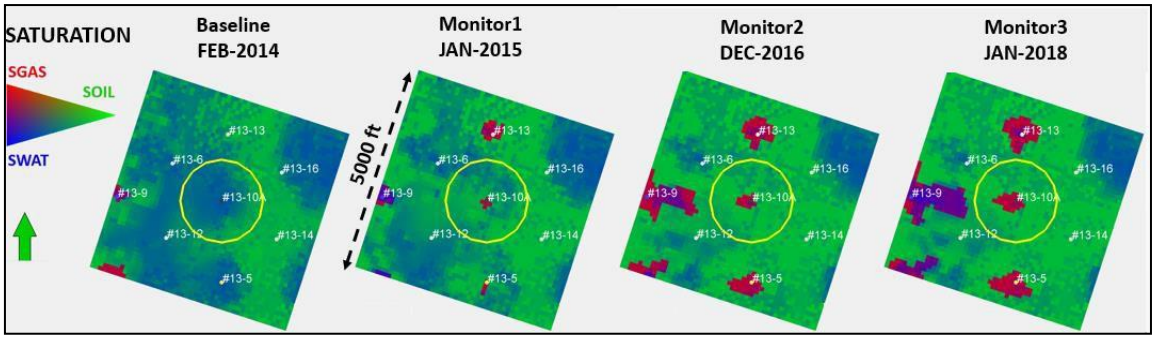

Figure 7.9: Snapshots of saturation within the compositional reservoir simulation sector model at Baseline, Monitor 1, Monitor 2, and Monitor 3. Saturation changes drive modifications in Shear and Compressional seismic velocities.

Extracted fluid saturations and fluid densities are used along with the matrix porosity and matrix density to compute the bulk formation density. The shear modulus is unimpacted by the changes in fluid saturation, and as such, only bulk density changes drive alterations in the shear seismic velocity changes. Figure 7.9 shows the delta-density for each monitor measurement computed relative to the baseline and compared to the shear seismic velocity impacts. Bright pink and blue regions on the areal distribution of delta density indicate reductions in bulk density. The areal extent of these specific regions correlates with increased time-lapse shear seismic velocity shown in bright red. These saturation distribution changes also impact the compressional seismic velocity through the fluid bulk modulus (K_f) and the bulk formation density (ρ). The relative impact of both variables determines the direction (increase/positive or decrease/negative) of the compressional seismic velocity change. Figure 7.10 shows the delta-fluid-bulk modulus changes and the compressional seismic velocity taken relative to the baseline measurements. The purple and blue in the delta-fluid-bulk modulus maps indicate regions of high gas saturation. High gas saturations reduce the fluid bulk modulus and lower both the saturated bulk modulus and the compressional seismic velocity. The directional effect of changing bulk density is the same for the shear seismic velocity, but for the Morrow B CO_2-EOR operation, the bulk formation density has a less significant impact than the fluid compressibility effect.

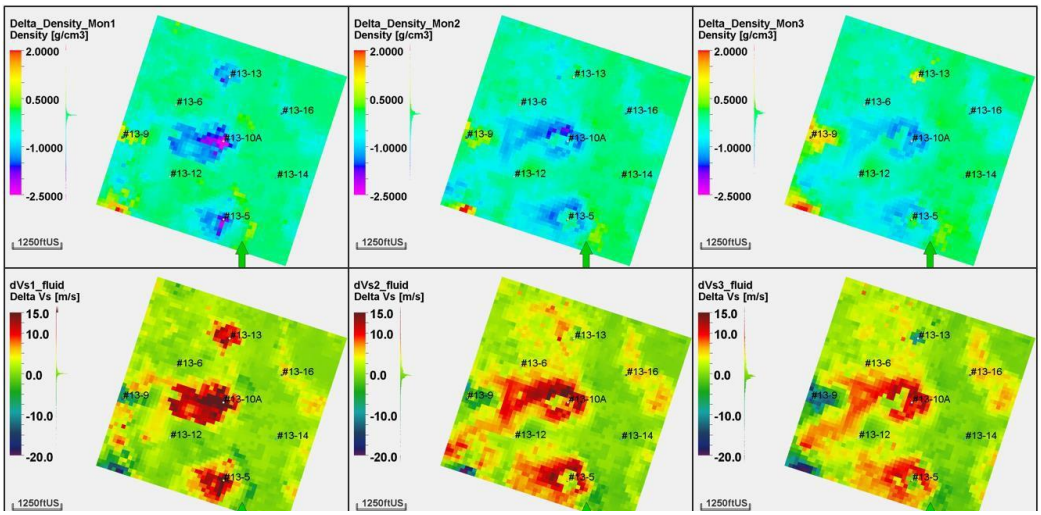

Figure 7.10: Time-lapse changes in formation bulk density (top) and time-lapse changes in shear-seismic velocity for every monitor time-step relative to Baseline VSP

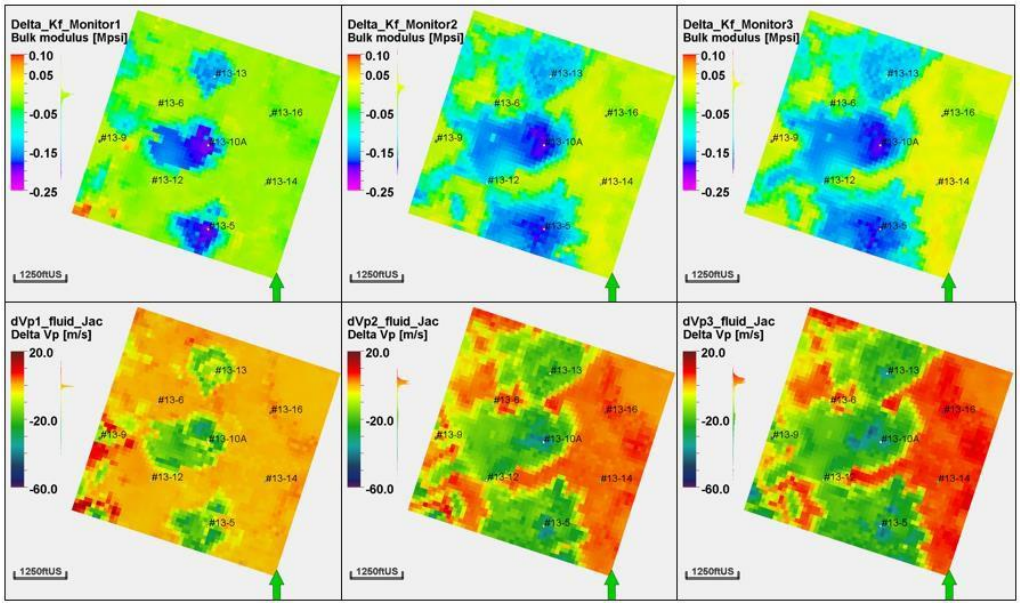

Figure 7.11: Shows the correlation between time-lapse changes in Bulk Modulus of the pore-filling fluid (top) and the Compressional Time-Lapse Seismic Velocity (relative to VSP Baseline) for Monitors 1, 2, and 3 (bottom row). The formation bulk density change, and fluid bulk modulus balance drive the resulting compressional seismic velocity change.

VSP monitor surveys are all taken at the end of the supercritical CO_2 injection cycles, and time-lapse seismic velocity changes are computed relative to the baseline. Figure 7.8 confirms a high-water saturation in the near-wellbore region of the 13-10A at the baseline. During CO_2-EOR operations, the injected CO_2 (4000-6500 psi and 100 oF) is a density similar to that of the in-situ oil (~50 $lb_m/ft3$) compared to the density of water is (~62.4 lbm/ft^3). The density differences result in a decrease in the formation bulk density. Furthermore, the simulation model also indicates that

even during the water injection cycles, the plumes of CO_2 are still evident in the near-wellbore region. Relative changes in shear seismic velocity range from modeled shear seismic velocity changes attributed to fluid substitution are largely positive. Interestingly, while all observed time-lapse shear seismic velocities are largely negative, the modeled time-lapse shear seismic velocities (within to 1000 ft. radius) are positive. The circumstance indicates that the modeled time-lapse shear seismic velocities must be sufficiently negative to overcome the positive time-lapse shear seismic velocities due to fluid substitution.

Changes in bulk density also impact time-lapse compressional seismic velocities. Injected supercritical CO_2 is a more compliant fluid than water, causing a decrease in the saturated bulk modulus. The fluid compressibility effect outweighs the bulk density effect resulting in a negative time-lapse compressional seismic velocity.

It is noteworthy that the compressional seismic velocity outstrips the shear seismic velocity. Observations from figures 7.6 and 7.7 at monitor time 2 show that, on average, the time-lapse compressional seismic velocity at the 13-10A region is ~-25 m/s compared to +10 m/s for the shear seismic velocity. Even within the time-lapse seismic velocities attributed to fluid substitution, the net effect is a negative time-lapse seismic velocity.

7.3.3 Modeled Seismic Velocity Due to Stress Change

The modeled time-lapse seismic velocity changes due to mean stress changes are determined from the time-lapse mean effective stress changes (Figure 7.11). The reservoir simulation model did not assess the pressure impacts on the overburden and underburden as these zones are carried as zero porosity and zero permeability. Figure 7.11 highlights the small effective stress changes occurring outside the Morrow B by using a constricted scale. In comparison, the effective stress changes with the Morrow B, monitor maximum negative time-lapse mean effective stress change is -318 psi, while monitor two and monitor 3 are -506 psi and -512 psi respectively. Time-lapse effective stress changes are small in the overlying and underlying formations and due to stress redistribution. Based on these large effective stress differences, the seismic velocity changes outside the Morrow B are not considered.

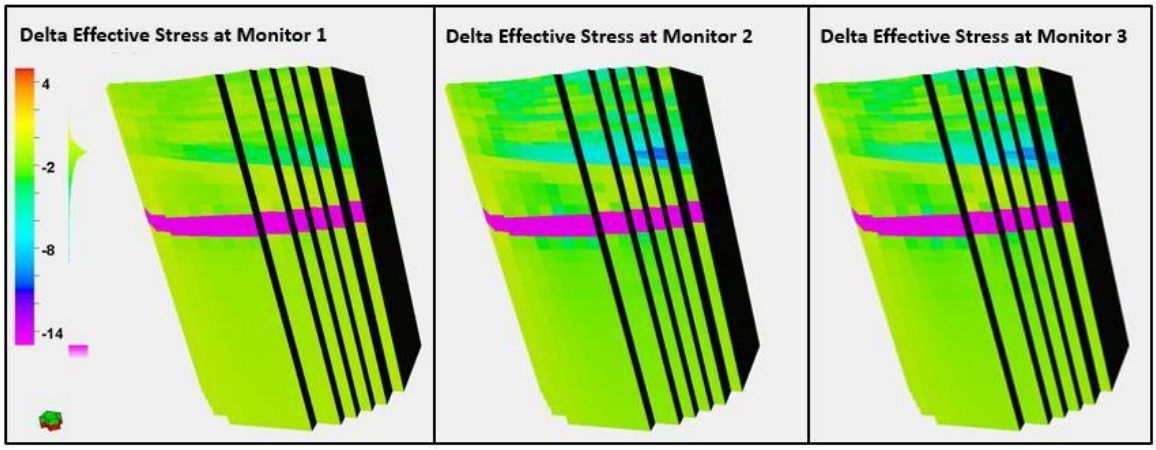

Figure 7.12: Effective Stress Changes outside of the Morrow B Formation are small in part because the reservoir simulation used zero porosity and permeability in the overlying and underlying formations. The time-lapse differences are due solely to stress redistribution.

Seismic velocity changes due to stress are computed by applying the seismic-velocity derivatives directly to the time-lapse mean effective stress changes. Figures 7.13 and 7.14 show the optimized changes in shear and compressional seismic velocity. The pore pressure changes drive the northwest increasing trend in the shear and compressional seismic velocity. The linear summation of the time- lapse velocity changes attributed to fluid substitution and that due to mean effective stress is computed for both the compressional and shear seismic velocity. A quick examination of relative contributions indicates that the stress changes have the dominant effect on the modeled seismic velocities, especially for the shear seismic velocity. For the shear seismic velocity, the positive time-lapse change seismic velocity changes attributed to fluid substitution are outstripped by the mean stress consideration. For compressional seismic velocity, the impact of the fluid ranges from 15% to 60%, so dominated mainly by stress. The stress impact can be explained in part by the highly heterogeneous, highly cemented nature of the Morrow B formation. These features add strength/ resilience to the reservoir rock, impacting the stress sensitivity of the Morrow B. The stronger the rock, the less stress sensitive.

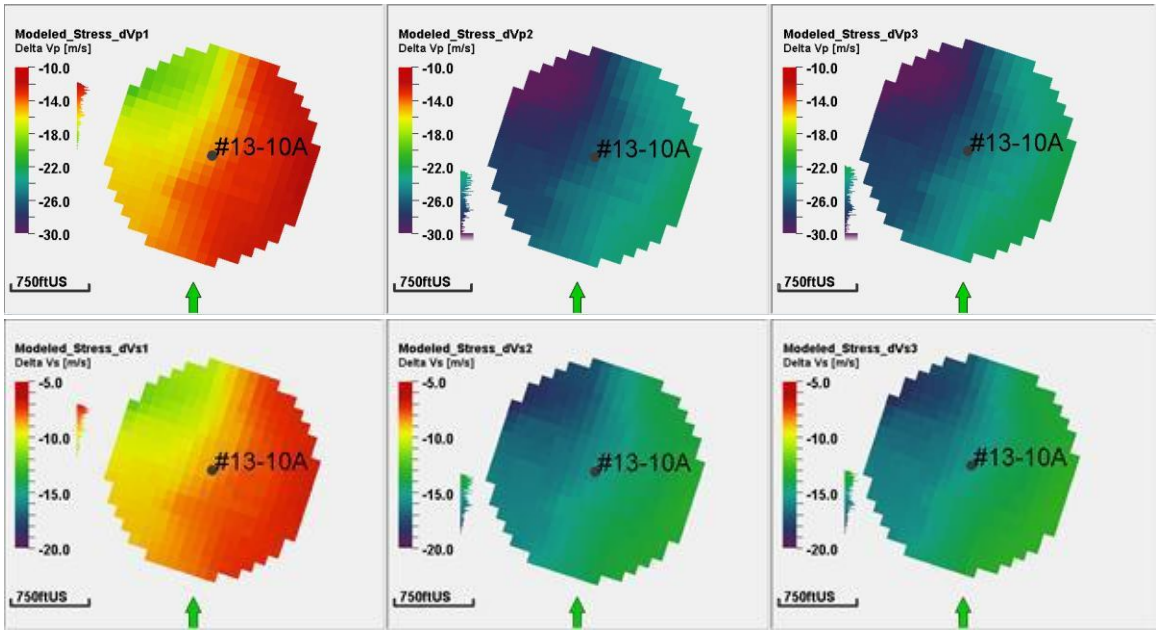

Figure 7.13: Time-lapse seismic velocity changes due to stress at every monitor time within a 1000 ft. radius of the 13-10A well. The top shows the compressional seismic velocity. The bottom shows the shear seismic velocity.

Figures 7.13 and 7.14 compare the observed and modeled time-lapse shear and compressional seismic velocities within a 1000 ft. radius of the 13-10A well. The top row displays the observed "raw" time- lapse VSP seismic velocity averaged over the Morrow B formation. Figure 7.13 (top row) shows the mark of the anisotropy in the observed time-lapse shear seismic velocity, more evident in monitors two and three. Figure 7.14 (top row) shows the observed compressional time-lapse seismic velocity dataset. For every successive monitor time step, the largest negative compressional seismic velocity region expands and rotates slightly from N45W to N50W.

Comparisons of the observed with the modeled seismic velocities deviate significantly in terms of pattern. Modeled seismic velocities are the result of the linear summation of the fluid substitution and stress seismic velocities. Seismic velocities due to fluid substitution are driven by saturation

distribution. The fluid saturation distribution is the main contributor to changes in the compressional seismic velocity. Increasing and decreasing the K_{smean} changes the computed saturated bulk modulus but does not alter the areal pattern. μ_{smean} appears in both the shear and compressional seismic velocity equations and similarly does not alter the areal pattern of the modeled time-lapse seismic velocity changes. Seismic velocities due to stress are driven by changes in pore pressure, which are extracted from the reservoir simulation model.

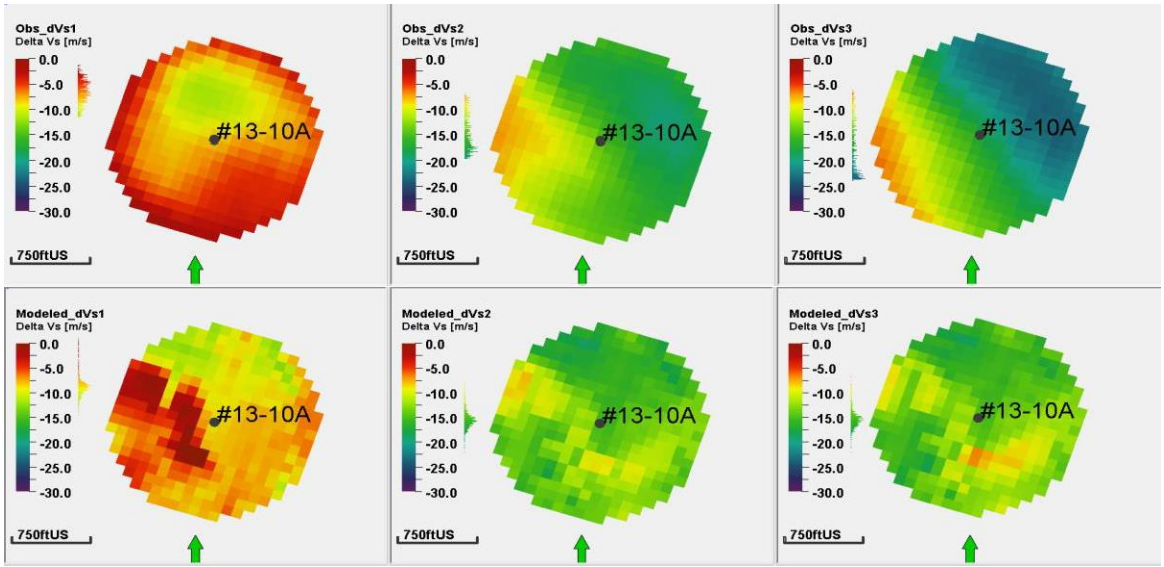

Figure 7.14: Time-Lapse Shear Seismic Velocity Changes. Row 1 presents the observed dataset, and Row 2 represents the modeled shear seismic velocity.

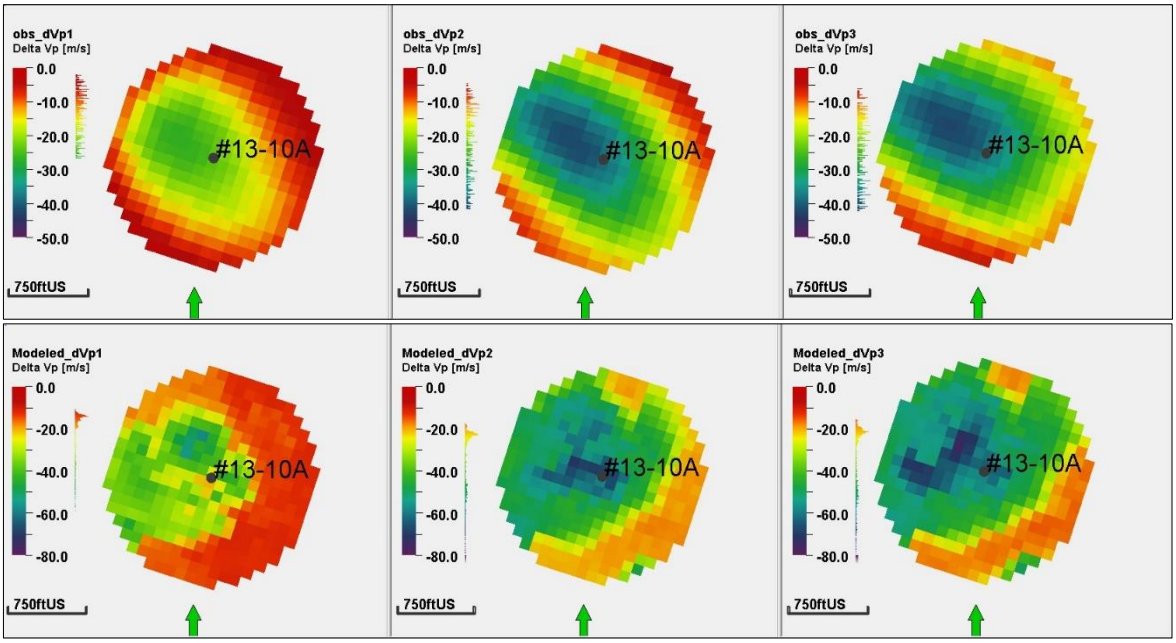

Figure 7.15: Time-Lapse Compressional Seismic Velocity Changes. Row 1 presents the observed dataset, and Row 2 represents the modeled compressional seismic velocity.

Closer replication of observed seismic velocity patterns would require an improved compositional reservoir simulation history match. Ideally, the simulated and observed bottomhole pressures at injectors and producers should match. Rates for all produced and injected fluids (oil, water and gas) should also match. The improved history match is the major improvement required in this work.

The main objective of this project is to perform a time-lapse VSP integration geared towards calibrating stress changes and enabling more confident predictions of the stress state. Using the time-lapse VSP dataset, initially acquired for monitoring the CO_2 plume expansion, for calibration enhances the value of the time-lapse VSP.

The Morrow B has a small vertical expanse (38 ft) compared to the acquired VSP dataset's resolution and wavelength. Thus, it is unsurprising that the VSP signature smears unto the overlying and underlying formations. However, the most negative compressional time-lapse seismic velocity occurs above the Morrow B (-43 m/s at monitor 3), while the most negative shear seismic velocity appears below the Morrow B (-27.2 m/s at monitor 3). VSP data is acquired with geophones in the borehole, so no depth readjustment is required.

For compressional seismic velocity differences, potential causes include the migration of injected CO_2 to the Morrow Shale- Morrow B interface. If the CO_2 changed phase from supercritical to gaseous, the bulk density of the formation would decrease. Reduced bulk formation density causes an increase in the compressional seismic velocity. However, the movement and mixing of the fluids during the miscible injection fluid may make this phenomenon less likely.

Another option includes a similar velocity-stress effect observed within Morrow B. Undoubtedly, while fluid flow occurs only within Morrow B, Figure 7.12 shows that pressure perturbation affects the overburden and underburden layers. Including these layers as live cells within the reservoir simulation model would increase the modeled effective stress and also *likely* the time-lapse effective stress changes.

Ultrasonic core data provided for the overlying Morrow shale indicate that a compressional seismic velocity–stress derivative of ~ 650 ft/s per 1000 psi change in mean effective stress (198.2 m./s per 1000 psi change in mean effective stress). Although the ultrasonic measurement provides over-estimations, direct utilization of the velocity-stress derivative suggests a time-lapse mean effective stress change of -241 psi at monitor three. The large time-lapse effective stress change would correlate with an increased pressure change observed in the reservoir simulation.

Prior simulation models which utilize overburden permeabilities on the order of 0.1 to 20 nanodarcies generate mean effective stress changes significantly smaller than 241 psi. Consequently, the velocity- stress derivative is not the source of the negative high compressional seismic velocity.

Stress changes have a much more significant impact on shear seismic velocity changes. A similar assessment to that performed for the compressional seismic velocity suggests that velocity-stress derivative is not responsible for shear seismic velocity falling beneath the Morrow B. Additional studies and theories are required to explain the locations of the most negative shear and compressional seismic velocities.

.

Chapter 8
Coupled Hydromechanical Modeling and Assessment of Induced Seismicity at FWU: Utilizing Time-Lapse VSP and Microseismic Data.

Summary
The objective of this work is to utilize integrated geomechanics, field VSP and microseismic data to characterize the complex subsurface stress conditions at Farnsworth Unit (FWU). The model is based on a five-spot sector model extracted from a primary geomechanical model. The five spot well injection pattern is characterized by extensive reservoir characterization data such well logs, extracted cores and borehole geophone data to facilitate detailed examination of stress changes and microseismic events occurrences. The study utilizes field vertical seismic volumes acquired from the injection well (#13- 10A). The seismic volumes successfully provided snapshots of the behavior of the reservoir at distinct times. The use of VSP and microseismic data provided direct and indirect estimates of the dynamic stress changes occurring in the overburden, reservoir and underburden rock formations. In order to illuminate the stress regions and identify rocks that have undergone inelastic failure, microseismic event occurrences were utilized. Microseismic activity has been detected at FWU; further study of its locations, timing, and magnitude was needed to deduce the nature of the changing stress state. The results of the study revealed that microseismic events were successfully modeled within the Morrow B formation. Moment magnitudes of seismic events were within the same magnitudes for events in the reservoir, suggesting the suitability of the model. The results of the study showed that the computed moment magnitudes for seismic events were insignificant to warrant safety concerns. The study findings showed the usefulness of coupled hydromechanical models in predicting the subsurface stress changes associated with CO_2 injection. The knowledge gained from this study will serve as a guideline for industries planning to undertake underground CO_2 storage and characterize the subsurface stress changes.
Keywords: VSP Integration, Coupled hydrodynamic-geomechanical model, Stress calibration, Microseismicity, CO_2-WAG, Carbon Capture, Utilization and Storage.

8.1 Introduction
The concentration of atmospheric CO_2 is steadily on the rise and a significant contributing factor is the worldwide consumption of fossil fuels. The burning of fossils fuels, especially with the release of carbon dioxide is having adverse effects on the climate. Harsh climate conditions such as increased droughts, intense heat waves, wildfires and floods are anticipated to occur. Carbon dioxide is responsible for 64% of enhanced greenhouse effect making it a target for geologic sequestration **(Intergovernmental Panel on Climate Change, 2022)**. Carbon dioxide (CO_2) sourced from the power and industry sectors forms 60% of the total CO_2 emissions **(Bradshaw et al., 2019)**. Instead of releasing these greenhouse gases into the atmosphere, it is captured and utilized for recovering oil and subsequently stored in geologic formations. Carbon capture technologies play vital roles in reducing CO_2 emissions. In addition, monitoring strategies are employed to ensure the safe storage of the greenhouse gas and avoid any potential leakage to the surface. With the adoption of the 45Q Tax Incentive, participation in carbon capture and storage

techniques has gained increasing attention (**Beck, 2020**). Nonetheless, the capture and storage of significant quantities of CO_2 raises possible geomechanical concerns, with channels developed in sealing rocks serving as potential conduits for injected CO_2. The creation of fractures/faults in rocks is accompanied by the release of seismic energy. Microseismic events recorded illuminate the locations of seismic energy release caused by variations in stress. Examining the timing, location, and magnitudes of microseismic occurrences can provide sufficient information into the dynamic and complex stress field at Farnsworth field unit (FWU). The production and geophysical dataset utilized in this study is from the ongoing CO_2-Enhanced oil recovery (EOR) operations at FWU. The FWU carbon, capture, utilization and storage (CCUS) project forms part of the Southwest Regional partnership on carbon sequestration (SWP). This study supports the SWP tasks in developing numerical reservoir simulation models to decrease the potential seismic hazard associated with CO_2 injection and improve the prediction of stress changes in a reservoir undergoing CO_2-EOR. The geomechanical impacts of stress fluctuations in and around the reservoir were investigated using a coupled hydromechanical simulation model.

8.2 Background Study

Numerous studies have been conducted on the effectiveness of carbon capture and storage (CCS) and CCUS technologies to mitigate atmospheric CO_2 emissions. CO_2 captured from industrial facilities are injected to enhance oil recovery or stored in deep geologic formations (Jenkins et al., 2012). Despite the successful implementation of CCS technologies, there are still concerns about potential leakages of CO_2 into underground water sources. Also, the high cost of deploying carbon capture and storage (CCS) technologies means that there is still some apprehension regarding its commercialization. Even though, geologic sites have stored oil and gas for centuries, they are often screened to assure the safe and lasting containment of CO_2 (NETL, 2017). The production/injection of fluids such as CO_2, and water is known to alter the formation pore pressures which impacts the stress distribution in the overburden, underburden and reservoir rock. Depending on the geology of the area, formation geomechanical properties, volumes and rates of fluid injection, there may be a potential for injection-induced seismicity (McClure & Horne, 2014; Tutuncu & Bui, 2016).

In recent decades, high magnitude earthquakes have occurred due to subsurface activities. For instance, an earthquake of magnitude Mw 5.0 occurred in the Delaware Basin on March 2020 as a result of wastewater disposal. Despite hydraulic fracturing operations and hydrocarbon production on the field, a study conducted by (Skoumal et al., 2021) attributed the primary cause of the induced seismicity to wastewater injection in the Devonian formation. The deep Devonian formation is in close proximity to the crystalline basement. The absence of an interbedded formation between the Devonian formation and the crystalline basement allows the triggering motion of high injection wells to be transferred to deeper fault structures. Injecting fluids at high rates into the deeper Devonian formation increases the tendency of matured faults in the basement rock to slip, resulting in increased seismic activities. Similar findings of high magnitude earthquake (Mw 5.8) happened in neighboring Oklahoma (Pei et al., 2018). Studies showed that majority of the microseismic events were related to deep wastewater injection. Although wastewater was injected heavily into a fault zone which could be a contributor to the earthquake occurrences, the main contributor to the observed seismicity was the triggering of faults in the basement rock neighboring the injection zone. Also, active faults in the sedimentary strata were intersecting the basement crystalline rock. The opposite situation can be observed in the rock stratigraphic sequence in Farnsworth Unit. In FWU, there exists a lower shale formation beneath the Morrow B sandstone. The presence of

an interbedded shale layer restricts vertical flow and pressure response from the injection interval to the Pre-Cambrian basement. Although microseismic events have been observed, they are of smaller magnitudes.

Microseismic events that occur during hydraulic fracturing activities in the oil and gas industry are primarily caused by shear slippage on pre-existing faults and fractures. However, the mechanisms and factors controlling fault reactivation during hydraulic fracturing are not fully understood (Zoback & Lund Snee, 2018). To address this knowledge gap, (Zoback & Lund Snee, 2018) investigated the conditions under which fault slippage occurs, considering pore pressure perturbation, stress state and fracture orientation. It was revealed from the study that as pressure increases, more poorly oriented planes tend to slip. However, the tendency for a fault to slip depends on the fault strike to the Shmax direction. At FWU, (McMillan 2019) reported the current stress state of the Morrow B formation as normal faulting regime with S_V > Shmax > *S*hmin, where S_V is the vertical principal stress and *S*hmin is the minimum horizontal principal stress.

Geomechanical models are constructed to model plastic deformation and pore pressure distribution. To study the occurrences of induced seismicity, (Tutuncu & Bui, 2016) utilized coupled geomechanics and fluid flow models to predict the potential for microseismic occurrences in the Eagle Ford formation during a hydraulic fracturing operation. The formation of interest had existing faults and the impact of the presence of faults at distances away from the injector wells were studied. The study revealed that high injection rates were considered as critical factors to the occurrence of induced seismicity. Again, faults located at larger distances from the injection site experienced lower shear stresses, which resulted in reduced fault reactivation. (Chen et al., 2019) examined the occurrence of seismic events in the Azle area, North Texas, from November 2013 through April 2014. The authors performed a coupled fluid flow and geomechanical simulation study of the overburden to the crystalline base rock, analyzing the contribution of oil and gas operations to seismic events. According to the study, pore pressures did not increase within the basement fault, however, noticeable seismicity was recorded at the basement formation. A plausible explanation for the observable seismic events was the unbalanced loading on different sides of the Azle fault, leading to an accumulation of plastic strain changes at the base rock.

At FWU, several numerical simulation studies have been performed by researchers in the Southwest Regional Partnership (SWP) team to monitor the migration of injected CO_2 in the Morrow B sandstone during an active CO_2-WAG injection. Monitoring was performed by examining the changes in the reservoir elastic and petrophysical properties with CO_2 injection. The competency of the simulation model results was enhanced by the integration of acquired field geophysical data and results from laboratory experiments. For instance, (Adu-Gyamfi et al., 2022) conducted a simulation study to examine the chemical and mechanical impact on the caprock integrity as a result of CO_2 injection. The simulation study indicated that the caprock maintained its elastic properties for the forecasted years despite changes in the formation petrophysical properties and CO_2 interactions in the caprock. Also, (Acheampong et al., 2022) performed a fluid substitution modeling to investigate the contribution of fluid saturation changes to the time-lapse velocity responses using a site-specific rock physics modeling. Although seismic velocities are widely known to be sensitive to stress changes, the study focused solely on the impact of fluid change to the saturated rock elastic and seismic properties. McMillan, (2021) developed a time-lapse VSP integration workflow that utilizes field VSP data to calibrate subsurface stress changes. The work examined how induced stress changes from CO_2-WAG injection could potentially impact the seismic velocities inverted from the field VSP data. The study showed that time-lapse acoustic measurements were suitable for calibrating the subsurface stress changes. Although, calibration of the geomechanical model was performed through time-lapse VSP profiling to estimate the stress changes, the study did not model the occurrence of microseismic events which are indications of stress changes in the subsurface. Again, defining the subsurface stress state with

the help of a numerical simulation model is non-unique – multiple realizations of the mechanical earth model (MEM) can be generated. To address the above-mentioned challenges, and reduce the solution non-uniqueness of the model, a robust integration framework that combines fluid flow models, coupled geomechanics, and microseismic data were utilized in an effort to improve the prediction of stress changes within a reservoir undergoing CO_2-EOR. Also, we confirmed that the method of using inelastic failure was successful in modeling the microseismic events.

8.3 Field Description

8.3.1 Site Description

The Southwest Regional Partnership on Carbon Sequestration (SWP) is one of the seven regional partnerships sponsored by the US Department of Energy and National Technology Laboratory (NETL) to evaluate the large-scale feasibility of permanently sequestering CO_2 in geologic formations. The study site for the SWP is the Farnsworth field unit, located in the Western Anadarko basin. The primary target for hydrocarbon production and CO_2 sequestration is the operationally-named Morrow B formation (Cather et al., 2021). FWU field has been under primary and secondary recovery stages and is currently undergoing an active CO_2 water-alternating-gas (WAG) injection. FWU CO_2 WAG injection commenced in 2010 with anthropogenic CO_2 sourced from the Arkalon Ethanol Plant in Liberal Kansas, and the Agrium Fertilizer Plant in Texas. Currently, CO_2 is supplied mainly from the Arkalon Ethanol Plant (Morgan et al., 2021). A (Xiao et al., 2020). A probabilistic study performed by (Asante et al., 2021) using the field's relative permeability curves showed that the Morrow B formation can store at least 7.81 MMtons of CO_2, with the highest estimate of CO_2 storage being 40.52 MMtons. Presently, more than 1 million metric tons of CO_2 have been sequestered in the Morrow B formation. Figure 8.1 shows the location of FWU in the Anadarko basin.

.

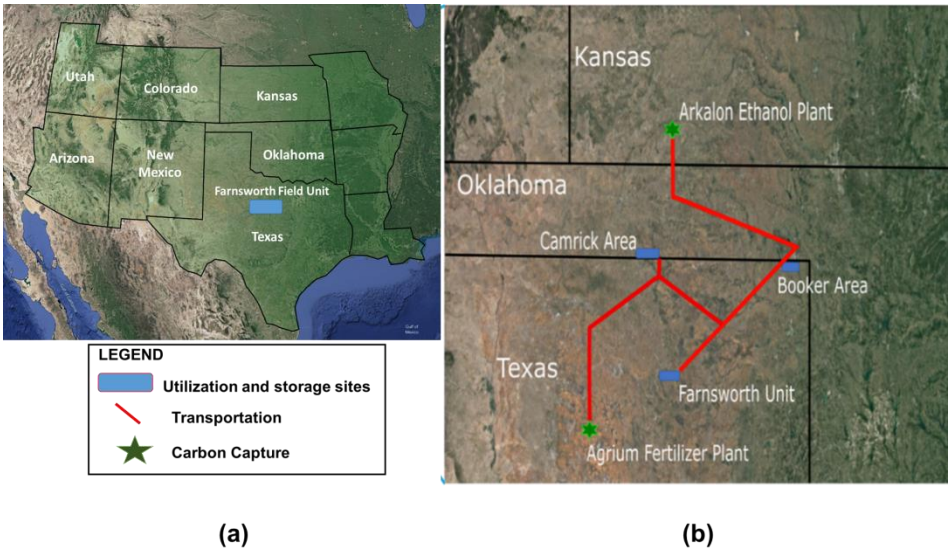

Figure 8.1: (a) Location of the Farnsworth Unit (FWU) in the Anadarko basin. (b) Detailed map showing anthropogenic CO_2 sources and utilization and storage sites.

8.4 Geology of the area

Extensive studies have been performed on the Morrow reservoirs since they are the primary targets for oil production (Rasmussen et al., 2019, Will et al., 2021; Asante et al., 2021; Acheampong et al., 2022; Adu-Gyamfi et al., 2022). The Morrow B formation is overlain by the Thirteen Finger limestone and Morrow shale which serve as excellent seals for the CO_2 sequestered reservoir. Early researchers characterized the geology of the Morrow B formation by investigating and interpreting its depositional settings (Munson, 1989; Ross-Coss et al., 2016; Cather et al., 2021). Preliminary studies classified the Morrowan sandstones as predominantly fluvial deposits, with the overlying Thirteen Finger limestone consisting of estuarine to marginal marine deposits (Cather et al., 2021). A general description of the stratigraphic sequence of the reservoir is provided by (Cather et al., 2021; Gallagher, 2014; Moodie et al., 2021) as series of rock units with coarse-grained conglomerates at the base, and fine estuarine sandstones lying on top. Figure 8.2 illustrates the stratigraphic column of the FWU, highlighting the main production interval and rock sections lying above and beneath the reservoir. A study performed by (van Wijk et al., 2021) using 3D seismic data and tracer experiments to understand the flow directions of the injected CO_2 indicated that the impermeable caprock makes it less likely for injected CO_2 to migrate vertically or flow southward. A defining characteristic of the FWU geology is that the injection zone (Morrow B) is not in direct contact with the Precambrian basement. The underlying Morrow shale reduces the likelihood for the triggering effect of CO_2 WAG injection to be transferred to the basement rock. The existence of faults within sequestration reservoirs can potentially serve as migration pathways for injected CO_2 to leak to surface. Also, faults within sedimentary strata intersecting basement rocks can lead to the occurrence of high magnitude seismic events when induced to slip. A study conducted by (van Wijk et al., 2021) found no direct evidence of faults in the reservoir or caprocks in FWU.

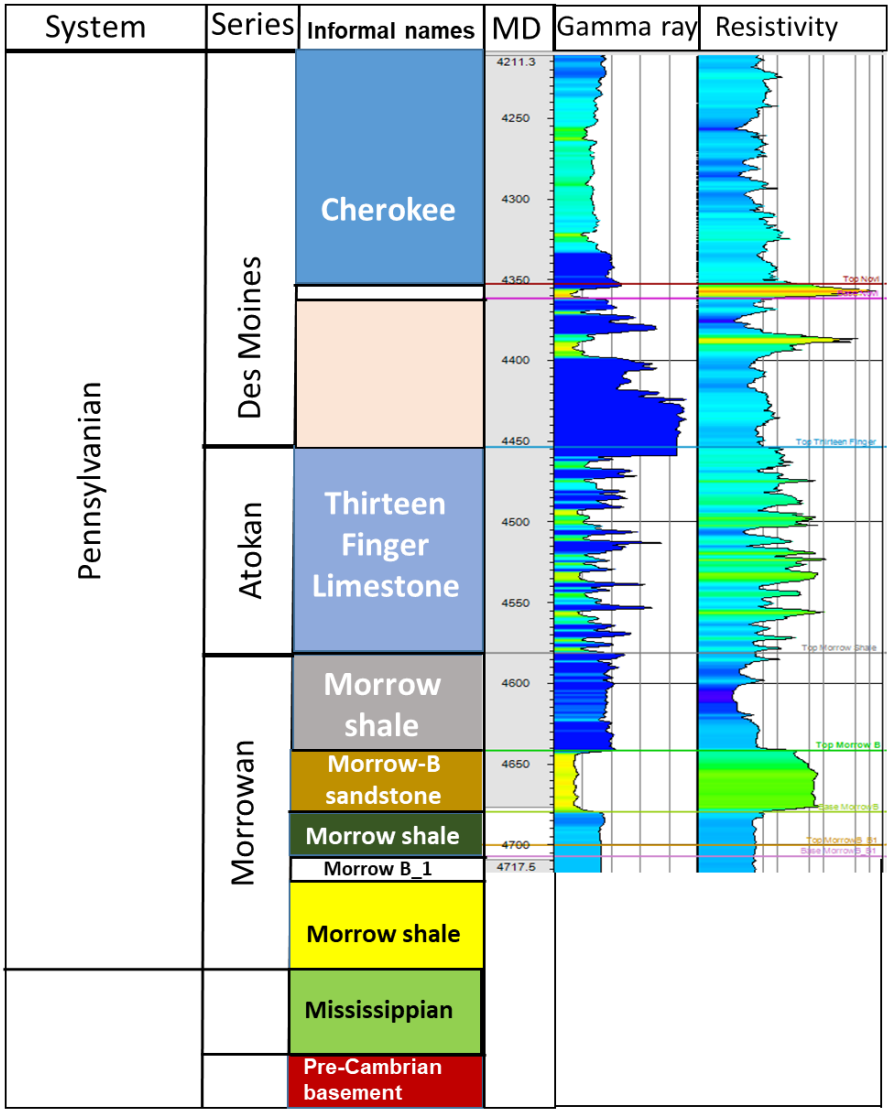

Figure 8.2: Stratigraphic sequence of different rock units at the Farnsworth Field area with the corresponding Gamma ray log from well 13-10A. Depths measured from the mean sea level. The different colors denote the different rock formations in FWU. (Figure modified from van Wijk et al., [26]).

8.4.1 Acquisition of Field Data

In order to investigate the mechanism of induced seismicity in FWU, multidisciplinary data were integrated in a simulation modeling effort to characterize the stress changes and model the microseismic occurrences. Time-lapse 3D VSP was utilized to monitor the impact of CO_2-WAG injection on the FWU reservoir properties. A total of four 3D VSPs were taken, including a baseline survey and three monitor VSPs. A detailed description of the acquisition of the 3D VSPs is provided by (Will et al., 2021). The processing of the VSP data to attenuate noise and subdue high energy amplitudes was discussed by (El-Kaseeh et al., 2019). Seismic velocities and depth shift

attributes were inverted from the 3D VSP. By computing the velocities, we can see how changes in fluid saturation affect the reservoir properties over time. Since the Morrow B formation is only about 24 feet thick, seismic velocities had to be focused on a smaller area to pick up on subtle changes within the reservoir. Seismic images were cropped outside a 1000 ft. radial distance from the monitoring well (13-10A). Figure 8.3 illustrates the temporal evolution of the velocity distribution. The seismic velocities during the monitor survey VSP times (dVp) were estimated relative to the baseline VSP. The increasing velocity differences observed on Figure 3 demonstrate a preferential migration of the injected CO_2 from the from the injector well (#13-10A) towards the producer well (13-6).

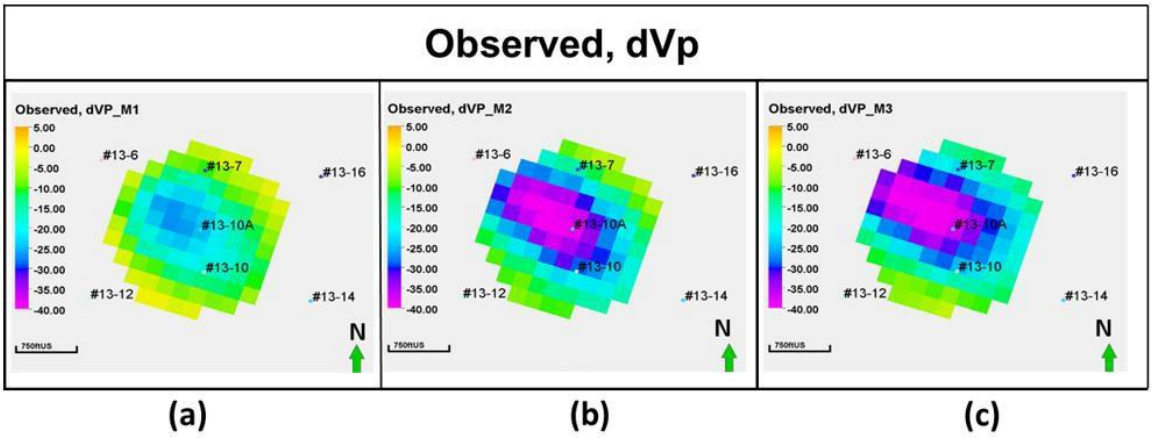

Figure 8.3: Depth slice of the compressional velocity distribution for each baseline-monitor pairs. Images acquired below the reservoir interval. Figure shows the velocities for the monitor 1-base (a), monitor 2-base (b) and monitor 3-base (c).

8.4.2 Microseismic Data

Microseismic events are observations of rock failure, providing valuable information about pore pressure changes and geomechanical behavior of oil and gas reservoirs. The progressive failure of a rock structure can be revealed by recording microseismic occurrences (Ma et al., 2020). Microseismic monitoring was performed at the FWU site with both surface and wellbore receivers to improve the coverage and location of the seismic events. Sixteen-level, 3-component OYO seismometer arrays were deployed in a single vertical well. A detailed description of the deployment of the borehole and surface receivers are provided in (Ampomah, Will, Mcmillan, et al., 2021). (Gao et al., 2021) presented a novel adaptive full waveform approach to compute the moment tensor inversion for more complex source mechanisms. This method was applied to waveforms of the microseismic events. Microseismic events were detected not only in the Morrow B formation but in rocks lying above and beneath the reservoir. Figure 8.4 shows the borehole geophones installed in a single vertical well (well 13-10A) and the locations of the surface stations.

.

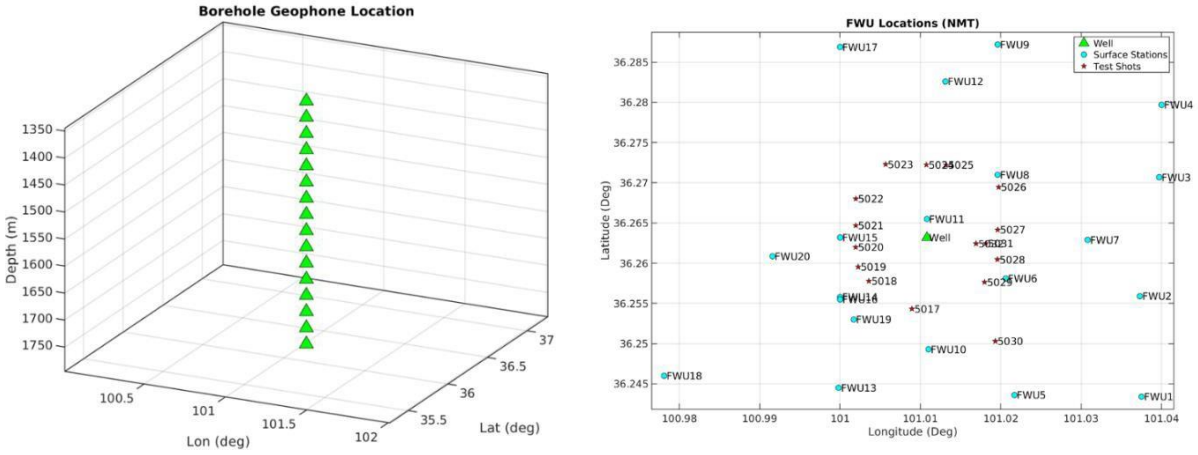

Figure 8.4: (a) Borehole geophones and (b) Location of the monitoring well (13-10A) and surface stations.

8.5 Materials and Methods

In order to predict the spatio-temporal stress variations and pore pressure distribution, a coupled mechanical-fluid flow model adopted from SWP research was integrated with multidisciplinary data. Data from cores, well logs and VSP were utilized to define the formation velocity variation due to stress changes. Other independent data such as microseismic data was integrated into the framework to improve the stress calibration and reduce the non-uniqueness of the simulation model. The dynamic reservoir model was calibrated for the primary and secondary recovery stages. However, this study focuses on the tertiary recovery period where time-lapse VSP acoustic measurements and microseismic data were obtained. Figure 8.5 illustrates a step-by-step framework employed to build and calibrate the coupled hydromechanical model. The calibration efforts were aided with the identification of uncertain model parameters. Among the uncertain parameters are the fracture properties (coefficient of friction, fault shear and normal Young's modulus). Preexisting natural fractures within the Morrow B formation were treated as small-like faults to help with fault property assigning. This study is based on the fact that microseismic event locations are known and small-like faults are added at the event locations. Key fault properties are varied until plastic failure occurs. Modeling microseismic events requires estimating the stress drop. The stress drop tensor estimated from the model is averaged across the fault. The seismic moment magnitudes (Mw) are computed using the stress tensor and compared to observed Mw. After attaining a well calibrated stress model, it will be utilized to predict the stress/strain changes and potential microseismicity. This study utilizes microseismic events to constrain the stress field and provide a more accurate representation of the dynamic stress changes in the subsurface. The situation in the Farnsworth field suggests that even though the average bottomhole pressure (BHP) increased from 4,000 psi (before August 2020) to 5,500 psi (after August 2020), the potential for fluid injection

to cause microseismicity in the subsurface did not result in the occurrence of several new microseismic events.

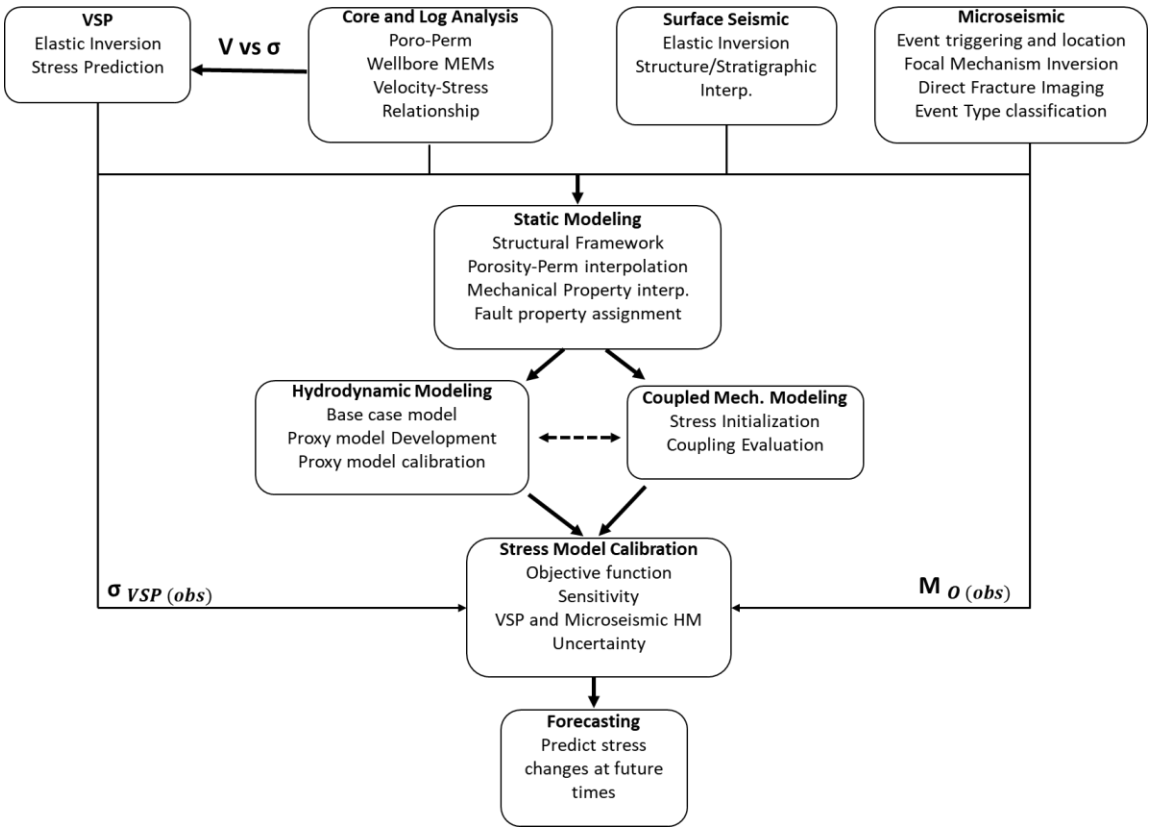

Figure 8.5: Schematic of the stress calibration workflow

8.5.1 Numerical Simulation Model Setup

Modeling microseismic events within the Morrow B was based on the coupled hydromechanical model. All simulation works were performed on the West side of the FWU. Figure 8.6 shows the reservoir geological model, main geomechanical model and the sector models. The geological model contains the structural framework of the formation with properties such as porosity and permeability associated with each cell. The main geomechanical model includes coarsened overburden, underburden and sideburden grid cells in addition to the 3D reservoir grid model. Sector models were derived from the primary geomechanical model in order to conduct detailed simulations in areas with microseismicity. The sector models utilized the main geomechanical model's VSP-constrained stress as their boundary condition. Grid cells within the sector model were assigned the same thickness but varying dimensions in the I and J direction. Modeling the changes in subsurface stress requires hydrodynamically derived estimations of pore pressures. The reservoir simulator models the fluid flow in the FWU reservoir and computes the resulting pressures, saturation distributions and temperature. All these works were performed in the Petrel environment. VISAGE (Schlumberger, 2018), a finite element simulator, utilized the output from the reservoir simulator to model a 3D stress loading on the reservoir grid model

and compute the rock stresses, deformations and failure. Table 1 shows the summary of the properties for each model utilized in the microseismic modeling.

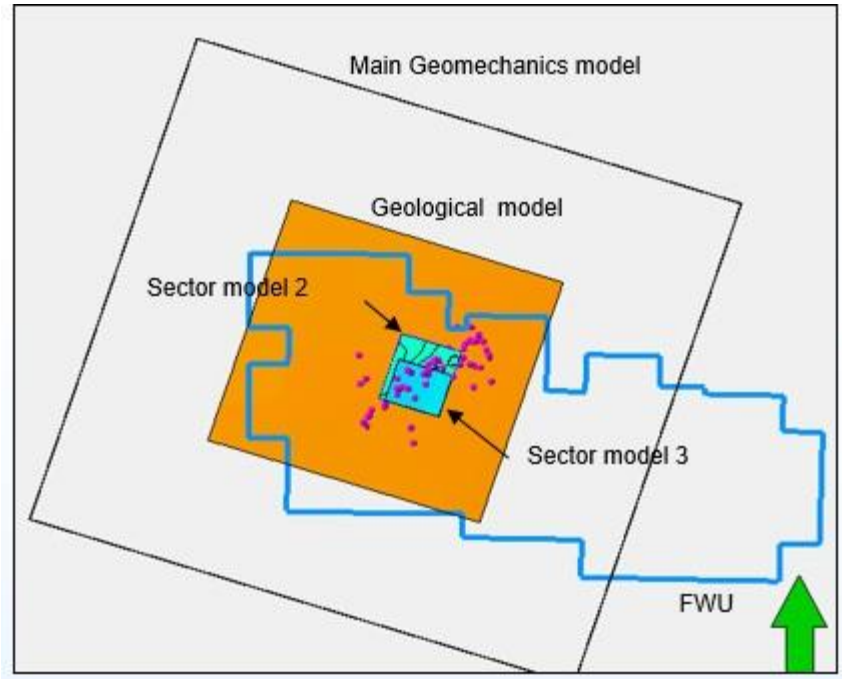

Figure 8.6: The several sector models created for investigating microseismic event occurrences.

Table 8.13: Summary of the properties for each model utilized in the microseismic modeling.

Model	Use	Cell size (I × J)	Total cells
Reservoir Simulation (Geological and fluid flow model)	Simulate fluid flow. Model pore pressure changes over time	100 × 100	2.7M
Main Geomechanical	Analyze effect of stress/strain on rock deformation	100 × 100	3.4M
Sector 2	Detail study on microseismic events	20 × 20	0.651M
Sector 3	Detail study on microseismic events	20 × 20	1.61M

8.5.2 Coupled Modeling

The 3D mechanical earth model was coupled with the reservoir simulation model to generate a dynamic geomechanical model. Even though two-way coupling appears rigorous, it is computationally costly, and requires input such as porosity-stress and permeability-stress relationships. For this reason, a one- way coupling method was utilized. The geomechanical simulation model takes as input, derived pore pressure distributions from the reservoir simulation model at the baseline and the monitor survey times. The production of hydrocarbons is associated with a decrease in pore pressures and an increase in the effective stress. In contrast, formation pore pressures increase during fluid injection with little or minimal fluid withdrawal. The production history at FWU is characterized by a gradual decline in reservoir pore pressure and an increase in the effective stress during the primary recovery stage. However, the implementation of waterflooding resulted in an opposite effect: an increase in the pore pressures and a decrease in effective stress. The tertiary recovery period is defined by fluctuating pore pressures as a result of the WAG injection, which influenced the effective stresses. This study modeled the effect of pore pressure fluctuations on the in-situ stresses using the Biot effective stress coefficient as expressed in equation (1). The effective stress is defined as a function of the Biot coefficient and pore pressure **(Biot, 1941)**,

$$\sigma' = \sigma - \alpha P \tag{8.1}$$

Where, P represents pore pressure, α is the Biot coefficient, σ' is the effective stress and σ is the total stress.

The Morrow B formation is heterogeneous and composed of quartz and clay minerals. For anisotropy materials, the Biot coefficient is expressed as,

$$\alpha = 1 - \frac{K_{dry}}{K_s} \tag{8.2}$$

where K_s is the mineral bulk modulus, and K_{dry} is the dry bulk modulus.

8.5.3 Fracture Plane Failure Criteria

Mohr-Coulomb failure criteria was utilized to determine the plastic failure at the fracture surface. The Mohr Coulomb failure criteria represents a set of linear equations that describes a failure envelope obtained from a plot of shear strength of a material and the applied normal stress. The failure criterion is represented mathematically as **(Karimnezhad et al., 2014)**,

$$\tau = c + (\sigma - P)tan(\theta) \tag{8.3}$$

Where τ is the shear stress, σ is the normal stress, P is the pore pressure and θ is the angle of internal friction.

By adjusting the normal and shear Young's modulus and the coefficient of friction, plastic failure occurs. Plastic failure is required to estimate the stress drop around the fault plane. The stress drop was evaluated as the differences in stresses for a coupled hydromechanical model without fault and a geomechanical model with fault added at microseismic event locations.

8.5.4 Microseismic Modeling

Microseismic events were simulated using a coupled hydromechanical model. Figure 8.7 classifies the events into distinct categories. Group 1 events can be found in the Morrow B, where model calibration, well log data, and field measurements are all readily available. Events in Group 2 and Group 3 occurred above and beneath the reservoir respectively. Modeling microseismic events below the Morrow B formation is challenging particularly due to the unavailability of well log data. This results in higher model uncertainty. Events classified under group 4 result from separate failure mode, which falls outside the scope of this study. Several microseismic events were identified and their moment tensors computed by fitting a waveform to the recorded data (Gao et al., 2021). Moment tensors only with good waveform fit were selected, hence not all events had moment tensor solutions. There were 32 tensor events and 136 magnitude events in the event collection. Tensor events had moment magnitude and sufficient quality (SNR) such that stress drop tensor and fault plane orientation information could be determined.

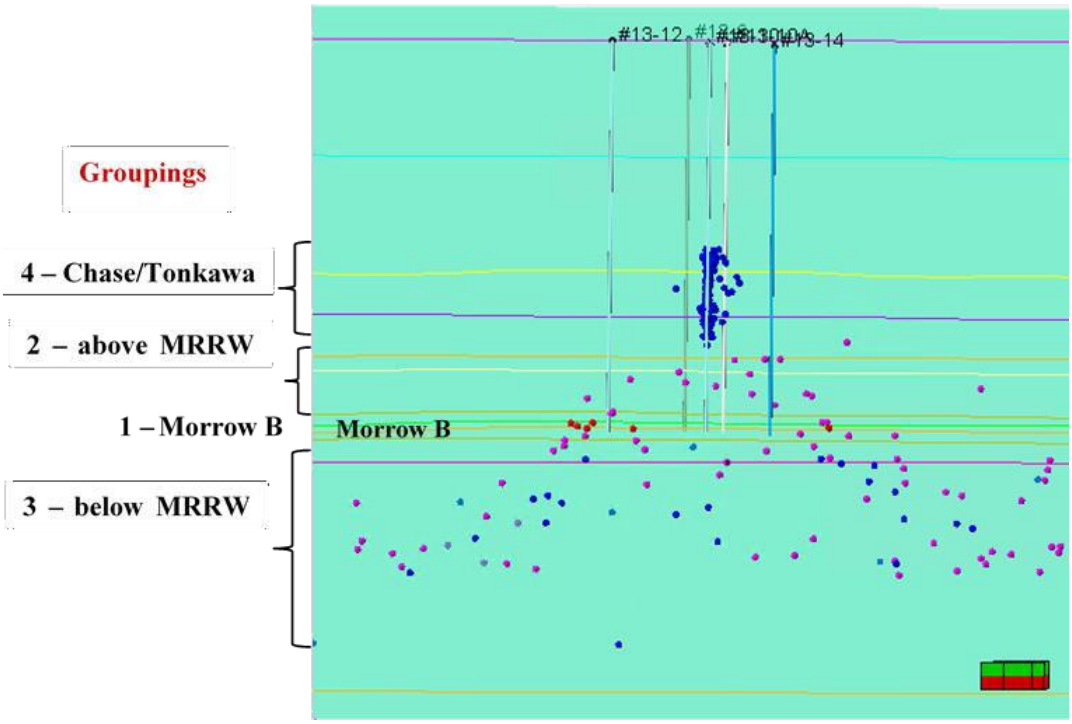

Figure 8.7: Cross-sectional view of the subsurface, showing microseismic events in the overlying formation, within the Morrow B and underlying formation.

8.5.5 Computation of Moment Magnitudes

Stress drops for the plastic cells were transformed into microseismic parameters (moment tensors and magnitudes) using a coupled hydro-geomechanical model. Moment tensor computation led to estimates of the seismic energy and moment magnitudes. Moment tensors describes the nature of forces acting at a seismic source that generates seismic waves. Moment tensors are useful for determining the focal mechanism of a seismic event. Mathematically, moment tensors can be expressed in terms of their eigenvalues (type of slip at seismic source) and eigenvectors (orientation of the slip). Each moment tensor can be decomposed into three constituents: an isotropic compression (IC) component, a compensated linear vector dipole (CLVD), and a double couple

(DC). Stress drops ($\Delta\sigma_{ik}$) and the displacement vector (r) are used to derive the seismic moment tensors, M_{ik}

$$M_{ik} = \int_V \Delta\sigma_{ik}(r).d^3r \approx \mu \int_V \Delta\gamma_{ik}(\underline{r}).d^3r \tag{8.4}$$

Alternatively, the moment tensor can be computed using a finite element model and focusing on elements that have undergone plastic deformation. As each element with linear interpolation functions has stress data at a single point, equation (8.4) simplifies as,

$$M_{ik} = \Delta\sigma V \tag{8.5}$$

Beginning with the plastic cells, the stress drops tensors ($\Delta\sigma_{ik}$ are computed. The volume of interest (V) is estimated using the cells that have undergone plastic failure. Although, the volume of interest is estimated from the numerical simulation model, it can be assigned as an uncertain. The strain energy which characterizes the energy released from rock deformation can be expressed as,

$$M_O = \left(\frac{1}{2}\sum_{i=1}^{3}\lambda_i^2\right)^{1/2} \tag{8.6}$$

The seismic energy is determined as,

$$E_s = M_O \times 1.6 \times 10^{-5} \tag{8.7}$$

The moment magnitude (M_w), expressed in dyne-cm is computed as,

$$M_w = \frac{2}{3}(logM_O - 16.1), \tag{8.8}$$

Where λ_1 to λ_3 are the eigenvectors of the moment tensor.
The above procedure was implemented in a python script to compute seismic energy and moment magnitudes utilizing cells that have undergone plastic deformation.

8.5.6 Fracture Parameterization

Fracture property parameterization permits the modeler to explore multiple fracture orientation scenarios and determine the optimal combination of parameters for simulating plastic failure in the rock formation. Variations in fracture parameters including fracture strike, dip, coefficient of friction, normal and shear Young's modulus were simulated and their impact to cause failure at the fault locations were evaluated. Table 2 summarizes the relative impact of the parameters on plastic failure. Figure 8.8 depicts the range of values selected for the fracture strike and dip.

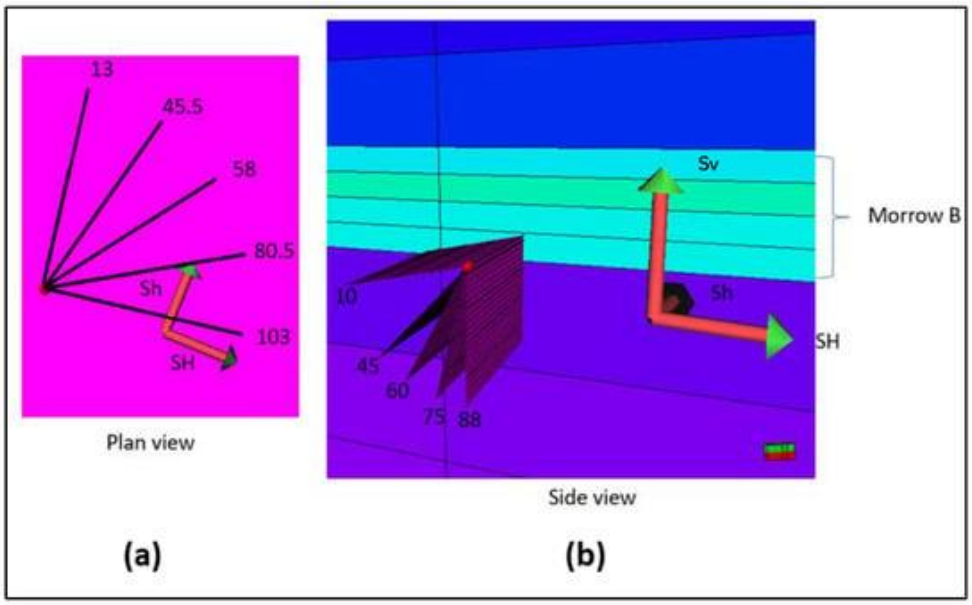

Figure 8.8. (a) Strikes and (b) dips illustrated during fracture property parameterization.

8.6 Simulation Results

This section presents the simulation results for utilizing a coupled hydromechanical model to predict the injection induced seismicity. Moment magnitudes computed using the finite element simulator are compared to the magnitudes derived from the field microseismic data. The primary contributing factor to the occurrence of microseismic events within the Farnsworth Field Unit is unknown despite the long history of waterflooding followed by CO_2 water-alternating-gas injection. The detection of microseismic events has been attributed to the reactivation of existing small fractures or aseismic geologic features within the formation. Results of a study is shown to identify the existence of a direct correlation of formation pore pressure changes and microseismic event occurrences. Analyses of a sensitivity study performed to determine the critical parameters and their impact on fault reactivation is demonstrated.

8.6.1 Effects of Injection Rates, Bottomhole Pressure on Microseismic occurrences

Figure 8.9 shows a plot of the gas injection and water injection rates. The accompanying bottomhole pressures and microseismic detections are plotted for the same time period (July 2020 – April 2021). The figure revealed that high bottomhole pressures are recorded during water injection periods and lower bottomhole pressures during gas injection. It can be seen from the plot that the microearthquakes detections are not directly correlated to the bottomhole pressure fluctuations. An increase in bottomhole pressure is not translated directly to high incidence of microearthquakes. The high spike in microearthquake detections is from shallow depths, shown by the large CLVD component, indicating a tensile cracking.

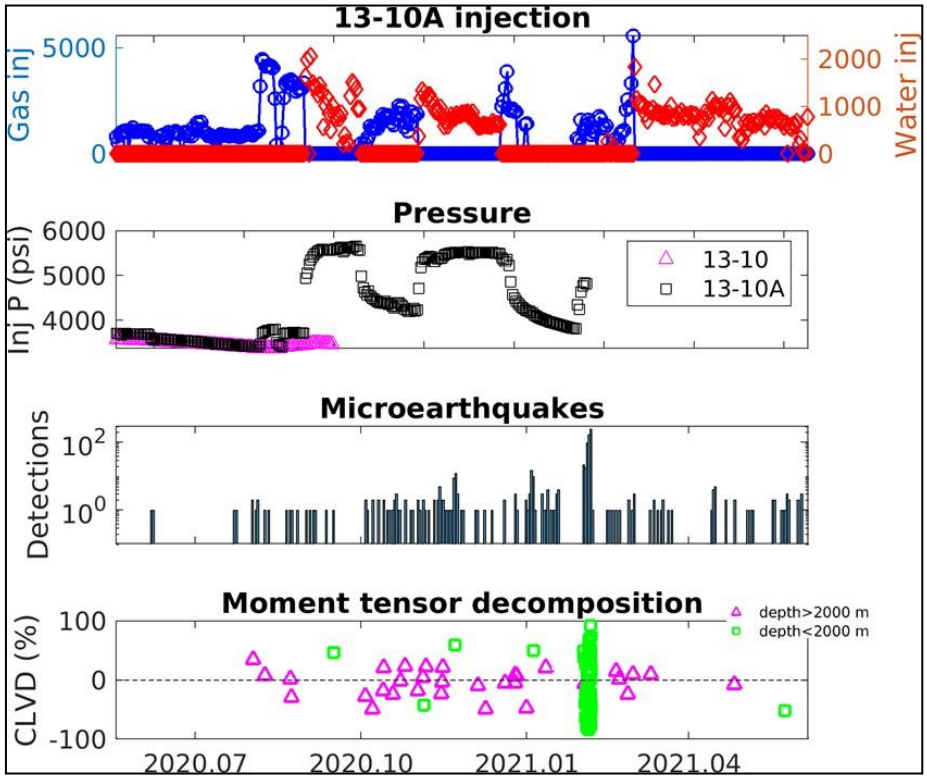

Figure 8.9: Plot showing the injection rates, bottomhole pressures and microseismic event detections from well 13-10A. Figure generated by Los Alamos National Lab (LANL).

Figure 8.10 depicts an extended plot of microseismic occurrences, bottomhole pressures, and the rate of water and gas injection from August 2019 to June 2021. Microseismic events are represented as magnitudes (green dots) with water injection rate shown in solid blue line, gas injection rate (solid red line) and the bottomhole pressures (black dots). A total of 136 microseismic events were analyzed for the time period. The magnitude of events ranges between -1.5 and +1.2, with the majority falling between -1.1 and 0. These occurrences are of small magnitudes and are therefore not felt at surface. The tertiary CO_2 WAG period shown in Figure 10, indicates increased water injectivity as high bottomhole pressures are recorded during water injection than CO_2 injection. Field operators tend to inject water at high bottomhole pressures to build the reservoir pressure and increase oil recovery. Although, this practice could lead to some oil recovered, there is a high likelihood of fractures being created. Injected water would preferentially travel through the fractures and channels created, leaving the oil behind.

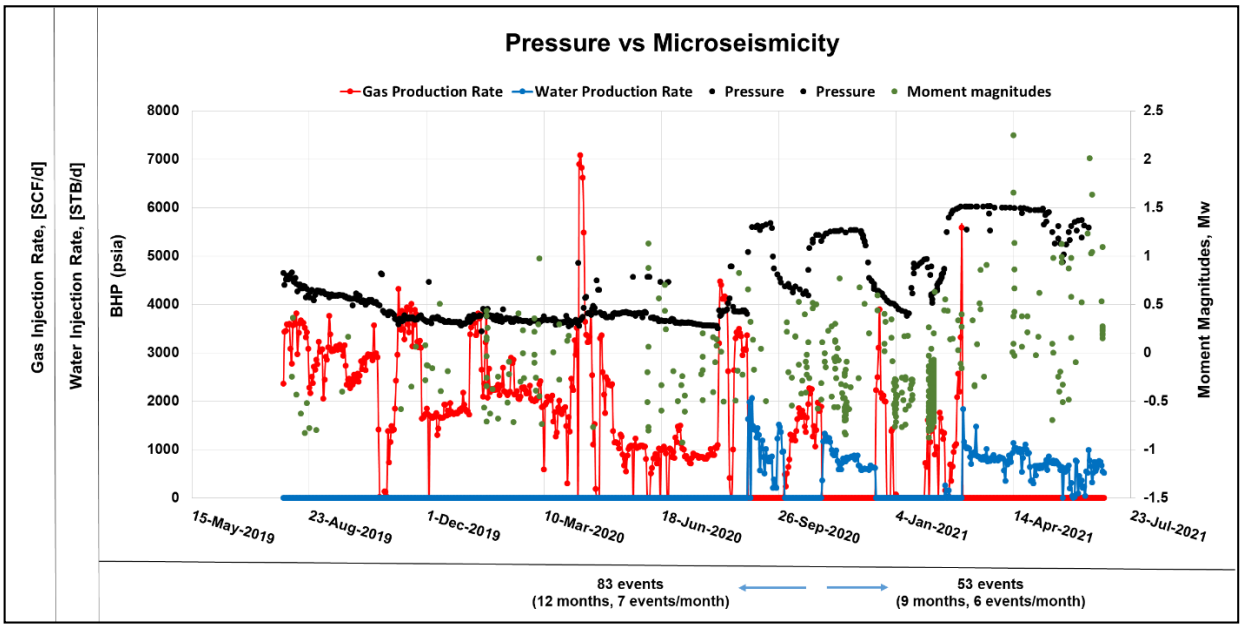

Figure 8.10: Extended plot of injection data, pressure and microseismic events with time. Moment magnitudes indicated in green dots.

In August 2020, there was an increase in bottomhole pressure (BHP). While the ratio of microearthquake occurrences per month did not increase much (from 7 events per month to 6 events per month), the events were spatially dispersed. Figure 8.11 shows the microseismic events around the 13-10A injection pattern. Prior to August 2020, microseismic occurrences clustered close to the injection well (#13-10A), but as pressure increased, the events occurred further from the injection well as shown in Figure 8.12.

.

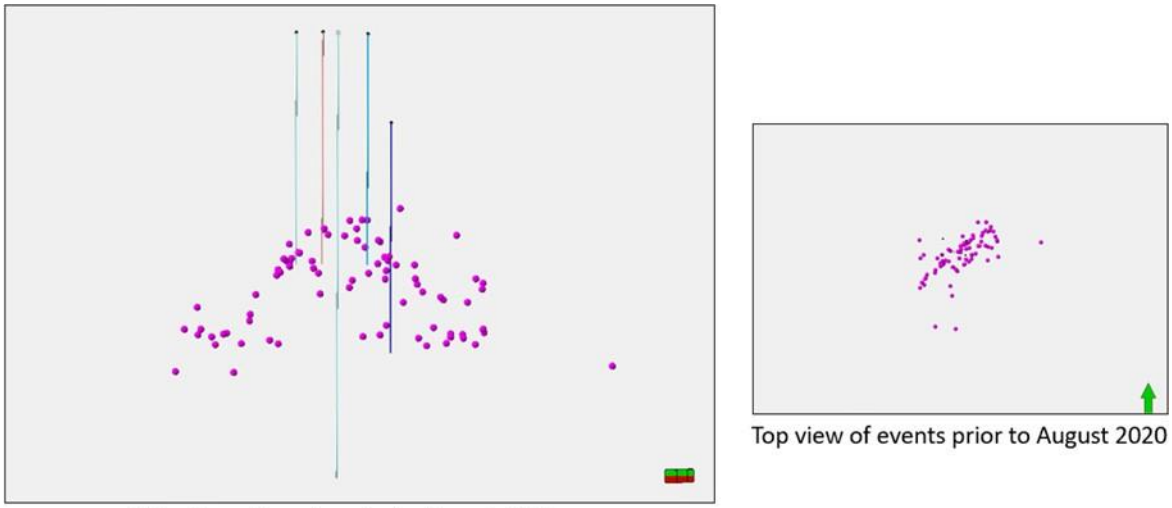

Figure 8.11: Side and top view of microseismic events prior to August 2020 around wells in the 13- 10A injection pattern.

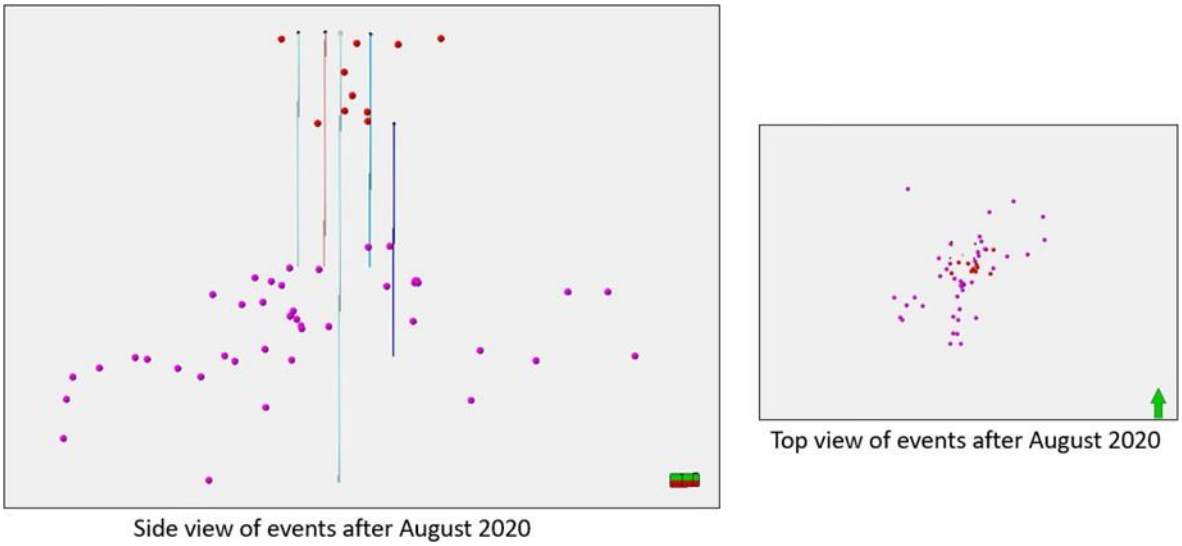

Figure 8.12: Side and top view of microseismic events after August 2020.

8.6.2 Main geomechanics and sector model calibration

Calibrating geomechanical models with 1D mechanical earth model (MEM) ensures that the predictions from the geomechanical simulations are in conformity with the prevailing in-situ stresses. The properties of the generated FWU geomechanical model were adjusted to produce a good agreement with the 1D MEM calibration at the wellbore. Figure 8.13 shows a comparison of 1D properties with 3D properties for the main geomechanics model. Elastic properties (Young's modulus, Poisson's ratio and Bulk density) are indicated in the first three tracks respectively. Pore pressure is shown in track four. The minimum horizontal stress, maximum horizontal and vertical stress at 1955 are in tracks five through seven, and shown again in tracks

eight to ten at 2014. The good agreement between the 1D MEM and the geomechanical model is seen within and around the Morrow B formation.

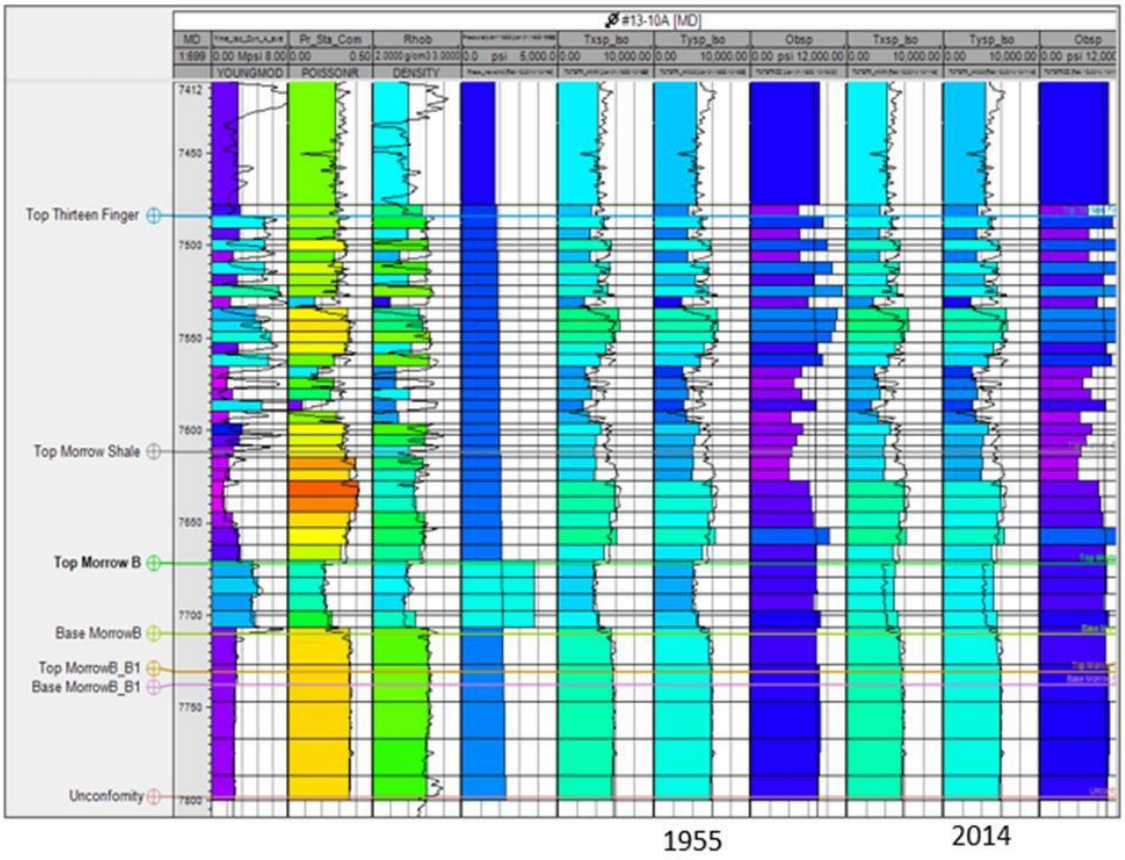

Figure 8.13: Comparison of 1D (black line) and 3D (shaded area) elastic and stress properties (1955 and 2014) for the Main Geomechanics model.

Sector models were created to examine detailed stress changes for time lapse VSP stress constraint and microseismic event modeling. However, it was important to ensure the same stress loading for the main geomechanical model is applied for the sector model. To verify that the loading has not changed, a comparison is made between the main geomechanical model and the sector model. A good agreement for the stress loading is observed between the sector model and the main geomechanical model as shown in Figure 8.14. After a successful calibration, the coupled geomechanical model is utilized to examine the stress changes and/or failure over time. The objective function for the time-lapse VSP and modeled velocity from stress change is formulated by running the sector model in the elastic region. For the microseismic event, plastic failure is required to identify the plastic cells and stress drop in cells around the fractures with microseismicity occurring.

.

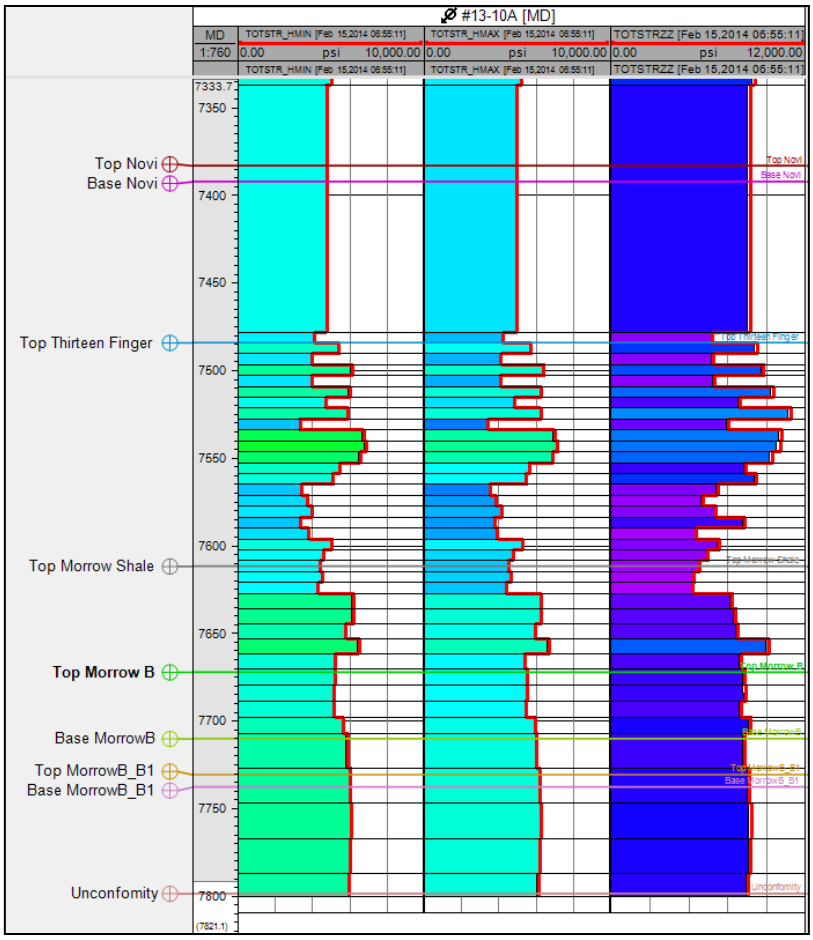

Figure 8.14: Comparison of stress between the main geomechanics model (area shade) and the sector model (red line).

8.6.3 Events within Morrow B Sandstone

As mentioned previously, microseismic events were separated into four groups and for the purpose of this study, events occurring in the Morrow B will be the main focus. Figure 8.15 shows a plan view of the stress drops. The amount of stress released is measured by the stress drop following an occurrence. The stress drops are closely related to the microseismic occurrence and reflects the magnitude of the microseismic event and the potential for future seismic activity. An event with a larger stress drop will have higher moment magnitudes. There are two events within the Morrow B formation with event 1 occurring on January 31, 2020 and event 2 occurring on March 2, 2020.

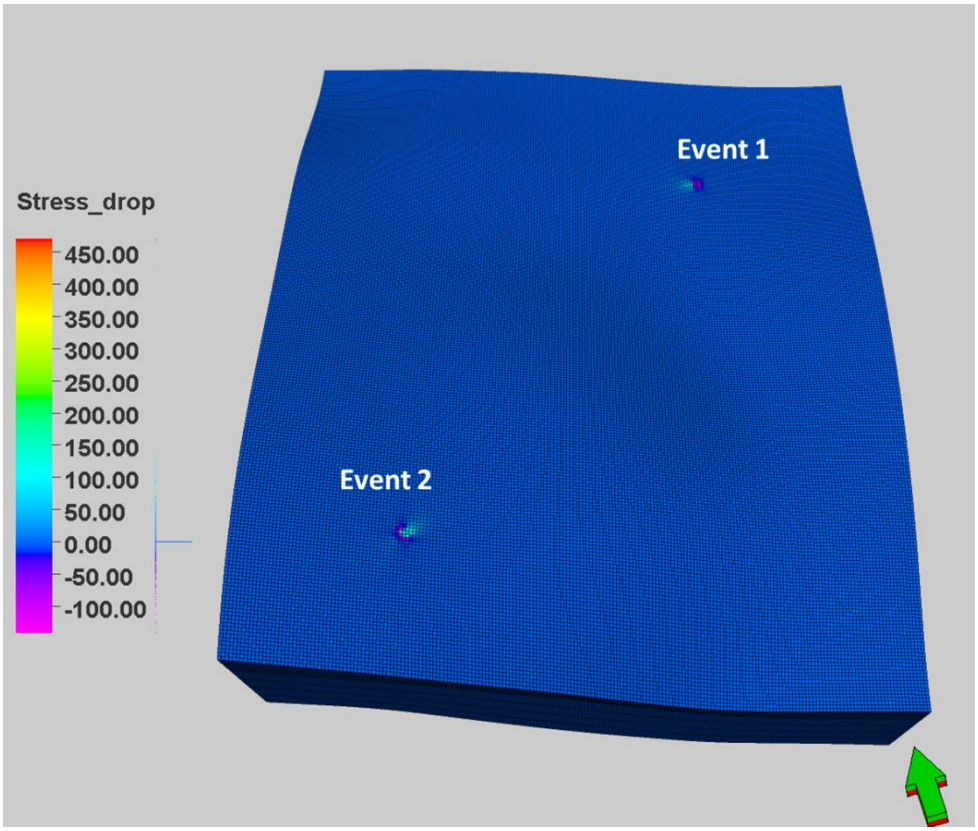

Figure 8.15: A spatial distribution of the stress drop (Δσ) with microseismic events (events 1 and 2) within the Morrow B formation.

8.6.4 Sensitivity Study on Fault Properties

A sensitivity analysis was conducted to determine the impact of uncertain fault properties on fault reactivation and associated seismicity during the historical period of CO_2-WAG injection. The parameter ranges of the fault strikes and dips, coefficient of friction, normal and shear Young's modulus were explored using the one variable at a time (OVAT) method. We determined that the normal and shear Young's modulus had a smaller impact on the results for the parameter ranges examined. Nevertheless, the study revealed that the friction coefficient (μ) was the most sensitive parameter, with inelastic failure occurring with lower (μ). Table 2 summarizes the parameter ranges and their relative impact on fault failure.

Table 8.14: Summary of the parameters, range modeled, and relative impact on plastic failure. The colors denote a low (gray), medium (orange), and large (green) observable impact on plastic failure.

Parameter	Range	Failure impact	Color bar
Fracture dip	13, 30.5, 58, 80.5, 103	more failure towards Sh	
Fracture strike	10, 45, 60, 75, 88	more failure in mid dips	
Grid cell size	20′, 50′, 100′	more failure with smaller cell	
Friction coefficient (μ)	0.36, 0.58, 0.84, 1.19	more failure with lower μ	
Normal / Shear Yme (Mpsi/ft)	(176/66), (135/52), (225/83)	very small change	

8.6.5 Moment Magnitudes Computation Results

Beginning with Scenario 1, faults are introduced at the locations of microseismic events and essential fault parameters are varied until inelastic failure occurs. Figure 8.16 depicts the plastic cells surrounding a fault plane. The graph on the bottom shows the simulated pressures and total stress for a single plastic cell over time. Only the plastic failure cells are utilized to calculate the stress drop around the fracture plane. The stress drop for each plastic cell is computed as the differential between the total stresses derived from a coupled mechanical model with no fault and a model with fault addition. Modeling the precise timing of event failure is outside the scope of this work, however we have leading knowledge of when the event happened and the stress prior to the event time. The statistics of the stress drop for a coupled hydromechanical case with a coefficient of friction (0.53), strike (322.25^{O}) and dip (78.99^{O}) is shown in Table 8.3.

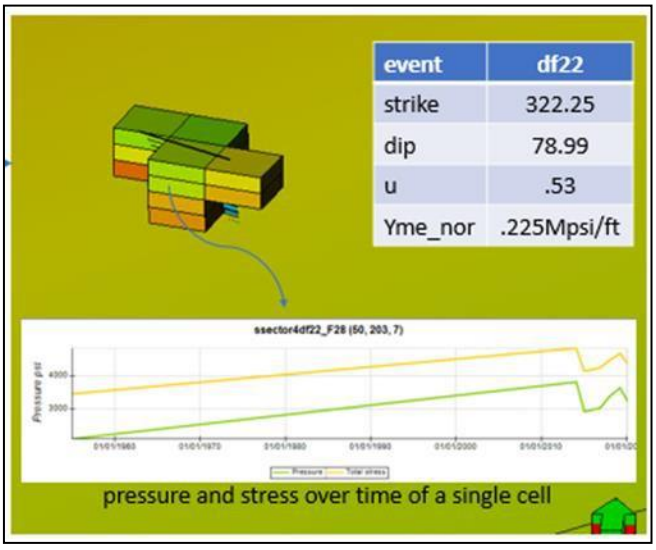

Figure 8.16: Microseismic event modeling with a single orientation fracture and cells showing plastic strain.

Table 8.15: Statistics of delta stress from plastic cells around the fracture plane.

Name	Type	Min	Max	Delta	N	Mean	Std	Var	Sum
xxdiff22	Continuous	-9.65	127.07	136.72	1100	77.20	39.28	1543.07	849.19
yydiff22	Continuous	-4.25	69.55	73.80	11.00	35.01	24.41	595.82	385.08
zzdiff22	Continuous	89.43	220.73	131.30	11.00	173.06	34.34	1179.40	1903.70
xydiff22	Continuous	1.38	42.45	41.07	11.00	14.12	12.41	154.00	155.33
yzdiff22	Continuous	104.11	195.97	91.85	11.00	146.97	27.18	738.86	1616.65
zxdiff22	Continuous	75.46	166.07	90.62	11.00	127.89	30.29	917.43	1406.84

The mean stress drops together with the volume of interest were utilized to generate the moment tensors. The unit of the moment tensor is dyne-cm. The stress drops were converted from psi to dyne/cm^2. The volume of interest (V) was estimated in cm^3. Utilizing the Python script, the moment magnitudes of the seismic event (event df22) is computed as shown in Figure 8.17.

```
event_df22.txt

input tensor (AR system) is:
 [[ 5.323e+14 -9.735e+13  8.818e+14]
 [-9.735e+13  2.414e+14 -1.013e+15]
 [ 8.818e+14 -1.013e+15  1.193e+15]]

Strain Energy (Mo) =  1641843594103896.0  dyne-cm

Seismic Energy (Es) =  26269497505.66234  dyne-cm

Moment Magnitude (Mw) =  -0.5531121447756964

Sorted e-values:
 [ 3.23298117e+14 -5.81223544e+14  2.22462543e+15]

Sorted eigen-vectors:
 [[ 0.79881047 -0.41321616 -0.4372119 ]
 [ 0.58859019  0.68706715  0.42602855]
 [-0.12435205  0.5976547  -0.79205141]]
```

Figure 8.17: Seismic moment magnitude calculated based on equations listed under computation of moment magnitudes. The input tensor is the moment tensor. The moment magnitude is highlighted.

For each microseismic event, Mw was determined for each potential fracture orientation using the equations outlined under moment magnitudes computation. Table 8.4 displays the simulated Mw and associated parameters. Just above the Morrow B sand, in the Morrow shale, is where Event 1 can be found. Event 2 is located in Morrow B.

Table 8.16: Results and parameters for modeled microseismic events.

Event	Observed Mw	Modeled Mw	Strike (degrees)	Dip (degrees)	Coefficient of friction	Yme normal (Mpsi/ft)	Yme shear (Mpsi/ft)
1	-0.839		276	66	0.36	0.135	0.051
1	-0.839	-0.585	18	66	0.36	0.135	0.051
2	-0.433		79	24	0.36	0.225	0.083
2	-0.433	-0.47	322	79	0.36	0.225	0.083

Starting with event 2 (located within the Morrow B sand), we find that the most probable orientation is the one with 322^O strike and 79^O dip. With a coefficient of friction of 0.53 (friction angle of 28^O), plastic failure develops. However, the orientation of 79^O strike and 24^O dip has a very modest failure even at 0.36 coefficient of friction; this indicates that it is more difficult for failure to occur in this stress orientation when the dip is closer to horizontal. This is congruent with findings from the section on fracture property parameterization. Each of the two probable orientations for Event 1 has a 66^O dip. Both orientations are viable. The moment magnitude for both modeled events fall within the same magnitude range as the observed Mw, and the magnitude of event 1 is less than that of event 2, which corresponds to the observed values.

8.7 Discussion

In the study of induced seismicity, especially in the setting of fluid injection/production, the use of coupled hydrogeomechanical modeling approaches has become more and more prominent. The outcomes of our modeling approach for examining the mechanisms underlying induced seismicity are discussed in this section, along with any potential ramifications regarding subsurface seismic hazard mitigation. Our modeling framework was based on a coupled hydromechanical approach that utilizes pore pressures estimates from the reservoir simulation model to simulate the spatiotemporal evolution of induced seismicity. Numerical simulations were conducted for a five-spot injection pattern in Morrow B formation. Numerical simulations were performed in Petrel environment where the Eclipse E300 computes the pressure and saturation distribution for each timestep and a finite element simulator (VISAGE), models the complex changing stress field. We showed how the method of inelastic failure was utilized to understand and model microseismic event occurrences. The outcomes of the geomechanical modeling were presented against observations of induced seismicity.

8.7.1 Stratigraphy

The stratigraphy of a formation can influence the likelihood of small seismic events occurring. Injecting into formations with close proximity to the crystalline base rock has resulted in the occurrence of high magnitude earthquakes. The crystalline basement is a dense and fractured formation that often underlies the sedimentary formation. The crystalline basement acts as barrier to fluid flow. The presence of faults intersecting the sedimentary strata and the close proximity of the injection formation and basement rock are two key factors that induces deep matured fault structures to slip (Skoumal et al., 2021). This was found to be the primary contributing factor to the occurrence of high magnitude earthquakes in West Texas Delaware basin and Oklahoma. At FWU, all wells inject into the Morrow B formation, which is overlain and underlain by excellent seal rocks. Also, there are no identified faults intersecting the producing formation and the crystalline basement.

8.7.2 Fluid injection

Wastewater injection has been associated with increased microseismic activities (Kozlowska et al., 2018). In waste disposal, produced water from oil and gas operations is injected into deep underground formation. The success of the underground disposal is dependent on the integrity of the geologic formation to safely contain the injected fluids to avoid contamination with underground water sources. Wastewater injection is different from oil and gas production with the former involving fluid injection without withdrawal. The result is a buildup of pore pressures which causes the subsurface rock to reach a critical stress state, causing the formation to rupture, generating small seismic events or trigger larger earthquakes. The situation observed in FWU

involves the simultaneous production of hydrocarbons and the injection of fluids. Pore pressure increase from fluid injection can be potentially balanced with hydrocarbon production. Although no direct correlation was found between fluid injection and occurrence of seismic events in FWU, pore pressure changes could be a primary contributing factor to induced seismicity, as they altered the effective stresses in the rock mass, inducing failure in the intact formation or along optimally oriented planes of weakness.

.

8.7.3 Analysis on Microseismic Modeling

Microseismic events are indications of subsurface stress changes typically have magnitudes less than 2.0 on the Richter scale. Although, low magnitude seismic events are not felt on surface, they are important indicators of rock behavior and can provide valuable information about the progressive failure of a rock mass due to hydrocarbon production or fluid injection. The method of using inelastic failure to model the process of rocks deforming and ultimately failing under stress was shown to be successful in this study. The magnitudes of events modeled in this study were small ($Mw < 2$), not large enough to raise safety concerns. While magnitudes may be small, the location and number of events play significant roles in determining safety. Microseismic events were seen to spread out from the injection/production wells with pressure increase. The low magnitude earthquakes occurred at lower rates with pore pressure variation. Overall, the results of our study demonstrate the effectiveness of geomechanical modeling as a tool for investigating induced seismicity.

8.8 Conclusion

Microseismic events were successfully modeled within the Morrow B by incorporating faults into the coupled hydromechanical model and running the simulation model for regions with plastic failure. The following findings resulted from the effective application of multidisciplinary data (time-lapse VSP seismic data and microseismic data) to characterize the dynamic stress field associated with the ongoing CO_2-EOR operation. The results of analysis are as follows:

1. A manual framework for integrating multidisciplinary data to improve stress prediction of the Morrow B using VSP and microseismic data was developed. The mechanical earth model was initially calibrated using the VSP data, which carries the combined effect of fluid substitution and stress changes on the seismic velocities. Integration of microseismic data allowed for further constraint of the model. To assess the impact of key model parameters on the stress calibration, the integration framework can be automated and several simulation cases could be run.

2. Having prior knowledge of the microseismic event locations, and adding fractures at these locations were useful in the geomechanical stress modeling and prediction. This procedure required the reservoir engineer to specify fault locations within the geomechanical model before running for failure. Moment magnitudes computed were within the same magnitude for events in the Morrow B, suggesting the suitability of this approach. Nonetheless, the coupled hydro-geomechanical model could be run for plastic failure and regions of deformations are identified and compared to the known microseismic event locations.

3. The magnitudes of the microseismic events observed in FWU are not large enough to cause safety concerns. The absence of active faults within the Morrow B and the presence of an underlying Morrow shale could be a major contributing factor to the occurrence of low magnitudes microseismic events.

References

Acheampong, S. A., Ampomah, W., Khaniani, H., Will, R., & Sarkodie-Kyeremeh, J. (2022). Quantitative interpretation of time-lapse seismic data at Farnsworth field unit: Rock physics modeling, and calibration of simulated time-lapse velocity responses. *Greenhouse Gases: Science and Technology*, *12*(6), 671–697. https://doi.org/https://doi.org/10.1002/ghg.2184

Adu-Gyamfi, B., Ampomah, W., Tu, J., Sun, Q., Erzuah, S., & Acheampong, S. (2022). Assessment of chemo-mechanical impacts of CO_2 sequestration on the caprock formation in Farnsworth oil field, Texas. *Scientific Reports*, *12*(1), 1–23.

Ahmmed, B., Appold, M. S., Fan, T., McPherson, B. J. O. L., Grigg, R. B., & White, M. D. (2016). Chemical effects of carbon dioxide sequestration in the Upper Morrow Sandstone in the Farnsworth, Texas, hydrocarbon unit. *Environmental Geosciences*, *23*(2), 81–93.

Ajo-Franklin, J. B., B. J. Minsley, and T. M. Daley, 2007, Applying compactness constraints to differential traveltime tomography: Geophysics, 72, no. 4, R67–R75.

Allen, R. V. (1978). Automatic earthquake recognition and timing from single traces. *Bulletin of the Seismological Society of America*, *68*(5), 1521–1532.

Amini, H., & MacBeth, C. (2015). Calibration of Rock Stress-sensitivity Using 4D Seismic Data. *77th EAGE Conference and Exhibition 2015*, *2015*(1), 1–5.

Ampomah, W., Balch, R., Cather, M., Rose-Coss, D., Dai, Z., Heath, J., Dewers, T., & Mozley, P. (2016). Evaluation of CO2 Storage Mechanisms in CO2 Enhanced Oil Recovery Sites: Application to Morrow Sandstone Reservoir. *Energy & Fuels*, *30*. https://doi.org/10.1021/acs.energyfuels.6b01888

Ampomah, W., Balch, R. S., & Grigg, R. B. (2015). Analysis of upscaling algorithms in heterogeneous reservoirs with different recovery processes. *SPE Production and Operations Symposium*.

Ampomah, W., Balch, R. S., Grigg, R. B., Will, R., Dai, Z., & White, M. D. (2016). Farnsworth field CO2- EOR project: performance case history. *SPE Improved Oil Recovery Conference*.

Ampomah, W., Will, R., McMillan, M., Bratton, T., Huang, L., El-Kaseeh, G., Liu, X., Li, J., & Lee, D. (2021). Improving Subsurface Stress Characterization for Carbon Dioxide Storage Projects. *Proceedings of the 15th Greenhouse Gas Control Technologies Conference*, 15–18.

Anderson, E. M. (1905). The dynamics of faulting. *Transactions of the Edinburgh Geological Society*, *8*(3), 387–402.

Asante, J., Ampomah, W., Rose-Coss, D., Cather, M., & Balch, R. (2021). Probabilistic assessment and uncertainty analysis of CO2 storage capacity of the morrow b sandstone—farnsworth field unit. *Energies*, *14*(22). https://doi.org/10.3390/en14227765

Asnaashari, A., R. Brossier, S. Garambois, F. Audebert, P. Thore, and J.Virieux, 2015, Time-lapse seismic imaging using regularized full-wave-form inversion with a prior model: Which strategy?: Geophysical Pro-specting, 63,78–98.

Baker, T., Granat, R., & Clayton, R. W. (2005). Real-time earthquake location using Kirchhoff reconstruction. *Bulletin of the Seismological Society of America*, *95*(2), 699–707.

Balch, R. and McPherson, B. (2022). Associated Storage With Enhanced Oil Recovery. In Geophysical Monitoring for Geologic Carbon Storage, L. Huang (Ed.). https://doi.org/10.1002/9781119156871.ch20

Balch, R., & McPherson, B. (2022). Associated Storage With Enhanced Oil Recovery: A Large-Scale Carbon Capture, Utilization, and Storage Demonstration in Farnsworth, Texas, USA. Geophysical Monitoring for Geologic Carbon Storage, 343-360.

Batzle, M. L., Han, D.-H., & Hofmann, R. (2006). Fluid mobility and frequency-dependent seismic velocity—Direct measurements. *Geophysics*, *71*(1), N1–N9.Beck, L. (2020). The US Section 45Q Tax Credit for Carbon Oxide Sequestration: An Update . April.

Bender, B. (1983). Maximum likelihood estimation of b values for magnitude grouped data. *Bulletin of the Seismological Society of America*, *73*(3), 831–851.

Biot, M. A. (1941). General Theory of Three-Dimensional Consolidation. *Journal of Applied Physics*, *12*(2), 155–164. https://doi.org/10.1063/1.1712886

Britt, L. K., & Schoeffler, J. (2009). The geomechanics of a shale play: What makes a shale prospective! SPE Eastern Regional Meeting.

Brune, J. N. (1970). Tectonic stress and the spectra of seismic shear waves from earthquakes. *Journal of Geophysical Research*, *75*(26), 4997–5009.

Byerlee, J. (1978). Friction of rocks. *Rock Friction and Earthquake Prediction*, 615–626.

Cather, M., Rose-Coss, D., Gallagher, S., Trujillo, N., Cather, S., Hollingworth, R. S., Mozley, P., & Leary, R. J. (2021). Deposition, Diagenesis, and Sequence Stratigraphy of the Pennsylvanian Morrowan and Atokan Intervals at Farnsworth Unit. *Energies*, *14*(4), 1057.

Carcione, J., S. Picotti, F. Cavallini, and J. Santos, 2012, Numerical test of the Schoenberg- Muir theory: Geophysics, 77, no. 2, C27–C35.

Chi, B., K. Gao, and L. Huang, 2017, Least-squares reverse time migration guided full-waveform inversion: 87th Annual International Meeting, SEG, Expanded Abstracts, 1471– 1475.

Chen, R., Xue, X., Park, J., Datta-Gupta, A., & King, M. J. (2019). New insights into the mechanisms of seismicity in the Azle area, North Texas. *Geophysics*, *85*(1), EN1–EN15. https://doi.org/10.1190/geo2018-0357.1

Czoski P., 2014, Geologic characterization of the Morrow B reservoir in Farnsworth Unit, TX using 3D VSP seismic, seismic attributes, and well logs: M.S. Thesis, New Mexico Tech.

Da Silva, F. V, Debande, G. F., Pereira, C. A., & Plischke, B. (1990). Casing collapse analysis associated with reservoir compaction and overburden subsidence. *European Petroleum Conference*.

Dai, Z., Viswanathan, H., Fessenden-Rahn, J., Middleton, R., Pan, F., Jia, W., Lee, S.-Y., McPherson, B., Ampomah, W., & Grigg, R. (2014). Uncertainty quantification for CO2 sequestration and enhanced oil recovery. *Energy Procedia*, *63*, 7685–7693.

Daley, T. M., L. Myer, J. E. Peterson, E. L. Majer, and G. M. Hoversten (2008), Time-lapse crosswell seismic and VSP monitoring of injected CO2 in a brine aquifer, Environ. Geol., 54(8), 1657–1665.

DiSiena, J. P., & Gaiser, J. E. (1983). Three-component vertical seismic profiles: An application of gal'perin's polarization-position correlation technique. In *SEG Technical Program Expanded Abstracts 1983* (pp. 522–524). Society of Exploration Geophysicists.

Dvorkin, J., Nur, A., & Chaika, C. (1996). Stress sensitivity of sandstones. *Geophysics*, *61*(2), 444–455.

Dziewonski, A. M., Chou, T., & Woodhouse, J. H. (1981). Determination of earthquake source parameters from waveform data for studies of global and regional seismicity. *Journal of Geophysical Research: Solid Earth*, *86*(B4), 2825–2852.

Eberhart-Phillips, D., Han, D.-H., & Zoback, M. D. (1989). Empirical relationships among seismic velocity, effective pressure, porosity, and clay content in sandstone. *Geophysics*, *54*(1), 82–89.

Egorov, A., R. Pevzner, A. Bóna, S. Glubokovskikh, V. Puzyrev, K. Tertysh-nikov, and B. Gurevich, 2017, Time-lapse full-waveform inversion of vertical seismic profile data: Workflow and application to the CO2CRCOtway project: Geophysical Research Letters, 44, 7211–7218.

El-Kaseeh, G., Czoski, P., Will, R., Balch, R., Ampomah, W., & Li, X. (2019). Time-lapse vertical seismic profile for CO 2 monitoring in carbon capture, utilization and sequestration/EOR, Farnsworth project. *2018 SEG International Exposition and Annual Meeting, SEG 2018*, *Figure 2*, 5377–5381. https://doi.org/10.1190/segam2018-2995747.1

Fei, T.W., Luo, Y., Yang, J., Liu, H., Qin, F., 2015. Removing false images in reverse time migration: the concept of de-priming. Geophysics 80 (6), S237¨CS244.

Freund, D. (1992). Ultrasonic compressional and shear velocities in dry clastic rocks as a function of porosity, clay content, and confining pressure. *Geophysical Journal International*, *108*(1), 125–135.

Gaiser, J. E., Ward, R. W., & DiSiena, J. P. (1982). Three component vertical seismic profiles:

Polarization measurements of P-wave particle motion for velocity analysis. In *SEG Technical Program Expanded Abstracts 1982* (pp. 162–165). Society of Exploration Geophysicists.

Gallagher, S. (2014). Depositional and Diagenetic Controls on Reservoir Heterogeneity: Upper Morrow Sandstone, Farnsworth Unit, Ochiltree County, Texas.

Gao, K., Huang, L., Qin, Y., Chen, T., Coblentz, D., El-kaseeh, G., & Bratton, T. (2021). Adaptive full- waveform moment-tensor inversion of microseismic data. In *SEG/AAPG/SEPM First International Meeting for Applied Geoscience & Energy* (p. D011S087R001). https://doi.org/10.1190/segam2021- 3594469.1

Gao, K., and L. Huang, 2019, Acoustic- and elastic-waveform inversion with total generalized p-variation regularization: Geophysical Journal International, 218, no. 2, 933–957.

Gunda, D., Ampomah, W., Grigg, R., & Balch, R. (2015). Reservoir fluid characterization for miscible enhanced oil recovery. *Carbon Management Technology Conference 2015: Sustainable and Economical CCUS Options*, *CMTC 2015*, *2*(December), 1142–1158. https://doi.org/10.7122/440176- ms

Han, L., Wong, J., & Bancroft, J. C. (2009). Hypocenter location using hodogram analysis of noisy 3c microseismograms. *Consortium for Research in Elastic Wave Exploration Seismology (CREWES) Research Report*, *29*.

Hawkes, C. D., McLellan, P. J., Zimmer, U., & Bachu, S. (2004). Geomechanical factors affecting geological storage of CO2 in depleted oil and gas reservoirs: risks and mechanisms. *Gulf Rocks 2004, the 6th North America Rock Mechanics Symposium (NARMS)*.

Heffer, K. J., Koutsabeloulis, N. C., & Wong, S. K. (1994). Coupled geomechanical, thermal and fluid flow modelling as an aid to improving waterflood sweep efficiency. *Rock Mechanics in Petroleum Engineering*.

Herwanger, J. (2014). Seismic geomechanics: how to build and calibrate geomechanical models using 3D and 4D seismic data. *Education Days Stavanger 2014*, cp-439.
Hudson, J. A., Pearce, R. G., & Rogers, R. M. (1989). Source type plot for inversion of the moment tensor. Journal of Geophysical Research: Solid Earth, 94(B1), 765–774.

Huang, L., 2022. Geophysical Monitoring for Geologic Carbon Storage, AGU-Wiley Monograph, John Wiley & Sons.

Hutton, A. C. (2015). Geophysical Modeling and Structural Interpretation of a 3D Reflection Seismic Survey in Farnsworth Unit, Tx.

Intergovernmental Panel on Climate Change. (2022). Climate Change 2022 - Mitigation of Climate Change.- Full Report. In *Cambridge University Press* (Issue 1).

Jenkins, C. R., Cook, P. J., Ennis-King, J., Undershultz, J., Boreham, C., Dance, T., ... & Urosevic, M. (2012). Safe storage and effective monitoring of CO2 in depleted gas fields. *Proceedings of the National Academy of Sciences*, *109*(2), E35-E41.

Jin, X., Shah, S. N., Roegiers, J.-C., & Zhang, B. (2015). An integrated petrophysics and geomechanics approach for fracability evaluation in shale reservoirs. *SPE Journal*, *20*(03), 518–526.

Kamei, R., and D. Lumley, 2017, Full waveform inversion of repeating seis-mic events to estimate time-lapse velocity changes: Geophysical Journal International, 209, 1239–1264.

Kanamori, H., & Brodsky, E. E. (2004). The physics of earthquakes. *Reports on Progress in Physics*, *67*(8), 1429.

Karimnezhad, M., Jalalifar, H., & Kamari, M. (2014). Investigation of caprock integrity for CO2 sequestration in an oil reservoir using a numerical method. *Journal of Natural Gas* Science and Engineering, 21,1127–1137. https://doi.org/https://doi.org/10.1016/j.jngse.2014.10.031

Khaksar, A., Griffiths, C., & McCann, C. (1999). Effective stress coefficient for P-and S-wave velocity and quality factor in sandstone, example from Cooper Basin-Australia. In *SEG Technical Program Expanded Abstracts 1999* (pp. 192–195). Society of Exploration Geophysicists.

Kozlowska, M., Brudzinski, M., Friberg, P., Skoumal, R., Baxter, N., & Currie, B. (2018). Maturity of nearby faults influences seismic hazard from hydraulic fracturing. *Proceedings of the National Academy of Sciences*, *115*, 201715284. https://doi.org/10.1073/pnas.1715284115

Liu, X., Y. Liu, and M. Khan, (2018), Fast least-squares reverse time migrationof VSP free-surface multiples with dynamic phase-encoding schemes:Geophysics, 83, no. 4, S321–S332,

Lumley, D. E. (2001). Time-lapse seismic reservoir monitoring. *Geophysics*, *66*(1), 50–53.

Lumley, D., D. C. Adams, M. Meadows, S. Cole, and R. Wright, 2003, 4D seismic data processing issues and examples: 73rd Annual International Meeting, SEG, Expanded Abstracts, 1394–1397.

Lynch, T., Fisher, Q., Angus, D., & Lorinczi, P. (2013). Investigating stress path hysteresis in a CO2 injection scenario using coupled geomechanical-fluid flow modelling. *Energy Procedia*, *37*, 3833–3841.

Ma, T., Lin, D., Tang, C., Yadav, K. P., Feng, Z., & Ma, K. (2020). Microseismic Monitoring, Positioning Principle, and Sensor Layout Strategy of Rock Mass Engineering. *Geofluids*, *2020*, 8810391. https://doi.org/10.1155/2020/8810391

MacBeth, C. (2004). A classification for the pressure-sensitivity properties of a sandstone rock frame. *Geophysics*, *69*(2), 497–510.

Martínez-Garzón, P., Kwiatek, G., Ickrath, M., & Bohnhoff, M. (2014). MSATSI: A MATLAB package for stress inversion combining solid classic methodology, a new simplified user-

handling, and a visualization tool. *Seismological Research Letters*, *85*(4), 896–904.

Mayr, S. I., & Burkhardt, H. (2006). Ultrasonic properties of sedimentary rocks: Effect of pressure, saturation, frequency and microcracks. *Geophysical Journal International*, *164*(1), 246–258.

McClure, M. W., & Horne, R. N. (2014). Correlations between formation properties and induced seismicity during high pressure injection into granitic rock. *Engineering Geology*, *175*, 74–80. https://doi.org/https://doi.org/10.1016/j.enggeo.2014.03.015

McKay, R. H., & Noah, J. T. (1996). Integrated perspective of the depositional environment and reservoir geometry, characterization, and performance of the Upper Morrow Buckhaults Sandstone in the Farnsworth Unit, Ochiltree County, Texas. *CIRCULAR-OKLAHOMA GEOLOGICAL SURVEY*, *98*, 101–114.

McMillan, M. D. (2021). Stepwise Dynamic Calibration of a Hydromechanical Simulation Using Time- Lapse Vertical Seismic Profile. In *ProQuest Dissertations and Theses*. New Mexico Institute of Mining and Technology PP - United States -- New Mexico.

McMillan, M., Will, R., Ampomah, W., Balch, R., & Czoski, P. (2019a). Coupled geomechanical modeling to assess cap rock integrity and mechanical fault stability: Application to Farnsworth field unit project. *SPE Western Regional Meeting Proceedings*, *2019*. https://doi.org/10.2118/195377-ms

McMillan, M., Will, R., Ampomah, W., Balch, R., & Czoski, P. (2019b). Coupled Hydrodynamic- Geomechanical Modelling of CO2-WAG Field Development at Farnsworth Unit: A Case Study . https://doi.org/10.2118/195484-MS

Michael, A. J. (1984). Determination of stress from slip data: faults and folds. *Journal of Geophysical Research: Solid Earth*, *89*(B13), 11517–11526.

Moodie, N., Ampomah, W., Jia, W., & McPherson, B. (2021). Relative Permeability: A Critical Parameterin Numerical Simulations of Multiphase Flow in Porous Media. In *Energies* (Vol. 14, Issue 9). https://doi.org/10.3390/en14092370

Morgan, A., Grigg, R., & Ampomah, W. (2021). A Gate-to-Gate Life Cycle Assessment for the CO2-EOR Operations at Farnsworth Unit (FWU). In *Energies* (Vol. 14, Issue 9). https://doi.org/10.3390/en14092499

Mousavi, S. M., Langston, C. A., & Horton, S. P. (2016). Automatic microseismic denoising and onset detection using the synchrosqueezed continuous wavelet transform. *Geophysics*, *81*(4), V341–V355.

Munson, T. W. (1989). Depositional, Diagenetic, and Production History of the upper Morrowan Buckhaults Sandstone, Farnsworth Field Ochiltree County Texas. 1–20.

Nagel, N. B. (2001). Compaction and subsidence issues within the petroleum industry: From Wilmington to Ekofisk and beyond. *Physics and Chemistry of the Earth, Part A: Solid Earth and Geodesy*, *26*(1–2), 3–14.

Nes, O.-M., Holt, R. M., & Fjær, E. (2000). The reliability of core data as input to seismic reservoir monitoring studies. *Spe European Petroleum Conference*.

Nes, O.-M., Holt, R. M., & Fjær, E. (2002). The reliability of core data as input to seismic reservoir monitoring studies. *SPE Reservoir Evaluation & Engineering*, *5*(01), 79–86.

NETL (National Energy Technology Laboratory). (2017). Site screening, site selection, and site characterization for geological storage projects. *Best Practices*. https://netl.doe.gov/sites/default/files/2018-10/BPM-SiteScreening.pdf%0Ahttp://files/42/BPM- SiteScreening.pdf

Pan, F., McPherson, B. J., Dai, Z., Jia, W., Lee, S.-Y., Ampomah, W., Viswanathan, H., & Esser, R. (2016). Uncertainty analysis of carbon sequestration in an active CO2-EOR field. *International Journal of Greenhouse Gas Control*, *51*, 18–28.

Parker, R. L. (1956). Farnsworth Morrow Oil Field. *Geonews*, *4*, 5–12.

Pattillo, P. D., Kristiansen, T. G., Sund, G. V, & Kjelstadli, R. M. (1998). Reservoir compaction and seafloor subsidence at Valhall. *SPE/ISRM Rock Mechanics in Petroleum Engineering*.

Pei, S., Peng, Z., & Chen, X. (2018). Locations of Injection-Induced Earthquakes in Oklahoma Controlled by Crustal Structures. *Journal of Geophysical Research: Solid Earth*, *123*. https://doi.org/10.1002/2017JB014983

Pranter, M., and N. F. Hurley. Dual-Lateral Horizontal Wells Successfully Target Bypassed Pay in the San Andres Formation, Vacuum Field, New Mexico. *AAPG Bulletin*, vol. 88, 2004, doi:10.1306/03b3c1f6-edc1-4327-b74d0f98bfaa446b.

Rascoe, B., & Adler, F. J. (1983). Permo-Carboniferous hydrocarbon accumulations, mid-continent, USA. *AAPG Bulletin*, *67*(6), 979–1001.

Raknes, E. B., and B. Arntsen, 2015, A numerical study of 3D elastic time-lapse full-waveform inversion using multicomponent seismic data: Geo-physics, 80, no. 6, R303–R315.

Rasmussen, L., Fan, T., Rinehart, A., Luhmann, A., Ampomah, W., Dewers, T., Heath, J., Cather, M., & Grigg, R. (2019). Carbon Storage and Enhanced Oil Recovery in Pennsylvanian Morrow Formation Clastic Reservoirs: Controls on Oil–Brine and Oil–CO2 Relative Permeability from Diagenetic Heterogeneity and Evolving Wettability. *Energies*, *12*, 3663. https://doi.org/10.3390/en12193663

Rickett, J., and D. E. Lumley, 2001, Cross-equalization data processing for time-lapse seismic reservoir monitoring: A case study from the Gulf of Mexico: Geophysics, 66, 1015–1025.

Rose-Coss, D., Wampomah, W., Hutton, A. C., Gragg, E., Mozley, P., Balch, R. S., & Grigg, R. (2015). Geologic characterization for co 2-eor simulation: A case study of the farnsworth unit, anadarko basin, texas. *AAPG Annual Convention and Exhibition*.

Ross-Coss, D., Ampomah, W., Cather, M., Balch, R., Mozley, P., & Rasmussen, L. (2016). *An Improved Approach for Sandstone Reservoir Characterization*. https://doi.org/10.2118/180375-

Routh, P., J. Krebs, S. Lazaratos, A. Baumstein, S. Lee, Y. H. Cha,I. Chikichev, N. Downey, D. Hinkley, and J. Anderson, 2011, Encoded simultaneous source full wavefield inversion for spectrally shaped marine streamer data: 81st Annual International Meeting, SEG, Expanded Abstracts, 2433–2438.

Rutledge, J. Interpreting reservoir microseismicity detected during CO2 injection at the Aneth Oil Field. In Proceedings of the AGU Fall Meeting Abstracts, 2009, Vol. 2009, pp. U41B–0021.

Schlumberger. VISAGE Reference Manual—Schlumberger Private; Schlumberger: Houston, TX, USA, 2018.

Shapiro, S. A. (2003). Elastic piezosensitivity of porous and fractured rocks. *Geophysics*, *68*(2), 482–486. Skoumal, R. J., Kaven, J. O., Barbour, A. J., Wicks, C., Brudzinski, M. R., Cochran, E. S., & Rubinstein, J.

Skoumal, R. J., Kaven, J. O., Barbour, A. J., Wicks, C., Brudzinski, M. R., Cochran, E. S., & Rubinstein, J. L. (2021). The induced Mw 5.0 March 2020 west Texas seismic sequence. *Journal of Geophysical Research: Solid Earth*, *126*(1), e2020JB020693.

Snee, J.-E. L., & Zoback, M. D. (2022). State of stress in areas of active unconventional oil and gas development in North America. *AAPG Bulletin*, *106*(2), 355–385.

Sorenson, R. P. (2005). A dynamic model for the Permian Panhandle and Hugoton fields, western Anadarko basin. *AAPG Bulletin*, *89*(7), 921–938.

Stork, A. L., Verdon, J. P., & Kendall, J.-M. (2014). Assessing the effect of velocity model accuracy on microseismic interpretation at the In Salah carbon capture and storage site. *Energy Procedia*, *63*, 4385– 4393.

Streit, J. E., & Hillis, R. R. (2004). Estimating fault stability and sustainable fluid pressures for underground storage of CO2 in porous rock. *Energy*, *29*(9–10), 1445–1456.

Taillander, C., Noble, M., Chauris, H., Calandra, H., 2009. First-arrival traveltime tomography based on the adjoint-state method. Geophysics 74 (6), WCB1–WCB10.

Thiercelin, M. J., & Plumb, R. A. (1994). Core-based prediction of lithologic stress contrasts in east Texas formations. *SPE Formation Evaluation*, *9*(04), 251–258.

Tutuncu, A. N., & Bui, B. T. (2016). A coupled geomechanics and fluid flow model for induced seismicity prediction in oil and gas operations and geothermal applications. *Journal of Natural Gas Science and Engineering*, *29*, 110–124. https://doi.org/https://doi.org/10.1016/j.jngse.2015.12.039

van Wijk, J., Hobbs, N., Rose, P., Mella, M., Axen, G., & Gragg, E. (2021). Analysis of Geologic CO2 Migration Pathways in Farnsworth Field, NW Anadarko Basin. In *Energies* (Vol. 14, Issue 22). https://doi.org/10.3390/en14227818

Vavryčuk, V. (2015). Moment tensor decompositions revisited. *Journal of Seismology*, *19*, 231–252.

Verdon, J. P., Kendall, J.-M., & Maxwell, S. C. (2010). A comparison of passive seismic monitoring of fracture stimulation from water and CO 2 injection. *Geophysics*, *75*(3), MA1–MA7.

Vigh, D., Jiao, K., Watts, D., & Sun, D. (2014). Elastic full-waveform inversion application using multicomponent measurements of seismic data collection. Geophysics, 79(2), R63-R77.

Virieux, J., and S. Operto, 2009, An overview of full-waveform inversion in exploration geophysics: Geophysics, 74, no. 6, WCC1–WCC26.

Wang, Z., M. E. Cates, and R. T. Langan, 1998, Seismic monitoring of a CO2 flood in a carbonate reservoir: A rock physics study: Geophysics, 63, 1604–1617.

White, D. (2009). Monitoring CO2 storage during EOR at the Weyburn-Midale Field. *The Leading Edge*, *28*, 838–842. https://doi.org/10.1190/1.3167786

White, M. D., McPherson, B. J., Grigg, R. B., Ampomah, W., & Appold, M. S. (2014). Numerical Simulation of Carbon Dioxide Injection in the Western Section of the Farnsworth Unit. *Energy Procedia*, *63*, 7891– 7912. https://doi.org/https://doi.org/10.1016/j.egypro.2014.11.825

Wiemer, S. (2001). A software package to analyze seismicity: ZMAP. *Seismological Research Letters*, *72*(3), 373–382.

Will, R., Bratton, T., Ampomah, W., Acheampong, S., Cather, M., & Balch, R. (2021a). Time-Lapse Integration at FWU: Fluids, Rock Physics, Numerical Model Integration, and Field Data Comparison. *Energies*, *14*(17), 5476. *Energies*, *14*, 5476. https://doi.org/10.3390/en14175476

Winkler, K. W. (1986). Estimates of velocity dispersion between seismic and ultrasonic frequencies. *Geophysics*, *51*(1), 183–189.

Woodward, M. J., D. Nichols, O. Zdraveva, P. Whitfield, and T. Johns, 2008, A decade of tomography: Geophysics, 73, no. 5, VE5–VE11.

Xiao, T., McPherson, B., Esser, R., Jia, W., Dai, Z., Chu, S., Pan, F., & Viswanathan, H. (2020). Chemical Impacts of Potential CO2 and Brine Leakage on Groundwater Quality with Quantitative Risk Assessment: A Case Study of the Farnsworth Unit. *Energies*, *13*, 6574. https://doi.org/10.3390/en13246574

Yue, T., & Xiao-Fei, C. (2005). A rapid and accurate two-point ray tracing method in horizontally layered velocity model. *Acta Seismologica Sinica*, *18*, 154–161.

Zhang, Z., and L. Huang, 2013, Double-difference elastic-waveform inversion with prior information for time-lapse monitoring Geophysics, 78, no. 6, R259-R273.

Zhou, R., Huang, L., & Rutledge, J. (2010). Microseismic event location for monitoring CO2 injection using double-difference tomography. *The Leading Edge*, *29*(2), 208–214.

Zoback, M. D., Barton, C. A., Brudy, M., Castillo, D. A., Finkbeiner, T., Grollimund, B. R., Moos, D. B., Peska, P., Ward, C. D., & Wiprut, D. J. (2003). Determination of stress orientation and magnitude in deep wells. *International Journal of Rock Mechanics and Mining Sciences*, *40*(7–8), 1049–1076.

Zoback, M. D., & Lund Snee, J.-E. (2018). Predicted and observed shear on preexisting faults during hydraulic fracture stimulation. In *SEG Technical Program Expanded Abstracts 2018* (pp. 3588–3592). Society of Exploration Geophysicists. https://doi.org/doi:10.1190/segam2018-2991018.1

Zoback, M. D., Moos, D., Mastin, L., & Anderson, R. N. (1985). Well bore breakouts and in situ stress. Journal of Geophysical Research: Solid Earth, 90(B7), 5523–5530.